

出藍 第35号

2022年5月

目次

【原著論文(査読有)】

- 1 Optimization of Residual Stress Measurement Conditions for a 2D Method Using X-ray Diffraction and Its Application for Stainless Steel Treated by Laser Cavitation Peening 1
Hitoshi Soyama, Chieko Kuji, Tsunemoto Kuriyagawa, Christopher R. Chighizola, Michael R. Hill:
Materials, Vol.14, No.11, pp.2772.
- 2 Laser-induced nanopillar structures around particles 18
Liwei Chen, Ziqi Chen, Keita Shimada, Masayoshi Mizutani, Tsunemoto Kuriyagawa:
Applied Surface Science, Vol.572, (2022) pp.151453.
- 3 Crystallization behavior and machining properties of annealed Fe-Si-B-Cr amorphous alloys 30
Chieko Kuji, Kana Takenaka, Masayoshi Mizutani, Keita Shimada, Tsunemoto Kuriyagawa, Toyohiko J. Konno:
Journal of Materials Science, Vol.56, No.29, pp.16697-16711.
- 4 パウダージェットデポジションによる歯冠色修復 45
本郷那美, 山本浩己, 簾内崇彰, 富江瑛彦, 泉田一賢, 佐々木啓一, 嶋田慶太, 水谷正義, 厨川常元:
砥粒加工学会誌, Vol.65, No.10, pp.556-561.
- 5 Picosecond laser-induced nanopillar coverage of entire mirror-polished surfaces of Ti6Al4V alloy 51
Liwei Chen, Yifei Zhang, Shuhei Kodama, Shaolin Xu, Keita Shimada, Masayoshi Mizutani, Tsunemoto Kuriyagawa:
Precision Engineering, Vol.72, pp.555-567.
- 6 軸対称非球面研削における研削条件の最適化 63
吉原 信人, 嶋田 慶太, 水野 雅裕, 厨川 常元:
精密工学会誌, Vol.88, No.2, pp.193-197.

【国際会議プロシーディング(査読有)】

- 1 Pico-Precision & Hybrid Machining for High Value Manufacturing 68
Tsunemoto Kuriyagawa, The 23rd International Symposium on Advances in Abrasive Technology(ISAAT2021)

2 Control of the porosity and its orientation of Bio-implants adopting Metal Additive Manufacturing	69
Masayoshi Mizutani, Shinji Ishibashi, Masaki Tsukuda, Takumi Mizoi, Masataka Chuzenji, Keita Shimada, Tsunemoto Kuriyagawa, The 23rd International Symposium on Advances in Abrasive Technology(ISAAT2021)	
3 The Exploration of the Frontiers of High Value Manufacturing Based on Nanotechnology	74
Tsunemoto Kuriyagawa, The CHINA-JAPAN International Conference on Ultra-Precision Machining Process (CJUMP2021)	
4 Effect of Heat Treatment on Blanking of Fe-Si-B-Cr Amorphous Alloys	75
Chieko Kuji, Masayoshi Mizutani, Keita Shimada, Toyohiko J Konno, Momoji Kubo, Tsunemoto Kuriyagawa, The CHINA-JAPAN International Conference on Ultra-Precision Machining Process (CJUMP2021)	

【解説記事・紹介記事】

1 高付加価値ものづくりを目指す機能創成加工	76
厨川 常元, JTEKT ENGINEERING JOURNAL, No.18, (2021) pp.3-8.	

【国内発表】

1 ウルトラファインバブルクーラントのぬれ性と研削性能	82
畑山陽介, 大越広夢, 水谷正義, 厨川常元, 2021 年度砥粒加工学会学術講演会(ABTEC2021)	
2 歯科用着色ジルコニアクラウンの 3D 造形技術の開発 第 1 報 : 着色ジルコニア粉末を用いたセラミックス 3D 造形への適応	84
近藤直樹, 水谷正義, 佐々木啓一, 厨川常元, 2021 年度砥粒加工学会学術講演会(ABTEC2021)	
3 アモルファス金属の加工技術開発	90
久慈 千栄子, 文部科学省ナノテクノロジープラットフォーム 令和 3 年度利用成果発表会	
4 放電加工時のデブリ発生とジャンプパラメータが加工効率に及ぼす影響	91
湯田健太郎, 黒川聡昭, 齊藤大揮, 水谷正義, 厨川常元, 2021 年度精密工学会東北支部学術講演会	

【博士論文】

1 Creation of Functional Three-Dimensional Structure with Metal Additive Manufacturing Technology (金属積層造形技術による機能性 3 次元構造創成に関する研究)	94
石橋 信治, 令和 3 年度機械機能創成専攻博士学位論文要旨	
2 歯科用パウダージェットデポジションにおける加工メカニズムに関する研究(Study of Processing Mechanism in Dental Powder Jet Deposition)	97
富江 瑛彦, 令和 3 年度医工学研究科修士学位論文要旨	

- 3 局在微細組織制御を援用したアモルファス合金の加工性向上に関する研究 (Study on machinability of amorphous alloys by localized microstructure control) 100
久慈 千栄子, 令和3年度機械機能創成専攻博士学位論文要旨

【修士論文】

- 1 金属積層造形法を用いた3次元窒素拡散チタン構造体創成に関する研究 102
伊藤 優汰, 令和3年度機械機能創成専攻修士学位論文要旨
- 2 ナノ精度研削砥石のための均一分散分級技術の開発 104
木島 悠, 令和3年度機械機能創成専攻修士学位論文要旨
- 3 Ti合金の切削加工における工具テクスチャリングの影響 106
皆川 敦暉, 令和3年度機械機能創成専攻修士学位論文要旨
- 4 プラズマ援用パウダージェットデポジションに関する研究 108
森田 隆輝, 令和3年度機械機能創成専攻修士学位論文要旨

【厨川研究室学位論文一覧】

- 1 厨川研究室博士・修士論文一覧 110.

Article

Optimization of Residual Stress Measurement Conditions for a 2D Method Using X-ray Diffraction and Its Application for Stainless Steel Treated by Laser Cavitation Peening

Hitoshi Soyama ^{1,*} , Chieko Kuji ², Tsunemoto Kuriyagawa ² , Christopher R. Chighizola ³ and Michael R. Hill ³ 

¹ Department of Finemechanics, Tohoku University, Sendai 980-8579, Japan

² Department of Mechanical Systems Engineering, Tohoku University, Sendai 980-8579, Japan; kuji.shinkou@gmail.com (C.K.); tkuri@tohoku.ac.jp (T.K.)

³ Department of Mechanical and Aerospace Engineering, University of California Davis, Davis, CA 95616, USA; crchighizola@ucdavis.edu (C.R.C.); mrhill@ucdavis.edu (M.R.H.)

* Correspondence: soyama@mm.mech.tohoku.ac.jp; Tel.: +81-22-795-6891

Abstract: As the fatigue strength of metallic components may be affected by residual stress variation at small length scales, an evaluation method for studying residual stress at sub-mm scale is needed. The $\sin^2\psi$ method using X-ray diffraction (XRD) is a common method to measure residual stress. However, this method has a lower limit on length scale. In the present study, a method using a 2D XRD detector with ω -oscillation is proposed, and the measured residual stress obtained by the 2D method is compared to results obtained from the $\sin^2\psi$ method and the slitting method. The results show that the 2D method can evaluate residual stress in areas with a diameter of 0.2 mm or less in a stainless steel with average grain size of 7 μm . The 2D method was further applied to assess residual stress in the stainless steel after treatment by laser cavitation peening (LCP). The diameter of the laser spot used for LCP was about 0.5 mm, and the stainless steel was treated with evenly spaced laser spots at 4 pulses/ mm^2 . The 2D method revealed fluctuations of LCP-induced residual stress at sub-mm scale that are consistent with fluctuations in the height of the peened surface.

Keywords: residual stress; X-ray diffraction; laser cavitation peening; pulse laser



Citation: Soyama, H.; Kuji, C.; Kuriyagawa, T.; Chighizola, C.R.; Hill, M.R. Optimization of Residual Stress Measurement Conditions for a 2D Method Using X-ray Diffraction and Its Application for Stainless Steel Treated by Laser Cavitation Peening. *Materials* **2021**, *14*, 2772. <https://doi.org/10.3390/ma14112772>

Academic Editors: Thomas Walter Cornelius and Souren Grigorian

Received: 23 April 2021
Accepted: 20 May 2021
Published: 24 May 2021

Publisher's Note: MDPI stays neutral with regard to jurisdictional claims in published maps and institutional affiliations.



Copyright: © 2021 by the authors. Licensee MDPI, Basel, Switzerland. This article is an open access article distributed under the terms and conditions of the Creative Commons Attribution (CC BY) license (<https://creativecommons.org/licenses/by/4.0/>).

1. Introduction

As residual stress is one of the most important factors related to the fatigue strength of metallic materials [1–8], it is worth measuring the residual stress in local areas subject to fatigue crack nucleation. It is well known that conventional welding causes tensile residual stress near the welded line due to the heat-affected zone (HAZ) [9–12]. Friction stir welding (FSW) also generates tensile residual stress near the FSW region [13–18], as FSW produces stirring and a thermo-mechanically affected zone. Residual stress is one of the key factors for mechanical surface treatments such as shot peening (SP) [19]. Laser peening can also improve fatigue properties by introducing compressive residual stress [20–23]. As the distribution of the residual stress of conventional welding and the FSWed part drastically changes with distance from the welding line, the residual stress of the laser-peened surface is also distributed with a laser spot size of the mm-order. One of the conventional methods used to evaluate the residual stress is X-ray diffraction. As the size of the measured area using X-ray diffraction is similar to that of the distribution of the residual stress of the welding part and/or the laser-peened surface in sub-millimeter order, it is necessary to improve the accuracy of residual stress measurements by using X-ray diffraction. Note that the most important factor of the stresses measurement accuracy in local area using X-ray diffraction is the number of the grains.

The $\sin^2\psi$ method is the most popular method for evaluating the residual stress of polycrystal metals using X-ray diffraction [24], and a 2D method using a two-dimensional

detector has been developed [25]. Regarding JSMS standard, 3×10^5 to 6×10^5 grains is required for the $\sin^2\psi$ method. Each method is based on its own theory, and each has advantages and disadvantages. For example, in the case of the $\sin^2\psi$ method, a simple goniometer is sufficient to evaluate the residual stress. On the other hand, the 2D method can evaluate the 3D stress state, but a highly accurate multi-axis goniometer is needed. The great advantage of using a 2D detector is that the Debye ring can be evaluated by interpolation and extrapolation. Namely, the 2D method using a 2D detector could be used to evaluate residual stress of very small area and/or coarse grain. A 2D method with specimen oscillation by moving the detector in the direction orthogonal to θ -direction was proposed to obtain better Debye ring in the reference [26], but the obtained result was not compared with the result obtained using the other method. One way to evaluate residual stress measurements using X-ray diffraction is to compare them with mechanical relaxation method such as a slitting method [27] and/or a hole drilling method [28]. The slitting method is relatively easy to perform, can be performed quickly, and provides excellent repeatability, which makes it very useful for actual laboratory residual stress measurements [27]. As the experimental deviation of the slitting method was smaller than that of the hole drilling method [29], the slitting method was chosen in the present experiment.

As mentioned above, laser peening introduces compressive residual stress and enhances the fatigue properties [20–23]. Y. Sano et al. measured the residual stress distribution with depth for stainless steel SUS304 and demonstrated an improvement in fatigue strength by laser peening without protective coating [21]. In the case of laser peening with coating [20,22], coating or tapes such as black polymer tape or metal foil is pasted on material to control laser energy absorption and prevent the surface from melting. The distributions of residual stress were precisely measured, but fluctuations due to the laser spot were not observed [30,31]. The distribution of changes in residual stress with depth was precisely measured, but there was no information provided for the distribution on the surface [32,33]. On the other hand, in the case of the numerical simulation, residual stress distributions due to laser spots were clearly observed [6,34–36]. Recently, the patterns of residual stress on the surface due to laser spots were also observed [37,38]. G. Xu et al. measured the residual stress of SUS316L by the $\sin^2\psi$ method, in which the diameter of the measured area was 2 mm with a 0.5 mm step; the laser spot was $3 \times 3 \text{ mm}^2$; the overlapping rates were 30%, 50% and 70%; and the cyclic pattern of the residual stress was obtained [37]. X. Pan et al. measured the residual stress of Ti6Al4V by the $\sin^2\psi$ method, in which the diameter of the measuring area was 2 mm with a 1 mm step, the laser spot was 2.4 mm, the overlapping rate was 40% and a cyclic pattern due to laser spots was not observed in the distribution of residual stress [39]. Using a synchrotron, Y. Sano et al. measured the distribution of the residual stress crossing over a single laser spot with 1D line irradiation by measuring an area of 0.2 mm in diameter; the laser spot was about 1 mm in diameter and the authors reported the tensile residual stress due to the laser spot [38]. It was determined by numerical simulation that the crack propagation was affected by the residual stress distribution due to laser peening [40,41]; therefore, the precise distribution of the residual stress had to be determined. Figure 1 shows the typical pattern of a fractured fatigue specimen of a stainless steel (a) non-peened specimen and (b) laser-peened specimen [23]. As shown in Figure 1b, the fatigue crack of the laser-peened specimen propagated nearly straight compared with that of the non-peened one, in which several cracks were propagated in parallel due to the increase of the hardness near the crack tips by plastic deformation. The distribution of residual stress of laser peened specimen. The distribution of residual stress of the laser peened specimen could be one of the reasons for crack propagation. Considering a previous report [38], the measurement of the residual stress in a submillimeter-order area is required. Thus, a method that can measure residual stress at a submillimeter level using a conventional X-ray diffraction apparatus is needed.

This paper consists of two parts. The first half reveals the optimization of measuring the condition of the 2D method using a two-dimensional detector for residual stress

measurements to evaluate the surface modification layer compared with the mechanical method, i.e., the slitting method [27], and the $\sin^2\psi$ method [24]. The second half demonstrates the residual stress measurement of the peened specimen by laser cavitation peening using the proposed 2D method.

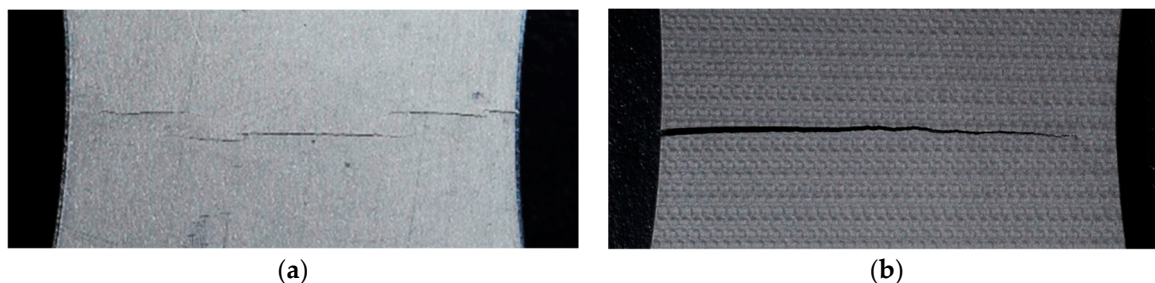


Figure 1. Aspect of a fractured fatigue specimen of stainless steel. (a) Non-peened specimen ($\sigma_a = 301$ MPa, $N_f = 7.8 \times 10^5$); (b) specimen treated by laser cavitation peening ($\sigma_a = 308$ MPa, $N_f = 4.8 \times 10^6$).

2. Experimental Apparatus and Procedures

2.1. Peening Systems

To prepare specimens with compressive residual stress, cavitation peening (CP) using a cavitating jet (see Figure 2) and laser cavitation peening (LCP) using a pulse laser (see Figure 3) were applied. In the case of CP, a high-speed water jet was injected into a water-filled chamber. The cavitating conditions were the same as those in a previous paper [8]; the injection pressure of the jet was 30 MPa, the diameter of the nozzle d was 2 mm and the standoff distance was 222 mm. To enhance the peening intensity, the nozzle had a cavitator with a diameter d_c of 3 mm [42] and an outlet bore with a diameter D and length L of 16 and 16 mm, respectively [43]. The specimen was installed in the recess. In the case of LCP, a Nd:YAG (Nd:Y₃Al₅O₁₂) laser with Q-switch was used to generate laser cavitation [12]. The repetition frequency of the pulse laser was 10 Hz. The used wavelength was 1064 nm. The pulse laser was focused onto the specimen, which was placed in a water-filled glass chamber. The standoff distance in the air s_a and in water s_w was optimized by measuring the peening intensity [12]. The specimen based the stage was moved perpendicularly to the direction of the laser axis by the stepping motors.

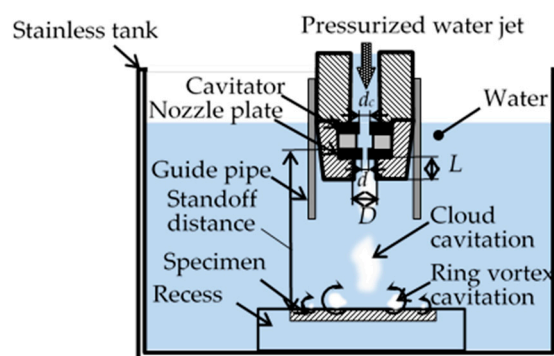


Figure 2. Schematic diagram of cavitation peening (CP) using a cavitating jet.

As the backside surface of the peened plate had compressive residual stress [44], a recirculating shot peening (SP) system accelerated by a water jet [45] was used for the peening. Note that compressive residual stress was introduced onto the backside surface, but the grain size on the back side was not affected, as the backside surface was not peened. At SP, the shots were installed a chamber, whose diameter was 54 mm, and accelerated by the water jet through three holes with a diameter of 0.8 mm. The diameter and the number of the shots were 3.2 mm and 500, respectively. The injection pressure of the water jet was

12 MPa. The distance from the nozzle to the specimen surface was 50 mm. To avoid a loss of shots, the specimen was set in the recess.

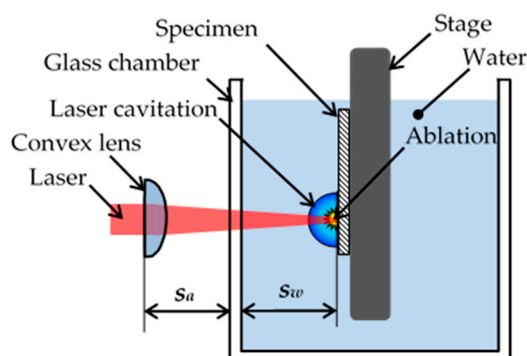


Figure 3. Schematic diagram of cavitation peening using a pulse laser, i.e., laser cavitation peening (LCP).

2.2. Material

The tested material was austenitic stainless steel, Japanese Industrial Standards JIS SUS316L. Four different specimens were used, as shown in Table 1. All specimens were made from plates 2, 3 and 6 mm in thickness, respectively, and all the plates featured a No. 2B surface finish accomplished by temper rolling. Specimen A was used to measure the residual stress of the peened side by the 2D method compared with the slitting method and $\sin^2\psi$ method. Specimens A, B and C were used to optimize the measuring conditions of the 2D method. Specimen D was used to demonstrate the effect of the laser spot on the residual stress distribution. During LCP, the surface was laser and the outermost surface showed tensile residual stress; the surface was then removed by electrochemical polishing. The peening intensity of CP, SP and LCP was controlled based on processing time per unit length, processing time and pulse density, respectively. The processing time per unit length of specimen A was chosen based on the values in the reference [8]. To introduce large compressive residual stress into the specimen, 100 pulses/mm² pulse density and 6 mm thickness were chosen for specimen B. Considering the results of the preliminary experiment by measuring the residual stress, 30 s and 3 mm thickness were chosen for specimen C. For specimen D, the pulse density of 4 pulses/mm² was optimized by measuring the fatigue life changes based on pulse density.

Table 1. Specimens for residual stress measurements.

Symbol	Peening Method	Peening Intensity	Thickness	Measured Side	Electrochemical Polishing
A	Cavitation peening CP	8 s/mm	2 mm	Peened side	None
B	Laser cavitation peening LCP	100 pulses/mm ²	6 mm	Peened side	39 μm
C	Shot peening SP	30 s	3 mm	Back side	None
D	Laser cavitation peening LCP	4 pulses/mm ²	2 mm	Peened side	33 μm

As mentioned above, the number of grains in the measurement area is important factor for the accuracy of the stresses using X-ray diffraction method. The average grain size, i.e., spatial diameter [46] and the grain size that occupied 50% of the area d_N were measured. The d_N was obtained by the following procedure. The area A_i of each grain was measured and they were sorted from small value to large value, then the cumulated area A_C was calculated as follows.

$$A_C = \sum_{i=1}^N A_i \quad (1)$$

when the number N at $A_C/A = 50\%$ was obtained, $d_N = 2\sqrt{A_N/\pi}$ was defined as the grain size that occupied 50%. Here, A was test area. 300 grains were measured in the present experiment.

Figure 4 illustrates a schematic diagram of specimen D and the coordinates of the residual stress with the scanning direction of the laser. The specimen was moved at 5 mm/s, and the repetition frequency of the laser was 10 Hz. Then, the specimen was stepped at 0.5 mm, as shown in Figure 4. The positional relationship of the laser spots in each row was different for each row as shown in Figure 4, as the stepping motors and pulse laser were not synchronized. Note that the rolling direction was y -direction in Figure 4.

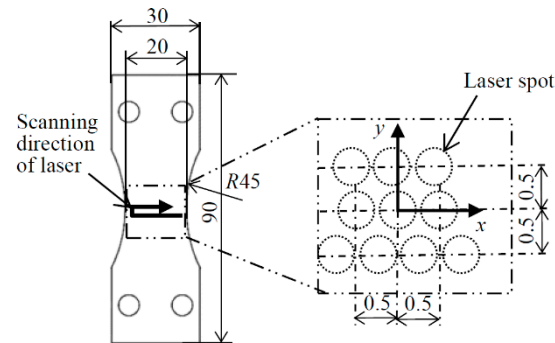


Figure 4. Schematic diagram of specimen D treated by laser cavitation peening and the coordinates for residual stress measurement.

2.3. Residual Stress Measurement

To confirm the compressive residual stress of specimen A introduced by cavitation peening, the residual stress was measured using the slitting method [27]. The slitting was done using a wire electric discharge machine (EDM, Sodick, Chicago, IL, USA), and the residual stress was evaluated from the strain obtained by the strain gage. The diameter of the wire was 0.254 mm and the gage length of the strain gage was 0.81 mm. The distribution of the residual stress with depth under the surface was obtained by using the recorded strain and solving an inverse problem following the procedure in the reference [15]. In the present paper, slitting of 0.0254 mm in depth was used as the reference value. The distribution of the residual stress with depth and more details on the slitting method can be found in the reference [8].

To measure the residual stress by X-ray diffraction, an XRD system (Bruker Japan K. K., Tokyo, Japan) with a two-dimensional position sensitive proportional counter (2D-PSPC) was used. The same system was used for the $\sin^2\psi$ method [24] and 2D method [47]. The schematic diagram and coordinates θ , ψ , ω , χ , φ of the XRD system with 2D-PSPC are shown in Figure 5. The $K\alpha$ X-rays from a Cr-tube operating at 35 kV and 40 mA were used. The used diffracted plane was γ -Fe (2 2 0), and the diffraction angle without strain was 128° . In the residual stress analysis for both the $\sin^2\psi$ method and the 2D method, Relevant software (Leptos ver 7.9, Bruker Japan K. K., Tokyo, Japan) was used. The used Young's modulus and Poisson ratio were 191.975 GPa and 0.3, respectively. To investigate the effects of the measuring area, five different collimators with diameters of 0.1460, 0.3, 0.5, 0.5724 and 0.8 mm were used. The 0.1460 and 0.5724 mm collimators were of the total reflection type, and the other collimators were of the double-holed type. Tables 2 and 3 show the measuring conditions and analyzed areas of X-ray diffraction obtained using each method based on the standard method [24] and the previous report [26]. Under both the $\sin^2\psi$ method and the 2D method, 24 frames were measured. In the case of the $\sin^2\psi$ method, the X-ray diffraction profile obtained an accumulating X-ray diffraction of $\chi = 85\text{--}95^\circ$, and diffracted peaks 2θ were obtained at each ψ . Then, the residual stress was calculated from the $\sin^2\psi - 2\theta$ diagram. To eliminate the ψ split, $+\psi$ and $-\psi$ were measured for each x and y direction. At the $\sin^2\psi$ method, σ_{Rx} was obtained by $\varphi = 90^\circ$ and 270° , σ_{Ry} was obtained

by $\varphi = 0$ and 180° , respectively. Namely, 12 frames in Table 2 were used to obtain σ_{Rx} and σ_{Ry} , respectively.

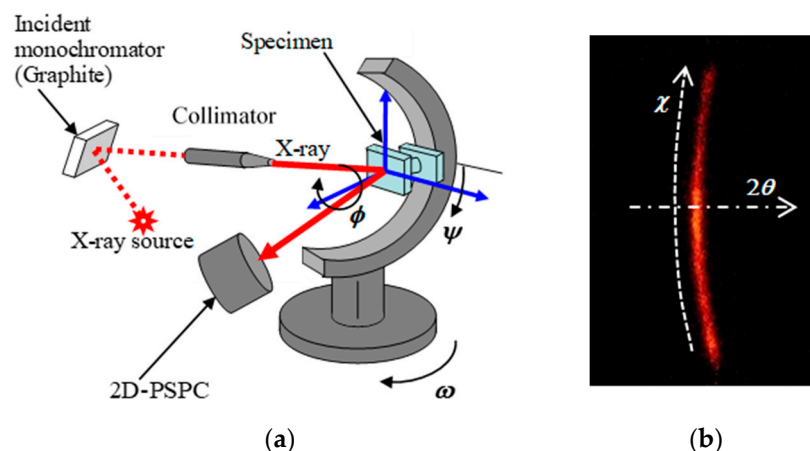


Figure 5. Schematic diagram and coordinates of XRD system with 2D-PSPC. (a) Coordinates of the system; (b) coordinates on the 2D-PSPC.

Table 2. Measuring conditions for each method.

Method	ψ°	φ°
$\sin^2\psi$ method	0	0, 90, 180, 270
	20.268	0, 90, 180, 270
	29.334	0, 90, 180, 270
	36.870	0, 90, 180, 270
	43.854	0, 90, 180, 270
	50.768	0, 90, 180, 270
2D method	0	0, 45, 90, 135, 180, 225, 270, 315
	30	0, 45, 90, 135, 180, 225, 270, 315
	60	0, 45, 90, 135, 180, 225, 270, 315

Table 3. Analyzed area of obtained X-ray diffraction.

Method	$2\theta^\circ$	χ°
$\sin^2\psi$ method	125–132	85–95
2D method	125–132	70–110

2.4. Observation of Specimen Surface

To investigate the grain size of the tested material, the surface was observed using a scanning electron microscope (SEM; JCM-7000, JEOL Ltd., Tokyo, Japan). The aspect of the laser-cavitation-peened specimen was also observed using a laser confocal microscope (VK-100, Keyence Corporation, Osaka, Japan) to obtain the surface profile.

3. Results

3.1. Comparison of Measured Residual Stress between the Slitting Method, $\sin^2\psi$ Method and 2D Method

In order to compare the residual stress measured by the slitting method, the $\sin^2\psi$ method and the 2D method, Figure 6 illustrates the residual stress σ_{Ry} of specimen A. For the $\sin^2\psi$ method and the 2D method, the effect of the measuring area was investigated by changing diameter of the collimator d_{col} . As shown in Figure 6, the exposure time at each frame t_{exp} was also changed based on the area of the collimator. In the case of $d_{col} = 0.8$ mm and $t_{exp} = 20$ s, the specimen was moved in both directions, $x = \pm 2$ mm and $y = \pm 2$ mm,

to minimize the exposure time. As shown in Figure 6, in the case of $d_{col} = 0.8$ mm and $t_{exp} = 40$ s at $x = \pm 0$ mm and $y = \pm 0$ mm, the residual stress σ_R measured using the $\sin^2\psi$ method and the 2D method was -220 ± 74 and -220 ± 14 MPa; these results are similar to -251 ± 16 MPa, which was measured by the slitting method. For the $\sin^2\psi$ method, the residual stress measured using $d_{col} \geq 0.5724$ mm was similar to that of the slitting method. However, at $d_{col} \leq 0.5$ mm, the residual stress was too small and the standard deviation of the residual stress was too large. For the reference, Appendix A reveals the diagram of $\sin^2\psi - 2\theta$ for $d_{col} = 0.146$ mm, $t_{exp} = 20$ min and $d_{col} = 0.8$ mm, $t_{exp} = 40$ s. On the other hand, in the case of the 2D method, the residual stress measured using $d_{col} = 0.146$ mm was -187 ± 29 MPa. Thus, it can be concluded that the 2D method can evaluate the residual stress by using $d_{col} = 0.146$ mm. Specifically, the 2D method can measure the residual stress in the 1/15 region of the $\sin^2\psi$ method under the presented conditions.

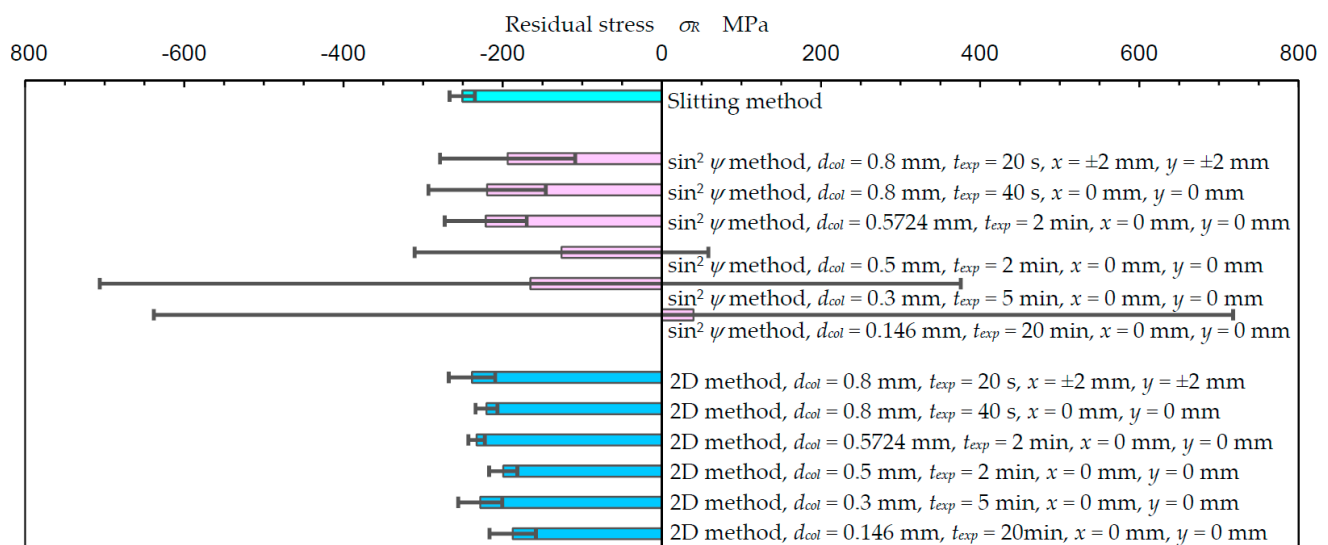


Figure 6. Comparison of the slitting method, $\sin^2\psi$ method, and the 2D method for the residual stress of stainless steel treated by cavitation peening (specimen A).

In order to investigate the difference in the measurement of residual stress between the $\sin^2\psi$ method and the 2D method for the austenitic stainless steel tested using a collimator of $d_{col} = 0.146$ mm, Figure 7 shows the aspects of the surface of the measured sample observed using a scanning electron microscope (SEM). The average grain size, i.e., spatial diameter [46], was 6.6 ± 4.0 μm in diameter, and the grain size that occupied 50% of the area was about 11 μm . As shown in Figure 7, specific anisotropy is not observed. Thus, at the present condition, the rolling direction did not affect the results of residual stress measurement.

Figure 8 illustrates a typical X-ray diffraction pattern that was a part of the Debye ring, as detected by 2D-PSPC from the stainless steel treated by cavitation peening—i.e., specimen A treated using $d_{col} = 0.146$ mm—and the analyzed area for (a) the $\sin^2\psi$ method and (b) the 2D method. As illustrated in Figure 7, the grain size was about 1/10 of the diameter of the collimator, and the X-ray diffraction pattern was a mottled pattern, as shown in Figure 8. In the case of the $\sin^2\psi$ method, the diffraction pattern located near $\chi \approx 90^\circ$ should be used due to the theory of the $\sin^2\psi$ method; the standard deviations of the $\sin^2\psi$ method at $d_{col} \leq 0.5$ mm were remarkably large, as the diffraction pattern at $\chi \approx 90^\circ$ was weak or not obtained. For the present residual stress analysis, $\chi = 85\text{--}95^\circ$ was used for the $\sin^2\psi$ method. The residual stress obtained by the $\sin^2\psi$ method for $d_{col} = 0.8$ mm, $t_{exp} = 40$ s, $x = 0$ mm and $y = 0$ mm was -300 ± 46 MPa based on analysis using $2\theta = 125\text{--}132^\circ$ and $\chi = 70\text{--}110^\circ$. These values were too large compared to the value of -251 ± 16 MPa measured by the slitting method. Namely, when large area, i.e., $\chi = 70\text{--}110^\circ$, was used, the number of counts of the X-ray diffraction was increased. However, $\chi = 70\text{--}110^\circ$ was too large for the $\sin^2\psi$ method.

On the other hand, $\chi = 70\text{--}110^\circ$ was used for the 2D method, as the 2D method obtained the residual stress from the distortion of the Debye ring. For the 2D method, the Debye ring was obtained by interpolation and extrapolation of the patchy patterns of the diffraction spots. It was concluded that the 2D method could evaluate the residual stress in a smaller area compared to the $\sin^2\psi$ method, as the Debye ring was used in the relatively large area of χ . Thus, it can be said that the key point for evaluating the residual stress in a small area is to obtain a more uniform Debye ring.

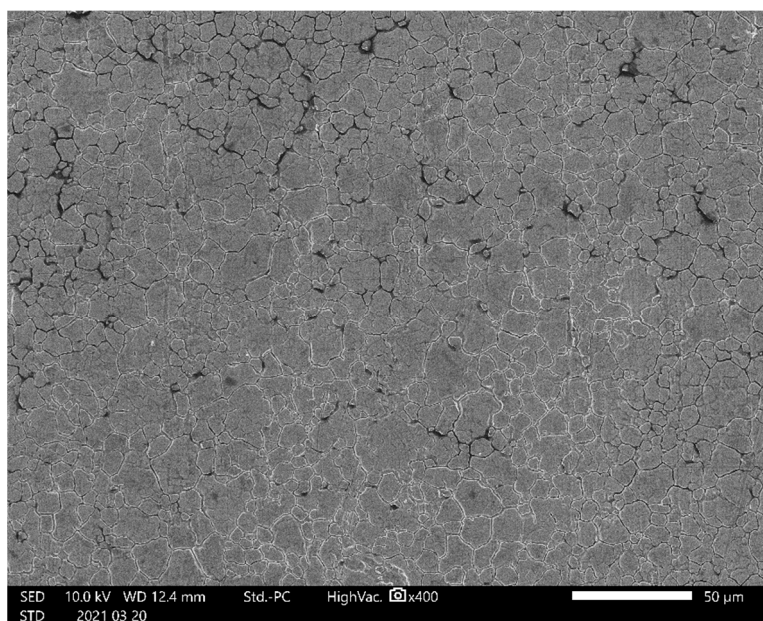


Figure 7. Aspect of the surface of specimen A observed by scanning electron microscope (SEM).

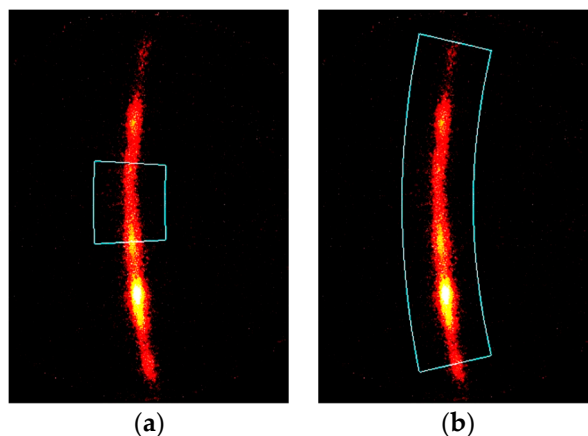


Figure 8. Typical X-ray diffraction pattern detected by 2D-PSPC from stainless steel treated using cavitation peening (Specimen A) and the analyzed area ($d_{col} = 0.146$ mm, $\psi = 0^\circ$, $\varphi = 0^\circ$, $\Delta\omega = 0^\circ$, $t_{exp} = 20$ min, $x = 0$ mm, $y = 0$ mm); (a) analyzed area for the $\sin^2\psi$ method ($2\theta = 125\text{--}132^\circ$, $\chi = 85\text{--}95^\circ$); (b) analyzed area for the 2D method ($2\theta = 125\text{--}132^\circ$, $\chi = 70\text{--}110^\circ$).

3.2. Optimum Condition for the 2D Method to Evaluate Residual Stress

In the present paper, to obtain a better Debye ring, specimen oscillation in the ω direction—i.e., ω -oscillation—was proposed. Figure 9 shows the X-ray diffraction pattern (a) without ω -oscillation (i.e., $\Delta\omega = 0^\circ$) and (b) with ω -oscillation at $\Delta\omega = 10^\circ$. As shown in Figure 9a ($\psi = 0$, $\varphi = 0$) and (b) ($\psi = 0$, $\varphi = 0$), the diffraction spot at $\chi \approx 102^\circ$ became a streak by ω -oscillation. Precisely, the diffraction spot became a streak in the χ direction by ω -oscillation of the specimen. The ω -oscillation helped to achieve a better

Debye ring. Note that, in the case of 2D method, there should be an optimum value of $\Delta\omega$, as the residual stress was obtained by the distortion of Debye ring. The optimum value of $\Delta\omega$ is discussed in the following.

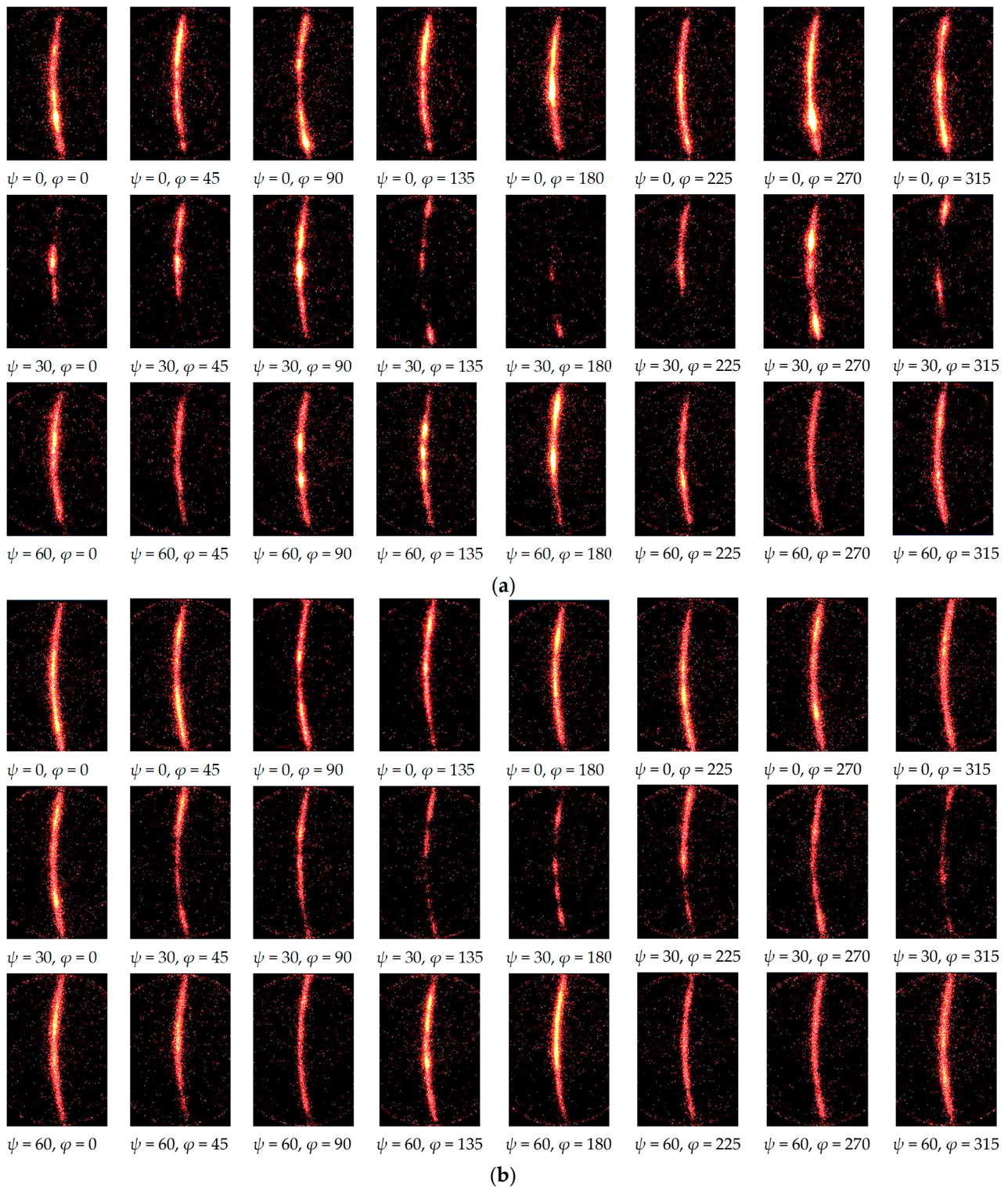


Figure 9. X-ray diffraction patterns detected by 2D-PSPC from the stainless steel treated by cavitation peening (Specimen A). (a) $\Delta\omega = 0^\circ$; (b) $\Delta\omega = 10^\circ$.

In order to investigate the ω -oscillation of the specimen both qualitatively and quantitatively, Figure 10 shows the typical X-ray diffraction pattern of specimen A at $\psi = 0^\circ$

and $\varphi = 0$ changing with (a) the collimator diameter d_{col} , (b) the exposure time t_{exp} and (c) the ω -oscillation angle $\Delta\omega$. Figure 11 illustrates the relationship between the total count of X-ray diffraction and the standard deviation of the residual stress $\Delta\sigma_R$. As shown in Figure 10a, the X-ray diffraction pattern became a mottled pattern with a decrease in the diameter of the collimator d_{col} . Then, the $\Delta\sigma_R$ increased with a decrease of d_{col} , as shown in Figure 11. When the exposure time t_{exp} was increased, the Debye ring became clear, as shown in Figure 10b, and then $\Delta\sigma_R$ decreased with an increase of t_{exp} . As shown in Figure 11, $\Delta\sigma_R$ decreased with an increase in the total count of X-ray diffraction for both d_{col} and t_{exp} . As shown in Figure 10c, the diffraction pattern changed from a mottled pattern to a streak-like pattern with an increase of $\Delta\omega$. The $\Delta\sigma_R$ was 64 MPa for $\Delta\omega = 0^\circ$, 49 MPa for $\Delta\omega = 2^\circ$, 49 MPa for $\Delta\omega = 4^\circ$, 37 MPa for $\Delta\omega = 6^\circ$, 29 MPa for $\Delta\omega = 8^\circ$ and 32 MPa for $\Delta\omega = 10^\circ$. Specifically, $\Delta\sigma_R$ decreased with an increase of $\Delta\omega$ at $\Delta\omega = 0-8^\circ$ and presented its minimum at $\Delta\omega = 8^\circ$; then, $\Delta\sigma_R$ slightly increased at $\Delta\omega = 10^\circ$. As the 2D method evaluates the residual stress caused by distortion of the Debye ring, a $\Delta\omega$ that is too large dims the distortion by averaging too large an area in the χ direction. Thus, it can be concluded that the ω -oscillation of the specimen was effective, and the optimum value of $\Delta\omega$ was 8° . In Figure 11, $\Delta\sigma_R = 64$ MPa. In Figure 11, $\Delta\sigma_R = 64$ MPa for $\Delta\omega = 0^\circ$ corresponds to $t_{exp} = 4$ or 5 min and $\Delta\sigma_R = 29$ MPa for $\Delta\omega = 8^\circ$ corresponds to $t_{exp} = 20$ min. Thus, ω -oscillation of the specimen has the effect of shortening the measurement time to 1/4–1/5.

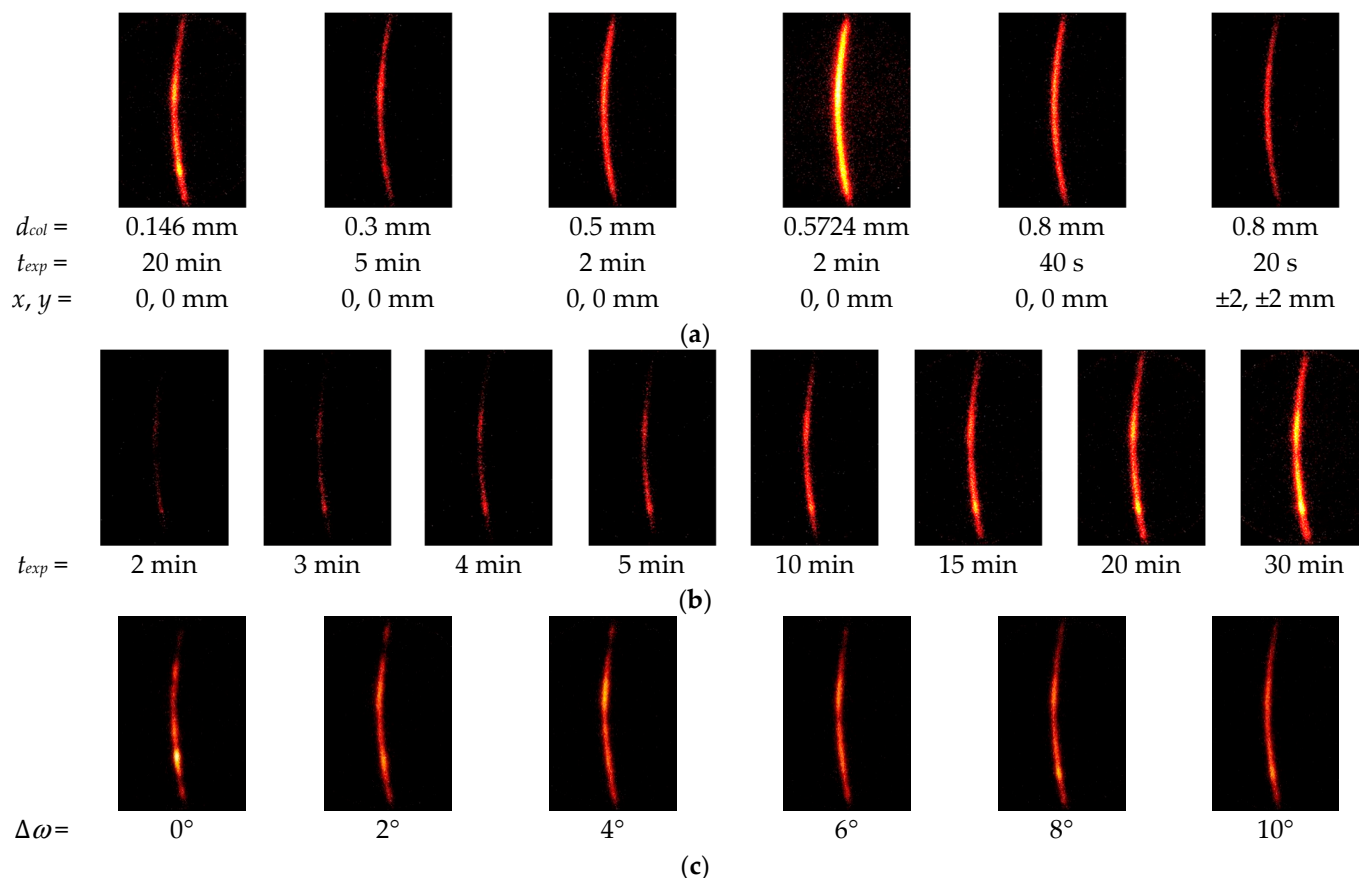


Figure 10. Typical X-ray diffraction patterns detected by 2D-PSPC at $\psi = 0^\circ$ and $\varphi = 0^\circ$ from stainless steel treated by cavitation peening (Specimen A). (a) effect of the collimator diameter d_{col} at $\Delta\omega = 8^\circ$; (b) effect of exposure time t_{exp} at $d_{col} = 0.146$ mm and $\Delta\omega = 8^\circ$; (c) effect of the ω -oscillation angle $\Delta\omega$ at $d_{col} = 0.146$ mm and $t_{exp} = 20$ min.

In order to confirm that the 2D method can evaluate the residual stress of the austenitic stainless steel by using the 0.146 mm-diameter collimator, Figure 12a reveals the residual stress (σ_{Rx} , σ_{Ry}) of specimen A, B and C as a function of the diameter of the collimator d_{col} ,

and Figure 12b shows the standard deviation of the residual stress. The data for specimen A in Figure 6 were used as the σ_{Ry} in Figure 12. For all three specimens, A, B and C, as both σ_{Rx} and σ_{Ry} at $d_{col} = 0.146$ mm were nearly equal to the values at $d_{col} = 0.8$ mm, the residual stresses of $d_{col} = 0.146$ mm for specimens A, B and C were able to be evaluated.

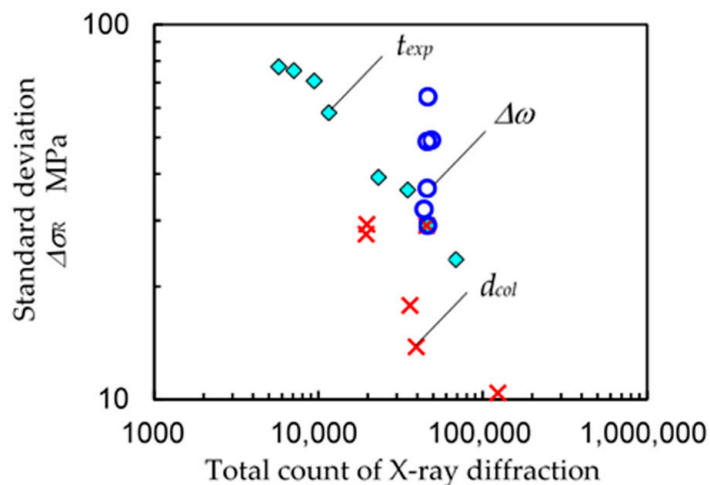


Figure 11. Relationship between the counts at $\psi = 0^\circ$ and $\varphi = 0^\circ$ detected by 2D-PSPC and the standard deviation of the residual stress of stainless steel treated by cavitation peening (specimen A) changing with exposure time t_{exp} , collimator diameter d_{col} and ω -oscillation angle $\Delta\omega$.

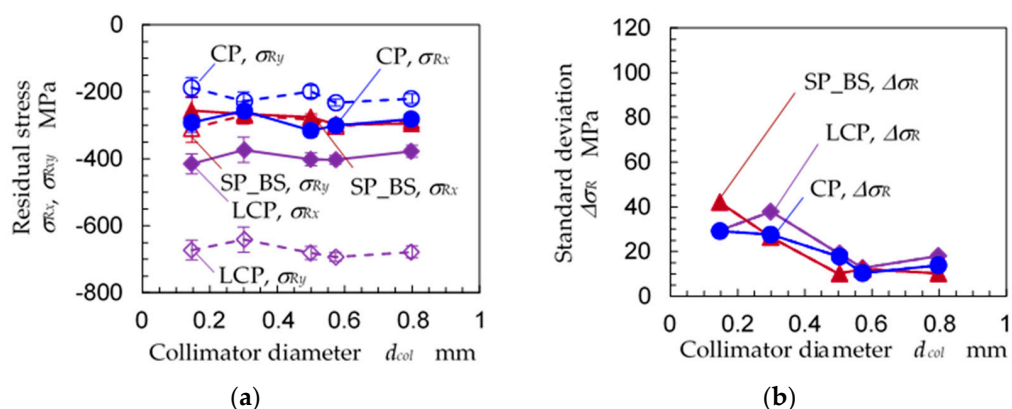


Figure 12. Effect of the collimator diameter on the residual stress measurement of the stainless steel by the 2D method ($\Delta\omega = 8^\circ$); CP: specimen A, LCP: specimen B, SP_BS: specimen C. (a) residual stress; (b) standard deviation of residual stress.

In the case of specimen B, i.e., LCP, the specimen was treated with 100 pulses/mm², as mentioned in Table 1. The specimen was moved in the x -direction at 1 mm/s. As the repetition frequency of the pulse laser was 10 Hz, the distance of each laser spot was 0.1 mm. After each specimen was treated in the x -direction, it was moved stepwise at 0.1 mm in the y -direction. As shown in Figure 12a, σ_{Rx} and σ_{Ry} were about -400 MPa and -670 MPa, respectively. Specifically, the compressive residual stress introduced in y -direction, i.e., the stepwise direction, under laser cavitation peening was 270 MPa larger than that in the x -direction. Even though the distances between the laser spots in both x - and y -direction were the same, the compressive residual stress introduced in the y -direction was larger than that in the x -direction. This tendency was similar to the results in the reference [38].

In the present experiment, SP was applied, then the residual stress on the back side of shot peened specimen was measured to avoid the effects of the change of the grain size etc.

If the treated surfaces by SP, CP and LCP were evaluated, the characteristics of the peened surfaces have different features. It was reported that the dislocation density of CP and LCP of austenitic stainless steel SUS316L was lower than that of SP at the equivalent peening condition, i.e., the equivalent arc height condition [48].

In order to investigate the effects of ω -oscillation of the specimen, Figure 13 reveals the residual stress (σ_{Rx} , σ_{Ry}) and the standard deviation of the residual stress $\Delta\sigma_R$ as a function of the ω -oscillation angle $\Delta\omega$ for specimens A, B and C. As shown in Figure 13, the residual stress of specimen A, B and C was roughly constant for all $\Delta\omega$ values, and $\Delta\sigma_R$ roughly decreased with an increase of $\Delta\omega$. In the case of LCP, i.e., specimen C, the compressive residual stress increased with an increase of $\Delta\omega$ at $\Delta\omega \leq 8^\circ$; then, the compressive residual stress slightly decreased at $\Delta\omega = 10^\circ$. Further, the $\Delta\sigma_R$ of specimen C had its minimum at $\Delta\omega = 8^\circ$, and the $\Delta\sigma_R$ at $\Delta\omega = 10^\circ$ was larger than the $\Delta\sigma_R$ of $\Delta\omega = 8^\circ$. As the 2D method obtained the residual stress from the distortion of the Debye ring, a $\Delta\omega$ value that was too large caused a decrease of the residual stress and an increase of $\Delta\sigma_R$, just as with specimen A. It can be concluded that the ω -oscillation of the specimen is effective for evaluating the residual stress and that the optimum value of $\Delta\omega$ is 8° .

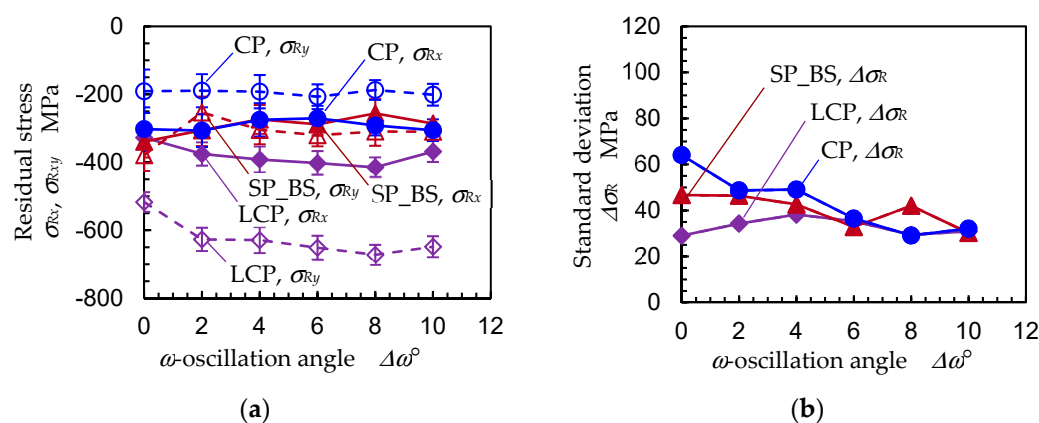


Figure 13. Effect of the ω -oscillation angle $\Delta\omega$ on the residual stress measurement of stainless steel using the 2D method ($d_{col} = 0.146$ mm, $t_{exp} = 20$ min); CP: specimen A, LCP: specimen B, SP_BS: specimen C; (a) residual stress; (b) standard deviation of residual stress.

In order to determine the optimum exposure time needed to obtain the X-ray diffraction pattern, Figure 14 shows (a) the residual stress σ_{Rx} , σ_{Ry} and (b) standard deviation of the residual stress $\Delta\sigma_R$ as a function of exposure time t_{exp} for specimens A, B and C. Under all measurement conditions in Figure 14, the specimens were oscillated at $\Delta\omega = 8^\circ$, and the diameter of the collimator was 0.146 mm. For specimens A and B, the σ_{Rx} and σ_{Ry} were nearly constant at all t_{exp} values. For specimen C, σ_{Rx} and σ_{Ry} decreased and became saturated at $t_{exp} = 15$ and 20 min. The $\Delta\sigma_R$ of specimens A, B and C decreased with an increase of t_{exp} and became saturated at $t_{exp} = 15$ or 20 min. Under the studied conditions, $t_{exp} = 20$ min is the optimum exposure time to obtain residual stress. The X-ray diffraction totaled about 4.6×10^4 counts.

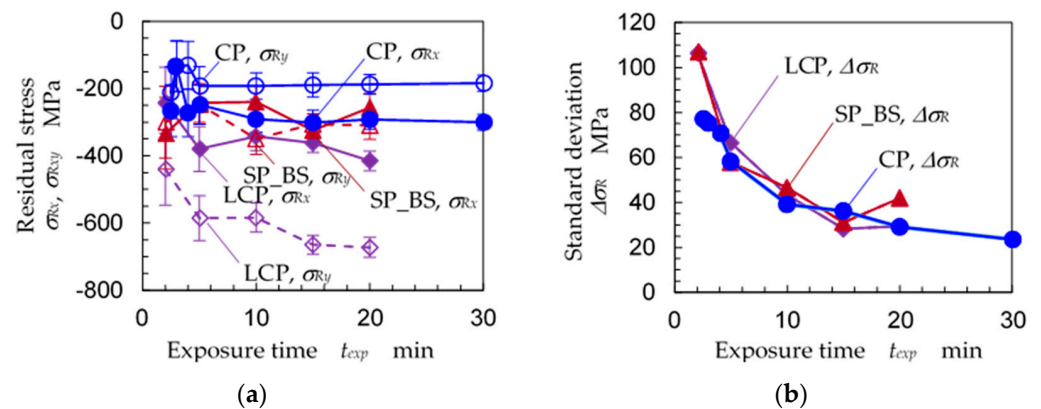


Figure 14. Effect of exposure time t_{exp} on the residual stress measurements of stainless steel under the 2D method ($d_{col} = 0.146$ mm, $\Delta\omega = 8^\circ$); CP: specimen A, LCP: specimen B, SP_BS: specimen C. (a) Residual stress; (b) standard deviation of residual stress.

3.3. Residual Stress Distribution of Specimen Treated by Laser Cavitation Peening

To determine the typical results for the residual stress of austenitic stainless steel JIS SUS316L in the local area measured by the 2D method, the residual stress of the specimen treated by laser cavitation peening, i.e., that of specimen D, was evaluated using the 2D method. Considering the results in Sections 3.1 and 3.2, the measuring conditions were as follows: The diameter of the collimator d_{col} was 0.146 mm, the ω -oscillation angle $\Delta\omega$ was 8° and the exposure time of each frame t_{exp} was 20 min. The pulse density of the laser cavitation peening d_L was 4 pulses/ mm^2 , as the fatigue life was greatest at $d_L = 4$ pulses/ mm^2 and changed with the pulse density [23]. Under these conditions, the laser spot distances in the x - and y -directions were 0.5 and 0.5 mm, respectively. As mentioned above, the top surface revealed tensile residual stress, and then the surface of 33 μm was removed by electrochemical polishing. Note that the residual stress at 30 μm accurately corresponded to the fatigue life, as the fatigue life estimated by the residual stress at 30 μm , the surface hardness and the surface roughness was proportional to the experimental value [23].

Figure 15 shows (a) the aspects of the laser-cavitation-peened specimen observed using a CCD camera on the XRD system and (b) the aspects of the same specimen observed using a laser confocal microscope. As the specimen was treated with $d_L = 4$ pulses/ mm^2 , the distances of the x - and y -directions between the laser spots were 0.5 and 0.5 mm. Under the presented conditions, the depth of the laser spot was about 10 μm . As shown in Figure 15, the laser spot diameter was about 0.5 mm after the 33 μm electrochemical polishing. The vertical positional relationship of the laser spots was not aligned, as the stepping motor and laser system were not synchronized.

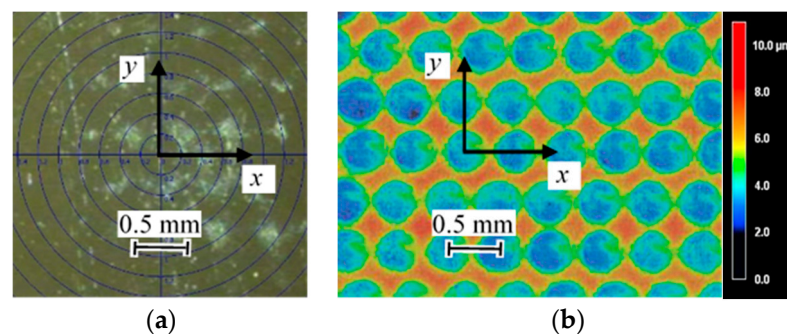


Figure 15. Aspects of the surface of the stainless-steel specimen treated by laser cavitation peening (specimen D); (a) observation using the CCD camera on the XRD system; (b) observations from the laser confocal microscope.

Figure 16 shows the residual stress distribution as a function of y at $x = 0, 0.125, 0.25, 0.375$ and 0.5 mm for (a) σ_{Rx} and (b) σ_{Ry} . The standard deviation at the residual stress was about 70 MPa. It was difficult to recognize the 0.5 mm interval period at each position of x , as shown in Figure 16a,b, because the positional relationships of the laser spots at $y = 0, 0.5, 1, 1.5$ and 2 mm were different, as shown in Figure 15. As σ_{Rx} and σ_{Ry} varied from 0 to -150 MPa, there was a difference of about 150 MPa depending on the location for both σ_{Rx} and σ_{Ry} .

Figure 17 reveals the residual stress σ_{Rx} and σ_{Ry} changing with distance x at $y = 0$ with the laser spot aligned in the x -direction. The σ_{Rx} was about -100 MPa at $x = 0$ mm; it had a peak of 0 MPa at $x = 0.125$ mm and then decreased with an increase in x . Then, σ_{Rx} had a minimum of 150 MPa at $x = 0.375$ mm and increased to 0 MPa at $x = 0.5$ mm. On the other hand, σ_{Ry} had a minimum at $x = 0.125$ mm and a maximum at $x = 0.375$ mm. Even though the standard deviations were somewhat large, a 0.5 mm cycle was observed for both σ_{Rx} and σ_{Ry} . It can be concluded from Figures 16 and 17 that the residual stress may differ by about 150 MPa depending on the location when austenitic stainless steel JIS SUS316L is treated using laser cavitation peening at 4 pulses/mm². As shown in Figures 12 and 13, when the residual stress was relatively uniform, the experimental deviation at the present condition using the 0.146 mm collimator was about ± 40 MPa. At the measurement of LCP specimen treated at 4 pulse/mm², the residual stress was changed from 0 MPa to -150 MPa within 0.25 mm in length, thus the experimental deviation using the 0.146 mm collimator was about ± 70 MPa due to the spatial distribution.

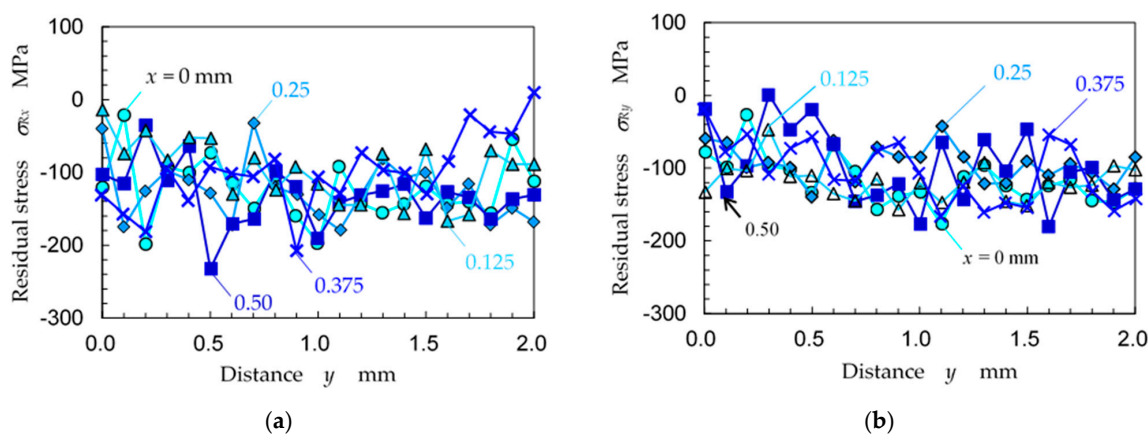


Figure 16. Distribution of the residual stress changing with distance y at various positions of x (specimen D); (a) residual stress in the x -direction σ_{Rx} ; (b) residual stress in the y -direction σ_{Ry} .

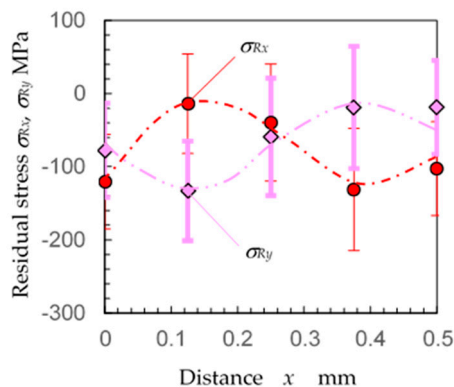


Figure 17. Distribution of the residual stress σ_{Rx} and σ_{Ry} changing with distance x (specimen D).

4. Conclusions

To clarify the possibilities and measure the conditions of residual stress in a mechanical-surface-modified layer with a small area by the 2D method using X-ray diffraction, the

residual stress of the austenitic stainless steel JIS SUS316L treated by cavitation peening was measured by the 2D method changing with the diameter of the collimator comparing with the $\sin^2\psi$ method and the slitting method. The measured sample was austenitic stainless steel with temper rolling. The average diameter and 50% area of the grain size of the tested specimen were $6.6 \pm 4.0 \mu\text{m}$ and about $11 \mu\text{m}$, respectively. The specimens were treated by cavitation peening using a cavitating jet and a pulse laser, i.e., laser cavitation peening. The results obtained can be summarized as follows:

- (1) Compared to the $\sin^2\psi$ method, the 2D method can evaluate the residual stress in a small area, which is 1/15 of the area ratio of the $\sin^2\psi$ method. In the present experiment, the measurable areas of the $\sin^2\psi$ method and 2D method were 0.5724 mm in diameter and 0.146 mm in diameter, respectively.
- (2) The ω -oscillation of the specimen using the 2D method had the effect of reducing the measurement error to 1/2. This result is equivalent to the effect of reducing the measurement time to 1/5–1/4. The optimum ω -oscillation angle $\Delta\omega$ was 8° .
- (3) The 2D method using optimized conditions can evaluate the residual stress distribution for a laser spot with a diameter of 0.5 mm.
- (4) The compressive residual stress under laser cavitation peening at 100 pulses/ mm^2 was larger in the stepwise direction than in the orthogonal direction.

Author Contributions: Conceptualization, H.S., C.K. and T.K.; methodology, H.S., C.K. and M.R.H.; validation, H.S. and C.R.C.; formal analysis, H.S. and C.R.C.; investigation, H.S. and C.R.C.; resources, H.S.; data curation, H.S. and C.R.C.; writing—original draft preparation, H.S.; writing—review and editing, H.S. and C.K.; funding acquisition, H.S.; supervision, T.K. and M.R.H. All authors have read and agreed to the published version of the manuscript.

Funding: This research was partly supported by JSPS KAKENHI Grant Number 18KK0103 and 20H02021.

Institutional Review Board Statement: Not applicable.

Informed Consent Statement: Not applicable.

Data Availability Statement: The data presented in this study are available on request from the author.

Conflicts of Interest: The authors declare no conflict of interest.

Appendix A

For the reference, Figure A1 shows the diagram of $\sin^2\psi - 2\theta$ for $d_{col} = 0.146 \text{ mm}$, $t_{exp} = 20 \text{ min}$ and $d_{col} = 0.8 \text{ mm}$, $t_{exp} = 40 \text{ s}$. As shown in Figure A1, the peak of the profile of the X-ray diffraction, i.e., the diffraction angle of $d_{col} = 0.146 \text{ mm}$ was scattered, therefore the experimental deviation in Figure 6 of $d_{col} = 0.146 \text{ mm}$ was large.

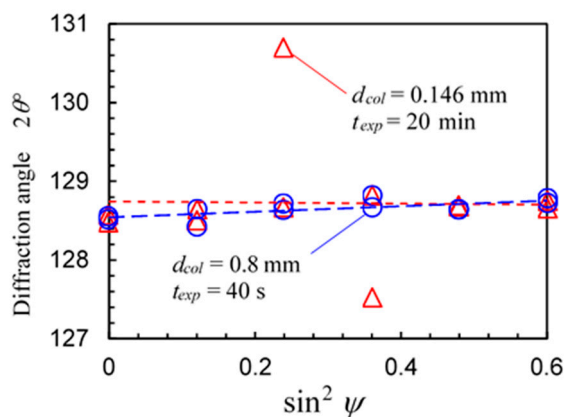
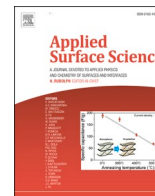


Figure A1. Relationship between $\sin^2\psi - 2\theta$ ($d_{col} = 0.146 \text{ mm}$, $t_{exp} = 20 \text{ min}$ and $d_{col} = 0.8 \text{ mm}$, $t_{exp} = 40 \text{ s}$).

References

1. Nikitin, I.; Scholtes, B.; Maier, H.J.; Altenberger, I. High temperature fatigue behavior and residual stress stability of laser-shock peened and deep rolled austenitic steel aisi 304. *Scr. Mater.* **2004**, *50*, 1345–1350. [[CrossRef](#)]
2. Withers, P.J. Residual stress and its role in failure. *Rep. Prog. Phys.* **2007**, *70*, 2211–2264. [[CrossRef](#)]
3. Gujba, A.K.; Medraj, M. Laser peening process and its impact on materials properties in comparison with shot peening and ultrasonic impact peening. *Materials* **2014**, *7*, 7925–7974. [[CrossRef](#)] [[PubMed](#)]
4. Soyama, H. Comparison between shot peening, cavitation peening and laser peening by observation of crack initiation and crack growth in stainless steel. *Metals* **2020**, *10*, 63. [[CrossRef](#)]
5. Arakawa, J.; Hanaki, T.; Hayashi, Y.; Akebono, H.; Sugeta, A. Evaluating the fatigue limit of metals having surface compressive residual stress and exhibiting shakedown. *Fatigue Fract. Eng. Mater. Struct.* **2020**, *43*, 211–220. [[CrossRef](#)]
6. Bikdeloo, R.; Farrahi, G.H.; Mehmanparast, A.; Mahdavi, S.M. Multiple laser shock peening effects on residual stress distribution and fatigue crack growth behaviour of 316L stainless steel. *Theor. Appl. Fract. Mech.* **2020**, *105*, 11. [[CrossRef](#)]
7. Tang, L.Q.; Ince, A.; Zheng, J. Numerical modeling of residual stresses and fatigue damage assessment of ultrasonic impact treated 304L stainless steel welded joints. *Eng. Fail. Anal.* **2020**, *108*, 23. [[CrossRef](#)]
8. Soyama, H.; Chighizola, C.R.; Hill, M.R. Effect of compressive residual stress introduced by cavitation peening and shot peening on the improvement of fatigue strength of stainless steel. *J. Mater. Process. Technol.* **2021**, *288*, 116877. [[CrossRef](#)]
9. Edwards, L.; Bouchard, P.J.; Dutta, M.; Wang, D.Q.; Santisteban, J.R.; Hiller, S.; Fitzpatrick, M.E. Direct measurement of the residual stresses near a ‘boat-shaped’ repair in a 20 mm thick stainless steel tube butt weld. *Int. J. Press. Vessels Pip.* **2005**, *82*, 288–298. [[CrossRef](#)]
10. Zhang, W.Y.; Jiang, W.C.; Zhao, X.; Tu, S.T. Fatigue life of a dissimilar welded joint considering the weld residual stress: Experimental and finite element simulation. *Int. J. Fatigue* **2018**, *109*, 182–190. [[CrossRef](#)]
11. Luo, Y.; Gu, W.B.; Peng, W.; Jin, Q.; Qin, Q.L.; Yi, C.M. A study on microstructure, residual stresses and stress corrosion cracking of repair welding on 304 stainless steel: Part i-effects of heat input. *Materials* **2020**, *13*, 2416. [[CrossRef](#)]
12. Soyama, H. Laser cavitation peening and its application for improving the fatigue strength of welded parts. *Metals* **2021**, *11*, 531. [[CrossRef](#)]
13. Webster, P.J.; Oosterkamp, L.D.; Browne, P.A.; Hughes, D.J.; Kang, W.P.; Withers, P.J.; Vaughan, G.B.M. Synchrotron X-ray residual strain scanning of a friction stir weld. *J. Strain Anal. Eng. Des.* **2001**, *36*, 61–70. [[CrossRef](#)]
14. Peel, M.; Steuwer, A.; Preuss, M.; Withers, P.J. Microstructure, mechanical properties and residual stresses as a function of welding speed in aluminium AA5083 friction stir welds. *Acta Mater.* **2003**, *51*, 4791–4801. [[CrossRef](#)]
15. Prime, M.B.; Gnaupel-Herold, T.; Baumann, J.A.; Lederich, R.J.; Bowden, D.M.; Sebring, R.J. Residual stress measurements in a thick, dissimilar aluminum alloy friction stir weld. *Acta Mater.* **2006**, *54*, 4013–4021. [[CrossRef](#)]
16. Haghshenas, M.; Gharghoury, M.A.; Bhakhri, V.; Klassen, R.J.; Gerlich, A.P. Assessing residual stresses in friction stir welding: Neutron diffraction and nanoindentation methods. *Int. J. Adv. Manuf. Technol.* **2017**, *93*, 3733–3747. [[CrossRef](#)]
17. Zhang, L.; Zhong, H.L.; Li, S.C.; Zhao, H.J.; Chen, J.Q.; Qi, L. Microstructure, mechanical properties and fatigue crack growth behavior of friction stir welded joint of 6061-T6 aluminum alloy. *Int. J. Fatigue* **2020**, *135*, 11. [[CrossRef](#)]
18. Soyama, H.; Simoncini, M.; Cabibbo, M. Effect of cavitation peening on fatigue properties in friction stir welded aluminum alloy AA5754. *Metals* **2021**, *11*, 59. [[CrossRef](#)]
19. Delosrios, E.R.; Walley, A.; Milan, M.T.; Hammersley, G. Fatigue-crack initiation and propagation on shot-peened surfaces in A316 stainless-steel. *Int. J. Fatigue* **1995**, *17*, 493–499. [[CrossRef](#)]
20. Peyre, P.; Fabbro, R.; Merrien, P.; Lieurade, H.P. Laser shock processing of aluminium alloys. Application to high cycle fatigue behaviour. *Mater. Sci. Eng. A* **1996**, *210*, 102–113. [[CrossRef](#)]
21. Sano, Y.; Obata, M.; Kubo, T.; Mukai, N.; Yoda, M.; Masaki, K.; Ochi, Y. Retardation of crack initiation and growth in austenitic stainless steels by laser peening without protective coating. *Mater. Sci. Eng. A* **2006**, *417*, 334–340. [[CrossRef](#)]
22. Gill, A.; Telang, A.; Mannava, S.R.; Qian, D.; Pyoun, Y.-S.; Soyama, H.; Vasudevan, V.K. Comparison of mechanisms of advanced mechanical surface treatments in nickel-based superalloy. *Mater. Sci. Eng. A* **2013**, *576*, 346–355. [[CrossRef](#)]
23. Soyama, H. Comparison between the improvements made to the fatigue strength of stainless steel by cavitation peening, water jet peening, shot peening and laser peening. *J. Mater. Process. Technol.* **2019**, *269*, 65–78. [[CrossRef](#)]
24. SMS Committee on X-ray Study of Mechanical Behavior of Materials. Standard method for X-ray stress measurement. *JSMS Stand.* **2005**, *JSMS-SD-10-05*, 1–21.
25. He, B.B.; Preckwinkel, U.; Smith, K. Advantage of using 2D detectors for residual stress measurements. *Adv. X-ray Anal.* **2000**, *42*, 429–438.
26. Takakuwa, O.; Soyama, H. Optimizing the conditions for residual stress measurement using a two-dimensional XRD method with specimen oscillation. *Adv. Mater. Phys. Chem.* **2013**, *03*, 8–18. [[CrossRef](#)]
27. Hill, M. The slitting method. In *Practical Residual Stress Measurement Methods*; Schajer, G.S., Ed.; John Wiley & Sons, Inc.: Hoboken, NJ, USA, 2013; pp. 89–108.
28. ASTM E837-13a. *Standard Test Method for Determining Residual Stresses by the Hole-Drilling Strain-Gage Method*; ASTM: West Conshohocken, PA, USA, 2020.
29. Chighizola, C.R.; D’Elia, C.R.; Weber, D.; Kirsch, B.; Aurich, J.C.; Linke, B.S.; Hill, M.R. Intermethod comparison and evaluation of measured near surface residual stress in milled aluminum. *Exp. Mech.* **2021**, in press.

30. Hatamleh, O.; Rivero, I.V.; Swain, S.E. An investigation of the residual stress characterization and relaxation in peened friction stir welded aluminum-lithium alloy joints. *Mater. Des.* **2009**, *30*, 3367–3373. [[CrossRef](#)]
31. Correa, C.; de Lara, L.R.; Diaz, M.; Gil-Santos, A.; Porro, J.A.; Ocana, J.L. Effect of advancing direction on fatigue life of 316L stainless steel specimens treated by double-sided laser shock peening. *Int. J. Fatigue* **2015**, *79*, 1–9. [[CrossRef](#)]
32. Kallien, Z.; Keller, S.; Ventzke, V.; Kashaev, N.; Klusemann, B. Effect of laser peening process parameters and sequences on residual stress profiles. *Metals* **2019**, *9*, 655. [[CrossRef](#)]
33. Wang, Z.D.; Sun, G.F.; Lu, Y.; Chen, M.Z.; Bi, K.D.; Ni, Z.H. Microstructural characterization and mechanical behavior of ultrasonic impact peened and laser shock peened AISI 316L stainless steel. *Surf. Coat. Technol.* **2020**, *385*, 19. [[CrossRef](#)]
34. Bhamare, S.; Ramakrishnan, G.; Mannava, S.R.; Langer, K.; Vasudevan, V.K.; Qian, D. Simulation-based optimization of laser shock peening process for improved bending fatigue life of Ti-6Al-2Sn-4Zr-2Mo alloy. *Surf. Coat. Technol.* **2013**, *232*, 464–474. [[CrossRef](#)]
35. Correa, C.; de Lara, L.R.; Diaz, M.; Porro, J.A.; Garcia-Beltran, A.; Ocana, J.L. Influence of pulse sequence and edge material effect on fatigue life of Al2024-T351 specimens treated by laser shock processing. *Int. J. Fatigue* **2015**, *70*, 196–204. [[CrossRef](#)]
36. Keller, S.; Chupakhin, S.; Staron, P.; Maawad, E.; Kashaev, N.; Klusemann, B. Experimental and numerical investigation of residual stresses in laser shock peened AA2198. *J. Mater. Process. Technol.* **2018**, *255*, 294–307. [[CrossRef](#)]
37. Xu, G.; Luo, K.Y.; Dai, F.Z.; Lu, J.Z. Effects of scanning path and overlapping rate on residual stress of 316L stainless steel blade subjected to massive laser shock peening treatment with square spots. *Appl. Surf. Sci.* **2019**, *481*, 1053–1063. [[CrossRef](#)]
38. Sano, Y.; Akita, K.; Sano, T. A mechanism for inducing compressive residual stresses on a surface by laser peening without coating. *Metals* **2020**, *10*, 816. [[CrossRef](#)]
39. Pan, X.L.; Li, X.; Zhou, L.C.; Feng, X.T.; Luo, S.H.; He, W.F. Effect of residual stress on S-N curves and fracture morphology of Ti6Al4V titanium alloy after laser shock peening without protective coating. *Materials* **2019**, *12*, 3799. [[CrossRef](#)]
40. Busse, D.; Ganguly, S.; Furfari, D.; Irving, P.E. Optimised laser peening strategies for damage tolerant aircraft structures. *Int. J. Fatigue* **2020**, *141*, 12. [[CrossRef](#)]
41. Sun, R.J.; Keller, S.; Zhu, Y.; Guo, W.; Kashaev, N.; Klusemann, B. Experimental-numerical study of laser-shock-peening-induced retardation of fatigue crack propagation in Ti-17 titanium alloy. *Int. J. Fatigue* **2021**, *145*, 13. [[CrossRef](#)]
42. Soyama, H. Enhancing the aggressive intensity of a cavitating jet by introducing a cavitator and a guide pipe. *J. Fluid Sci. Technol.* **2014**, *9*, 1–12. [[CrossRef](#)]
43. Soyama, H. Enhancing the aggressive intensity of a cavitating jet by means of the nozzle outlet geometry. *J. Fluids Eng.* **2011**, *133*, 1–11. [[CrossRef](#)]
44. Nishikawa, M.; Soyama, H. Two-step method to evaluate equibiaxial residual stress of metal surface based on micro-indentation tests. *Mater. Des.* **2011**, *32*, 3240–3247. [[CrossRef](#)]
45. Naito, A.; Takakuwa, O.; Soyama, H. Development of peening technique using recirculating shot accelerated by water jet. *Mater. Sci. Technol.* **2012**, *28*, 234–239. [[CrossRef](#)]
46. ASTM E112-13. *Standard Test Methods for Determining Average Grain Size*; ASTM: West Conshohocken, PA, USA, 2020.
47. He, B.B. *Two-Dimensional X-Ray Diffraction*; John Wiley & Sons, Inc.: Hoboken, NJ, USA, 2009; pp. 249–328.
48. Kumagai, M.; Curd, M.E.; Soyama, H.; Ungár, T.; Ribárik, G.; Withers, P.J. Depth-profiling of residual stress and microstructure for austenitic stainless steel surface treated by cavitation, shot and laser peening. *Mater. Sci. Eng. A* **2021**, *813*, 141037. [[CrossRef](#)]



Full Length Article

Laser-induced nanopillar structures around particles

Liwei Chen, Ziqi Chen, Keita Shimada¹, Masayoshi Mizutani^{*}, Tsunemoto Kuriyagawa

Department of Mechanical Systems Engineering, Graduate School of Engineering, Tohoku University, Sendai, 980-8579, Japan



ARTICLE INFO

Keywords:

LIPSS
Electromagnetic field
Nanopillar
Short-pulsed laser
FDTD

ABSTRACT

In biomedical engineering, laser-induced periodic surface structures (LIPSSs) have been extensively applied where laser irradiation of selective laser-melted (SLMed) samples to generate LIPSS-covered free-form samples is a promising technique. Using this technique, nanopillars around a spheroidal particle that was not molten during the SLM process have been formed, indicating that nanopillars can be induced around spheroidal particles on a material surface. This study investigates the mechanism of LIPSS and nanopillar formation on SLMed and uneven surfaces experimentally and through finite-difference time-domain simulation. A 50 Hz picosecond laser with 1064 nm fixed wavelength, 20 ps pulse duration, 0.5 J/cm² laser fluence, and 400 μm/s scanning speed was employed to irradiate Ti6Al4V alloy samples with 100 μs exposure time. The results show that induced nanopillars form a concentric area around a single particle with curvature radius approximately twice the particle radius. The simulated electric field intensity is ripple-like distributed for particle size beyond 5 μm, with approximately 1 μm periodic length and is close to the laser wavelength. This matches the experimental results from scanning electron microscopy for 800–00 nm LIPSS periodic length, indicating that desired nanostructures can be generated by appropriately designing the surface topography before laser irradiation.

1. Introduction

Laser-induced periodic surface structures (LIPSSs), first studied by Birnbaum in 1965 [1], have been observed on many materials [2], including semiconductors [3,4], metals [5], and polymers [6]. Since the discovery of LIPSSs, numerous researchers have focused on the physical mechanisms of LIPSS formation. The widely accepted theoretical techniques for LIPSS formation are based on either electromagnetic deposition theories [7–12] or matter reorganization theories [13–17]. The former suggests that the surface roughness results in optical scattering that may lead to the excitation of surface plasmon polaritons (SPPs) that interface with the incident light, modulating the absorbed fluence, and then modulated ablation in periodic surface structures [17,18]. Finally, the ripple-like structures were generated as LIPSS. The latter may involve thermodynamic phase transitions and hydrodynamic effects of the transiently melted surface [19,20], which indicates that the interference between the laser beam and electromagnetic field will cause spatial modulation of the electron density and electron temperature with periodic distribution. The subsequent coupling of the electronic system and solid lattice through electron–phonon coupling and thermal diffusion leads to a modulated lattice temperature distribution, local

ablation, and solidification, resulting in the final LIPSS pattern [17].

There have also been various experimental studies to discover the mechanism of LIPSS formation, and they have revealed that many conditions, including the materials, laser fluence, wavelength, pulse duration, polarization direction, surface roughness, and environment, influence LIPSS formation [21–25]. For instance, Reif et al. [20] presented a theoretical model to explain the process of LIPSS formation whose results exhibited excellent agreement with the experimental results. Their model showed that directional asymmetry in the pattern could result from spatial asymmetry of the initial excitation induced by a corresponding distribution of excited-electron kinetic energies. Based on the numerical simulation results, they concluded that the laser polarization direction played a decisive role in structure generation. Gurevich et al. [26] analyzed the different possible mechanisms of LIPSS formation during single-pulse and multipulse femtosecond laser irradiation. Plasmon excitation due to the surface roughness was tested, and a rapid decrease in the LIPSS period with the number of laser pulses was implied in multishot laser ablation experiments. Kodama et al. [27] studied the effects of surface microstructures formed before short-pulse laser irradiation on the resultant LIPSS and concluded that submicrometer-deep grooves facilitated the periodic propagation of surface plasma waves

^{*} Corresponding author.

E-mail addresses: chen.liwei.q3@dc.tohoku.ac.jp (L. Chen), masayoshi.mizutani.b6@tohoku.ac.jp (M. Mizutani).

¹ Present address: Applied Research Laboratory, High Energy Accelerator Research Organization, Tsukuba, 305-0801, Japan.

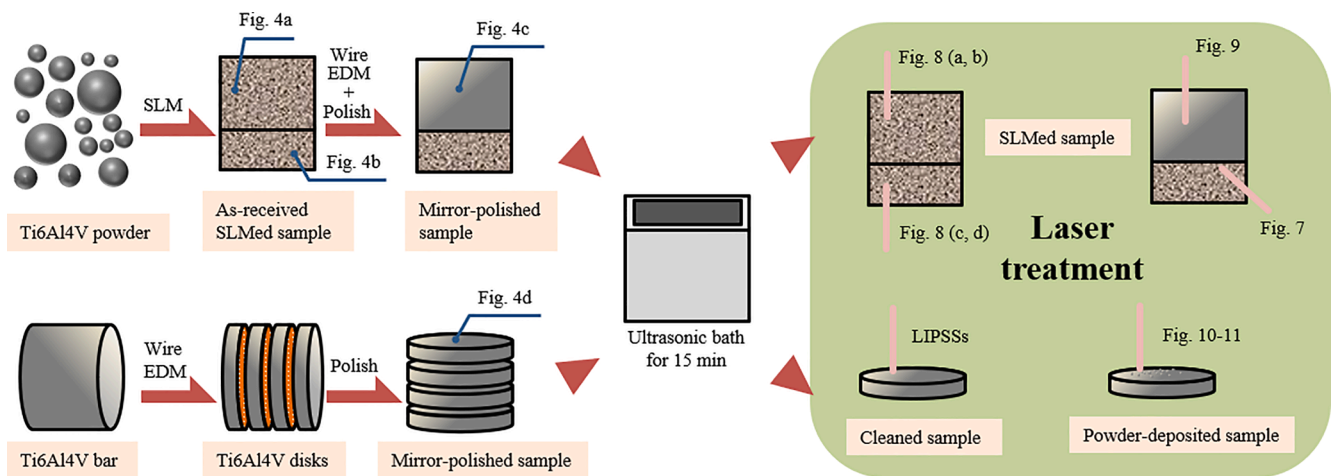


Fig. 1. Sample preparation process.

Table 1
Experimental conditions of the SLM process.

Parameters	Data
Scanning speed	290 mm/s
Laser power	50 W
Laser beam diameter	80 mm
Powder layer size range	45 μm
Hatch spacing	25 μm
Exposure time	100 μs
Laser wavelength	1070 nm
Chamber atmosphere	Argon
Laser type	Yb-fiber laser

Concurrently with the research to discover the mechanism of LIPSS generation mentioned above, applications of LIPSS in the industry have also been studied. LIPSS-covered material surfaces are beneficial for application in fields such as aerospace [31], environment [32], and coatings [33,34]. In biomedical engineering, highly structured surfaces can be employed as antibacterial surfaces, which are exceedingly desirable for implants to prevent bacterial adhesion on material surfaces [21,35]. Besides LIPSS application, additive manufacturing (AM) technologies such as selective laser melting (SLM) have also played an increasingly important role in biomedical engineering [36–38].

Based on the above situations, we considered that LIPSSs combined with SLM might be promising for the fabrication of implants or customized medical devices and performed laser-induced processes on selective laser-melted (SLMed) samples. After laser irradiation, scanning electron microscopy (SEM) unexpectedly revealed that not only LIPSSs, but also nanopillars (hereafter, “LIPSS” specifically refers to ripple-like nanostructures to distinguish from “nanopillars,” pillar-like nanostructures) were on them (see Section 4.1 for details), and additional experiments demonstrated that nanopillars were created around the particles that incompletely melted in the SLM process. In this study, we investigated the mechanism of nanopillar generation around particles through experiments and numerical simulation. Based on the preliminary experiment, we assumed that the particles on the material surface influenced the electric field intensity (EFI) distribution of the laser and induced nanopillars. To verify this assumption experimentally, we laid different particles on polished surfaces and irradiated them with a picosecond laser. Although the LIPSS formation mechanism is a complex physical process influenced by not only the EFI but also the temperature [39], surface plasma [40], environment [28], surface roughness [41], etc., our previous works demonstrated that the EFI distribution is one of the main factors influencing LIPSS formation [41,42]; therefore, we focused on the EFI alone in this study.

The EFI was simulated by using the finite element method (FEM) and numerically stable boundary element discretization and combined with preconditioning and solving the sparse matrix of the obtained equation system. The results can show the three-dimensional distribution of the EFI, which was easy to compare with the experimental results. However, the simulated model size was limited by random-access memory (RAM) via FEM; therefore, the finite-difference time-domain (FDTD) numerical simulation method, which has been extensively applied to study LIPSS formation [12,43–49], was also employed to investigate the EFI when forming nanopillars or LIPSSs around a particle using a picosecond laser. Between the FEM and FDTD approach, the FEM can use unstructured tetrahedral grids to adapt to the boundaries of complex shapes [48] accurately; nevertheless, the FDTD method can simulate a model with a larger size and save a considerable amount of computation time. For the

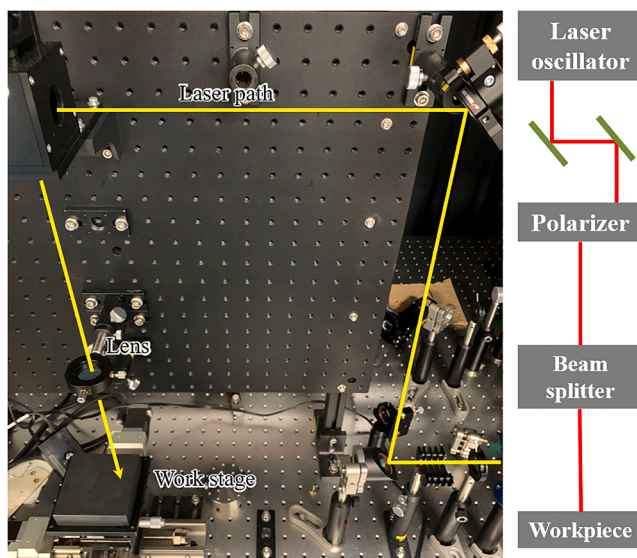


Fig. 2. Laser processing setup; same as [57].

on Ni-P and 304 stainless steel surfaces. Daminielli et al. [28] investigated the effects of silicon irradiation through a femtosecond laser in water and air environments. The results showed that compared to silicon irradiation in an air environment, silicon irradiated under water had a smaller ablation depth, higher modification threshold, smaller periodic length, etc. Connor et al. [29,30] compared the ablation of 175 nm ITO film on glass for patterning and substrate by 10 ps and 150 laser pulses. They demonstrated that shorter pulse laser is more appropriate for selective and partial ablation.

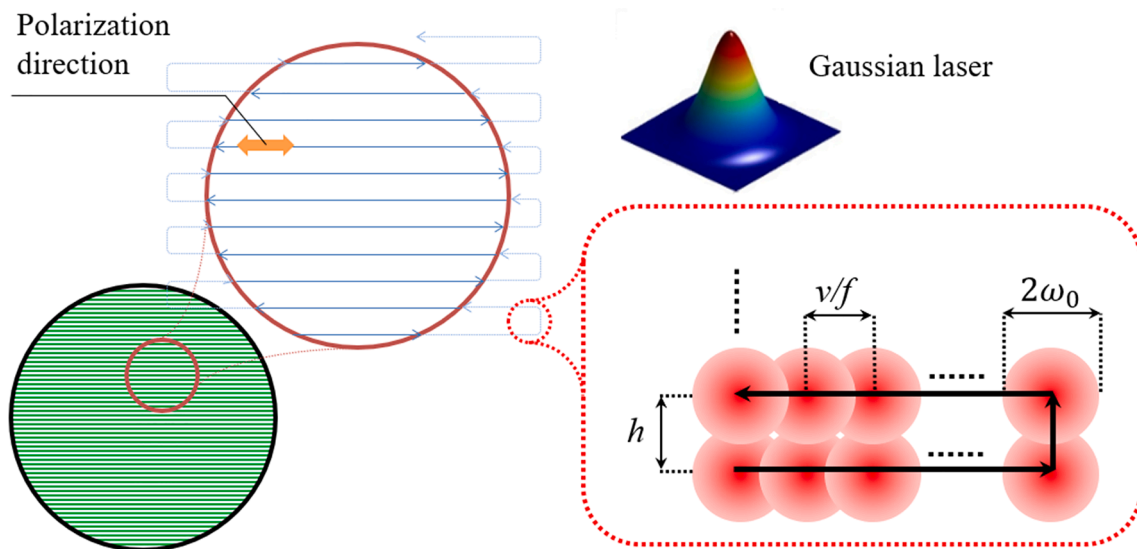


Fig. 3. Scanning path of the laser irradiation process.

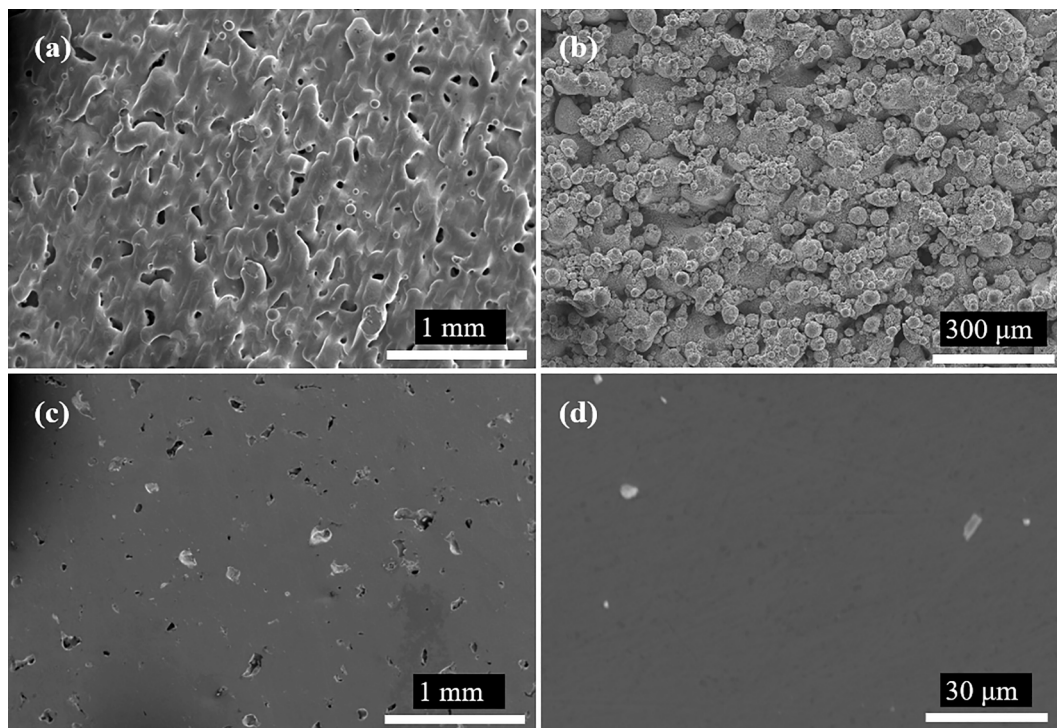


Fig. 4. SEM micrograph images of the surface texture: (a) top and (b) side surfaces of the SLM sample, (c) SLM structure, and (d) bulk plate cut using wire EDM and polished.

Table 2
Experimental conditions of the pulse laser treatment process [57].

Parameters	Data
Laser wavelength	1064 nm
Pulse duration	20 ps
Pulse frequency	50 Hz
Laser beam waist radius	150 μm
Laser fluence	0.5 J/cm ²
Hatch spacing	120 μm
Scanning speed	400 μm/s
Overlap ratio	96%

above reasons, the FEM and FDTD were both employed to simulate the EFI distribution. The simulated EFI distribution results well matched the generated LIPSSs and nanopillars, demonstrating that the surface structure influences the EFI distribution significantly and suggesting that the expected LIPSSs can be obtained by suitably designing the surface structure before irradiation.

2. Experimental

2.1. Material and facilities

Titanium 6 wt% aluminum 4 wt% vanadium (Ti6Al4V) alloy, which is the most popular titanium alloy because of its low density, high

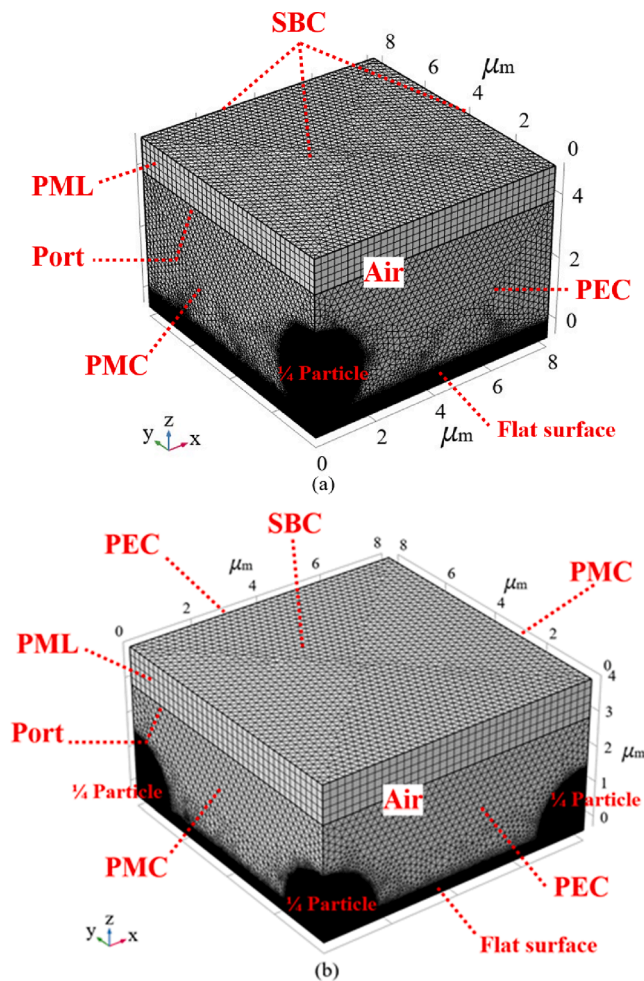


Fig. 5. (a) Single and (b) four-particle mesh models in FEM simulation and boundary conditions settings.

strength, excellent corrosion resistance, and superior biocompatibility [50–53], is extensively used in both the biomedical and SLM industries [54–56]. Hence, we selected Ti6Al4V alloy for our experiment. Fig. 1

depicts the sample preparation process. The SLMed workpieces were fabricated on an SLM machine (ProX 100, 3D Systems Corp.) using Ti6Al4V alloy powder (TILOP64–45, Osaka Titanium Technologies, Co., Ltd.) with an average particle diameter of 18 μm under the conditions listed in Table 1.

The samples other than the SLMed ones were prepared from commercially available bar material, which was cut into a disk shape with a thickness of 1 mm through wire electrical discharge machining (EDM). The samples were then finished with a surface grinder and emery paper to obtain a mirror-polished surface with an Sa roughness of 0.06 μm , and surface texturing was induced by a picosecond laser machine with a fixed wavelength of 1064 nm, pulse duration of 20 ps, and frequency of 50 Hz (PL 2250–50P20, Ekspla) as shown in Fig. 2 [57]. The picosecond laser has a Gaussian power distribution, and the average power and laser fluence were tested using a laser power meter (Field-MaxII-TOP, Coherent, Inc.) and a charge-coupled device camera (SP620U, Ophir–Spiricon, LLC.), respectively. All the samples were cleaned by ultrasonication with ethanol for 15 min before they were irradiated by a laser beam and observed through SEM at an accelerating voltage of 15 kV. A high-vacuum environment was employed in SEM to capture the surface morphology after the laser-induced modifications on the sample surface.

2.2. Laser treatment

The samples were placed on a workbench with a movable stage, which was numerically controlled to follow an S-shaped laser scanning path, as shown in Fig. 3. The Gaussian picosecond laser was focused through a telecentric lens with a focal length of 150 mm, and the beam diameter $2\omega_0$ (e^{-2}) was estimated to be approximately 300 μm experimentally. The surface textures before laser irradiation are displayed in Fig. 4. We previously [57] demonstrated that the LIPSSs were generated on the surface of Ti6Al4V alloy only when the laser conditions, including the laser fluence and scanning speed, were set in a specific range; therefore, the laser conditions were set as listed in Table 2 according to [57] and these conditions were consistently used throughout this paper. To study the influence of particles in the nanostructure generation process, Ti6Al4V alloy powder particles with an average diameter of 18 μm were deposited on the polished surface and irradiated by a picosecond laser.

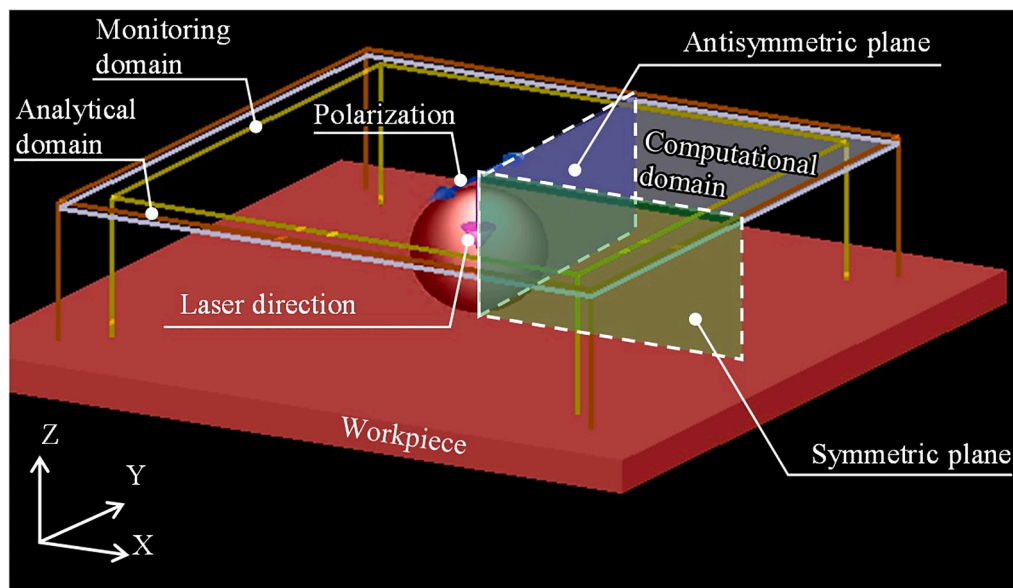


Fig. 6. FDTD analytical model.

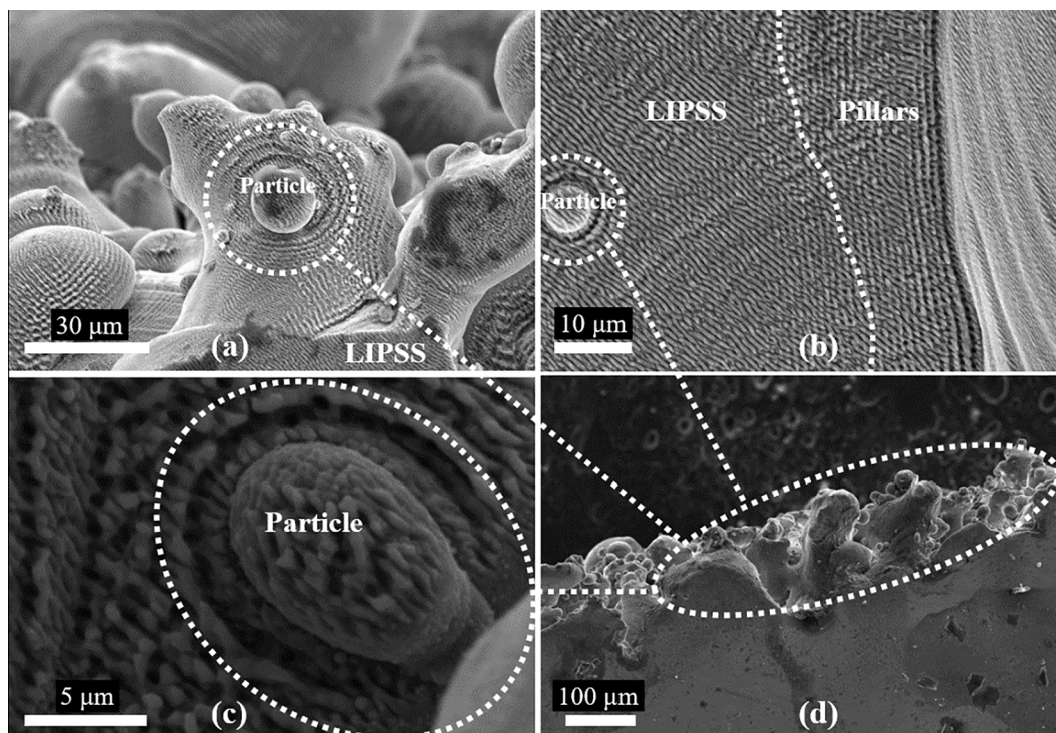


Fig. 7. SEM micrographs of the edges of an SLMed sample irradiated by a picosecond laser.

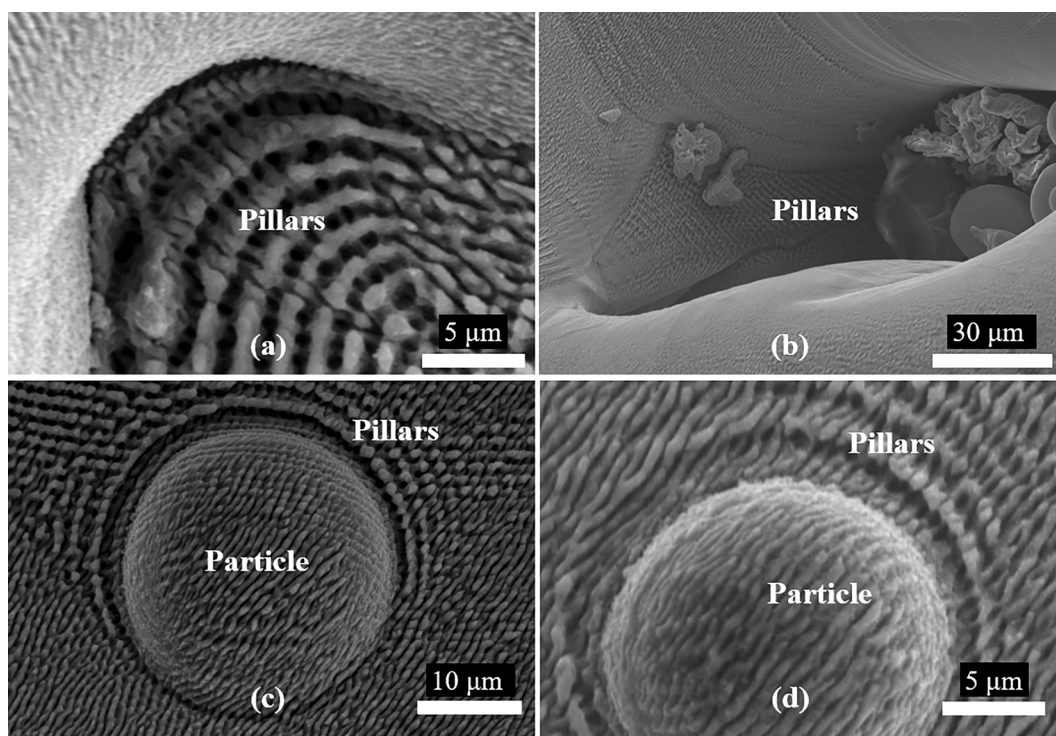


Fig. 8. SEM micrographs of the (a, b) top and (c, d) sides of an SLMed surface irradiated by a picosecond laser.

3. Numerical simulation

3.1. FEM model

The EFI distribution was simulated using commercial software (COMSOL Multiphysics 5.6). A symmetrical quarter model was analyzed to save computation time and avoid a shortage of RAM. The laser

polarization direction was parallel to the Y-axis, and the top layer was set as a perfectly matched layer (PML). Two areas along the X- and Y-axes were set as a perfect electric conductor (PEC) and perfect magnetic conductor (PMC), respectively, whereas the others were set to a scattering boundary condition (SBC), as shown in Fig. 5a. The EFI distribution with four particles was also simulated, as shown in Fig. 5b, which illustrates the mesh model of a quarter of the spherical particles on the

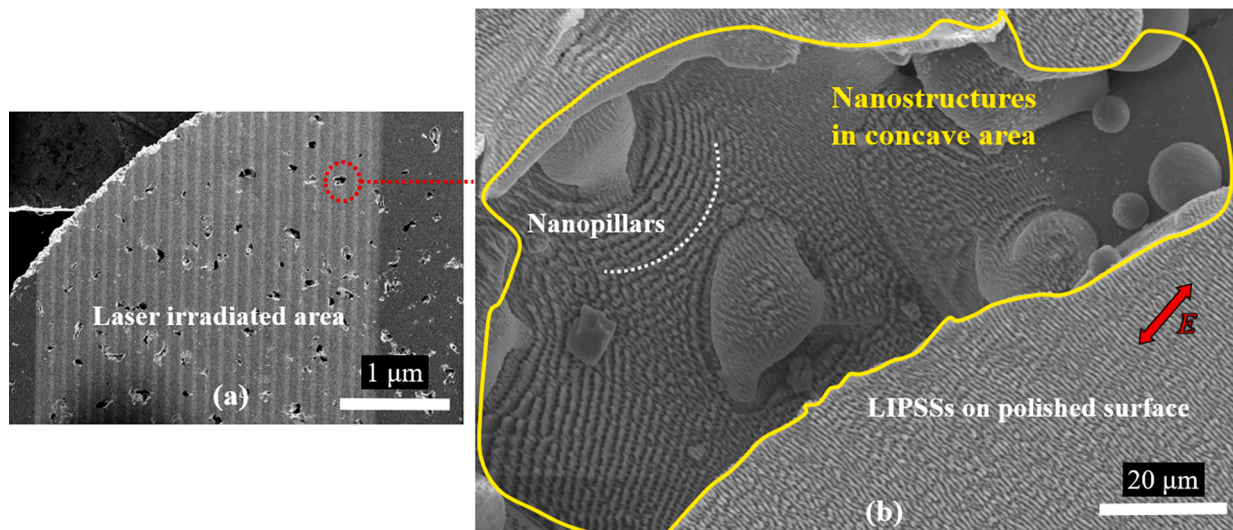


Fig. 9. SEM micrographs of the concave area of the polished-SLMed surface irradiated by a picosecond laser.

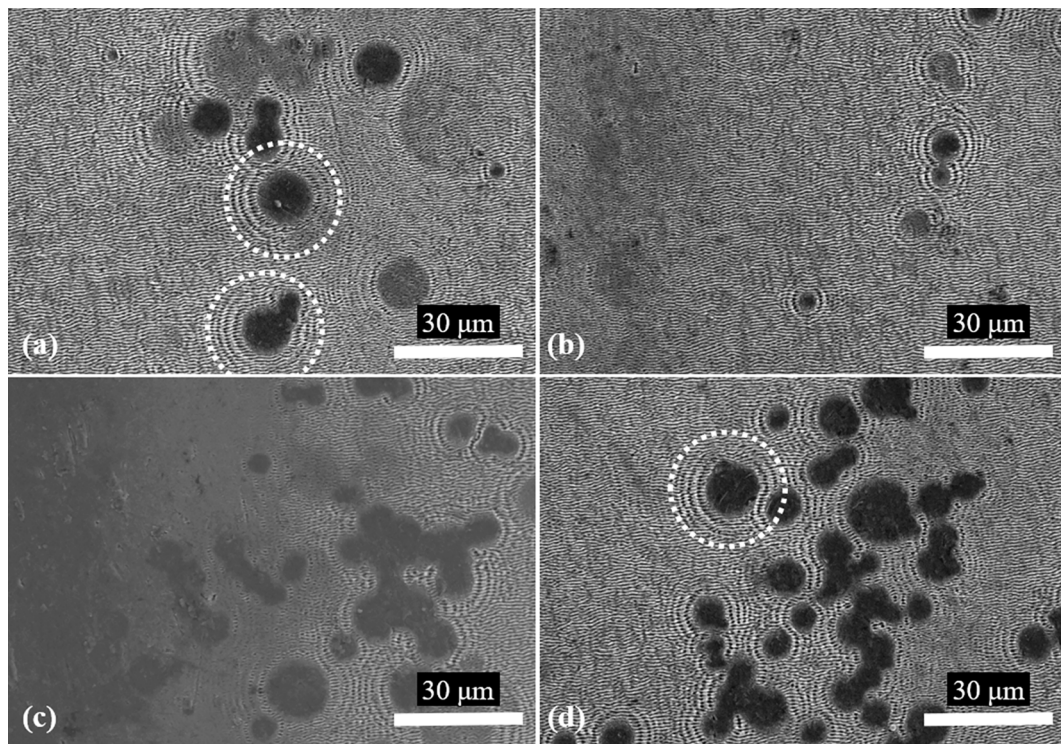


Fig. 10. SEM micrographs of the powder particles deposited on a polished surface and irradiated by a picosecond laser.

polished surface and irradiated by a polarized laser and all the boundary conditions. The particle and workpiece materials were set as Ti6Al4V alloy, with n (refractive index) and k (extinction coefficient) values of 3.57 and 3.50, respectively [58–60]. The following equations were employed to normalize the analyzed EFIs:

$$I_0 = P_0/A \quad (3)$$

$$E_0 = \sqrt{2I_0 Z_0} \quad (4)$$

$$E = E_{\text{ewfd}}/E_0 \quad (5)$$

where P_0 is the default power (1 W), A is the laser irradiation area in the model, Z_0 is the characteristic impedance of vacuum, which is a default parameter in COMSOL (376.73 Ω); E_{ewfd} is the analyzed result of the EFI; and E is the normalized EFI.

3.2. FDTD model

The maximum particle size that can be simulated by FEM is 1.5 μm due to the RAM limitation. Therefore, an FDTD simulation (nanophotonic FDTD simulation software, Lumerical Inc.) was also performed to investigate the EFI distribution of a flat surface on which a larger size single particle was deposited, induced by a 20 ps laser pulse with a wavelength of 1064 nm. The main idea of the FDTD is to solve Maxwell's equations [61,62]:

$$\mu_0 \frac{\partial \mathbf{H}}{\partial t} = -\nabla \times \mathbf{E} \quad (1)$$

$$\epsilon_0 \epsilon_r \frac{\partial \mathbf{E}}{\partial t} + \sigma \mathbf{E} = -\nabla \times \mathbf{H} \quad (2)$$

where \mathbf{E} and \mathbf{H} are the electric field and magnetic field, respectively; t is the time; μ_0 is the vacuum permeability, ϵ_0 is the vacuum permittivity,

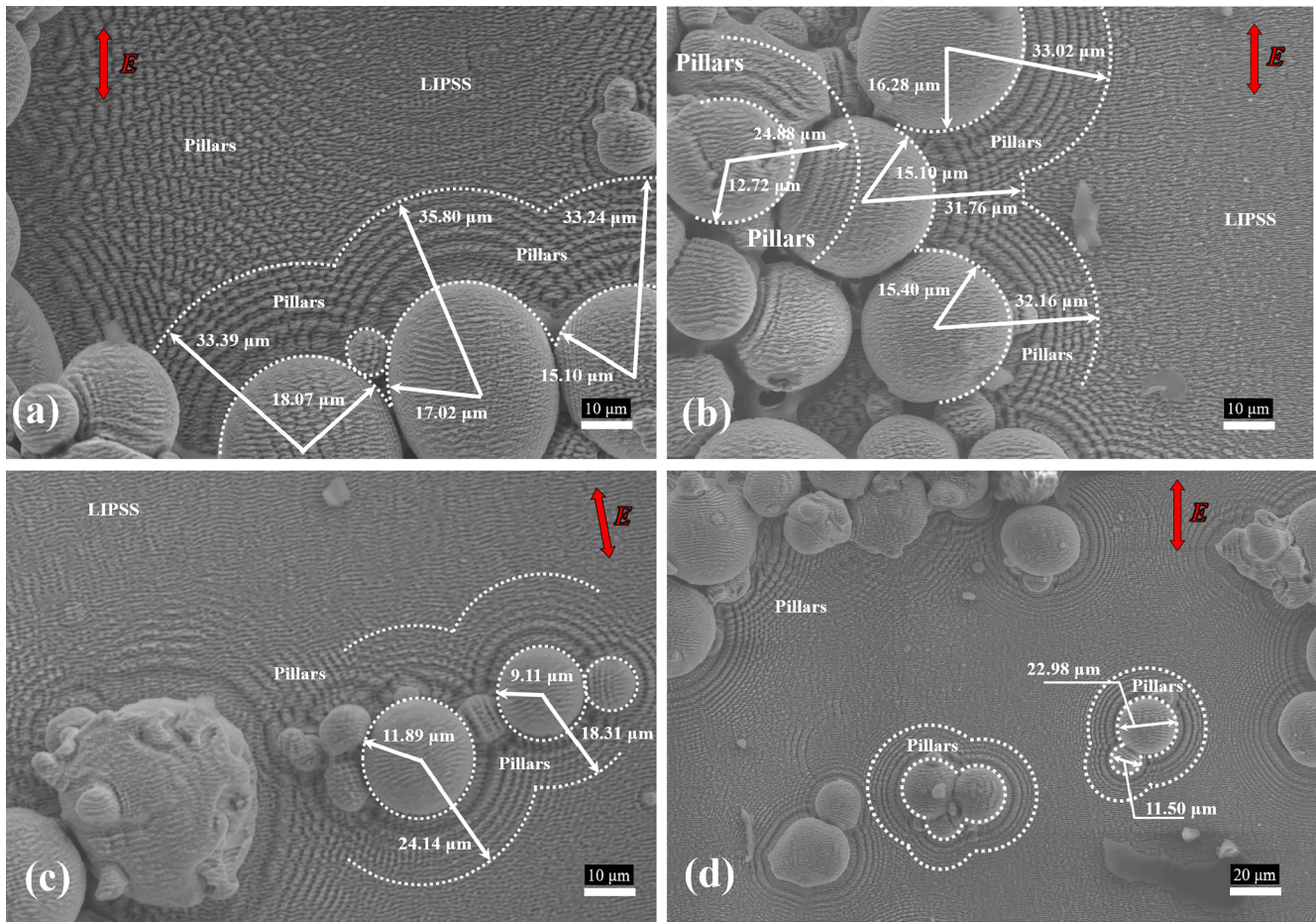


Fig. 11. SEM micrographs of the powder particles deposited on a polished surface and irradiated by a picosecond laser.

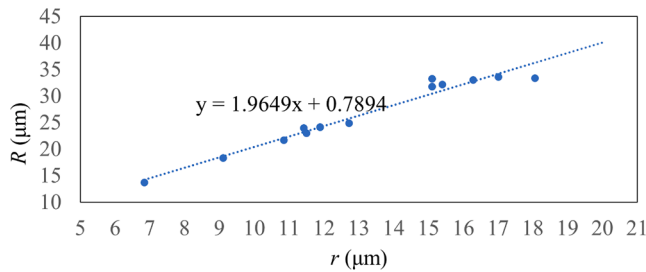


Fig. 12. Statistics of the curvature radius (R) of nanopillar area (NPA) and the radius (r) of the particle.

ϵ_r is the relative permittivity of the material, and σ is the electric conductivity of the material.

A preliminary experiment confirmed that nanopillars arose around various particles whose shapes were spherical and polygonal, but we specifically focused on the spherical one in the calculation because its symmetry saves computing time and memory space. Additionally, because a sphere is isotropic to the polarization direction, comparison between the calculation and experiment becomes easy. The laser polarization was parallel to the polished surface in the Y-direction, and the model was quartered, as shown in Fig. 6. The boundary conditions at X_{\min} and Y_{\min} were set as antisymmetry and symmetry, respectively, whereas the other boundaries were set as a PML. The material computational data, namely, the refractive index of Ti6Al4V and air, were the same as those in the FEM simulation.

4. Results and discussion

4.1. SLM specimen with laser treatment

The SLMed sample with different regions (Fig. 4b–d), including concave and convex parts, cracks, and incompletely melted particles on their surfaces, was irradiated by the picosecond laser and nanostructures were formed on and around these small structures as shown in Figs. 7 and 8. Their high-magnification images illustrate that nanopillars seem to be distributed irregularly.

Fig. 9 shows that nanopillars were generated in the concave area of the polished SLMed workpiece, which corresponds to Fig. 4c. In contrast, the polished area was covered by LIPSSs, indicating that the surface structure before irradiation is a vital factor for the morphology and distribution of the generated nanostructures. Although the generated nanostructures seemed to be distributed irregularly on the whole SLM samples, the areas around the particles seem to be where nanopillars are specifically generated, as shown in Figs. 7–9. Therefore, we assumed that the surface particles play a crucial role in the nanopillar formation process.

4.2. Generation of nanopillars around the particles

To verify the assumption introduced towards the end of the previous section, the Ti6Al4V powder particles with an average diameter of 18 μm used in the SLM process were deposited on a polished surface and a scanning laser irradiated the entire surface. Fig. 10 demonstrates that many nanopillars were generated around the dark areas where powder particles were deposited prior to being moved away by the scanning

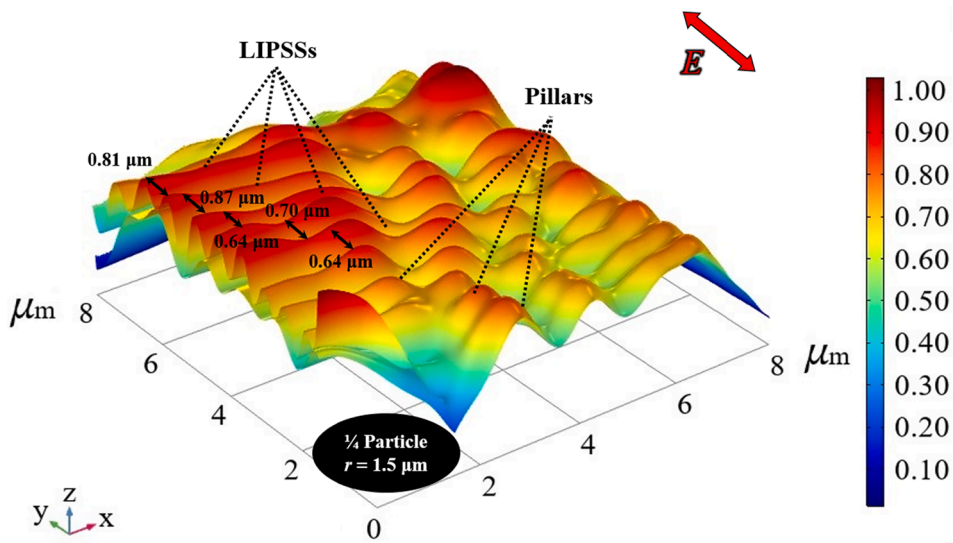


Fig. 13. Normalized EFI around the quarter particle model simulated using FEM.

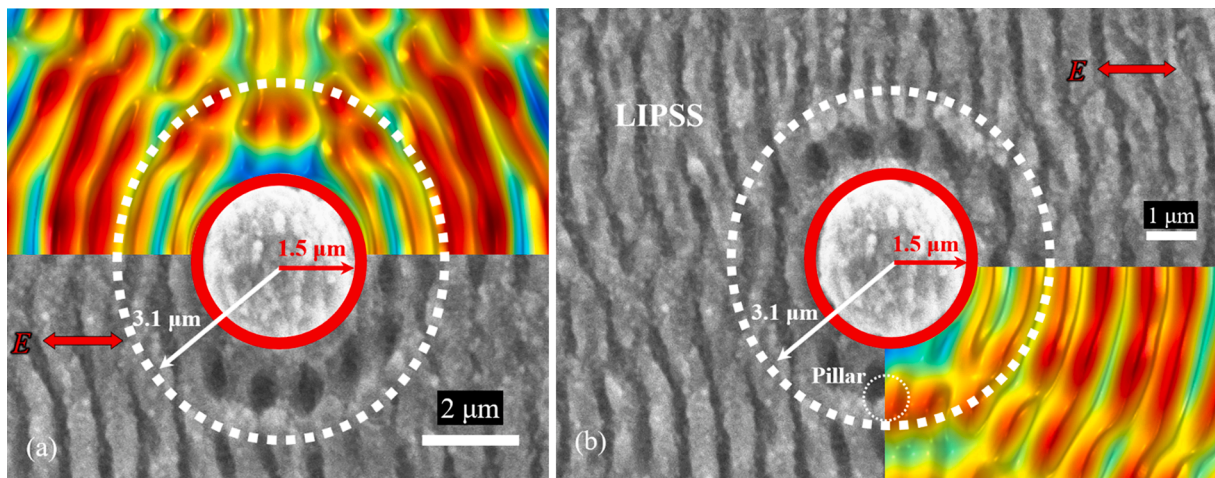


Fig. 14. Comparison of the (a) half and (b) quarter FEM simulation EFI result with the LIPSS structure.

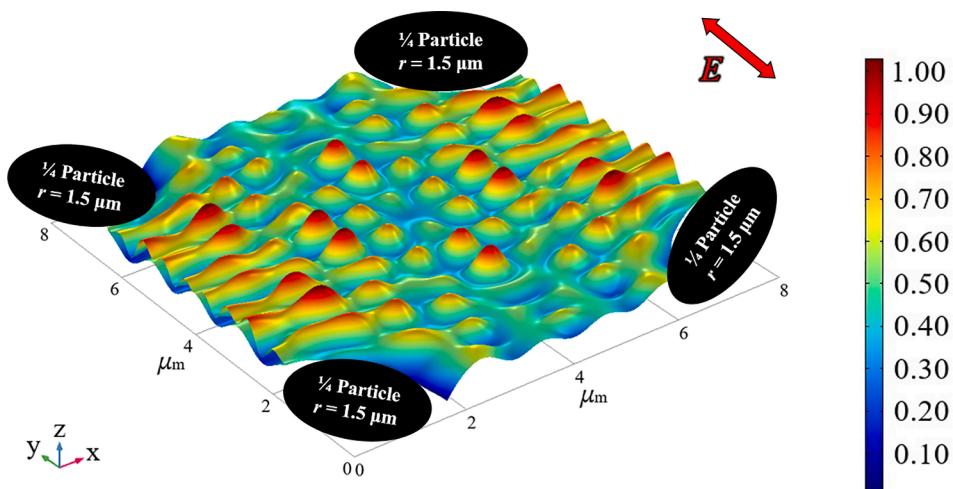


Fig. 15. EFI distribution of four particles irradiated by picosecond laser.

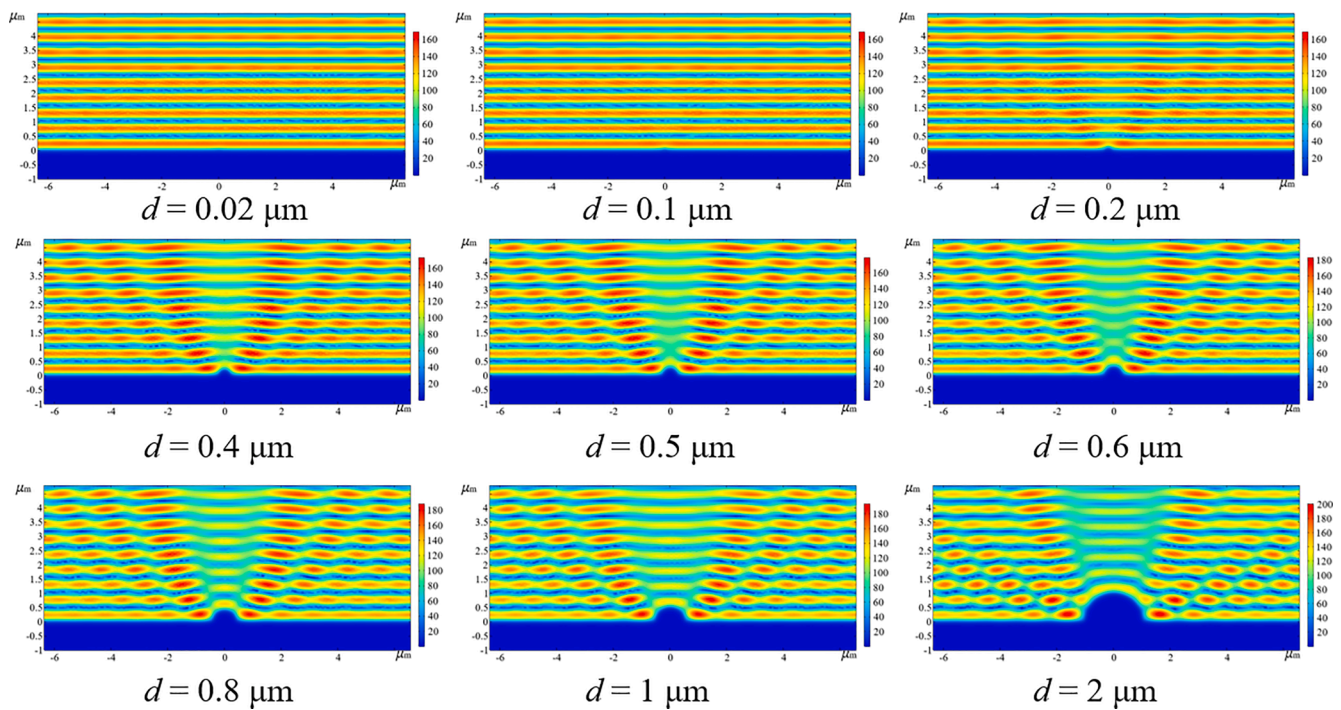


Fig. 16. Illustration of the nanopillars formed near the powder particles on a laser-irradiated surface.

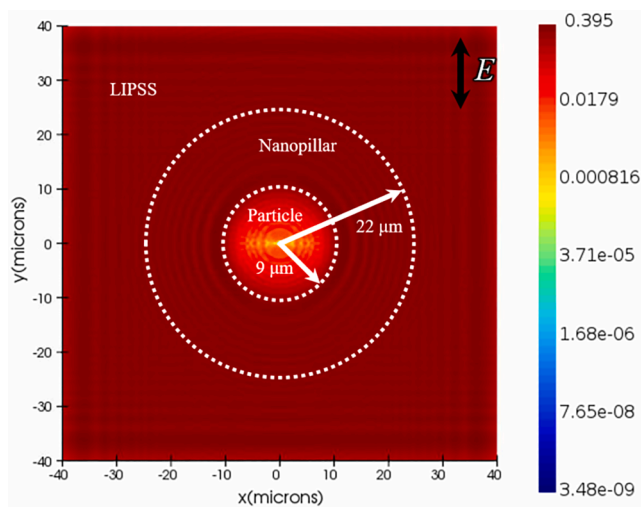


Fig. 17. EFI around the particle simulated using the FDTD method.

laser. Further, we fixed the powder particles on the polished surface using melted wax before laser treatment to ensure that the particles influenced the nanostructures generated during the laser irradiation process. Fig. 11 shows that nanopillars were generated around the powder particles and LIPSSs are formed farther from the area whose boundary is marked by the white dotted line, indicating that the curvature radius (R) of the formed nanopillar area (NPA) around the particles is related to the particles (r). Count the data of R and r in Fig. 11, and couple out the prediction line of $R-r$ as shown in Fig. 12, indicating that R is approximately twice as r . However, in such certain areas as the upper-left image of Fig. 11, nanopillars were generated instead of LIPSSs farther from the NPA. This may be because the surrounding particles influence electromagnetic wave transfer and the EFI distribution in the laser irradiation process.

4.3. Comparison of the simulation and experimental results

Fig. 13 displays the normalized EFI distribution on a flat surface; the ripple orientation along the X-axis is similar to the LIPSS morphology. The ripple pitch length in the Y-direction, ranging from 0.64 to 0.87 μm , matches the LIPSS periodic length (800–900 nm), and pillar-like structures are present in the area near the particle. Fig. 14 shows nanostructures around a 1.5- μm -radius particle on the polished surface and compares them with the EFI simulation. The LIPSS morphology matches the EFI distribution tendency well, implying that the LIPSS generation mechanism might be explained by the EFI distribution in the laser irradiation process.

Fig. 15 shows a model with four particles with a radius of 1.5 μm , displaying that the orientation of the ripple-like structure is perpendicular to the polarization direction, which is along the Y-axis direction, and the center area where is far from particles ($R > 2r$) was the pillar-like structure. This may explain that many particles closely located each other can cause to generate nanopillars on the area far away ($R > 2r$) as shown in Fig. 11a.

To investigate the influence of the particle size on EFI distribution in laser irradiation, particles with different diameters irradiated by the picosecond laser were simulated. The 2D EFI distribution results are shown in Fig. 16. The laser wavelength is 1064 nm, and the particle size ranges from 0.02 μm to 2 μm . It shows that when the particle size is less than 0.4 μm , the EFI distribution on the material surface is almost the same, which does not affect the LIPSS and nanopillars' generation. However, for particle size of $>0.5 \mu\text{m}$, the EFI around the particle is distributed as ripple-like, which is different from the EFI distribution far from the particle.

Fig. 17 shows the FDTD analytical result of a single particle ($r = 9 \mu\text{m}$) located on a flat surface irradiated by a picosecond laser. The area inside the white dotted line is pillar-like and around the particle. The NPA has a curvature radius of 22 μm , which is approximately 2.4 times as large as the particle radius (9 μm). The EFI is automatically normalized in the FDTD approach, and its distribution appears similar to the LIPSS and nanopillar distribution. Hence, the LIPSS/nanopillar generation mechanism might be explained by the EFI distribution in a laser-induced process.

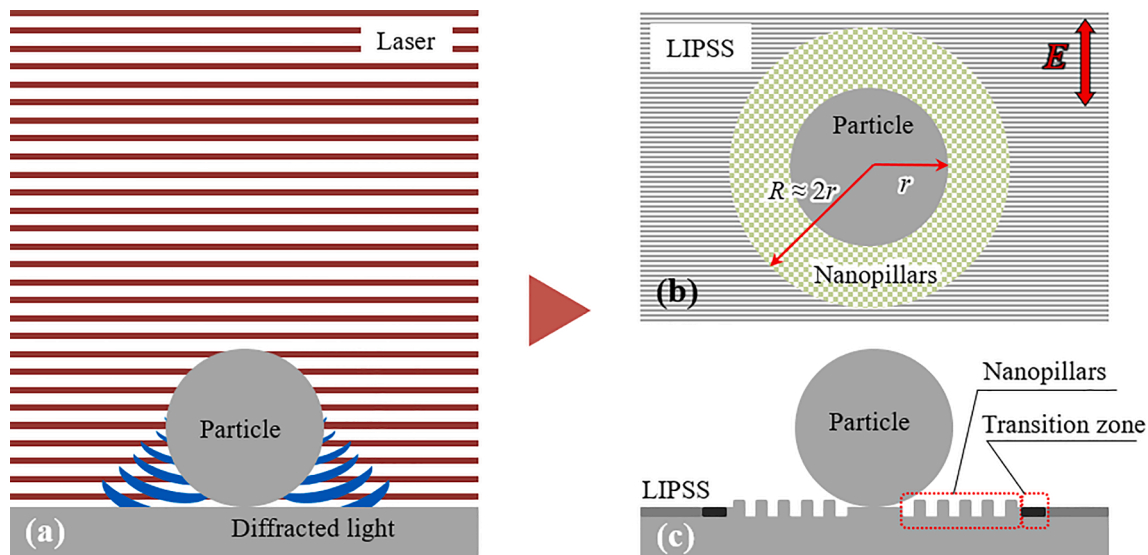


Fig. 18. Illustration of the nanopillars formed near the powder particles on a laser-irradiated surface.

4.4. Mechanism

Fig. 18 is a schematic of the generation of nanopillars around a powder particle irradiated by a Gaussian laser source. Nanopillars are formed around the particles, and LIPSSs are formed farther away. The nanopillars surrounding the particle form a concentric area with a curvature radius approximately twice the spheroidal particle radius. This trend exists because the particle influences the EFI distribution in the laser irradiation process, as proved by comparing the simulation and experimental results. However, specific nanostructures are formed with an irregular distribution of particles of different sizes or shapes. For instance, electromagnetic wave transfer is affected when many particles are discharged close to each other, affecting the EFI distribution formed by the laser irradiation area, as shown in Fig. 11a. On the other hand, the LIPSS and nanopillar generation is also influenced by the thermodynamic phase transitions or hydrodynamic effects of the transiently melted surface. The EFI distribution influences the heat distribution of the surface and then leads to selective ablation and solidification. Therefore, the surface morphology before laser treatment plays a significant role in nanostructure generation.

Moreover, in the area outside the NPA ($R > 2r$), nanopillars are generated instead of LIPSSs because the neighboring particles influence the EFI distribution. Hence, the expected nanostructures may be formed by suitably designing the surface structure prior to laser induction.

5. Conclusions

We irradiated a 50 Hz picosecond laser with 1064 nm fixed wavelength, 20 ps pulse duration, 0.5 J/cm² laser fluence, and 400 μm/s scanning speed on SLMed samples for the first time and found that LIPSSs and nanopillars were generated mainly on the boundary and uneven surfaces, revealing that the nanopillars that arose specifically on the areas around the particles melted incompletely in the SLM process. Assuming that particles play a major role in generating nanopillars, we then irradiated the laser on the particles placed on the polished surface. The results clarified that the nanopillars formed within the concentric area of a single spherical particle whose curvature radius was approximately twice the particle radius, and LIPSSs were formed outside of the area; note that nanopillars were generated far from the particles if multiple particles are close to each other. These results seemed to be attributable to electromagnetic wave transfer, and the surrounding particles influenced the EFI distribution in the laser irradiation process. The simulation results demonstrated that the EFI distribution and LIPSS

morphology features were well matched, implying that the LIPSS irradiation mechanism could be explained by the EFI distribution in a laser-induced process.

The influence of the EFI distribution in a laser irradiation process is determined by several factors, including the surface roughness and morphology, laser fluence, polarization direction, pulse duration, frequency, environment, and materials. Surface morphology is one of the critical factors affecting the EFI distribution. The desired nanostructures can be obtained by designing the surface structure, including the surface particle size or shape and periodic length, before laser irradiation.

CRediT authorship contribution statement

Liwei Chen: Conceptualization, Methodology, Software, Formal analysis, Validation, Investigation, Writing – original draft, Writing – review & editing. **Ziqi Chen:** Software. **Keita Shimada:** Writing – original draft, Writing – review & editing. **Masayoshi Mizutani:** Supervision, Project administration, Funding acquisition. **Tsunemoto Kuriyagawa:** Project administration, Funding acquisition.

Declaration of Competing Interest

The authors declare that they have no known competing financial interests or personal relationships that could have appeared to influence the work reported in this paper.

Acknowledgement

This work was supported by the National Key Research and China Scholarship Council (grant number 201906270253), in part by JSPS KAKENHI (Grant Numbers JP17K06074 and JP17KK0126), and the Machine Tool Engineering Foundation.

References


- [1] M. Birnbaum, Semiconductor surface damage produced by Ruby lasers, *J. Appl. Phys.* 36 (11) (1965) 3688–3689, <https://doi.org/10.1063/1.1703071>.
- [2] I. Gnilytskyi, T.J.Y. Derrien, Y. Levy, N.M. Bulgakova, T. Mocek, L. Orazi, High-speed manufacturing of highly regular femtosecond laser-induced periodic surface structures: Physical origin of regularity, *Sci. Rep.* 7 (2017) 1–11, <https://doi.org/10.1038/s41598-017-08788-z>.
- [3] D.C. Emmony, R.P. Howson, L.J. Willis, Laser mirror damage in germanium at 10.6 μm, *Appl. Phys. Lett.* 23 (11) (1973) 598–600, <https://doi.org/10.1063/1.1654761>.

- [4] J. Sipe, J. Young, J. Preston, H. Van Driel, Laser-induced periodic surface structure. II. experiments on Ge, Si, Al, and brass, *Phys. Rev. B* 27 (1983) 1155–1172, <http://prb.aps.org/abstract/PRB/v27/i2/p1141.1>.
- [5] M. Siegrist, G. Kaech, F.K. Kneubühl, Formation of a periodic wave structure on the dry surface of a solid by TEA-CO₂-laser pulses, *Appl. Phys.* 2 (1) (1973) 45–46, <https://doi.org/10.1007/BF00900492>.
- [6] S. Baudach, J. Bonse, W. Kautek, Ablation experiments on polyimide with femtosecond laser pulses, *Appl. Phys. A Mater. Sci. Process.* 69 (7) (1999) S395–S398, <https://doi.org/10.1007/s003390051424>.
- [7] J.Z.P. Skolski, G.R.B.E. Römer, J. Vincenc Obona, A.J. Huis in 't Veld, Modeling laser-induced periodic surface structures: Finite-difference time-domain feedback simulations, *J. Appl. Phys.* 115 (10) (2014) 103102, <https://doi.org/10.1063/1.4867759>.
- [8] J.Z.P. Skolski, G.R.B.E. Römer, J.V. Obona, V. Ocelik, A.J. Huis in 't Veld, J.T. M. De Hosson, Laser-induced periodic surface structures: Fingerprints of light localization, *Phys. Rev. B - Condens. Matter Mater. Phys.* 85 (2012) 1–9, <https://doi.org/10.1103/PhysRevB.85.075320>.
- [9] T.Q. Jia, H.X. Chen, M. Huang, F.L. Zhao, J.R. Qiu, R.X. Li, Z.Z. Xu, X.K. He, J. Zhang, H. Kuroda, Formation of nanogratings on the surface of a ZnSe crystal irradiated by femtosecond laser pulses, *Phys. Rev. B - Condens. Matter Mater. Phys.* 72 (2005) 1–4, <https://doi.org/10.1103/PhysRevB.72.125429>.
- [10] D. Dufft, A. Rosenfeld, S.K. Das, R. Grunwald, J. Bonse, Femtosecond laser-induced periodic surface structures revisited: A comparative study on ZnO, *J. Appl. Phys.* 105 (3) (2009) 034908, <https://doi.org/10.1063/1.3074106>.
- [11] A. Dauscher, V. Feregotto, P. Cordier, A. Thomy, Laser induced periodic surface structures on iron, *Appl. Surf. Sci.* 96–98 (1996) 410–414, [https://doi.org/10.1016/0169-4332\(95\)00495-5](https://doi.org/10.1016/0169-4332(95)00495-5).
- [12] Jörn Bonse, Stephan Gräf, Maxwell meets Marangoni—a review of theories on laser-induced periodic surface structures, *Laser Photonics Rev.* 14 (10) (2020) 2000215, <https://doi.org/10.1002/lpor.v14.10.1010.1002/lpor.202000215>.
- [13] O. Varlamova, J. Reif, S. Varlamov, M. Bestehorn, The laser polarization as control parameter in the formation of laser-induced periodic surface structures: comparison of numerical and experimental results, *Appl. Surf. Sci.* 257 (12) (2011) 5465–5469, <https://doi.org/10.1016/j.apsusc.2010.11.157>.
- [14] F. Costache, M. Henyk, J. Reif, Surface patterning on insulators upon femtosecond laser ablation, *Appl. Surf. Sci.* 208–209 (2003) 486–491, [https://doi.org/10.1016/S0169-4332\(02\)01443-5](https://doi.org/10.1016/S0169-4332(02)01443-5).
- [15] F. Costache, S. Kouteva-Arguirova, J. Reif, Sub-damage-threshold femtosecond laser ablation from crystalline Si: Surface nanostructures and phase transformation, *Appl. Phys. A Mater. Sci. Process.* 79 (4-6) (2004) 1429–1432, <https://doi.org/10.1007/s00339-004-2803-y>.
- [16] J. Reif, F. Costache, M. Henyk, S.V. Pandelov, Ripples revisited: Non-classical morphology at the bottom of femtosecond laser ablation craters in transparent dielectrics, *Appl. Surf. Sci.* 197–198 (2002) 891–895, [https://doi.org/10.1016/S0169-4332\(02\)00450-6](https://doi.org/10.1016/S0169-4332(02)00450-6).
- [17] J. Bonse, Quo vadis LIPSS?—recent and future trends on laser-induced periodic surface structures, *Nanomaterials* 10 (2020) 1–19, <https://doi.org/10.3390/nano10101950>.
- [18] E.L. Gurevich, Mechanisms of femtosecond LIPSS formation induced by periodic surface temperature modulation, *Appl. Surf. Sci.* 374 (2016) 56–60, <https://doi.org/10.1016/j.apsusc.2015.09.091>.
- [19] Y. Levy, T.J.Y. Derrien, N.M. Bulgakova, E.L. Gurevich, T. Mocek, Relaxation dynamics of femtosecond-laser-induced temperature modulation on the surfaces of metals and semiconductors, *Appl. Surf. Sci.* 374 (2016) 157–164, <https://doi.org/10.1016/j.apsusc.2015.10.159>.
- [20] J. Reif, O. Varlamova, S. Varlamov, M. Bestehorn, The role of asymmetric excitation in self-organized nanostucture formation upon femtosecond laser ablation, *Appl. Phys. A Mater. Sci. Process.* 104 (3) (2011) 969–973, <https://doi.org/10.1007/s00339-011-6472-3>.
- [21] C. Albu, A. Dinescu, M. Filipescu, M. Ulmeanu, M. Zamfirescu, Periodical structures induced by femtosecond laser on metals in air and liquid environments, *Appl. Surf. Sci.* 278 (2013) 347–351, <https://doi.org/10.1016/j.apsusc.2012.11.075>.
- [22] H. Mustafa, M. Mezera, D.T.A. Matthews, G.R.B.E. Römer, Effect of surface roughness on the ultrashort pulsed laser ablation fluence threshold of zinc and steel, *Appl. Surf. Sci.* 488 (2019) 10–21, <https://doi.org/10.1016/j.apsusc.2019.05.066>.
- [23] J. Yan, J. Noguchi, Y. Terashi, Fabrication of single-crystal silicon micro pillars on copper foils by nanosecond pulsed laser irradiation, *CIRP Ann. - Manuf. Technol.* 66 (1) (2017) 253–256, <https://doi.org/10.1016/j.cirp.2017.04.134>.
- [24] F. Fraggelakis, G. Mincuzzi, J. Lopez, I. Manek-Hönninger, R. Kling, Controlling 2D laser nano structuring over large area with double femtosecond pulses, *Appl. Surf. Sci.* 470 (2019) 677–686, <https://doi.org/10.1016/j.apsusc.2018.11.106>.
- [25] K.M. Tanvir Ahmmed, C. Grambow, A.M. Kietzgi, Fabrication of micro/nano structures on metals by femtosecond laser micromachining, *Micromachines* 5 (2014) 1219–1253, <https://doi.org/10.3390/mi5041219>.
- [26] E.L. Gurevich, S.V. Gurevich, Laser induced periodic surface structures induced by surface plasmons coupled via roughness, *Appl. Surf. Sci.* 302 (2014) 118–123, <https://doi.org/10.1016/j.apsusc.2013.10.141>.
- [27] S. Kodama, H. Yamaguchi, K. Shimada, M. Mizutani, T. Kuriyagawa, Control of short-pulsed laser induced periodic surface structures with machining—picosecond laser nanotexturing with magnetic abrasive finishing-, *Precis. Eng.* 60 (2019) 428–436, <https://doi.org/10.1016/j.precisioneng.2019.06.015>.
- [28] G. Daminelli, J. Krüger, W. Kautek, Femtosecond laser interaction with silicon under water confinement, *Thin Solid Films* 467 (1-2) (2004) 334–341, <https://doi.org/10.1016/j.tsf.2004.04.043>.
- [29] N Farid, A Sharif, R K Vijayaraghavan, M Wang, H Chan, A Brunton, P J McNally, K L Choy, G M O'Connor, Improvement of electrical properties of ITO thin films by melt-free ultra-short laser crystallization, *J. Phys. D. Appl. Phys.* 54 (18) (2021) 185103, <https://doi.org/10.1088/1361-6463/abe266>.
- [30] N. Farid, H. Chan, D. Milne, A. Brunton, G.M. O'Connor, Stress assisted selective ablation of ITO thin film by picosecond laser, *Appl. Surf. Sci.* 427 (2018) 499–504, <https://doi.org/10.1016/j.apsusc.2017.08.232>.
- [31] Y.Z. Hu, T.B. Ma, Tribology of nanostructured surfaces (2019), <https://doi.org/10.1016/B978-0-12-803581-8.00614-7>.
- [32] Z. Liu, X. Zhou, Y. Qian, Synthetic methodologies for carbon nanomaterials, *Adv. Mater.* 22 (17) (2010) 1963–1966, <https://doi.org/10.1002/adma.200903813>.
- [33] K.D. Esmeryan, Y.I. Fedchenko, G.P. Yankov, K.A. Temelkov, Laser irradiation of super-nonwetterable carbon soot coatings—physicochemical implications, *Coatings* 11 (2021) 1–7, <https://doi.org/10.3390/coatings11010058>.
- [34] A. Volpe, C. Gaudiuso, L. Di Venere, F. Licciulli, F. Giordano, A. Ancona, Direct femtosecond laser fabrication of superhydrophobic aluminum alloy surfaces with anti-icing properties, *Coatings* 10 (6) (2020) 587, <https://doi.org/10.3390/coatings10060587>.
- [35] A. Jaggessar, H. Shahali, A. Mathew, P.K.D.V. Yarlagadda, Bio-mimicking nano and micro-structured surface fabrication for antibacterial properties in medical implants, *J. Nanobiotechnology* 15 (1) (2017), <https://doi.org/10.1186/s12951-017-0306-1>.
- [36] A. Macpherson, X. Li, P. McCormick, L. Ren, K. Yang, T.B. Sercombe, Antibacterial titanium produced using selective laser melting, *Jom.* 69 (12) (2017) 2719–2724, <https://doi.org/10.1007/s11837-017-2589-y>.
- [37] X. Hu, R. Xu, X. Yu, J. Chen, S. Wan, J. Ouyang, F. Deng, Enhanced antibacterial efficacy of selective laser melting titanium surface with nanophase calcium phosphate embedded to TiO₂ nanotubes, *Biomed. Mater.* 13 (4) (2018) 045015, <https://doi.org/10.1088/1748-605X/aa1a3>.
- [38] N. Kamboj, M.A. Rodríguez, R. Rahmani, K.G. Prashanth, I. Hussainova, Bioceramic scaffolds by additive manufacturing for controlled delivery of the antibiotic vancomycin, *Proc. Est. Acad. Sci.* 68 (2019) 185–190, <https://doi.org/10.3176/proc.2019.2.10>.
- [39] S. Kodama, A. Shibata, S. Suzuki, K. Shimada, M. Mizutani, T. Kuriyagawa, Fabrication and control of fine periodic surface structures by short pulsed laser, *Int. J. Autom. Technol.* 10 (4) (2016) 639–646.
- [40] A.M. Gouda, H. Sakagami, T. Ogata, M. Hashida, S. Sakabe, The formation mechanism of the periodic nanograting structure by the Weibel instability, *Appl. Phys. A Mater. Sci. Process.* 122 (2016) 1–6, <https://doi.org/10.1007/s00339-016-9958-1>.
- [41] S. Kodama, S. Suzuki, K. Hayashibe, K. Shimada, M. Mizutani, T. Kuriyagawa, Control of short-pulsed laser induced periodic surface structures with machining - Picosecond laser micro/nanotexturing with ultraprecision cutting, *Precis. Eng.* 55 (2019) 433–438, <https://doi.org/10.1016/j.precisioneng.2018.10.013>.
- [42] S. Kodama, K. Shimada, M. Mizutani, T. Kuriyagawa, Effects of pulse duration and heat on laser-induced periodic surface structures, *Int. J. Autom. Technol.* 14 (4) (2020) 552–559.
- [43] H. Zhang, K. Du, X. Li, Enhancement and blueshift of high-frequency laser-induced periodic surface structures with preformed nanoscale surface roughness, *Opt. Express* 27 (14) (2019) 19973, <https://doi.org/10.1364/OE.27.019973>.
- [44] E.M. Garcell, S.C. Singh, H. Li, B. Wang, S.A. Jalil, C. Guo, Comparative study of femtosecond laser-induced structural colorization in water and air, *Nanoscale Adv.* 2 (7) (2020) 2958–2967, <https://doi.org/10.1039/C9NA00804G>.
- [45] H. Zhang, J.P. Colombier, S. Witte, Laser-induced periodic surface structures: Arbitrary angles of incidence and polarization states, *Phys. Rev. B* 101 (2020) 1–15, <https://doi.org/10.1103/PhysRevB.101.245430>.
- [46] L. Jiao, D. Kong, X. Zhang, H. Wang, Y. Dai, J. Song, Ripple period adjustment on SiC surface based on electron dynamics control and its polarization anisotropy, *Appl. Phys. A Mater. Sci. Process.* 127 (2021) 1–9, <https://doi.org/10.1007/s00339-020-04181-2>.
- [47] A. Lübcke, Z. Pápa, M. Schnürer, Monitoring of evolving laser induced periodic surface structures, *Appl. Sci.* 9 (17) (2019) 3636, <https://doi.org/10.3390/app9173636>.
- [48] M. Mezera, S. Alamri, W.A.P.M. Hendriks, A. Hertwig, A.M. Elert, J. Bonse, T. Kunze, A.F. Lasagni, G.W.R.B.E. Römer, Hierarchical micro-/nano-structures on polycarbonate via uv pulsed laser processing, *Nanomaterials* 10 (2020) 1–19, <https://doi.org/10.3390/nano10061184>.
- [49] J.M. Guay, A. Calà Lesina, G. Killaire, P.G. Gordon, C. Hahn, S.T. Barry, L. Ramunno, P. Berini, A. Weck, Laser-written colours on silver: Optical effect of alumina coating, *Nanophotonics* 8 (2019) 807–822, <https://doi.org/10.1515/nanoph-2018-0202>.
- [50] S. Liu, Y.C. Shin, Additive manufacturing of Ti6Al4V alloy: a review, *Mater. Des.* 164 (2019) 107552, <https://doi.org/10.1016/j.matdes.2018.107552>.
- [51] C. Cui, B. Hu, L. Zhao, S. Liu, Titanium alloy production technology, market prospects and industry development, *Mater. Des.* 32 (3) (2011) 1684–1691, <https://doi.org/10.1016/j.matdes.2010.09.011>.
- [52] Y. Li, C. Yang, H. Zhao, S. Qu, X. Li, Y. Li, New developments of ti-based alloys for biomedical applications, *Materials (Basel)* 7 (2014) 1709–1800, <https://doi.org/10.3390/ma7031709>.
- [53] Q. Feng, L. Zhang, H. Pang, P. Zhang, X. Tong, D. Wang, Q. Gao, M. Jawaid, E.-R. Kenawy, Microstructure and Properties of Low Cost TC4 Titanium Alloy Plate, *MATEC Web Conf.* 67 (2016) 05025, <https://doi.org/10.1051/mateconf/20166705025>.
- [54] D. Agius, K. Kourousis, C. Wallbrink, A review of the as-built SLM Ti-6Al-4V mechanical properties towards achieving fatigue resistant designs, *Metals (Basel)* 8 (1) (2018) 75, <https://doi.org/10.3390/met8010075>.

- [55] L.-C. Zhang, H. Attar, Selective laser melting of titanium alloys and titanium matrix composites for biomedical applications: a review, *Adv. Eng. Mater.* 18 (4) (2016) 463–475, <https://doi.org/10.1002/adem.201500419>.
- [56] F. Trevisan, F. Calignano, A. Aversa, G. Marchese, M. Lombardi, S. Biamino, D. Ugués, D. Manfredi, Additive manufacturing of titanium alloys in the biomedical field: processes, properties and applications, *J. Appl. Biomater. Funct. Mater.* 16 (2) (2018) 57–67, <https://doi.org/10.5301/jabfm.5000371>.
- [57] L. Chen, Y. Zhang, S. Kodama, S. Xu, K. Shimada, M. Mizutani, T. Kuriyagawa, Picosecond laser-induced nanopillar coverage of entire mirror-polished surfaces of Ti6Al4V alloy, *Precis. Eng.* 72 (2021) 556–567, <https://doi.org/10.1016/j.precisioneng.2021.07.004>.
- [58] A.I. Aguilar-Morales, S. Alamri, T. Kunze, A.F. Lasagni, Influence of processing parameters on surface texture homogeneity using Direct Laser Interference Patterning, *Opt. Laser Technol.* 107 (2018) 216–227, <https://doi.org/10.1016/j.optlastec.2018.05.044>.
- [59] M.K. Khalaf, H.F. Al-Taay, D.S. Ali, Effect of radio frequency magnetron sputtering power on structural and optical properties of Ti6Al4V thin films, *Photonic Sensors.* 7 (2) (2017) 163–170, <https://doi.org/10.1007/s13320-017-0390-8>.
- [60] P.B. Johnson, R.W. Christy, Optical constants of transition metals, *Phys. Rev. B.* 9 (1974) 5056–5070.
- [61] G.R.B.E. Römer, J.Z.P. Skolski, J.V. Oboña, A.J. Huis In 't Veld, Finite-difference time-domain modeling of laser-induced periodic surface structures, *Phys. Procedia.* 56 (2014) 1325–1333, <https://doi.org/10.1016/j.phpro.2014.08.058>.
- [62] J.L. Déziel, J. Dumont, D. Gagnon, L.J. Dubé, S.H. Messaddeq, Y. Messaddeq, Toward the formation of crossed laser-induced periodic surface structures, *J. Opt. (United Kingdom)* 17 (2015) 1–8, <https://doi.org/10.1088/2040-8978/17/7/075405>.



Crystallization behavior and machining properties of annealed Fe–Si–B–Cr amorphous alloys

Chieko Kuji^{1,2}, Kana Takenaka³, Masayoshi Mizutani^{2,*} , Keita Shimada^{2,4},
Tsunemoto Kuriyagawa⁵, and Toyohiko J. Konno³

¹Iwate Industrial Promotion Center, Morioka 020-0857, Japan

²Graduate School of Engineering, Tohoku University, Sendai 980-8579, Japan

³Institute for Materials Research, Tohoku University, Sendai 980-8577, Japan

⁴Present address: Applied Research Laboratory, High Energy Accelerator Research Organization, Tsukuba 305-0801, Japan

⁵Graduate School of Biomedical Engineering, Tohoku University, Sendai 980-8579, Japan

Received: 23 April 2021

Accepted: 13 July 2021

© The Author(s), under exclusive licence to Springer Science+Business Media, LLC, part of Springer Nature 2021

ABSTRACT

We have systematically prepared diverse microstructures by annealing B-rich Fe–Si–B–Cr amorphous sheets to obtain the optimum mechanical property and cutting machinability of the alloy. Thermal, structural, and mechanical analyses showed that the early reaction sequence of the amorphous alloy upon annealing is characterized by structural relaxation, heterogeneous nucleation of the α -Fe(Si) phase at the surface, and homogeneous nucleation of metastable Fe₃B core, which is enclosed by the α -Fe shell. The development of the core–shell structure, approximately 200 nm, is governed by the repeated partitioning out of Si and B from the Fe₃B and α -Fe phases, respectively. The hardness and specific cutting resistance force (SCRF) were found maximum for the alloy annealed to 873 K, which is filled with the aforementioned core–shell crystalline phases. On the other hand, the best cutting performance with minimum burrs and chips, and the lowest SCRF, was realized for the alloy annealed at 763 K, which exhibits a heterogeneous microstructure, where the core–shell units are finely dispersed in the amorphous matrix.

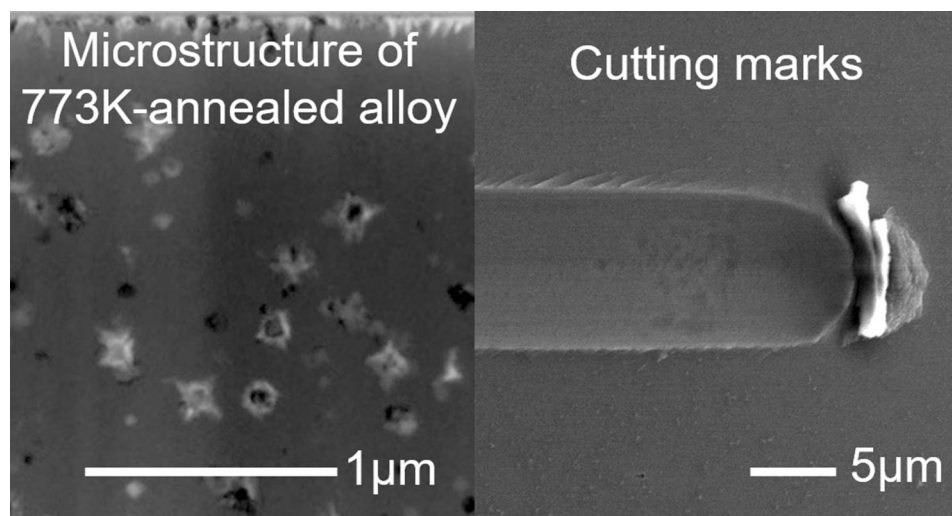
Handling Editor: Megumi Kawasaki.

Address correspondence to E-mail: masayoshi.mizutani.b6@tohoku.ac.jp

<https://doi.org/10.1007/s10853-021-06346-7>

Published online: 30 July 2021

GRAPHICAL ABSTRACT



Introduction

Many electrical devices use soft magnetic materials as magnetic cores, and the development of magnetic materials with high energy conversion efficiency and low iron loss is required [1–4]. The authors have focused on amorphous alloys among the various magnetic materials currently being developed [1–12]. Amorphous alloys are fabricated by rapid quenching from a liquid or a gas state [5, 6]; consequently, they solidify without translational symmetry and do not have grain boundaries or crystalline magnetic anisotropy [7]. This structure exhibits unique physical properties that are not found in crystalline metals [8–12]. Especially when used as an iron core material, Fe-based amorphous alloys have excellent soft magnetic properties, such as a high specific permeability of 5000 at 1 kHz and low iron loss, compared to the conventional 6.5% silicon steel with a specific permeability of 1200 at 1 kHz [8–13]. Amorphous alloys have excellent mechanical properties such as high strength, high toughness, and high elasticity, expected to be used in applications, such as motor core or transformers. To employ them practically, it is required that these amorphous sheets be cut/machined to a specific size. However, they are very

difficult to machine, and only a few studies have been done on their machining characteristics [14–19].

To overcome this problem, we have proposed a novel efficient processing method to shear or blank the amorphous sheet as desired by using their amorphous/crystal state change depending on the temperature. By heating an amorphous alloy, the atoms in the thermodynamically metastable state are rearranged and then crystallized by nucleation and growth mechanisms [20–22]. This rearrangement of the atoms below the crystallization temperature is called structural relaxation, which changes the material's physical properties such as mechanical properties while maintaining the amorphous structure [22–25]. With increasing the temperature more, the formation of crystalline structures causes the embrittlement of materials [22, 24]. Considering these characteristics, we have employed a focused laser that can provide a high energy input in such a short time as femtoseconds to picoseconds in a limited zone to modify the irradiated zone to a more machinable state like the ones obtained via structural relaxation and crystallization. In other words, we have been investigating applications of laser cutting to punching and cutting of selected regions.

This paper assesses the feasibility of the proposed selective machining by local laser heating: We

examined the effects of heat treatment on Fe-based amorphous alloys to clarify the relationship between material structure and mechanical properties. Specifically, we have chosen, as the material to be studied, an alloy based on the Fe–Si–B system, whose crystallization behavior has been well documented; in this system, the crystallization sequence depends on Si/Fe and B/Fe ratios [26]. Particularly, in a B-rich system, crystallization starts with the formation of the metastable Fe₃B phase as a nucleus, followed by its growth and the subsequent emergence of the α -Fe phase with increasing temperature [27, 28]. Focusing on this point, we prepared samples with different microstructures by heat treatment near the crystallization temperature and examined their mechanical properties.

Materials and methods

An amorphous thin strip, known as Metglas 2605S-3A [29] manufactured by Hitachi Metals, Ltd., was used in this study. The composition of this sample was analyzed using a high-frequency inductively coupled plasma optical emission spectrometer (ICP-OES: ARCOS FHM22 MV130) of SPECTRO Analytical Instruments, and the results are shown in Table 1. In this alloy, Cr is added to improve corrosion resistance [11].

The samples were thermally analyzed using a Rigaku Corporation differential scanning calorimetry (DSC) system (DSC-8230). As-received samples were sealed in alumina pans and heated from room temperature to 873 K at a heating rate of 20 K/min in a reducing atmosphere (0.998% H₂–Ar gas) to investigate the phase transition phenomena. Likewise, calorimetric measurements were performed for heating rates of 5, 10, 20, 40, and 80 K/min, and effective activation energies were determined from the shifts of the crystallization peak temperatures, based on several methods proposed by Kissinger [30], Marseglia [31], and Gao-Wang [32].

For the heat treatment of the samples, a thermo-gravimeter–differential thermal analyzer (TG–DTA: TG8120) by Rigaku Corporation was used because of

its ability to control the temperature with high accuracy. The samples were cut into 3 mm widths and 5 mm lengths and annealed from room temperature to 673, 693, 713, 733, 753, 763, 773, 873, and 1073 K at a heating rate of 20 K/min in the aforementioned atmosphere, followed by immediate cooling at 20 K/min in the same atmosphere. Hereafter, these heat-treated samples are simply referred to using the peak temperature, e.g., as 1073 K samples.

An X-ray diffraction (XRD) analyzer (SmartLab 9SW) of Rigaku Corporation was used for structural analyses of the samples before and after the heat treatments, with Cu K α (wavelength: 1.5418 Å, 45 kV, 200 mA). The microstructures before and after heating were observed using transmission electron microscopes (TEMs) (JEM-2000EXII and JEOL ARM-200F). The TEM samples were thinned down to an observable thickness using a focused ion beam (FIB) system (Quanta3D) manufactured by Thermo Fisher Scientific Inc. A fully automatic micro-Vickers hardness tester (HM-221) of Mitutoyo Corporation was used to evaluate the mechanical properties. The test conditions were selected according to the JIS standard (JIS Z 2244), with a load of 0.05 kgf and a load holding time of 10 s. Since small indentations with a diagonal length of fewer than 20 μ m are known to cause large measurement errors, ten indentations were measured for each sample and the average was calculated.

To determine the cutting resistance force, a scratching test was conducted using a wear tester (FPR-2100) from RHESCA Corporation. The indenter was a diamond scribe with a tip radius of curvature of 15 μ m and a cone angle of 60° of Asahi Diamond Industries Co., Ltd. The applied load was 50 gf, the scratching speed was 0.1 mm/s, and the scratching test was conducted three times for each sample. The cutting area was measured using a confocal laser microscope (HYBRID L7) manufactured by Lasertec Corporation, and the specific cutting resistance force was determined. The cutting marks and chips were observed using a field emission electron microanalyzer (FE-EPMA: JXA-8530F) of JEOL.

Table 1 Alloy composition (mol%)

Fe	B	Cr	Si
77.39	15.44	2.04	5.13

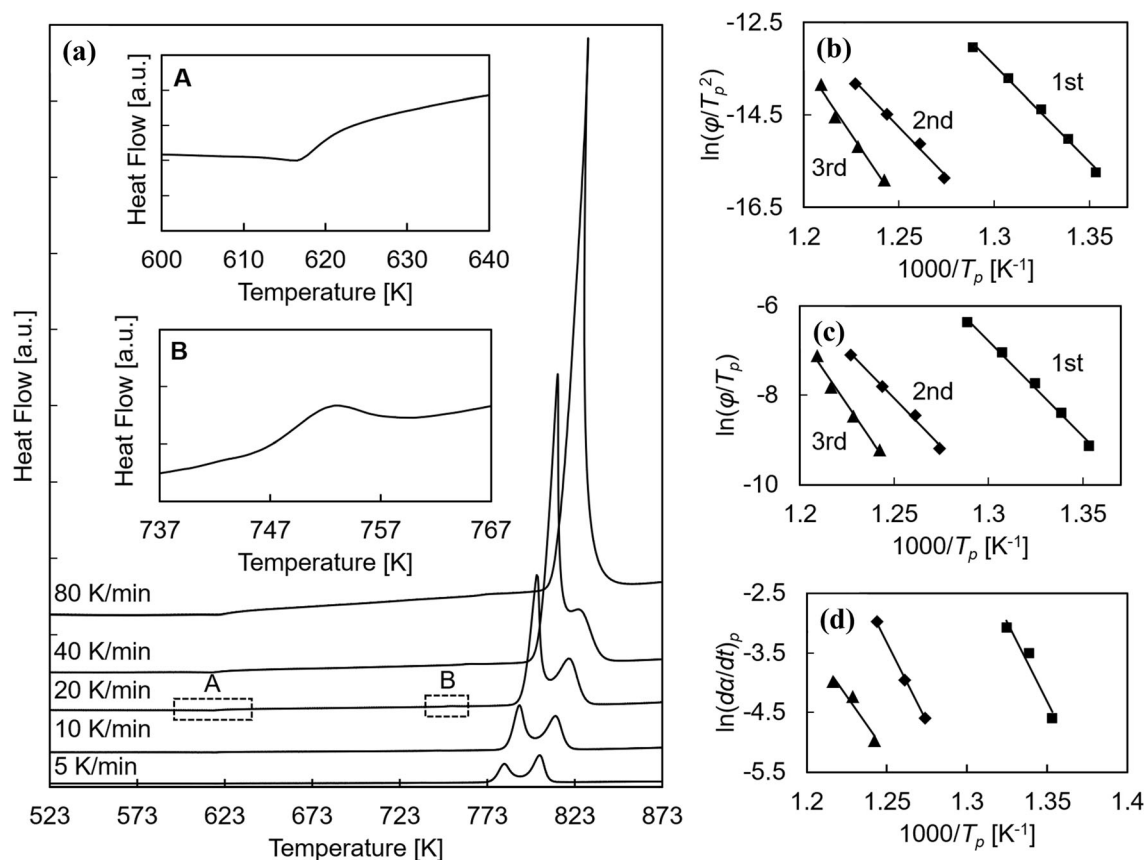


Figure 1 Differential scanning calorimetry (DSC) profiles of the amorphous alloy. **a** DSC curves were obtained with the heating rates of 5, 10, 20, 40, and 80 K/min. Insets A, B are magnified partial profiles indicated by boxes A and B, corresponding to the

Curie point and the first exothermic peak. **b**, **c** Kissinger and Marseglia plots of peak temperatures for the profiles obtained with heating rates of 5, 10, 20, 40, and 80 K/min. **d** Gao-Wang plots obtained for the profiles with 5, 10, and 20 K/min.

Experimental results

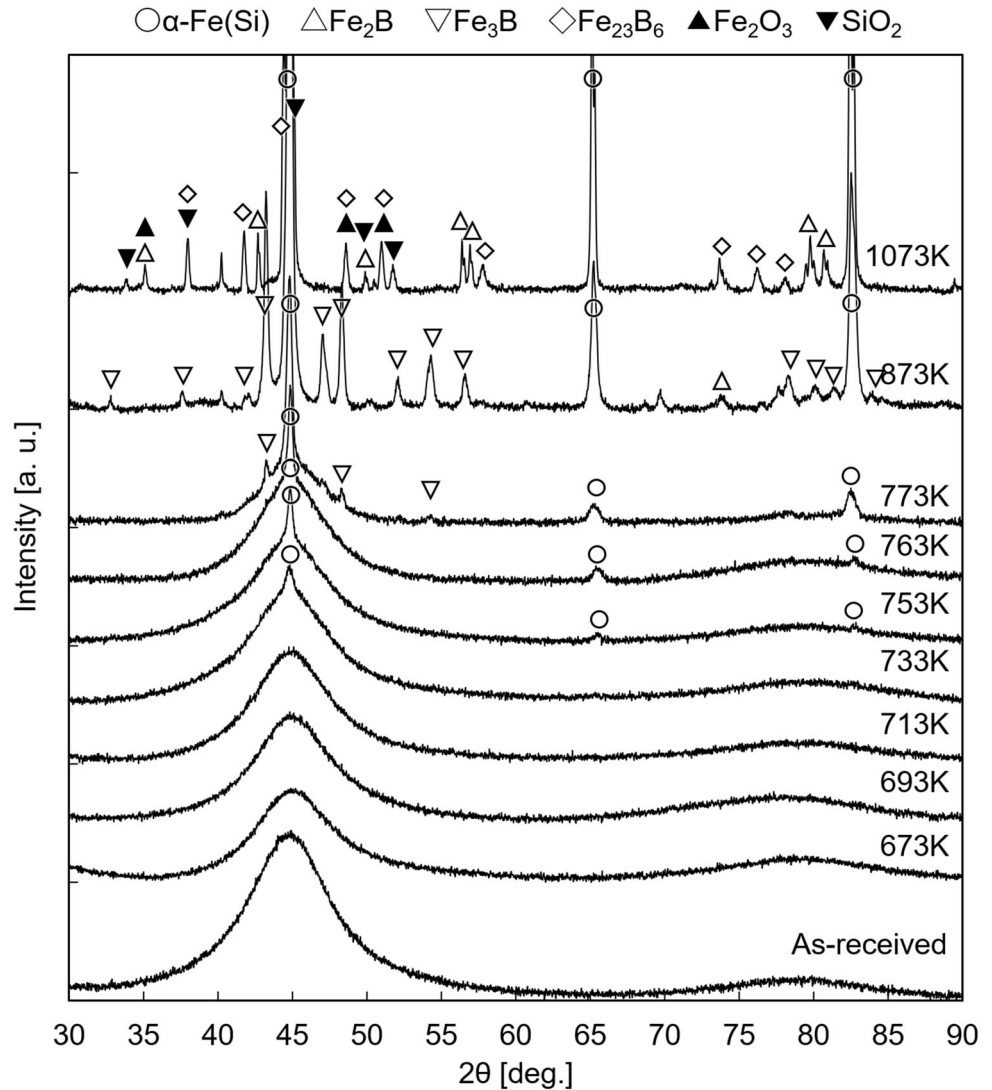
Figure 1a shows DSC thermograms obtained by a series of measurements carried out on the as-received amorphous ribbons at heating rates of 5, 10, 20, 40, and 80 K/min. For all the profiles, there is a small step at about 620 K (inset A), which can be ascribed to the ferromagnetic to paramagnetic transition, i.e., the Curie temperature [33]. Following this, the thermograms can generally be characterized by three peaks. For example, for the profile taken at 20 K/min, it can be seen that a small exothermic peak appeared at 755 K (inset B), followed by a dominant exothermic reaction starting at 795 K with the major peak at 804 K, which is then followed by a relatively small peak at around 822 K (third peak). The average heat evolution for all the thermograms was 120 ± 8 J/g, which can be compared to the reported values of 82 J/g ($\text{Fe}_{78}\text{B}_{13}\text{Si}_9$) [34]. On the other hand, although

the five thermograms display this basic trend, as seen, their appearances are strongly influenced by the heating rate. Namely, not only do the peaks shift to a higher temperature range but also the ratio of the second to the third peaks increases with the rate. This is the phenomenon reported for B-rich Fe–Si–B amorphous ribbons [28] and will be discussed in detail in conjunction with our microstructural

Table 2 Effective activation energies of crystallization determined from several methods proposed by Kissinger [30], Marseglia [31], and Gao-Wang [32]

Peak no.	Activation energy (kJ/mol)		
	Kissinger	Marseglia	Gao-Wang
1	378	354	445
2	416	361	449
3	554	512	323

Figure 2 X-ray diffraction (XRD) patterns of the alloys annealed to 673, 693, 713, 753, 763, 773, 873, and 1073 K.



characterization by TEM. Here, we show, in Fig. 1b–d, the results of assessments for effective activation energies by three methods, proposed by, respectively, Kissinger [30], Marseglia [32], and Gao-Wang [33] and summarize the values in Table 2.

Figure 2 shows XRD profiles for the as-received sample and those annealed in the temperature range of 673–1073 K. The profiles up to 713 K are characterized by the broad halos, typical of an amorphous structure, while peaks arising from crystalline phase(s) appear as the annealing temperature increases, with their assignment, which is indicated in the figure. Namely, these XRD results indicate that the α -Fe phase emerges in the early stage, followed by metastable Fe_3B and finally by the stable Fe_2B and Fe_{23}B_6 , apart from peaks due to oxides. In the early stage of the crystallization process, it was difficult to

evaluate the proportion of the phases from the profile because of the amorphous background. Nevertheless, the average crystalline sizes have been evaluated by using the Scherrer formula [35], which yielded the following values: α -Fe: 20 nm (773 K), 47 nm (873 K), 117 nm (1073 K); Fe_3B : 30 nm (773 K), 42 nm (873 K); Fe_2B : 134 nm (1073 K).

Figure 3a–c shows a bright-field (BF) image, selected area diffraction (SAD) patterns obtained from inside the sample, and that taken from the surface area circled in (a), respectively, for the 753 K specimen. Similarly, Fig. 3d–f and g–i shows the sets of the BF and SAD images obtained from the 763 K and 773 K samples, respectively. The BF image (a) shows mostly gray featureless contrast, while the SAD pattern (b) shows halos, both of which are typical of an amorphous structure. On the other hand, as

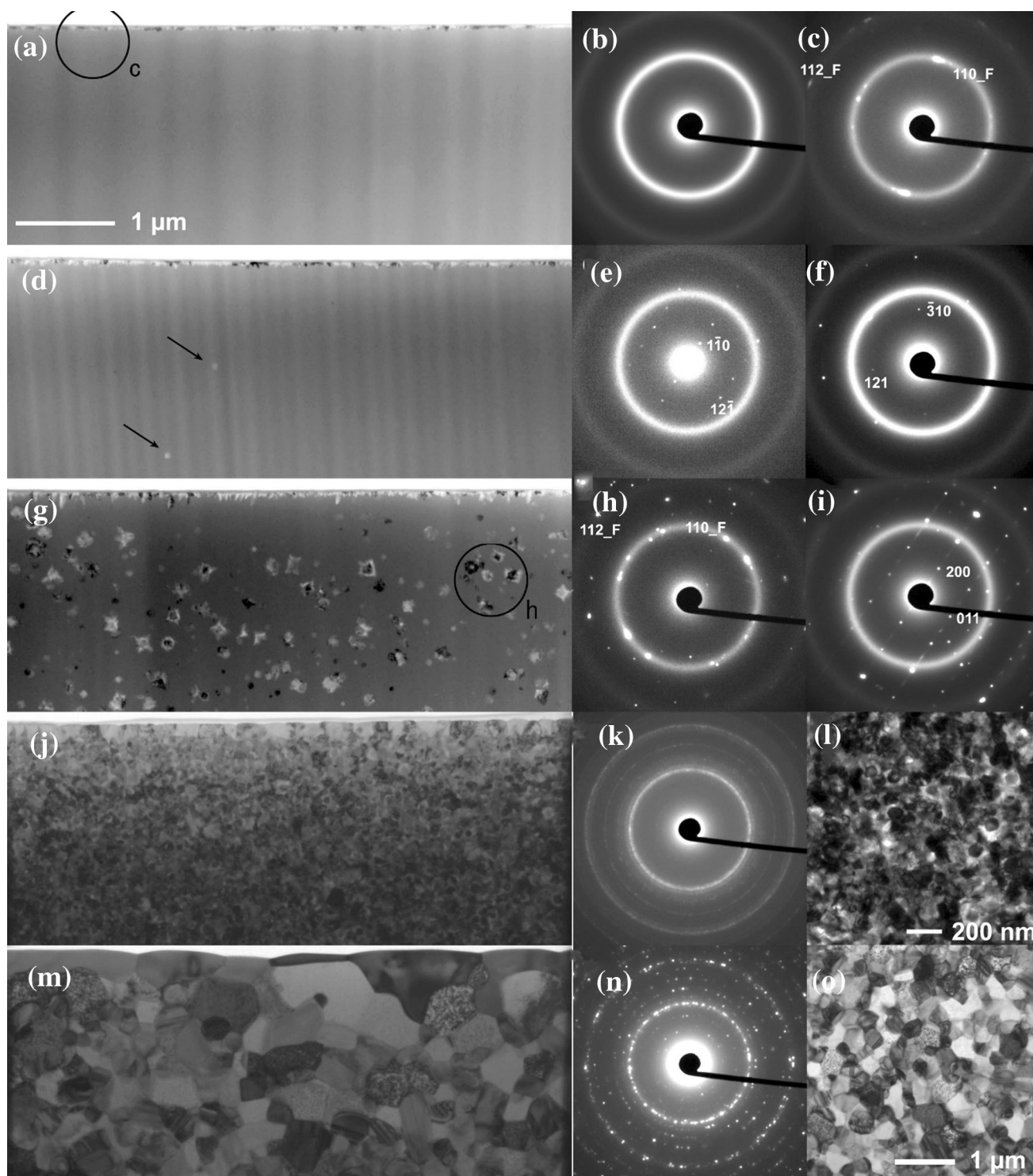


Figure 3 Cross-sectional transmission electron microscope bright-field (BF) images and selected area diffraction (SAD) patterns. **a** BF image for 753 K sample. **b** SAD pattern $[11\bar{7}][1\bar{1}0]$ taken from the inside of sample, showing a halo pattern. **c** SAD pattern taken from the circled region in (a), showing that the partial rings arise from the ferrite (α -Fe) phase. **d** BF image for 763 K sample. The arrows indicate crystalline particles. **e**, **f** SAD patterns taken from particles inside and identified with $[113]$ and zone axis patterns of the metastable Fe_3B phase. **g** BF for 773 K sample. **h** SAD patterns from the circled region in **g**, showing the presence of the α -Fe, while the pattern **i** identified with of the Fe_3B phase. **j**, **k** BF image and SAD for 873 K sample, while **l** a magnified BF image, showing an agglomerate of the core-shell structures. **m**, **n** BF image and SAD for 1073 K sample and **o** slightly demagnified BF image.

shown in (a), there exists a strongly contrasted layer, about 50 nm thick at the surface. The SAD pattern (c) indicates partial rings, which can be assigned to 110 and 112 rings of the α -Fe phase. Contrastingly, the BF image (d) shows contrasts of small particles approximately 50 nm in size, in reasonable agreement with the value obtained by the Scherrer method [35, 36]. These particles exist throughout inside the specimen. The SAD patterns (e) and (f) were obtained from these particles inside the TEM sample and can be identified, respectively, as $[113]$ and $[13\bar{7}]$ patterns of the Fe_3B phase. As shown in Fig. 3g, there are many core-shell particles in the amorphous matrix. The SAD pattern (h) was obtained from the circled area in (g), showing diffractions spots that can be assigned to those of 110 and 112 of the α -Fe phase, while pattern (i) was taken from another particle and can be identified with $[110]$ pattern of the Fe_3B phase. Figure 3j, k shows, respectively, a BF image, and the SAD pattern is taken from the specimen annealed to 873 K, while (l) is a BF image with different magnifications, showing that the sample is completely transformed into the agglomerates of the core-shell crystalline units. Finally, Fig. 3m–o shows similar sets for the 1073 K annealed specimen, showing that the microstructure now consists of grains of several hundred nanometers of the α -Fe and stable boride phases, which compare favorably with the values obtained by XRD as mentioned above.

Figure 4a shows a BF image of particles observed in the 773 K specimen, (b) the corresponding SAD pattern, and (c) and (d) dark-field (DF) images obtained with the diffraction spots indicated by the

circles in (b). The spot (c) is located at 200 positions of the Fe_3B phase, while (d) corresponds to 110 of the α -Fe as well as 231 and/or 330 of the Fe_3B phases. Thus, these DF images suggest that the rectangular core and the shell are composed of the Fe_3B and α -Fe phases, respectively. Figure 4e–h shows the scanning transmission electron microscopic energy-dispersive spectroscopy mappings of Fe, Cr, Si, and B, respectively, showing redistribution of these atoms upon the crystallization process. Particularly, it is noted that Si atoms are partitioned out from the Fe_3B core, while B and, to a minor extent, Cr atoms are ejected from the α -Fe shell.

Figure 5 shows the hardness of the 676–1073 K samples measured by a micro-Vickers hardness tester. The hardness increased with increasing heating temperature, with the maximum observed at 873 K; conversely, the hardness of the 1073 K sample is the smallest.

Figure 6a–f shows the cutting traces at the end of cutting in the scratching test performed on the as-received, 713, 763, 773, 873, and 1073 K samples, respectively. Figure 6a shows that the sheared chips evacuated from the center of the cut and burrs arose at the edge of the cutting marks. This burr was observed in almost all the cutting marks in this specimen. Figure 6b shows that the burrs in the cutting marks began to decrease and about 1- μm -long periodic microcracks arose at the edge of the cutting marks. Figure 6c shows, on the other hand, the burr almost disappeared from the edge of the cutting trace and only microcracks appeared. Figure 6d exhibits a cutting mark with sharp edges without burrs and a protruding region due probably to plastic deformation that appeared in front of the cutting direction. Figure 6e shows that burrs that had disappeared in (c) and (d) appeared again, and many small chips arose. Figure 6f shows that the cutting generated large ductile chips, while burrs adhered to the entire edge of the cutting marks.

Figure 7 shows the cross-sectional profiles of the cutting traces. Because the test load was the same on each sample, the depth of cut reflects the material hardness. The figure illustrates that both edges of the scratch trace protrude due probably to elastic recovery of the material and burr. The amount of cutting on the 1073 K specimen was significantly larger than the other specimens due to softening.

Figure 8 shows the cutting resistance forces during the scratching test and magnified SEM images of chip

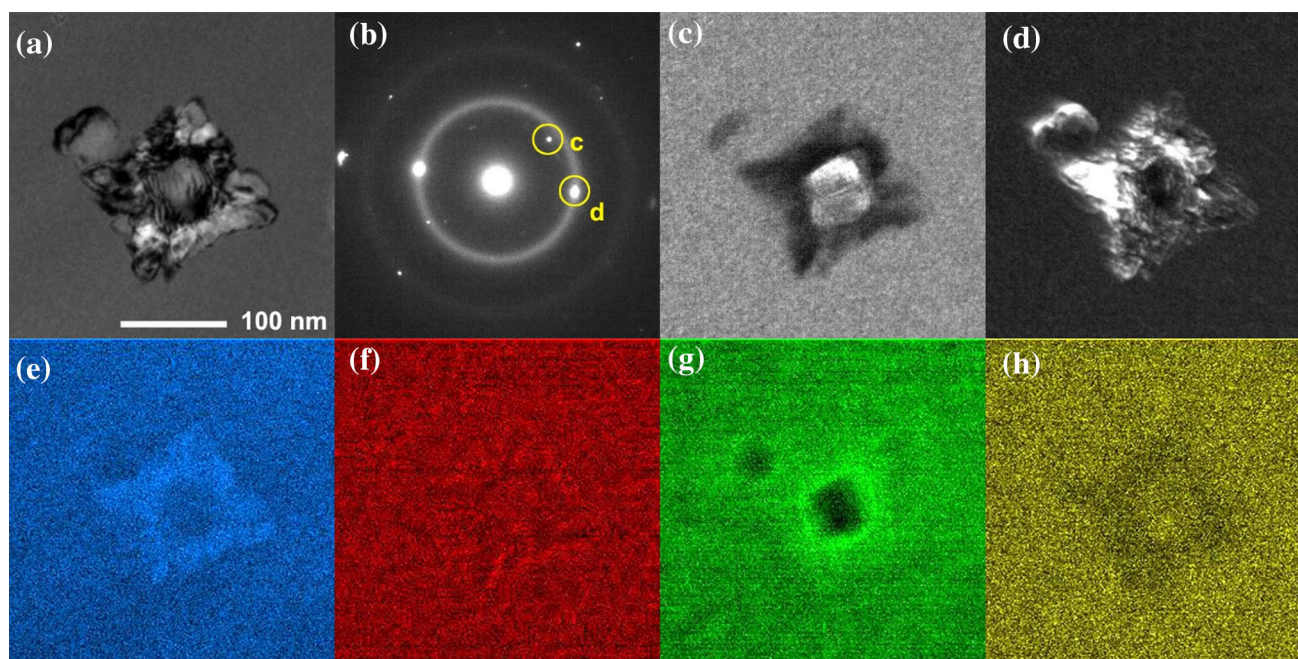


Figure 4 BF/DF images and energy-dispersive X-ray spectroscopy (EDS) mapping of the core-shell structure observed in the 753 K sample. **a** BF image, **b** SAD pattern, **c**,

d DF images taken with the diffraction spots, respectively, at circles **c** (400 of Fe_3B) and **d** (110 of $\alpha\text{-Fe}$) in **b**. **e–h** EDS mappings of, respectively, Fe, Cr, Si, and B.

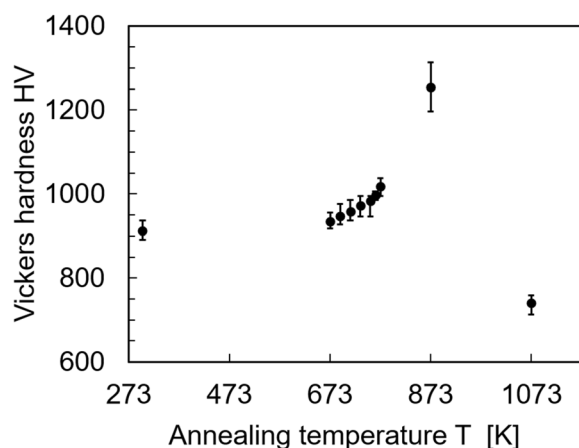


Figure 5 Vickers hardness of the alloys, annealed to 673, 693, 713, 753, 763, 773, 873, and 1073 K.

shapes. As shown in Fig. 8a, c, the resistance periodically undulated from the as-received sample to the 873 K sample. In comparison, Fig. 8e shows that the undulation interval of the resistance became extremely narrow in the 1073 K sample. As shown in Fig. 8b, shear-type discontinuous chips like Piispanen's card model were discharged from the as-received samples [37], and similar discontinuous chips formed on the 873 K sample as shown in Fig. 8d. On the contrary, on the 1073 K sample shown in Fig. 8f

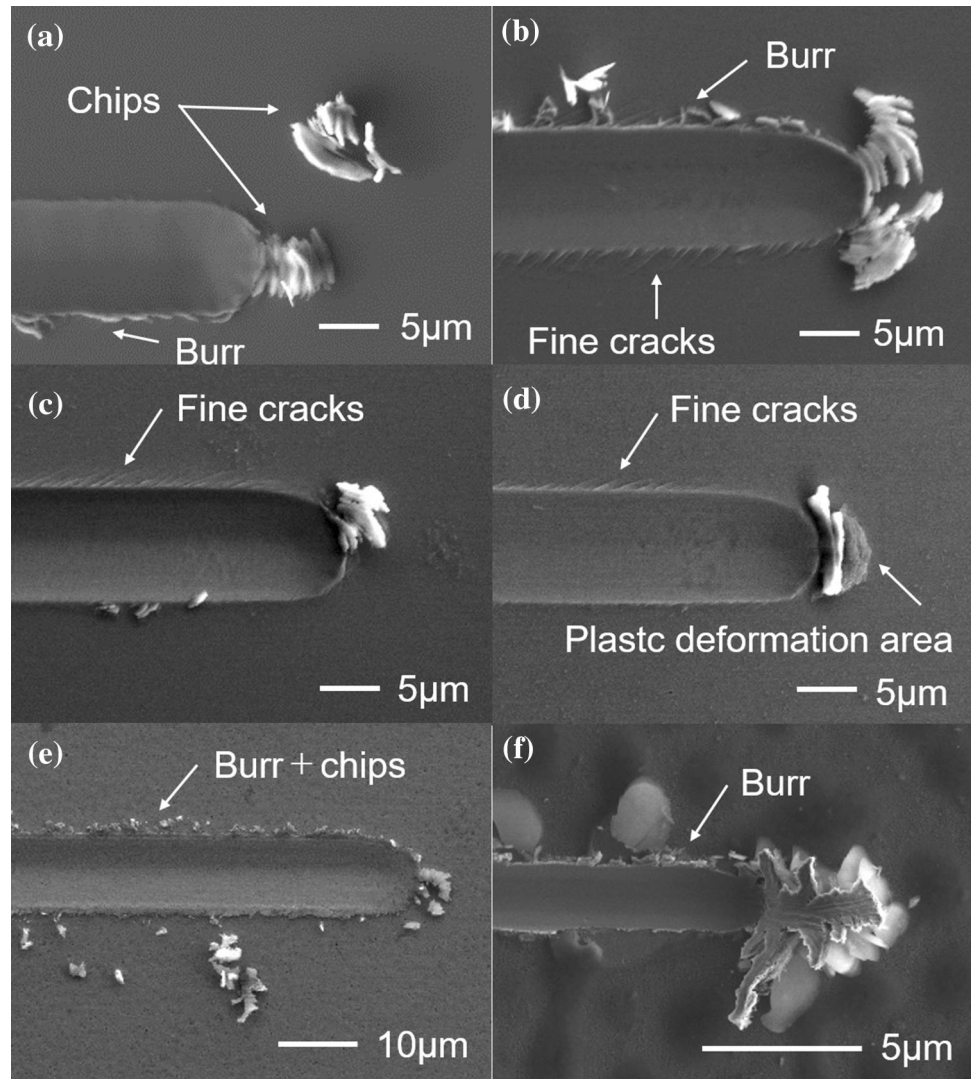
discharged chips emerge continuously with finely layered slippage.

Figure 9 shows, as a function of the annealing temperature, the specific cutting resistance force (SCRF), which is defined by the cutting resistance force divided by the cut width obtained from the cross-sectional profile of the scratch traces in Fig. 8. As shown, the SCRF decreased initially and became the lowest on the 763 K sample, followed by a gradual increase. By comparing the results of cutting quality and specific cutting resistance force, it can be said that the SCRF decreases linearly with the disappearance of the burr. The decrease in the SCRF observed on 713 K can be ascribed to structural relaxation because no crystalline phase was detected on this specimen (Fig. 2). Note also that the Vickers hardness has already started to increase before crystallization.

Discussion

The experimental results have demonstrated that the machining behaviors of a Fe–Si–B-based amorphous alloy strongly depend on the annealing temperatures, where the underlying mechanism is closely related to

Figure 6 SEM images of cutting marks after scratch tests. **a** As-received sample. **b–f** samples annealed, respectively, to 713, 763, 773, 873, and 1073 K.



the microstructure of the annealed alloys. In brief, they can be summarized as structural relaxation [38], heterogeneous nucleation of α -Fe at the surface of the amorphous ribbon, homogeneous nucleation of metastable Fe_3B crystallites with surrounding α -Fe shell, and finally the dominance of equilibrium and α -Fe and Fe_2B phases. These changes are reflected not only in the direct TEM observation but also in the subtle changes in DSC thermograms. In what follows, we discuss the present findings from the viewpoints of structural evolution upon annealing observed by DSC and TEM and of their responses to machining.

Crystallization behavior

First, we discuss in some detail the observed DSC thermograms taken at different heating rates. One of

the commonly employed techniques to obtain *effective activation energy* is due to the analysis outlined by Kissinger [30]. Even though this method is obtained for Eyring n th-order transformations, Henderson has shown that [39] the functionally identical procedure is valid for Johnson–Mehl–Avrami–Kolmogorov (JMAK)-type isothermal transformations [40]:

$$x = 1 - \exp\{A_0 \exp(-E/RT)t^n\}$$

provided the reaction rate dx/dt is separable in temperature T and x , where x is the ratio of transformation; t time; n , so-called the Avrami exponent; R gas constant; and A_0 a constant.

Since it is often desirable to obtain kinetic parameters, such as n , various methods have been proposed, [32, 40, 41] which are well documented and compared by Hasani et al. [36, 42–46].

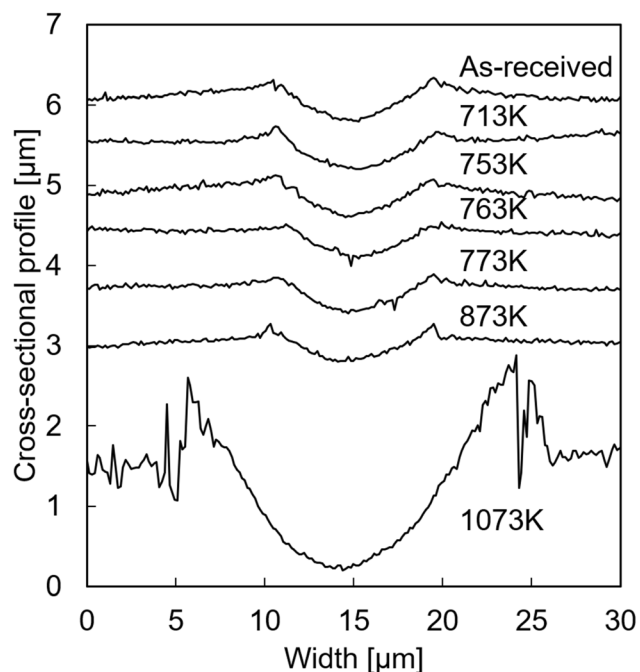


Figure 7 Cross-sectional profile of cutting marks obtained after the scratch tests.

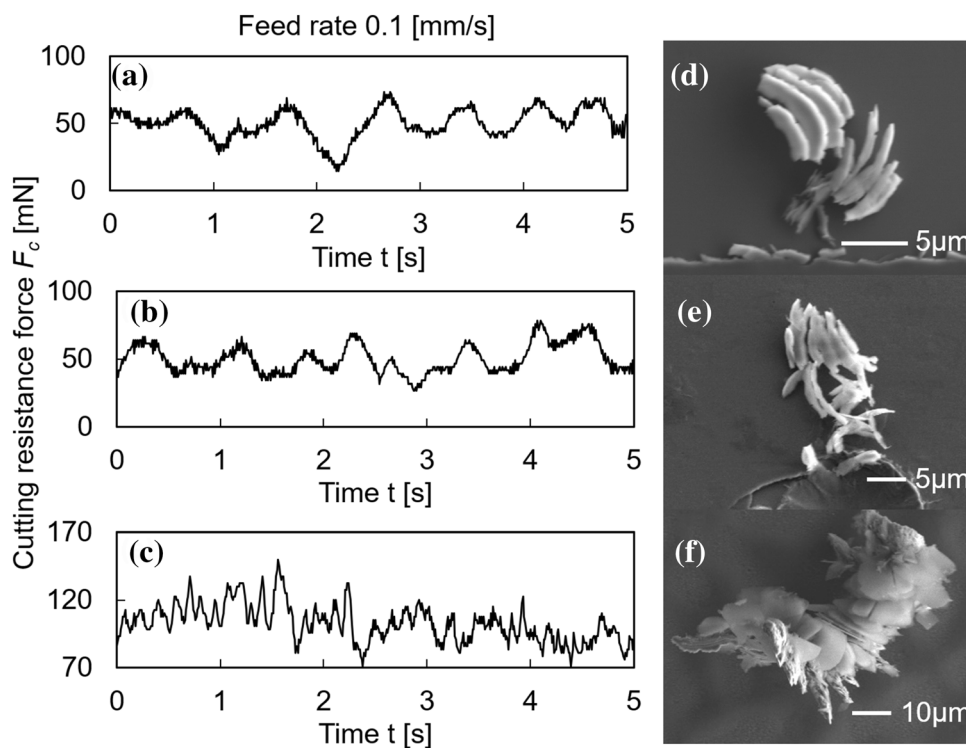
It should be emphasized that these analytical techniques based on the JMAK formula are valid, provided that nucleation is spatially random and the growth rate depends only on temperature, and not on

time [39]. In fact, since the JMAK formula was derived based on the concept of extended volume [40], for a simple case of constant growth rate, the so-called Avrami exponent n is equal to $m + 1$ for an m -dimensional growth. And if nucleation and growth are both thermally activating processes, we can write $E = E_N + mE_G$, where E_N and E_G are activation energies for nucleation and growth, respectively. Therefore, the effective activation energy, E/n , gives only a rough knowledge of the transformation process. Conversely, if E_N and E_G are known and the JMAK mechanism is operative, DSC curves upon crystallization can well be reproduced [47].

With these restrictions in mind, the values listed in Table 2 compare favorably with the published data. For example, in the Fe-based amorphous ribbons, it is 222 ± 4.82 kJ/mol for $\text{Fe}_{80}\text{Si}_{20}$ [48], 261 kJ/mol for $\text{Fe}_{78}\text{B}_{22}$ [49], 318 kJ/mol for $\text{Fe}_{80}\text{B}_{10}\text{Si}_{10}$ [49], and 434 kJ/mol for $\text{Fe}_{78}\text{B}_{16}\text{Si}_6$ [49]. In addition, the activation energy of Fe-based bulk metallic glasses is 470 to 1100 kJ/mol for $\text{Fe}_{41}\text{Co}_7\text{Cr}_{15}\text{Mo}_{14}\text{Y}_2\text{C}_{15}\text{B}_6$ [42, 44–46] and 157 to 280 kJ/mol for $[(\text{Fe}_{0.9}\text{Ni}_{0.1})_{77}\text{Mo}_5\text{P}_9\text{C}_{7.5}\text{B}_{1.5}]_{100-x}\text{Cu}_x$ ($x = 0.1$ at%) [36, 43].

Next, we focus on the behaviors specific to the FeSiB melt-spun amorphous alloy. First, the minor exothermic peak observed at 753 K (Fig. 1) and the corresponding XRD peaks in the profile (Fig. 2) can

Figure 8 Cutting resistance forces measured during the scratch tests, and chip images observed by SEM. **a, b** as-received sample; **c, d** 873 K sample; and **e, f** 1073 K sample.



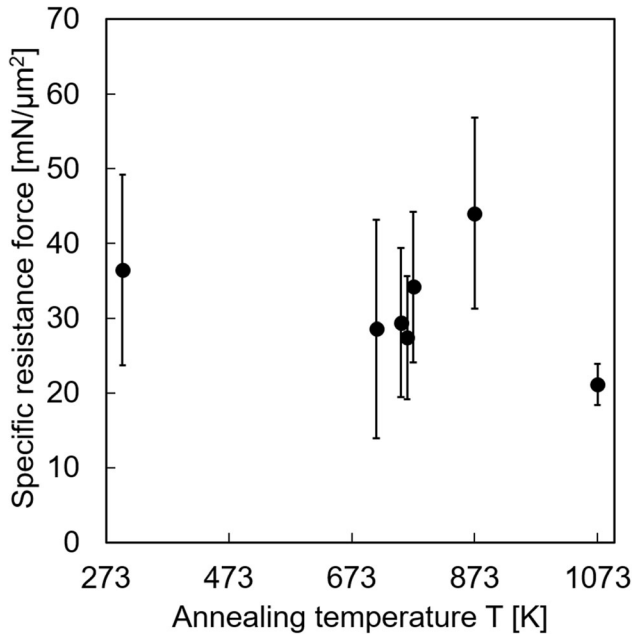


Figure 9 Specific cutting resistance force (SCRf), i.e., SCRf normalized to the scratched area, obtained from the scratch tests, as a function of annealing temperature of the alloys. Error bars indicate the standard deviation.

be ascribed to the heterogeneous crystallization at the surface of the amorphous ribbon. The reaction sequence of Fe–Si–B-based melt-spun amorphous alloy has been the subject of numerous studies in the past [26], among which Załuska and Matyja suggested that the metastable Fe_3B phase formation not only depends on the B content but are related also to the formation of the $\alpha\text{-Fe}$ phase, which in return influenced by the ordering tendency upon the introduction of Si. Gibson and Delamore reported that dendritic $\alpha\text{-Fe}$ has grown on a core of metastable Fe_3B in B-rich Fe–Si–B amorphous alloys [28], to which the crystallization mode observed in the present study is identical. Yet, the underlying mechanism for the emergence of this distinct microstructure has not hitherto been described. In particular, it is interesting to note that the enclosing $\alpha\text{-Fe}$ shells start to form only when the Fe_3B cores have grown to a size of about 50 nm and that the size of the composite structure is always approximately 200 nm, resulting in a uniform dispersion of the composite crystalline structure in the amorphous matrix.

The compositional mappings in Fig. 4 indicate that Si was partitioned out during the growth of the Fe_3B core. This movement of Si atoms means that the driving force for the formation of $\alpha\text{-Fe}$ in the

peripheral amorphous matrix regions increases by the Si enrichment, which is well-known ferrite former. In return, the growth of the dendritic $\alpha\text{-Fe}$ is accompanied not by the diffusion of Si, but by the ejection of B, thus reducing the driving force for the $\alpha\text{-Fe}$ formation, resulting in a limited size of each core–shell crystalline composite.

Given these findings, we are now able to propose reasoning on the rather puzzling trend observed in the DSC thermograms: not only peak position but also their ratio changes as the heating rate increases. Gibson suggested that this was due to the saturation of nucleation rate with time, but we can modify the suggestion that it is rather the growth rate that decreased because they must involve partitioning out of Si and B.

Machinability

Generally, amorphous alloys are deformed when local plastic deformation occurs in unstable regions, which then transform into macroscopic shear zones [50]. The initial increase in hardness with increasing heating temperature is considered to be due to the minor atomic shifts from quenched-in positions to stable ones, i.e., structural relaxation. Upon further annealing, the hardness increases monotonically, while the SCRf drops continuously to 763 K, followed by a slight increase at 773 K, at which the annealed specimen exhibits the best cutting performance. A molecular dynamics study reported that deformation concentrates in the amorphous phase in a small-crystal-scattered amorphous alloy [51]. This report suggests that deformation due to the shearing of the amorphous phase is dominant in the early stage of crystalline particle formation. The cutting tests also suggested that the difference in hardness due to the change in microstructure significantly affects the cutting quality, the mechanisms of chip evacuation, and burr formation. In the as-received specimens, during shear-type chip evacuation, the edge of the cutting trace remained on the substrate due to the toughness of the material and appeared as burrs. On the other hand, the heat treatment up to 773 K decreases the toughness, but hardens the material, and the edge of cutting trace, which causes burrs, was also ejected as chips, and burrs were reduced. With reducing burrs, microcracks appeared on the machined edge, and the periodicity of microcracks corresponded to the period of slip surface of

shear-type chips as shown in Fig. 7b, d. This result suggests that the microcracks are caused by brittle fracture caused by the impact of sliding during the formation of a new shear surface of the chip.

The most favorable cutting trace with the least burr was observed in the 773 K sample, and its structure was amorphous with crystallites scattered inside. In fact, this structure is similar to those of sulfur free-cutting steel and/or lead free-cutting steel, and in these materials, spherical inclusions in solid solution effectively facilitate chip evacuation because they become starting points of cracks [52–54]. Similarly, the precipitated crystals in the 773 K sample became the starting points of deformation like additives in free-cutting steel and improved the cutting quality. Additionally, studies on the precision cutting of amorphous alloys have reported that good machinability can be obtained when a plastic deformation region smaller than the cutting width occurs in front of the cutting direction [19]. It should also be pointed out that the cutting marks in Fig. 6d are notably similar to the previously reported burr suppressed cutting marks [19], indicating that the cutting conditions were favorable.

Conversely, the cutting quality on the 873 K specimens decreased again due to the transition from the deformation of the amorphous layer to the deformation mode of the crystalline metal originating from grain boundaries and defects. The undulations of cutting resistance force observed in Fig. 7a, c, and e are considered to correspond to the process of chip evacuation due to periodic slippage, especially in the 1073 K sample, where the cutting phenomenon changed significantly due to softening caused by crystal coarsening. Under the condition where the crystals were scattered in the amorphous microstructure, the cutting quality was the best, but the specific cutting force gradually increased. When the number of crystal grains increased to the extent that crystals were adjacent to each other, the cutting quality decreased regardless of the specific cutting force.

The maximum hardness was observed for the 873 K sample, and this result is thought to be due to the increase in grain boundaries caused by crystal growth, and a shift from deformation of the amorphous phase to deformation caused by dislocation migration, which is characteristic of crystalline metals. On the other hand, the decrease in hardness of the 1073 K sample is ascribed to the large grain size.

According to the Hall–Petch rule, the smaller the grain size becomes, the stronger the crystalline metal becomes [55, 56]. The grain size of the composite crystals, which was about 100–200 nm in the 873 K sample, grew to the order of several hundred nanometers by heating at high temperatures. Therefore, the 873 K sample is considered to be the hardest due to the grain refinement strengthening in the Hall–Petch rule.

Conclusions

We investigated the effects of annealing of B-rich Fe–Si–B–Cr amorphous ribbon and thereby the changes in the inner structures, upon their mechanical properties, especially the machinability. The major findings are as follows:

- (i) The hardness and specific cutting resistance force (SCRF) exhibit, respectively, a gradual increase and decrease before crystallization at 753 K, which have been ascribed to structural relaxation.
- (ii) Early crystallization sequence of this alloy is heterogeneous crystallization of α -Fe at the surface of the ribbon at 753 K, homogeneous nucleation and growth of Fe₃B to a size of 50 nm at 763 K, followed by the nucleation and growth of α -Fe on the Fe₃B core at 773 K.
- (iii) Silicon is ejected during the growth of Fe₃B core, accumulating in the adjacent amorphous matrix, thereby increasing the driving force for the nucleation of the α -Fe phase.
- (iv) The α -Fe phase grows into the surrounding Si-rich amorphous until the excess Si, or equivalently, the driving force is exhausted. This process results in the microstructure, where crystalline core–shell particles of about 200 nm are dispersed uniformly in the amorphous matrix.
- (v) The minimum SCRF was observed for 763 K annealed specimen. No chips or burrs were ejected upon cutting, exhibiting the ideal machinability.
- (vi) Upon further heating, the hardness and SCRF of the alloys increase up to 873 K and finally decrease, resulting in degraded machinability, which can best be understood from the polycrystalline nature of the alloys.

Acknowledgements

We would like to express our gratitude to the Materials Processing Technology Department of the Iwate Prefectural Industrial Technology Center for the use of the SEM, Vickers hardness tester, and confocal laser microscope; Dr. Y. Kodama and Mr. Y. Hayasaka in the Institute for Metals Research, Tohoku University, respectively, for the preparation of TEM samples and the help in TEM observation; and the Second Fabrication Technology Group of the Engineering Department of Tohoku University for providing the scratching test jig. The part of this work was supported by the Nanotechnology Platform Project (Tohoku University Microstructure Analysis Platform) of the Ministry of Education, Culture, Sports, Science and Technology of Japan (JPMX09A20TU0017) and the Iwate Industrial Technology Center (Iwate Prefecture).

Authors' contributions

C. Kuji conducted all the heat treatments, mechanical property evaluation, and cutting tests of the specimens. K. Takenaka performed DSC and XRD measurements and prepared TEM specimen by using FIB. T. J. Konno carried out the TEM study. K. Shimada and M. Masayoshi advised on this study, and T. Kuriyagawa supervised this study.

Declarations

Conflict of interest The authors declare that they have no conflict of interest.

Data and code availability All data can be provided upon request.

References

- [1] Yoshizawa Y (2017) Development trend and outlook for soft magnetic materials. *Mater Jpn* 56:186–189. <https://doi.org/10.2320/materia.56.186>
- [2] Murakami K (1987) The trend of applied magnetic engineering and the expectation to development of magnetic materials. *Tetsu-to-Hagané* 73:1485–1495. https://doi.org/10.2355/tetsutohagane1955.73.11_1485
- [3] Okazaki Y (2002) Ecotechnology and development of magnetic materials for power use. *Trans Inst Electr Eng Jpn* 122:887–890. <https://doi.org/10.1541/ieejfms.122.887>
- [4] Murakami K (1988) IV Magnetic materials. *J IEE Japan* 108:314–318. <https://doi.org/10.11526/ieejjournal1888.108.314>
- [5] Sato T (1981) Properties and application of amorphous metals. *Jitsumu Hyomen Gijutsu* 28:556–562. <https://doi.org/10.4139/sfj1970.28.556>
- [6] Tomita S, Suzuki H (1984) The relation between the process conditions and shape of amorphous metal ribbons fabricated by the single roll method. *J Jpn Inst Met Mater* 48:202–208. https://doi.org/10.2320/jinstmet1952.48.2_202
- [7] Fukunaga T (1987) Partial structure of amorphous metal. *Bull Jpn Inst Metals* 26:481–489. <https://doi.org/10.2320/materia1962.26.481>
- [8] Takeuchi T, Arai K, Tsuya N (1985) Amorphous materials. *J Soc Instrum Control Eng* 24:503–507. <https://doi.org/10.11499/sicej1962.24.503>
- [9] Shingu H (1987) Thermodynamics of amorphous metals. *Resour Process* 34:30–37. <https://doi.org/10.4144/rpsj1986.34.30>
- [10] Masumoto T, Fukamichi K, Mizoguchi T (1998) Recent studies of amorphous alloys. *Oyo Buturi* 50:790–806. <https://doi.org/10.11470/oubutsu1932.50.790>
- [11] Masumoto T (1998) Flow in studies of amorphous metallic materials. *Mater Jpn* 37:339–346. <https://doi.org/10.2320/materia.37.339>
- [12] Yoshida S, Mizushima T, Makino A, Inoue A (1999) Magnetic properties of thick amorphous alloy sheets in Fe-metalloid systems. *Trans Inst Electr Eng Jpn* 119:1255–1260. https://doi.org/10.1541/ieejfms1990.119.10_1255
- [13] Hitachi Metals, Nanocrystalline soft magnetic material. <https://www.hitachimetals.com/materials-products/amorphous-nanocrystalline/common-mode-choke-cores/documents/Hitachi-Metals-FINEMET-material.pdf>. Accessed 4 November 2020
- [14] Nakagawa T, Aoki I (1986) Blanking of amorphous alloy metal foils. *J JSPE* 52:409–414. <https://doi.org/10.2493/jjspe.52.409>
- [15] Ueda K, Suda A, Sugita T (1987) Microcutting of amorphous metals: chip formation mechanism of rapidly quenched Fe-base alloys. *J JSPE* 53:1785–1790. <https://doi.org/10.2493/jjspe.53.1785>
- [16] Koga N, Okada S, Yamaguchi T (2018) Effect of various blanking conditions on properties of cut surface of amorphous alloy foil and tool life. *J JSTP* 59:176–180. <https://doi.org/10.9773/sosei.59.176>
- [17] Kobayashi R, Xu S, Shimada K, Mizutani M, Kuriyagawa T (2017) Defining the effects of cutting parameters on burr

- formation and minimization in ultra-precision grooving of amorphous alloy. *Precis Eng* 49:115–121. <https://doi.org/10.1016/j.precisioneng.2017.01.018>
- [18] Qiu P, Teraoka S, Xu S, Shimada K, Mizutani M, Kuriyagawa T (2020) Surface defect inhibition mechanisms of laser assisted microcutting on Ni-P amorphous alloy. *J Manuf Process* 60:644–653. <https://doi.org/10.1016/j.jmapro.2020.11.005>
- [19] Kobayashi R, Shimada K, Mizutani M, Kuriyagawa T (2017) Materials removal mechanisms in fabrication of microstructures by using ultraprecision cutting: effect of material properties on chip formation. *J JSPE* 83:687–693. <https://doi.org/10.2493/jjspe.83.687>
- [20] Inoue A, Masumoto T, Kikuchi M, Minemura T (1978) Compositional effect on crystallization of (Fe, Ni, Co)–Si–B amorphous alloys. *J Jpn Inst Met Mater* 42:294–303. https://doi.org/10.2320/jinstmet1952.42.3_294
- [21] Takahara Y, Tamenari J, Matsuda H (1994) Compositional dependence of crystallization process in Fe–B–Si amorphous alloys. *J Jpn Inst Metals* 58:245–251. https://doi.org/10.2320/jinstmet1952.58.3_245
- [22] Takahara Y, Hatade K, Matsuda H (1987) Structural relaxation and crystallization of amorphous Fe₇₉B₁₆Si₅. *J Japan Inst Met Mater* 51:95–101. https://doi.org/10.2320/jinstmet1952.51.2_95
- [23] Takahara Y, Fujii N, Matsuda H (1988) Reversible changes in electrical resistivity and Mössbauer spectroscopy in structural relaxation of amorphous Fe–B–Si alloys. *J Jpn Inst Metals* 52:1–7. https://doi.org/10.2320/jinstmet1952.52.1_1
- [24] Yoshihiro T, Narita N (1999) Local atomic structure in an Fe–B–Si amorphous alloy and its relaxation upon annealing. *J Jpn Inst Met Mater* 63:557–560. https://doi.org/10.2320/jinstmet1952.63.5_557
- [25] Oguni M (2009) Thermal studies on structural relaxation and ordering in disordered molecular-arrangement systems. *Netsu Sokutei* 36:2–9
- [26] Załuska A, Matyja H (1983) Crystallization characteristics of amorphous Fe–Si–B alloys. *J Mater Sci* 18:2163–2172. <https://doi.org/10.1007/BF00555011>
- [27] Bang JY, Lee RY (1991) Crystallization of the metallic glass Fe₇₈B₁₃Si₉. *J Mater Sci* 26:4961–4965. <https://doi.org/10.1007/BF00549877>
- [28] Gibson MA, Delamore GW (1992) Nucleation kinetics of primary crystallization products in FeSiB metallic glasses. *J Mater Sci* 27:3533–3538. <https://doi.org/10.1007/BF01151830>
- [29] Metglas[®], Inc., Magnetic Alloy 2605S3A (Iron-based) Technical Bulletin. <https://metglas.com/wp-content/uploads/2016/12/2605S3A-Technical-Bulletin.pdf>. Accessed 18 November 2020
- [30] Kissinger HE (1957) Reaction kinetics in differential thermal analysis. *Anal Chem* 29:1702–1706. <https://doi.org/10.1021/ac60131a045>
- [31] Marseglia EA (1980) Kinetic theory of crystallization of amorphous materials. *J Non-Cryst Solids* 41:31–36. [https://doi.org/10.1016/0022-3093\(80\)90188-x](https://doi.org/10.1016/0022-3093(80)90188-x)
- [32] Gao YQ, Wang W (1986) On the activation-energy of crystallization in metallic glasses. *J Non-Cryst Solids* 81:129–134. [https://doi.org/10.1016/0022-3093\(86\)90262-0](https://doi.org/10.1016/0022-3093(86)90262-0)
- [33] Williams HW, Chamberland BL (1969) Determination of Curie, Neel, or crystallographic transition temperatures via differential scanning calorimetry. *Anal Chem* 41:2084–2086. <https://doi.org/10.1021/ac50159a056>
- [34] Soltani ML, Touares A, Aboki TAM, Gasser JG (2017) Thermal effect on structural and magnetic properties of Fe₇₈B₁₃Si₉ annealed amorphous ribbons. *EPJ Web Conf* 151:07002. <https://doi.org/10.1051/epjconf/201715107002>
- [35] Cullity BD (1978) *Elements of X-ray diffraction*, 2nd edn. Addison-Wesley, Philippines, p 102
- [36] Jaafari Z, Seifoddini A, Hasani S, Rezaei-Shahreza P (2018) Kinetic analysis of crystallization process in [(Fe_{0.9}Ni_{0.1})₇₇-Mo₅P₉C_{7.5}B_{1.5}]_{100-x}Cu_x (x = 0.1 at.%) BMG: non-isothermal condition. *J Therm Anal Calorim* 134:1565–1574. <https://doi.org/10.1007/s10973-018-7372-y>
- [37] Piispanen V (1948) Theory of formation of metal chips. *J Appl Phys* 19:876. <https://doi.org/10.1063/1.1697893>
- [38] Antonione C, Baricco M, Riontino G (1988) Structural relaxation kinetics in FeSiB amorphous alloys. *J Mater Sci* 23:2225–2229. <https://doi.org/10.1007/bf01115792>
- [39] Henderson DW (1979) Thermal analysis of non-isothermal crystallization kinetics in glass forming liquids. *J Non-Cryst Solids* 30:301–315. [https://doi.org/10.1016/0022-3093\(79\)90169-8](https://doi.org/10.1016/0022-3093(79)90169-8)
- [40] Christian JW (1975) *The theory of transformations in metals and alloys*, part I. 2nd edn. Pergamon Press, Oxford, pp 15, 525
- [41] Augis JA, Bennett JE (1978) Calculation of the Avrami parameters for heterogeneous solid state reactions using a modification of the Kissinger method. *J Therm Anal* 13:283–292. <https://doi.org/10.1007/BF01912301>
- [42] Rezaei-Shahreza P, Seifoddini A, Hasani S (2017) Non-isothermal kinetic analysis of nano-crystallization process in (Fe₄₁Co₇Cr₁₅Mo₁₄Y₂C₁₅)₉₄B₆ amorphous alloy. *Thermochim Acta* 652:119–125. <https://doi.org/10.1016/j.tca.2017.03.017>
- [43] Hasani S, Jaafari Z, Seifoddini A, Rezaei-Shahreza P (2020) Nucleation and growth of nano-crystallites in a new multi-component Fe-based BMG during the partial crystallization process. *J Therm Anal Calorim*. <https://doi.org/10.1007/s10973-020-09718-4>

- [44] Redaei H, Rezaei-Shahreza P, Seifoddini A, Hasani S (2020) Effect of cooling rate on glass forming ability of novel Fe-based bulk metallic glass. *Acta Phys Pol A* 138:265–267. <https://doi.org/10.12693/APhysPolA.138.265>
- [45] Rezaei-Shahreza P, Seifoddini A, Hasani S, Jaafari Z, Sliwa A, Nabialek M (2020) Isokinetic analysis of $\text{Fe}_{41}\text{Co}_7\text{Cr}_{15}\text{Mo}_{14}\text{Y}_2\text{C}_{15}\text{B}_6$: effect of minor copper addition. *Materials*. <https://doi.org/10.3390/ma13173704>
- [46] Hasani S, Rezaei-Shahreza P, Seifoddini A (2021) The effect of Cu minor addition on the non-isothermal kinetic of nanocrystallites formation in $\text{Fe}_{41}\text{Co}_7\text{Cr}_{15}\text{Mo}_{14}\text{Y}_2\text{C}_{15}\text{B}_6$ BMG. *J Therm Anal Calorim* 143:3365–3375. <https://doi.org/10.1007/s10973-020-09716-6>
- [47] Konno TJ, Sinclair R (1993) Crystallization and decomposition of co-sputtered amorphous silicon–aluminum thin-films. *Mater Chem Phys* 35:99–113. [https://doi.org/10.1016/0254-0584\(93\)90183-m](https://doi.org/10.1016/0254-0584(93)90183-m)
- [48] Greer AL (1982) Crystallization kinetics of $\text{Fe}_{80}\text{B}_{20}$ glass. *Acta Metal* 30:171–192. [https://doi.org/10.1016/0001-6160\(82\)90056-6](https://doi.org/10.1016/0001-6160(82)90056-6)
- [49] Ramanan VRV, Fish GE (1982) Crystallization kinetics in Fe–B–Si metallic glasses. *J Appl Phys* 53:2273–2275. <https://doi.org/10.1063/1.330797>
- [50] Shibutani Y, Wakeda M (2009) Mechanical properties and deformation mechanism of metallic glasses. *J Soc Mater Sci Jpn* 58:199–204. <https://doi.org/10.2472/jsms.58.199>
- [51] Matsumoto R, Nakagaki M (2006) Mechanical properties of amorphous metal with dispersed nanocrystalline particles: molecular dynamics analysis on appearance of particle size effects. *Trans JSME* 72:361–368. <https://doi.org/10.1299/kiikaia.72.361>
- [52] Yamane Y (1999) Possibility of a new type of free-cutting rope. *Trans JSME* 102:694. https://doi.org/10.1299/jsmemag.102.972_694
- [53] Ito T, Kato T, Yamada H (1967) Machinability of several free-cutting steels. *Denki Seiko* 38:237–257. <https://doi.org/10.4262/denkiseiko.38.237>
- [54] Ito T (1983) The latest free machining steel. *J Jpn Soc Precis Eng* 49:1278–1283. <https://doi.org/10.2493/jjspe1933.49.1278>
- [55] Hall EO (1951) The deformation and ageing of mild steel: III discussion of results. *Proc Phys Soc Sect B* B64:747–752
- [56] Petch NJ (1953) The cleavage strength of polycrystals. *J Iron Steel Inst* 174:25–28

Publisher's Note Springer Nature remains neutral with regard to jurisdictional claims in published maps and institutional affiliations.

パウダージェットデポジションによる歯冠色修復

本郷那美*1, 山本浩己*1, 簾内崇彰*1, 富江瑛彦*2, 泉田一賢*3,
佐々木啓一*3, 嶋田慶太*1, 水谷正義*1, 厨川常元*2

Restoring tooth color by Powder Jet Deposition

Nami HONGO, Hiroki YAMAMOTO, Takaaki SUNOUCHI, Akihiko TOMIE, Kuniyuki IZUMITA,
Keiichi SASAKI, Keita SHIMADA, Masayoshi MIZUTANI and Tsunemoto KURIYAGAWA

パウダージェットデポジション(PJD)は、常温大気圧環境下で微粒子材料を対象物に高速衝突させて付着させる膜形成手法である。著者らは本手法を用いて、ヒト歯の主成分であるハイドロキシアパタイト(HA)を歯冠に成膜する歯科治療法を推進している。しかし、純粋なHA膜は明度と隠蔽性に乏しく、PJDの審美歯科治療への応用は実現されていない。そこで本研究では、白色不透明の歯科材料であるZrO₂の粒子、およびHA粒子とZrO₂粒子で作製した複合粒子の成膜を試み、形成した膜の成膜性と審美性を評価した。前者はHA膜、複合粒子膜、ZrO₂膜の順に大きく、単位膜厚における明度はその逆順で大きい結果となり、膜全体では複合粒子膜が最大の明度を有した。また、複合粒子膜においてZrO₂が偏りなく層状に存在していることを明らかにした。

Key words: hydroxyapatite, zirconium dioxide, composite particles, powder jet deposition

1. 緒言

近年、歯科医療分野では生体機能の回復・改善に加え、審美歯科治療の需要が高まっている¹⁾。本報では審美歯科治療を「変色した歯冠の色調を修復し、歯の本来具備すべき自然の色調を保存する修復治療」に限定して定義する。既存の審美歯科治療では、コンポジットレジンやセラミックスなどの歯科修復材料を、接着性材料を介して歯面や歯冠に直接的に充填・被覆する治療法が一般的である¹⁾²⁾。一方、現行の歯科修復材料と歯質の化学的・機械的特性が大きく異なることから、前者に微小漏洩や疲労破壊、溶解が生じ、結果として修復物が脱離したり齶蝕が発生したりすることが問題となっている³⁾。そこで、接着性材料を介さず直接的に歯質と同等の材料で歯冠を修復する新たな審美歯科治療法が求められている。この点に対して著者らは、常温大気圧下での膜形成手法であるパ

ウダージェット加工(Powder Jet Processing)を提案しており、本手法を歯科治療法に適用することを考えている。

パウダージェット加工とは、金属またはセラミックスなどの微粒子を対象物に高速衝突させることによって形状創成を行う噴射加工法の総称である⁴⁾⁵⁾。粒径や衝突速度などの加工パラメータおよび粒子・基板材料の機械的特性により、除去現象のアブレイシブジェット加工(AJM: Abrasive Jet Machining)と付着現象のパウダージェットデポジション(PJD: Powder Jet Deposition)の2つの加工現象に分類される。PJDについて、水谷ら⁶⁾は、PJDにおける成膜は粒子の衝突界面近傍の材料のみが衝突作用により数ns以内に塑性変形して対象物に付着し、その繰り返により膜が形成されると報告している。また1粒子あたりの付着量は粒子体積の7%程度であり⁶⁾、その付着した粒子材料が、基板材料との間で化学的な結合を形成し、基板に高強度で付着していることも明らかとなっている⁷⁾⁸⁾。

以上の特性をもつPJDを利用してヒト歯の主成分であるハイドロキシアパタイト(Ca₁₀(PO₄)₆(OH)₂、以下HA)膜を形成する技術は、補綴および予防歯科の分野で有用であることが臨床試験により実証されている⁹⁾。一方で、純粋なHA膜では下地の隠蔽性に乏しく、PJDの審美歯科治療への応用は実現されていない。そこで著者らは、インプラント材として利用が拡大しているZrO₂の粒子をHA粒子と複合し成膜することで歯冠

*1 東北大学大学院工学研究科機械機能創成専攻: 〒980-8579 宮城県仙台市青葉区荒巻字青葉6-6-01

Department of Mechanical Systems Engineering, Graduate School of Engineering, Tohoku University

*2 東北大学大学院医工学研究科: 〒980-8579 宮城県仙台市青葉区荒巻字青葉6-6-01

Graduate School of Biomedical Engineering, Tohoku University

*3 東北大学大学院歯学研究科: 〒980-8575 宮城県仙台市青葉区星陵町4-1

Graduate School of Dentistry, Tohoku University

(学会受付日: 2020年12月15日)

(採録決定日: 2021年3月11日)

の色調を制御し、審美性を兼ね備えた膜の形成に取り組んでいる。本報ではとくに PJD による審美歯科治療の実現に向けた基礎検討結果について報告する。具体的にはまず PJD で ZrO_2 粒子単体をガラス板に成膜し、その成膜性と審美性を検証した。本報で評価する審美性とは、白さを表す値である明度の大きさとした。また、同粒子と HA 粒子の複合粒子を作製して同様に成膜し、HA 膜および ZrO_2 膜との成膜性と審美性を比較した。最終的に、ヒト歯に成膜することを想定して、HA 基板に複合粒子を成膜し、その断面の ZrO_2 分布を確認した。

2. ZrO_2 粒子の成膜と膜の色調評価

2.1 成膜実験装置の構成

本研究で用いる成膜実験装置(PJD 装置)の外観と、成膜実験の様子を図 1 に示す。本装置は、PJD 法を歯科治療に応用するために開発した装置である。同装置のハンドピースは歯科治療用ドリルを模して設計されており、PJD による歯科治療の実用化に向けて開発が進行している¹⁰⁾。同図のチャンパー内に粒子を充填したあと、加速圧力制御器で噴射条件を設定し噴射を開始すると、圧縮された供給エアがチャンパーに流入し(破線矢印)、ゴムチューブを通して粒子をハンドピースへ搬送する(白矢印)。搬送された粒子はハンドピース噴射口付近で加速エア(黒矢印)と合流して加速されたあと、対象物へ衝突して付着、成膜に至る。ハンドピースは X, Y, Z の 3 軸自動ステージに固定されており、走査しながらの成膜が可能である。

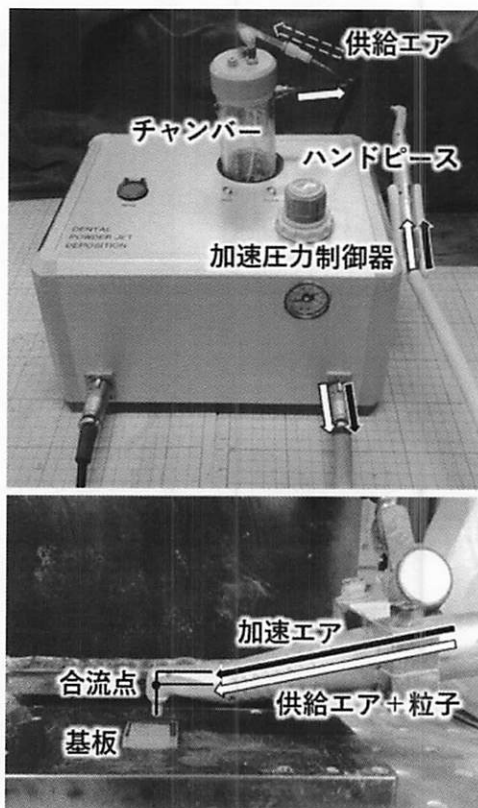


図 1 PJD 装置

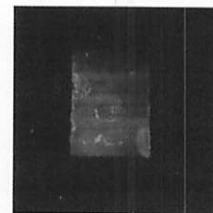
2.2 歯科用バイオセラミックス粒子単体の成膜実験

本実験の噴射粒子には、PJD 法で標準的に使用されてきた HA 粒子の粒径^{9)~11)}と同程度の平均径 $1.8 \mu m$ の HA 粒子および平均径 $2.2 \mu m$ の ZrO_2 粒子を用いた。粒子の噴射条件を表 1 に示す。同表の加速圧力は、噴射速度を決めるパラメータであり、PJD か AJM かという加工形態に大きく影響する¹²⁾。HA 粒子の加速圧力は 0.50 MPa とした。なお、この条件で HA 粒子がヒト歯に成膜可能であることは確認されており、臨床試験でも用いられた⁹⁾。一方、 ZrO_2 粒子の密度(約 6 g/cm^3)¹³⁾は HA 粒子の密度(約 3 g/cm^3)¹⁴⁾の約 2 倍である。そのため、運動エネルギーの差異を考慮して、 ZrO_2 の加速圧力は 0.50 MPa と、その半分の 0.25 MPa の 2 条件とした。また、ヒト歯の色調の個人差が膜の色調評価に影響を及ぼすことを避けるため、ガラス基板を噴射対象物として用いた。ただし、ガラス基板とヒト歯の硬さの違いが成膜性に影響を与えることをヒト歯への治療の際には留意する必要がある。

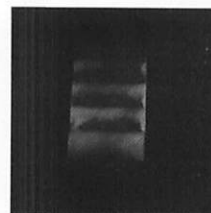
成膜後の試料を図 2 に示す。同図(a)~(c)で膜の形成が確認でき、PJD 法による ZrO_2 粒子の成膜が可能であることが確認された。次に、非接触式 3 次元形状測定機により膜形状を測定した。図 3 の計測結果のとおり、(a)は十数 μm 、(c)は約 $5 \mu m$ 、そして(b)はそれ未満と、 ZrO_2 粒子の成膜性が HA 粒子に比べて顕著に乏しいことが明らかとなった。パウダージェット加工では、粒子衝突による衝撃が①基板の破砕強度(以下、単

表 1 噴射条件

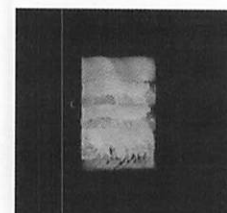
基板材料	シリカガラス
搬送流体	空気
加速圧力	0.25 MPa , 0.50 MPa
供給圧力	0.5 MPa
走査速度	$3000 \mu m/s$
走査ピッチ幅	$700 \mu m$
噴射距離	1.0 mm



(a) HA膜 加速圧力 0.50 MPa



(b) ZrO_2 膜
加速圧力 0.25 MPa



(c) ZrO_2 膜
加速圧力 0.50 MPa

図 2 HA 膜と ZrO_2 膜の実物写真

に基板強度)を上回らず粒子の破碎強度(以下,単に粒子強度)に達すれば付着が優位になり粒子の一部が付着⁶⁾,②基板強度に達した場合には除去が優位になり基板の除去,③粒子強度と基板強度のいずれにも達しなければ粒子の基板上での跳ね返りが生じると予想される¹²⁾.各粒子および基板の箇所によって粒子衝突の衝撃,基板強度,粒子強度は異なることから粒子の基板への付着と除去が同時に発生し,現象の集積が付着優勢の場合は PJD,除去優勢である場合に

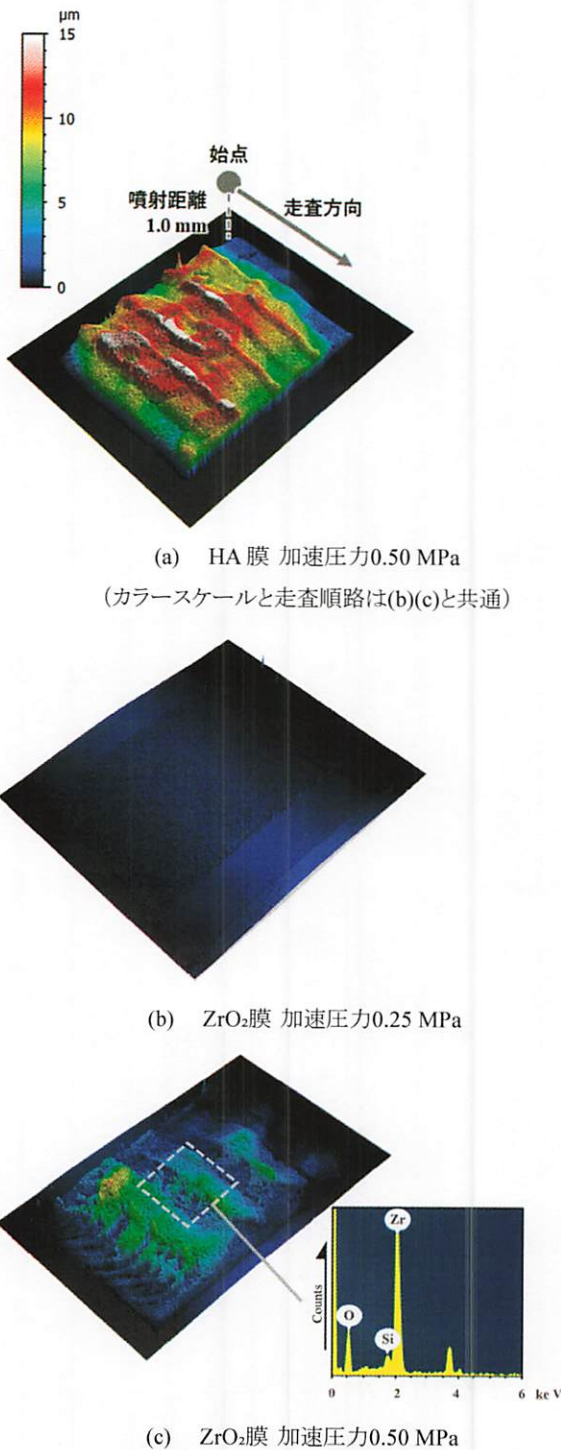


図3 HA膜とZrO₂膜の3次元プロファイル

はAJMとなる。ただし,付着現象では付着する材料同士の親和性もまたPJDの必要条件となる。HAは水酸基に高い吸着性を示し,自身もまた水酸基を有することから¹⁵⁾,HA粒子間の付着が誘起されるため,HA粒子は成膜性が高かったと考えられる。このことは,HAを主成分とするヒト歯に対してHA粒子を成膜することの有効性を示唆するものである。一方,ZrO₂はHAより比重が大きく,強度も大きい材料であるため¹⁶⁾,0.50 MPa下のZrO₂粒子噴射では付着と同時に基板材料の除去が進展し,結果としてZrO₂膜の膜厚がHA膜より低くなったと考察できる。また,0.25 MPa下で形成したZrO₂膜の膜厚が最小となったのは,加速圧力の減少で粒子の衝突エネルギーE_cが不十分な状態③になったためであると考えられる。さらにZrO₂には,インプラント材料に適した軟組織への吸着性が確認されているが¹³⁾,ヒト歯やZrO₂自身といった硬い材料に対してはHAのもつ化学的吸着性が確認されていない。そのため,ZrO₂膜の堆積率が小さいだけでなく,ヒト歯においても低い成膜性を有すると推測され,同粒子単体での成膜を実用するには成膜性の向上が課題となる。

2.3 色調評価方法

前節で作製した膜の審美性を検証するために,JIS Z 8722に準拠した分光測色計(村上色彩研究所,CMS-35FS型)を用い,円周照射-垂直受光方式,視野角2度,D₆₅光源,測定径1.6 mmの条件下で色調評価を行った。各試料の背景は黒色板とし,1試料につき膜中央部を4回測色して,その平均値を測色値とした。同装置は試料の分光反射率の分布(以下,分光分布)と,色の表示方法JIS Z 8729に従って算出したCIE(国際照明委員会)L*a*b*表色系におけるL*,a*,b*値を出力する。L*,a*,b*値はそれぞれ,明暗,赤緑,青黄の度合いを表し,図4の色空間における座標,つまり色を決定する値である。2色の差,すなわち色差ΔE_{ab}は同図における2点間の距離として以下の式で求められる。ここでΔL*,Δa*,Δb*は色空間内での明度と色度の差である。色差ΔE_{ab}が3以内の場合,ヒトは色の違いを認識できないとされる¹⁷⁾。

$$\Delta E_{ab} = \sqrt{(\Delta L^*)^2 + (\Delta a^*)^2 + (\Delta b^*)^2} \quad (1)$$

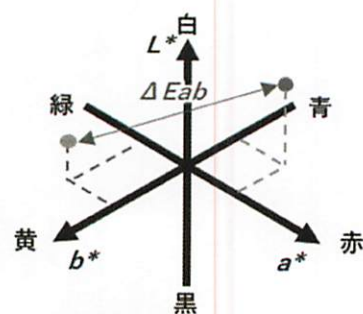


図4 式空間の模式図

2. 4 HA 膜と ZrO₂ 膜の測色

HA 膜と ZrO₂ 膜(加速圧力 0.25 および 0.50 MPa)の分光分布を図 5 に示す. HA 膜と ZrO₂ 膜はともにガラス基板より反射率が大きく, 明度が大きいことが定性的に読み取れる. 特に 0.50 MPa の ZrO₂ 膜は, HA 膜より膜厚が 2 倍以上小さいが, HA 膜より反射率が大きい.

次に, 明度と色度を定量評価するため, 図 5 の分光分布を CIE L*a*b*表色系に変換したデータを表 2 に示す. いずれの膜においても, ガラス板と比較して色度 a*, b*値の変化が少なく, L*値が顕著に増加しており, これらの膜が定量的に色の偏りの少ない白色であることを示している. 膜の明度は大きい方から順に 0.50 MPa の ZrO₂膜, HA 膜, 0.25 MPa の ZrO₂膜であり, 分光分布の反射率の大きさと一致した. また HA 膜を基準とし, 式(1)により求めた色差はどれも閾値 3 を大きく上回るため, 有効な色差だといえる. 同表から, 求めた色差は ΔE*が支配的であった. したがって, HA 膜より明度が高かった 0.50 MPa の ZrO₂は, 従来の HA 膜と比較して明度が有効に向上したといえる.

以上の成膜実験および測色結果より, ZrO₂粒子は HA 粒子より PJD による成膜性は劣るものの, ZrO₂膜は HA 膜より大きい審美効果を発揮できることが明らかとなった. このことから PJD 法を審美歯科に応用するためには, 成膜性と審美性を兼ね備えた粒子が必要となる. これを実現すべく, 次節では, HA 粒子と ZrO₂ 粒子の複合粒子を作製する.

3. 複合粒子の作製

3. 1 機械的作用を用いた複合手法

複合粒子の作製には, 図 6 の複合化装置(ホソカワミクロン製, ナノキュラ)を用いた. 装置の主要部は, アルミナセラミックスを溶射した円筒容器およびアルミナセラミックス製の攪拌翼からなる. 円筒容器内に充填された粒子は翼の高速回転により攪拌され, 粒子は翼と容器内壁の間で衝撃, 圧縮, せん断の力を受ける. その機械的エネルギーにより, 子粒子が母粒子表面に埋め込まれて固定されるものと考えられる¹⁸⁾. なお, 別途行った予備試験において, 複合化処理による粒子の凝集や解砕は生じないことが確認されている.

また同装置は, 高周波電圧でプラズマ化された大気を円筒容器内へと流し込む機構を有する. この機能を粒子の攪拌時に用いると, プラズマが粒子表面の有機物を除去し, 粒子の化学的活性を上昇させ, 粒子の複合化を促進させる.

3. 2 複合粒子の分析

粒子の複合条件を表 3 に示す. 同表の複合比率は, 粒子全体における子粒子の重量比率を意味する. 複合化処理前の HA 粒子および処理後の複合粒子の走査型電子顕微鏡(SEM)像を図 7 に示す. 同図 (b)では, 処理前の同図(a)では見られなかった母粒子表面上の微粒子の付着が確認でき, その大きさが子粒子として妥当であることから, 複合粒子の作製に成功したと判断した.

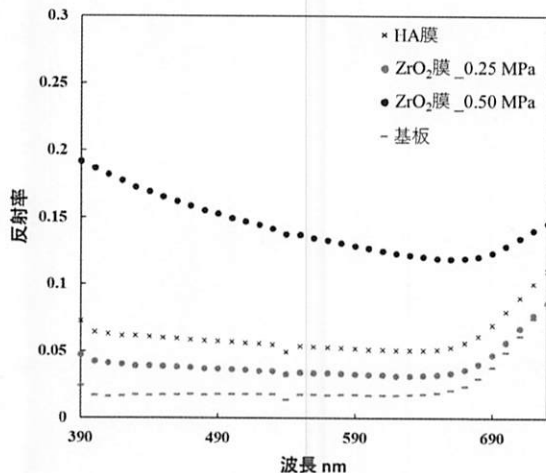
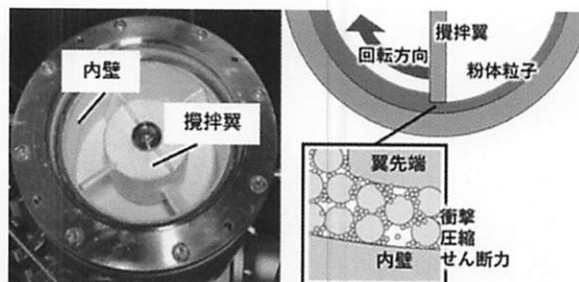


図 5 分光分布

表 2 HA 膜と ZrO₂ 膜の CIE L*a*b*表色系データ

	L*	a*	b*	ΔE _{ab}
HA	27.64	0.43	-2.94	(基準)
ZrO ₂ (0.25 MPa)	21.54	0.09	-2.66	6.12
ZrO ₂ (0.50 MPa)	43.64	-0.09	-6.66	16.44
Substrate	14.10	0.59	-0.20	13.82



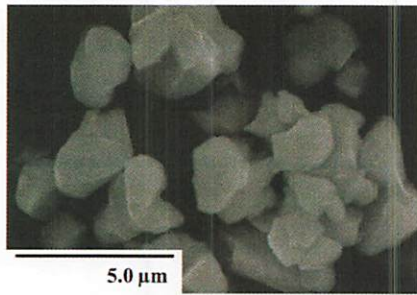
(a) 装置の内部 (b) 複合化処理の模式図

図 6 複合化装置

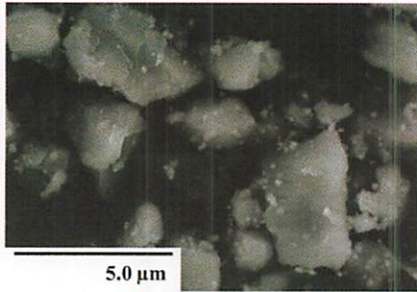
表 3 複合条件

母粒子材料	平均径	HA	1.8 μm
子粒子材料	平均径	ZrO ₂	0.62 μm
複合時間			10 min
回転数			1500 rpm
ZrO ₂ 複合比率			5%

次に, 複合前後の組成変化を調べるため, 作製した複合粒子における Zr 元素の重量比率を誘導結合プラズマ(ICP)発光分光分析法を用いて分析した. 得られた実測値, および複合条件である複合率から計算した仕込み粒子中の Zr 元素の重量比率を表 4 に示す. 同表の Zr 元素の結果より, 粒子の複合前後で組成に大きな変化は認められず, 母粒子と子粒子は過不足なく複合したと考えられる.



(a) HA 母粒子



(b) 複合粒子

図7 母粒子と複合粒子のSEM像

表4 複合前後における組成変化

重量%	Zr
仕込み粒子	3.70(複合率から得た計算値)
複合粒子	3.11(ICP発光分析による実測値)

4. 複合粒子膜の評価

4.1 複合粒子膜の成膜性と審美性

表1で加速圧力を0.50 MPaとした条件下、前節で作製した複合粒子を噴射し成膜を行った。その3次元プロファイルを図8に示す。同図より、複合粒子膜の膜厚は同条件下で作製したZrO₂膜(図3)の約2倍であり、HA膜よりやや小さかった。次に、複合粒子膜の測色結果を図9と表5に示す。複合粒子膜は、本研究で作製した膜の中で、最大の反射率とL*値を有した。同様に、HA膜との明度差と色差も最大であった。

以上の結果から、母粒子としてHAを使用し、子粒子としてZrO₂を使用した複合粒子を用いることで、HA粒子のもつ高い成膜性を維持しつつ、ZrO₂粒子の高い審美性を付与可能であることが示された。ここで、一般臨床の場で審美性評価の基準として広く用いられる、人歯の色調を模擬したシェードガイド(Lumin-Vacuum, VITA社製)のL*値は、本論文で使用した測色計で49.45~58.67である¹⁹⁾。今回得た複合粒子膜のL*値が上記の下限値と同程度であったこと、また複合率の調整によって、それに起因する膜の明度の制御が期待できることから、本研究で提案された複合粒子膜の審美歯科治療への適用可能性が示唆されたといえる。

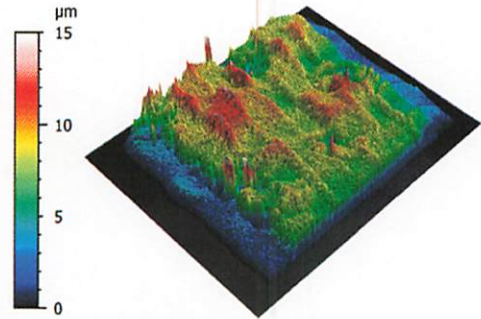


図8 複合粒子膜の3次元プロファイル

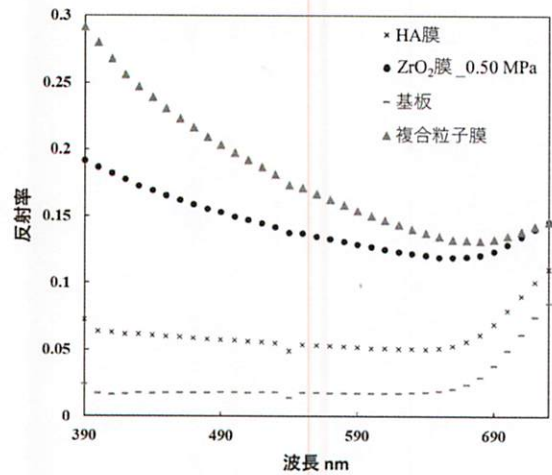


図9 複合粒子膜の分光分布

表5 複合粒子膜のCIE L*a*b*表色系データ

	L*	a*	b*	ΔE _{ab}
複合粒子膜	48.21	-0.11	-11.52	22.29

*ΔE_{ab}はHA膜(表2)との色差

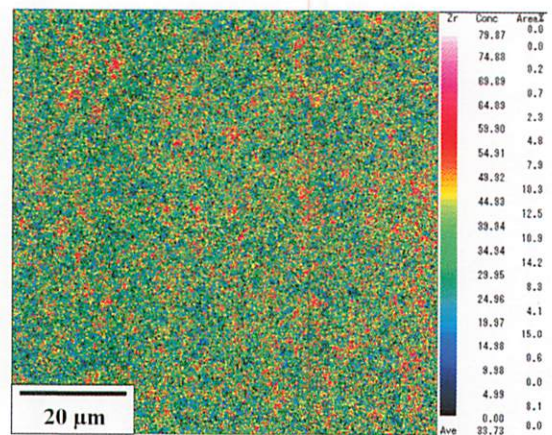


図10 複合粒子膜成膜面のZr元素濃度

4.2 複合粒子膜におけるZrO₂分布

前項で作製した複合粒子膜の成膜面(100×100 μm², 約0.6 μm深さ領域)を電子線マイクロアナライザ(EPMA)により分析し、Zr元素の重量比率分布を得た(図10)。同図は、15~50%

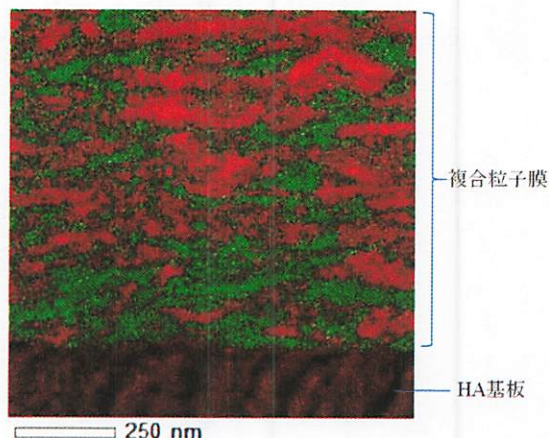


図 11 複合粒子膜断面のEDS分析

の Zr 元素濃度が測定領域中の 7.5 割以上を占め、平均濃度が 33.73%であること、またその分布が全体に均一に分布していることを示している。これより、複合粒子膜の ZrO_2 分布は均一と推定でき、膜厚が一定の同一膜中において、局所的な色の差異は少ないと考えられる。なお、表 4 では複合粒子中の Zr 元素重量比率が 3.11%を示しており、今回の結果と大きく異なる点については後述する。

次に、複合粒子によるヒト歯への成膜とその膜の性質について検証する。同複合率で作製した複合粒子を、ヒト歯を模擬した HA 基板に成膜し、その膜の断面を透過型電子顕微鏡 (TEM) により観察した。TEM 試料をエネルギー分散型 X 線分光 (EDS) により元素分析した結果を図 11 に示す。同図は Zr 元素を緑色、Ca 元素を赤色で表しており、膜中で ZrO_2 と HA がともに層状に交互に存在するラメラ状構造で存在していることを示している。緒言で述べたように、PJD では衝突界面近傍の約 7%の粒子体積のみが対象物に付着し、それを繰り返すことで膜が形成される。したがって複合粒子を成膜する場合、母粒子表面の子粒子、次いで子粒子付近の母粒子の一部のみが対象物へと接触衝突して付着することが繰り返され、ラメラ状構造に成膜されたと考察できる。表 3 で複合粒子中の Zr 元素重量比率が 3.11%だったのに対し、図 10 で成膜面の平均 Zr 元素重量比率が 33.73%だったのも、子粒子の優先的な付着によるものだと考えられる。

5. 結論

本研究では膜厚と膜中 ZrO_2 含有率が、膜の明度を左右する重要なパラメータであること、また複合粒子膜は複合粒子より大きい ZrO_2 濃度を有し、その分布が膜中で均一であることを示した。本研究の結論を以下に記す。

- (1) PJD により ZrO_2 粒子の成膜に成功し、 ZrO_2 膜が HA 膜より高い明度を有したことから、PJD を審美歯科治療へ応用する可能性を示した。
- (2) 高い成膜性を有する HA 粒子と審美性のある ZrO_2 粒子の複合粒子は、HA 粒子に近い大きな成膜性を保持し、

その複合粒子膜は ZrO_2 膜より大きな明度を有した。

- (3) EPMA 分析結果より、複合粒子膜中の ZrO_2 分布および同厚膜における色調は均一だと推定できる。また、複合粒子の ZrO_2 混合率を変化させ、膜中 ZrO_2 量を調整することで、膜の明度が制御可能であると期待できる。

以上の結論より、本研究で提案した複合粒子は ZrO_2 複合率を調整可能であり、それに起因する膜厚と膜の明度を同時に制御可能であるといえる。このことは、本提案手法を患者一人一人に応じたテーラーメイド治療へ展開できることの可能性を示唆するものである。

謝辞

本研究は平成28年度新エネルギー・産業技術総合開発機構 戦略的基盤技術高度化支援事業(プロジェクト委託型)の助成を受けたものである。また本研究の一部は、文部科学省ナノテクノロジープラットフォーム事業(東北大学微細構造解析プラットフォーム)の支援を受けて実施された。(JPMX09F(A)-18-TU0033)

6. 参考文献

- 1) 田上順次, 千田彰, 奈良陽一郎, 桃井保子, 水末摩美, 第四版 保存修復学 21, 永末書店, (2011).
- 2) M. Fukushima: Treatment of Discolored Teeth -Past, Present and Future-, Niigata Dent. J., 39, 2, (2009) 1-15 (in Japanese).
- 3) K. Izumita: Development of Powder Jet Deposition Technique and New Treatment for Discolored Teeth, Interface Oral Health Science, TOHOKU UNIVERSITY SCHOOL OF DENTISTRY., (2016) C21, 257.
- 4) C. Nishikawa and T. Kuriyagawa: Film formation under normal temperature and pressure utilized powder jet deposition, J. Jpn. Soc. Abras. Technol., 57, 12, (2013) 782.
- 5) C. Nishikawa, et al.: Characteristics of Thick Film Deposition in Powder Jet Machining, Int. J. Autom. Technol., 7, 6, (2013) 630.
- 6) M. Mizutani, et al.: Particle fracture behavior and deposition mechanism in powder jet deposition (PJD), J. Jpn. Soc. Abras. Technol., 61, 1 (2017) 28 (in Japanese).
- 7) K. Mizutani, et al.: Numerical Study of Impact Phenomena of Fine Particles -Study of Ceramics Film Creation by Powder Jet Deposition-, Proc. Spring Meet. Jpn. Soc. Prec. Eng., D17(2008), 277 (in Japanese).
- 8) R. Akatsuka, et al.: Characteristics of hydroxyapatite film formed on human enamel with the powder jet deposition technique, J. Biomed. Mater., 98B, 2 (2011), 210.
- 9) R. Akatsuka, et al.: Exploratory Trial to Evaluate the Hydroxyapatite Layer Formed by a New Dental Treatment System, Open Journal of Stomatology, 5, 2(2015), 281.
- 10) H. Yamamoto, et al.: 歯科用 PJD ハンドピースにおける微粒子流動ダイナミクス, Jpn. Soc. Mech. Eng., 第 12 回生産加工・工作機械部門講演会 (2018) C23.
- 11) K. Sato, et al.: Creation of hydroxyapatite film on human enamel utilized powder jet deposition. Trans. Jpn. Soc. Mech. Eng., Series C, 79, 808 (2013) 109 (in Japanese).
- 12) C. Nishikawa, et al.: Study on the mechanism of powder jet machining, J. Jpn. Soc. Abras. Technol., 56, 3 (2012) 179 (in Japanese).
- 13) 安楽照男, et al.: 歯科用 CAD/CAM ハンドブック V -ナノジルコニアとは、口腔内スキャナーの臨床応用の現状と課題-, YAMAKIN 株式会社, (2017)11, 45.
- 14) 青木秀希: 驚異の生体物質 アパタイト, 医歯薬出版, (1999).
- 15) H. Aoki, T. Yajima, T. Koyama: Apatite as a Marvelous Biomaterial and the Surface Technology, J. Surf. Finish. Soc. Jpn, 58, 12 (2007), 744 (in Japanese).
- 16) 田端恒雄: アパタイト・セラミックス・インプラント その生物化学的特性と臨床術式の検討, 日本補綴歯科学会雑誌, 31, 2 (1987), 258.
- 17) 嶋野法之: 色彩工学の基礎と応用, コロナ社, (2009), 53.
- 18) M. Kawahara: The Transition of Mechanical Particle Composing Machine and the Future Prospects, The Micromeritics, 63 (2020) 97 (in Japanese).
- 19) 司馬超, 宇野光乗, 石神元, 倉知正和: 硬質レジンによるシェードガイド色調の再現方策, 岐歯学誌 35, 3 (2009), 149.



Picosecond laser-induced nanopillar coverage of entire mirror-polished surfaces of Ti6Al4V alloy

Liwei Chen^a, Yifei Zhang^b, Shuhei Kodama^c, Shaolin Xu^d, Keita Shimada^a, Masayoshi Mizutani^{a,*}, Tsunemoto Kuriyagawa^a

^a Department of Mechanical Systems Engineering, Graduate School of Engineering, Tohoku University, Sendai, 980-8579, Japan

^b Department of Mechanical Engineering, Undergraduate School of Engineering, Dalian University of Technology, Dalian, 116024, People's Republic of China

^c Department of Mechanical Systems Engineering, Tokyo University of Agriculture and Technology, Koganei, Tokyo, 184-0012, Japan

^d Department of Mechanical and Energy Engineering, Southern University of Science and Technology, Shenzhen, 518055, People's Republic of China

ARTICLE INFO

Keywords:

LIPSS
Picosecond laser
Ultrashort pulses
Pillar structure
Nanometer-scale

ABSTRACT

The goal of this study was to investigate a study for the efficient generation of pillar-like nanostructure (nanopillar) on a material surface over a large area. In this research, a vertical cross-scanning (VCS) strategy using two linearly-polarized lasers with different laser conditions was proposed for the generation of nanopillars on a mirror-polished surface on a large scale. It found that the laser fluence and scanning speed of the second laser scanning should be controlled within a specific range to generate the nanopillars. Additionally, the distance between scan lines, which is defined as hatch distance, h , of the second scan, is also a non-negligible factor to induce nanopillars to cover the entire surface. This work demonstrated that the VCS method is a feasible strategy for the fabrication of nanopillars on the entire mirror-polished surface of Ti6Al4V alloy by linearly-polarized picosecond laser conveniently and efficiently.

1. Introduction

The surfaces of metallic material covered with many micro/nano-structures that are usually beneficial for the applications of these materials in many fields, including biomedical [1], environmental [2,3], and aerospace [4]. Particularly in biomedical engineering, highly nanostructured surfaces can be used as antibacterial surfaces that are highly desirable for implants to prevent the adhesion of bacteria on the material surfaces [5,6]. Any surface can be endowed with antibacterial capability by covering it with pillar-like structures (nanopillars). For instance, Ivanova et al. [7] have demonstrated that nanopillar-covered surfaces have a significant impact on the bactericidal effect of penetrating cells. In investigations of the physical surface structure of cicada wings, individual bacterial cells were killed on the nanopillar-covered surface of cicada wings within approximately 3 min [7]. Gudur et al. [8] found that nanopillar surface makes it more valuable than traditional flat surfaces in biological applications, such as medical treatment, neuron pinning, biosensors, tissue engineering, DNA analysis, and antibacterial materials. Cunha et al. [6] demonstrated that nanopillar surface could reduce *Escherichia coli* (E.coli) and *Staphylococcus Aureus*

(S.a) adhesion because the nanopillar size and the average distance between them are approximate to the bacterial size ($1\ \mu\text{m}$) that reducing the area of the contact interface between the individual bacterium and the metal. Furthermore, the surface covered with the micro/nano-structure could also be used in many other bio-applications, such as tissue engineering, medical treatments, and biosensing due to its capability of altering the wettability of biological fluids and other liquids as well as the cell behavior on the implant surface [9]. Therefore, it is necessary to fabricate the functional surfaces covered by micro/nano-structures. To achieve this purpose, ultraprecision cutting and ultrasonic-vibration-assisted machining techniques have been employed [10–12]. However, these techniques have many disadvantages, such as long fabrication time, complicated machining processes, and the inability to fabricate nano-scale structures. On the other hand, laser micromachining technology is gradually becoming the preferred technology for various micro-scale materials processing applications [13].

The femtosecond laser has become one of the most common lasers in surface processing to create surface structures at micro-and nano-scale on metals and semiconductors due to its flexibility and simplicity [14, 15]. However, compared with femtosecond lasers, picosecond lasers are

* Corresponding author.

E-mail addresses: chen.liwei.q3@dc.tohoku.ac.jp (L. Chen), masayoshi.mizutani.b6@tohoku.ac.jp (M. Mizutani).

<https://doi.org/10.1016/j.precisioneng.2021.07.004>

Received 8 April 2021; Received in revised form 7 June 2021; Accepted 5 July 2021

Available online 6 July 2021

0141-6359/© 2021 Published by Elsevier Inc.

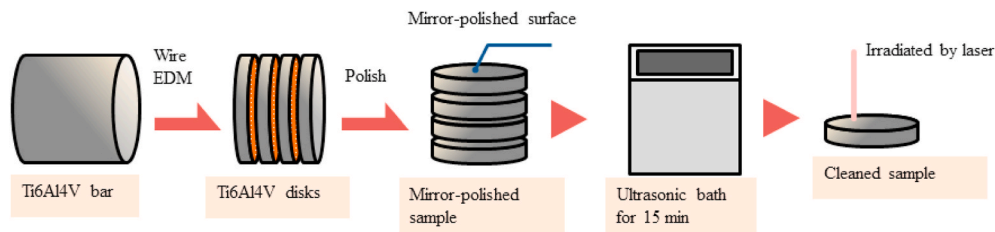


Fig. 1. The sample preparation process.

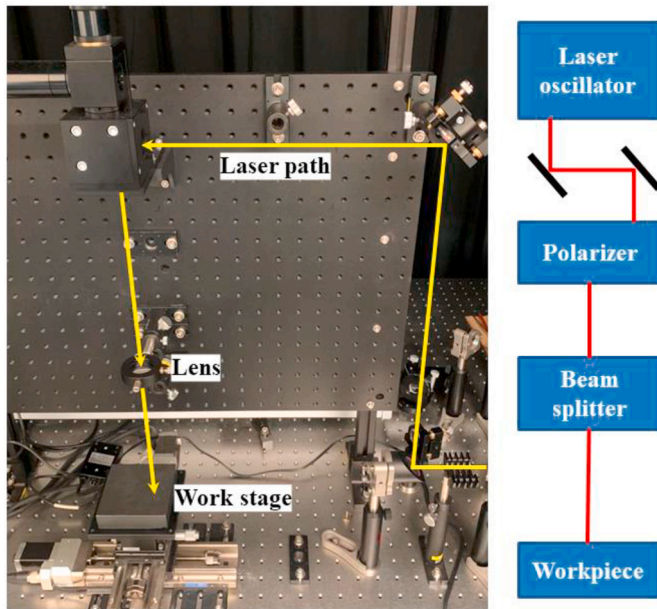


Fig. 2. Setup of laser processing.

more stable, reliable, and at a lower cost. Picosecond laser technology has made many remarkable achievements, such that it has become a reliable tool in the micro-processing industry with an excellent performance in both accuracy and efficiency [16]. The picosecond laser possesses many advantages; for example, it can be used for micro-scale patterning of almost all materials, including but not limited to metals [16–19], silicon wafers [17,20–22], semiconductors [23], and solar cells [24–26]. It also can drill smaller hole sizes ($\sim 100 \mu\text{m}$) through 1 mm steel [27]. According to the above reasons, the picosecond laser has been chosen to fabricate components surface covered with micro-/nanostructures such as nanopillars and microgrooves.

Various research studies found that many laser irradiation factors, including but not limited to laser fluence, scanning speed, wavelength, polarization, scanning path, surface roughness, and environment, will affect the size, periodicity, and morphology of the nanostructures [28–33]. Yan et al. [29] have successfully proposed and demonstrated a novel nanostructure generation method based on the nanosecond pulsed laser irradiation of a mixture of silicon powders, polyimide, and carbon black deposited on copper foil. Olivera et al. [30] conducted the experiments of fixed point irradiation of a femtosecond laser on a fixed titanium surface within stable conditions. They found that ripples were primarily obtained on the titanium surfaces for the fluences close to the ablation threshold of titanium ($0.2 \pm 0.1 \text{ J/cm}^2$), while microcolumns formed when the first 200 pulses had the fluences between 0.6 ± 0.2 and $1.7 \pm 0.2 \text{ J/cm}^2$. The results provide reference values for our selection of the experimental laser fluence. Regarding other factors such as surface roughness and the processing environment, Mustafa et al. [31] reported that the initial surface roughness should be lower for high ablation

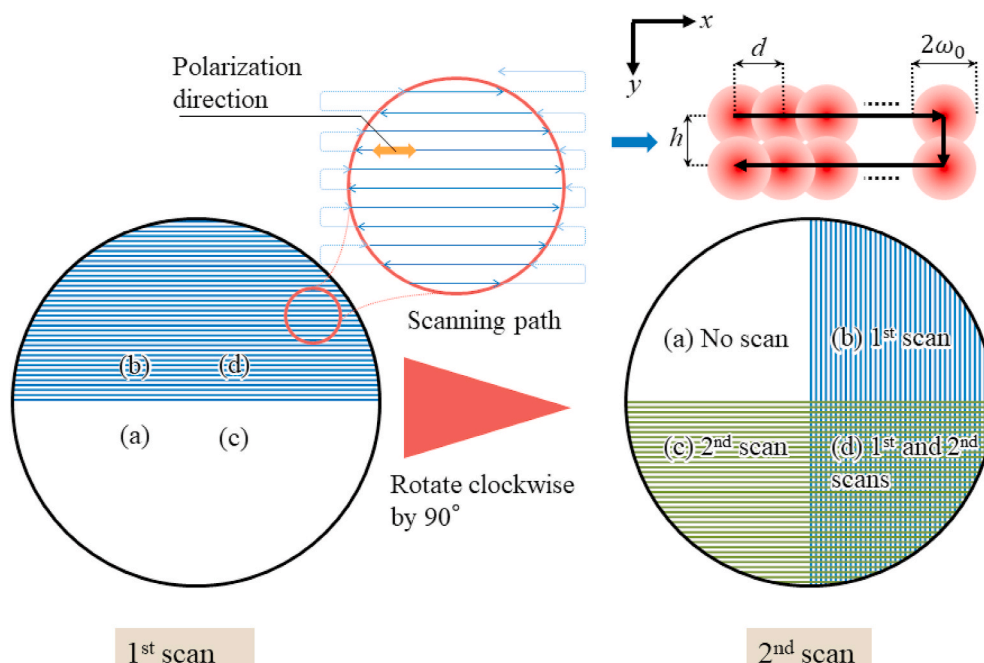


Fig. 3. Laser scanning path of the VCS method.

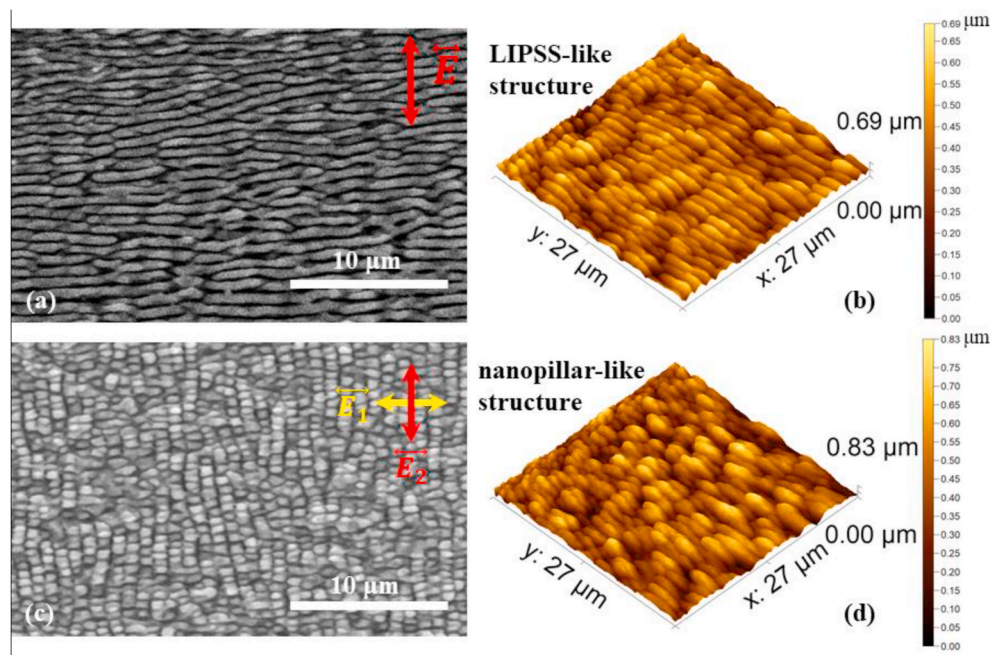


Fig. 4. SEM micrographs and AFM images of the surface textures. Laser-induced periodic surface structures (LIPSS) (a, b) and nanopillars (c, d). The polarization directions are the same as the arrow.

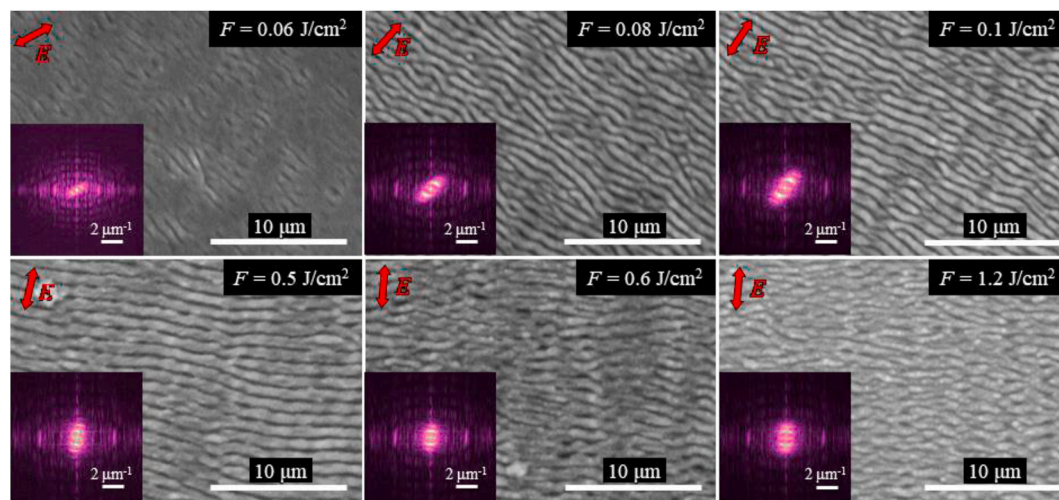


Fig. 5. Mirror-polished surface irradiated by the laser with different fluences at the scanning speed of 300 $\mu\text{m}/\text{s}$, and all of the polarization directions are the same as the red arrow. (For interpretation of the references to colour in this figure legend, the reader is referred to the Web version of this article.)

efficiency. It was also discovered that only the periodicity and depth of the produced structure differed in different environments such as air, water, ethanol, or chloroform [32].

To date, many researchers have found that a laser with an S-shaped scanning path could easily create laser-induced periodic surface structures (LIPSS). However, it is challenging to obtain nanopillars via this scanning strategy, only controlling the energy density or scanning speed of the laser. The fabrication of microgrooves via ultraprecision cutting followed by laser irradiation was also investigated [34]; however, this method is yet to generate nanopillars. On the other hand, Peter et al. [35] used a linearly polarized picosecond laser with two pulses to fabricate the nanopillars on tool steel via two different polarization directions; however, this method only fabricates the nanopillars within a spot but changing to generate over a large area effectively. Therefore, we attempted to fabricate nanopillars over a large area effectively by a linearly-polarized laser via controlling laser scanning speed or laser

fluence.

In this work, we seek to produce nanopillars over the entire surface using a linearly-polarized picosecond laser and study the mechanism of nanopillar generation. Therefore, we examined different laser irradiation conditions required to generate novel micro/nanostructures on the mirror-polished surface. The experiment results show that vertical-cross scanning (VCS) could induce nanopillars by a linearly-polarized laser with different laser fluences. The first laser scan (LS1) induces the LIPSS and then irradiated by the second laser scan (LS2) with varying scanning speeds or fluences, creating the nanopillars on the entire mirror-polished surface. The experimental result demonstrates that the LS2 with an excessive fluence breaks the LS1-generated LIPSS and that with an insufficient fluence does not induce nanopillars. The nanopillars are only induced when the laser fluence of the LS2 is within a specified limit. On the other hand, the distance between scanlines, defined as the hatch distance of the LS2 is also an essential factor to induce the nanopillars to

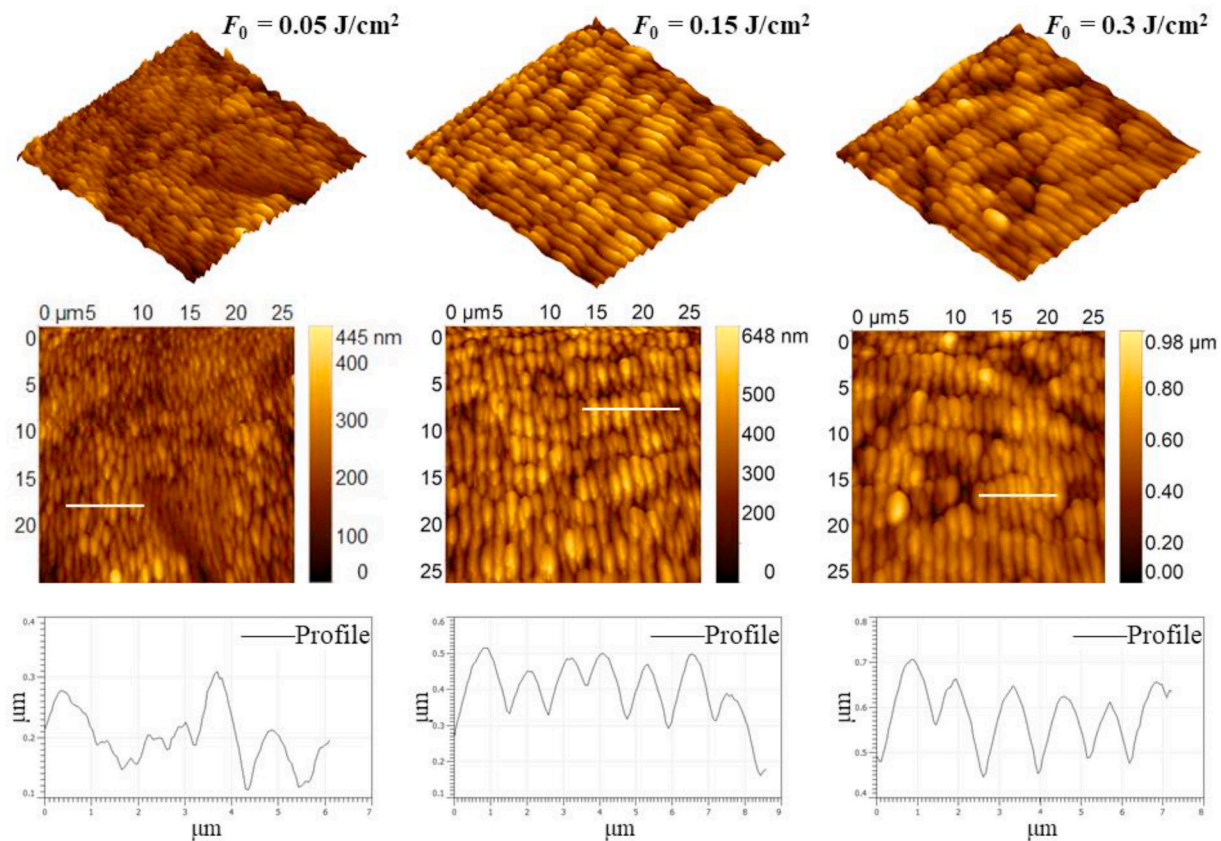


Fig. 6. 3D (top row) and 2D (middle row) AFM images and 2D (bottom row) cross-section images of LIPSS illuminated by scanning laser with different laser fluences.

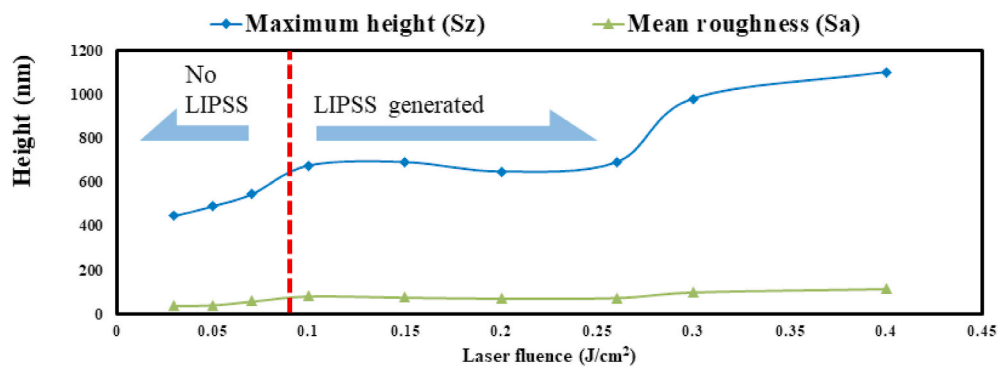


Fig. 7. Maximum height (Sz) and mean roughness (Sa) of LIPSS illuminated by scanning laser with different laser fluence.

cover the whole surface.

2. Experimental setup

2.1. Material

Ti6Al4V alloy is widely used in orthopedic and dental applications owing to its excellent heat resistance, low density, strength, plasticity, toughness, corrosion resistance [36–40]. And especially its biocompatibility, which enhances the adhesion between native tissue and the implanted material [41]. Meanwhile, implant with nanostructured surfaces has antibacterial or biocompatibility effects, and Ti6Al4V alloy is one of the most common materials in the implants. In this research, we aimed to fabricate nanostructure on metal surface, which might be applied in biomedical engineering. Therefore, we chose Ti6Al4V alloy in this research to induce nanostructures on the material surface by pulse

laser. Commercially available bar material was separated into disks by wire electrical discharge machining (EDM) with 1 mm thickness and then polished by a grinding mill and emery paper to obtain a mirror-polished surface with an average roughness of $S_a = 0.06 \mu\text{m}$. All of the disks were cleaned by ultrasonication with ethanol for 15 min before they irradiated by the laser beam and captured the micrographs by the scanning electron microscope (SEM), as shown in Fig. 1.

2.2. Laser system

The atmosphere has a specific influence on the nanostructure generation process, and the main factor is a variety of gas types in the air. In addition, if a technique requires to be performed in a specific environment such as vacuum or argon, it will become a significant obstacle to its popularization. Moreover, only a few researchers have done similar experiments to study the chemical effects accompanying the formation

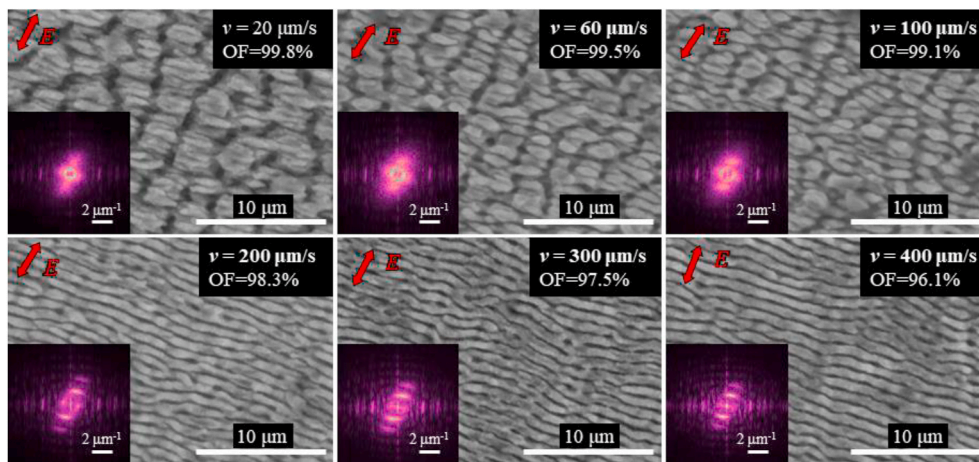


Fig. 8. Mirror-polished surface irradiated by the laser with different scanning speeds at the fluence of 0.184 J/cm². All of the polarization directions are the same as the red arrow. (For interpretation of the references to colour in this figure legend, the reader is referred to the Web version of this article.)

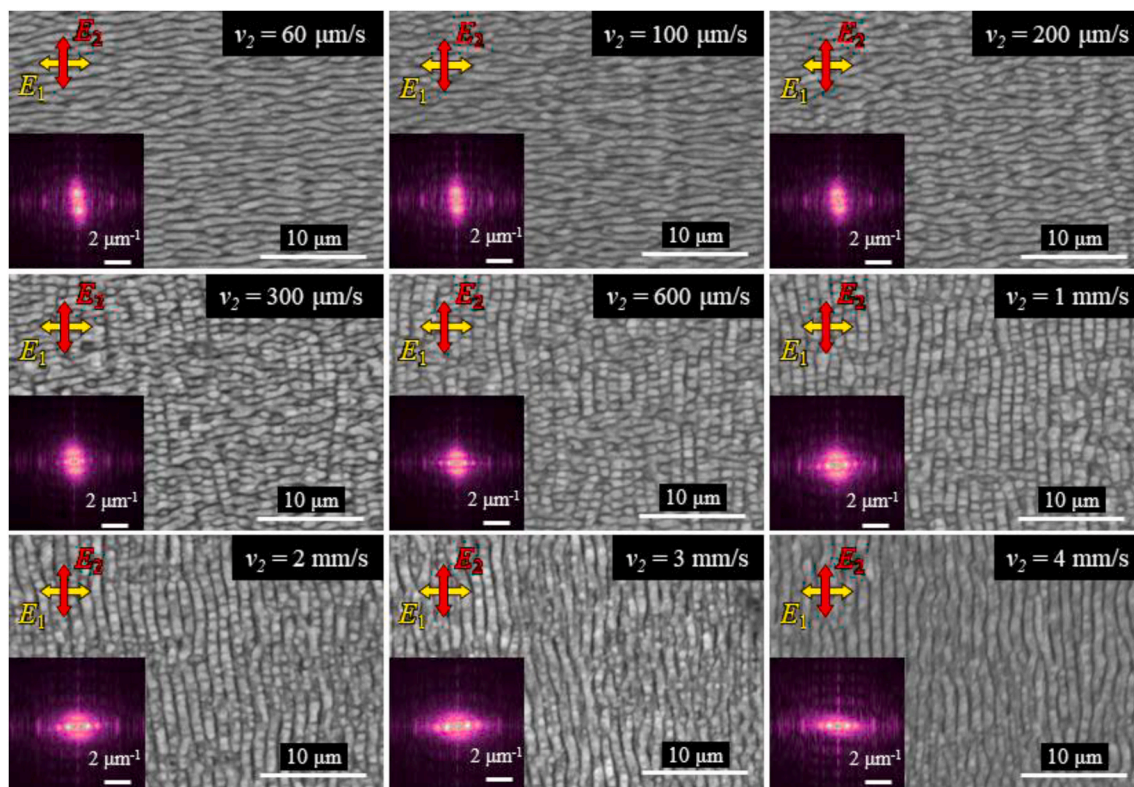


Fig. 9. Nanostructures induced by the first laser scan: $F_1 = 528 \text{ mJ/cm}^2$ and $v_1 = 300 \text{ } \mu\text{m/s}$, and the second laser scan: $F_2 = 51 \text{ mJ/cm}^2$ and different scanning speeds (v_2). All of the polarization directions are the same as the red and yellow arrows. (For interpretation of the references to colour in this figure legend, the reader is referred to the Web version of this article.)

of LIPSS [42]. Therefore, all of the experiment was conducted in the air environment.

The texturing was performed via a picosecond laser source (EKSPILA, PL 2250-50P20) with a fixed frequency of 50 Hz, pulse duration of 20 ps, and four wavelengths of 1064 nm, 532 nm, 355 nm, and 256 nm, as shown in Fig. 2. In this work, only the wavelength of 1064 nm was chosen because LIPSS or nanopillars were challenging to be fabricated by the wavelength of 532 nm and could not be induced with the other two wavelengths showed in our previous work [43]. A fixed lens focused the laser with a 150-mm focal length, and the spot diameter $2\omega_0$ at e^{-2} is estimated experimentally to be around 300 μm . The sample was on the work stage, and a movable stage was numerically controlled to follow

the S-shaped laser scanning path, as shown in Fig. 3. The laser source is a Gaussian light source whose average power (P) is tested by a laser power meter at first, and then use the measured data (P) to test the laser fluence (F_0) by a CCD camera.

The distance between two consecutive spot centers, d , is given by:

$$d = \frac{v}{f}, \tag{1}$$

where v is the scanning speed, and f is the irradiation frequency.

It could be assumed that the Gaussian beam is a simple astigmatic one, and its orientation stays constant at every point along the beam

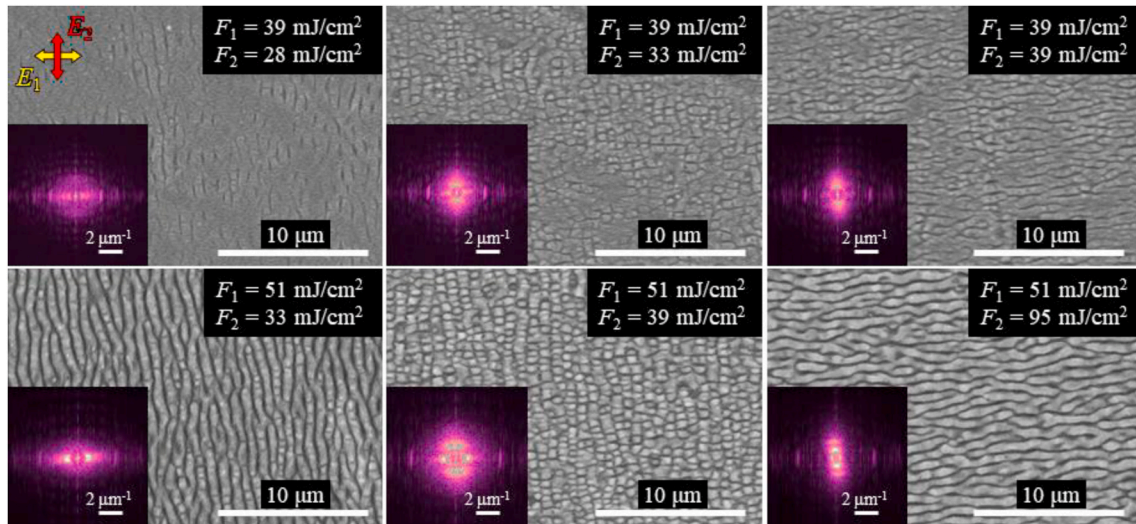


Fig. 10. Nanostructures induced by the first and second laser scan under the scanning speed of 300 μm/s and hatch distance of 120 μm with the different laser fluences. All of the polarization directions are the same as the red and yellow arrows. (For interpretation of the references to colour in this figure legend, the reader is referred to the Web version of this article.)

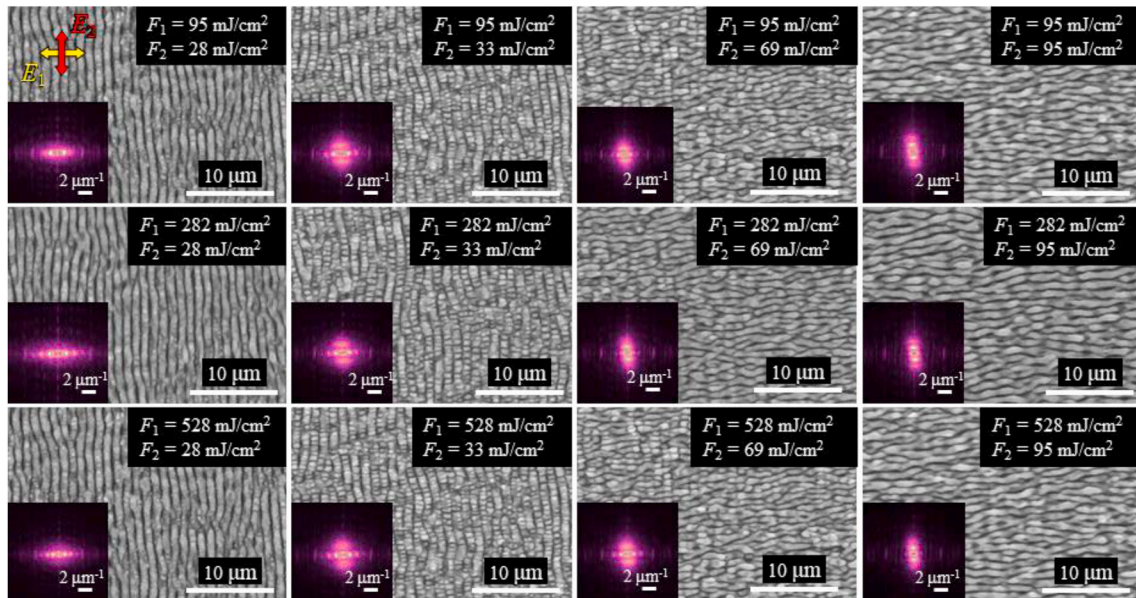


Fig. 11. Nanostructures induced by the first and second laser scans under the scanning speed of 300 μm/s and different laser fluences. All of the polarization directions are the same as the yellow and red arrows. (For interpretation of the references to colour in this figure legend, the reader is referred to the Web version of this article.)

path. The following equation can describe the two-dimensional local fluence intensity distribution of such beam on a processed surface:

$$F(x, y) = F_0 e^{-\frac{2(x-x_0)^2 + (y-y_0)^2}{\omega_0^2}} \quad (2)$$

where x_0 and y_0 are the coordinates of the central point and F_0 is the peak fluence of Gaussian beam expressed as:

$$F_0 = \frac{2P}{f\pi\omega_0^2} \quad (3)$$

where P is the average power.

By combining Eqs. (1) and (2) and Fig. 3, the accumulated fluence can be expressed as follow:

$$\phi(x, y) = F_0 \sum_i e^{-\frac{(x-id)^2}{\omega_0^2}} \sum_j e^{-\frac{(y-hj)^2}{\omega_0^2}} \quad (4)$$

where h is the distance between the scan line, which is defined as hatch distance.

While, the effective accumulated fluence per unit area, ϕ , will be deduced from Eqs. (3) and (4) as the following equation:

$$\phi = \frac{F_0 f \pi \omega_0^2}{2vh} = \frac{P}{vh} \quad (5)$$

The overlapping factor (OF) also illustrated in Fig. 3 and can be calculated as [44,45].

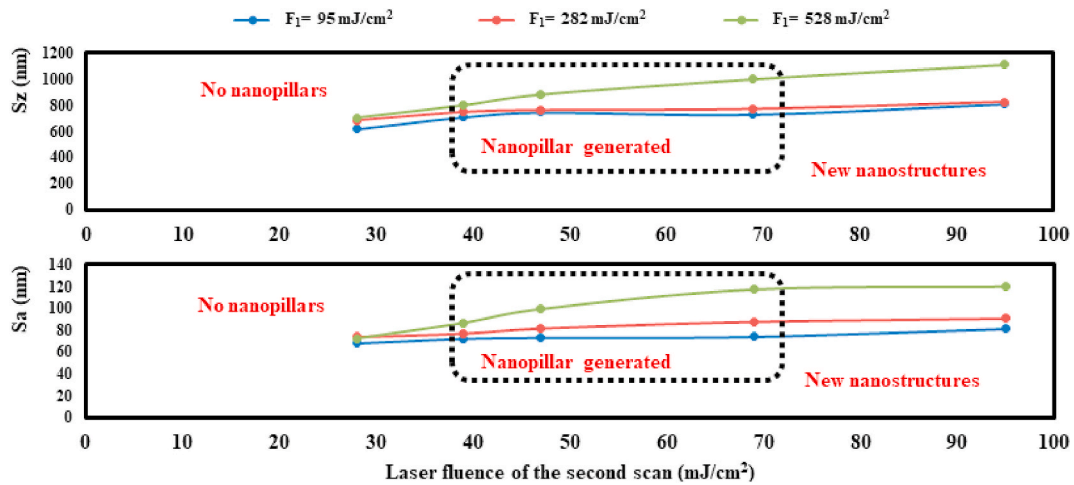


Fig. 12. Maximum height (S_z) and mean roughness (S_a) of nanostructures induced by different laser fluence laser scans with the scanning speed of 300 $\mu\text{m/s}$.

$$OF = \frac{1}{\pi\omega_0} \left[2\omega_0 \arccos\left(\frac{d}{2\omega_0}\right) - d\sqrt{1 - \left(\frac{d}{2\omega_0}\right)^2} \right] \quad (6)$$

Additionally, we propose the VCS method as a laser scanning strategy shown in Fig. 3 to create the nanopillars on the mirror-polished surface by laser irradiation. First, the LS1 performs with a scanning speed and a fluence to create LIPSS. Then, the sample was rotated by 90°, and the LS2 performs. The cross-scan area predicted that nanopillars would be obtained.

2.3. Inspection of LIPSS morphology

The open source software Gwyddion was used to perform two-dimensional fast Fourier transform (2D FFT) of the SEM micrographs, which provides an effective method to analyze the orientation and period of LIPSS [46–48]. Since the relation between the LIPSS period (Λ) and the distance between 2D FFT peaks is given by equation $\Lambda = 2/d$, the scale bar was set at 2 μm^{-1} to estimate the frequency domain and the generated LIPSS period.

3. Results

3.1. Topography of the laser-treated surfaces

Two types of produced textures (LIPSS and nanopillar) are defined and presented by SEM micrographs and atomic force microscope (AFM) images, as shown in Fig. 4. A linearly-polarized picosecond laser irradiated the mirror-polished surface with an S-shaped scanning path to figure out the conditions of LIPSS generation. Fig. 5 shows the laser-irradiated surfaces by different laser fluences (F_0) at the scanning speed (v) of 300 $\mu\text{m/s}$ and hatch distance (h) of 120 μm with the S-shaped scanning strategy. A well-defined LIPSS was not fabricated clearly when laser $F_0 \leq 0.06 \text{ J/cm}^2$, while when $F_0 = 0.08\text{--}0.5 \text{ J/cm}^2$, and similar LIPSSs were fabricated. However, unclear nanostructures were induced when $F_0 > 0.6 \text{ J/cm}^2$. It was concluded that the laser fluence within a specific range provided no noticeable effect on the LIPSSs' features, such as the periodic length and the direction described in our previous research [40]. However, the height (S_z and S_a) of LIPSS increased with increasing the laser fluence, as shown in Figs. 6 and 7. The AFM images and 2D cross-section images of LIPSS are shown in Fig. 6 and conclude that the surface texture is smooth when the laser fluence can induce the LIPSS and rough when the fluence is insufficient to induce a clear LIPSS.

On the other hand, different nanostructures were generated by different scanning speeds ranged from 20 $\mu\text{m/s}$ to 400 $\mu\text{m/s}$ when the

fluence of the scanning laser was fixed to 0.2 J/cm^2 . Fig. 5 shows that bumps induced if the scanning speed was lower than 100 $\mu\text{m/s}$. In comparison, the LIPSSs were generated if the scanning speed was controlled within 200–400 $\mu\text{m/s}$ and OF was less than 99%, and with no noticeable difference in the morphology and the periodical length with different scanning speeds.

Based on the results of Figs. 5 and 8, the approximate ranges of the laser fluence and scanning speed for the LIPSS generation could be considered to 0.08–0.5 J/cm^2 and 200–400 $\mu\text{m/s}$, respectively. And the LIPSS periodicity, Λ , given by the 2D FFT at around 1 μm . It also can be concluded that controlling the laser fluence or scanning speed alone cannot create nanopillars via the scanning strategy of the S-shaped scan. Therefore, the VCS strategy was proposed to generate nanopillars on the entire mirror-polished surface showed in Fig. 3. To study the influence of different laser conditions on the nanopillars' creation, we examined different scanning speeds (v_2), laser fluences (F_2), and hatch distance (h) of the LS2 in Sections 3.2, 3.3, and 3.4, respectively.

3.2. Scanning speed

The scanning laser first irradiated the mirror-polished surface with a laser fluence ($F_1 = 528 \text{ mJ/cm}^2$) and a scanning speed ($v_1 = 300 \mu\text{m/s}$) to create the LIPSS structures. The LS2 then irradiated the LIPSS with different scanning speeds (v_2) under a fixed fluence ($F_2 = 51 \text{ mJ/cm}^2$). The SEM micrographs of the obtained surfaces are displayed in Fig. 9.

The top row in Fig. 9 depicts that the created nanostructures are LIPSS because the low scanning speed, $v_2 < 300 \mu\text{m/s}$, provided the surface with much time to absorb enough energy to destroy the existed LIPSS and created a new one. On the other hand, the LS2 with the speeds, $v_2 = 0.3\text{--}1 \text{ mm/s}$, created the nanopillar-like structures as shown in the middle row of Fig. 9. Meanwhile, the bottom row of Fig. 9 shows that the nanopillars could not be fabricated obviously when $v_2 \geq 2 \text{ mm/s}$. This is because the high scanning speed leads to the absorbed energy was insufficient to induce the nanopillars' generation on the first created LIPSS due to the short irradiation time. It concluded that the scanning speed of the LS2 is a crucial factor for the generation of the nanopillars because it determines the effective accumulated fluence per unit area, which is also decided by the distance between scan lines (h) and the average power (P), as shown in Eq. (5). Based on this analysis, the laser fluence, which is affected by the average power, is an essential factor for the morphology of the generated nanostructures. Therefore, we set different laser fluences to the LS2 to irradiate the LS1-created LIPSS. Figs. 8 and 9 show the nanostructures created by different laser fluences under the scanning speed of 300 $\mu\text{m/s}$ for both the LS2 and LS2.

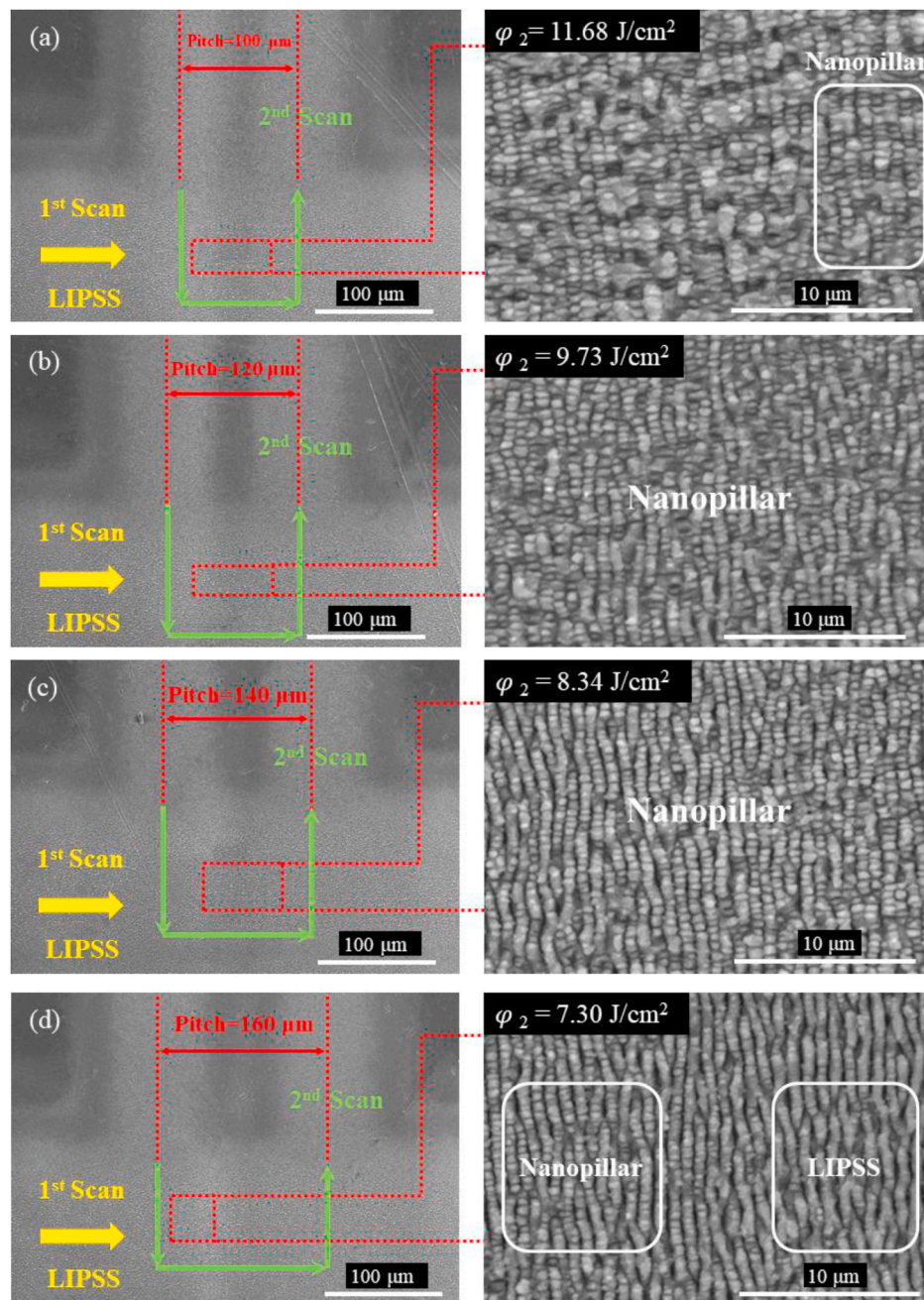


Fig. 13. Nanostructures induced by the second laser scan under the scanning speed of 300 $\mu\text{m/s}$ and laser fluence of 51 mJ/cm^2 with different hatch distances of (a) 100 μm , (b) 120 μm , (c) 140 μm , and (d) 160 μm .

3.3. Laser fluence

In the study by Peter et al. [35], nanopillars were fabricated by two pulses; however, they only studied polarization direction and pulse numbers but never researched the laser fluence of the relationship between the two pulses. Therefore, the relationship of laser fluences of LS1 and LS2 to influence the nanopillars generation was studied in this work.

The top row of Fig. 10 illustrates that neither LIPSS nor nanopillars were obtained due to the low laser fluence of the LS1 ($F_1 = 37 \text{ mJ/cm}^2$). With the increase of the laser fluence of the LS2, the nanostructures similar to the nanopillar could be obtained but not clearly. Meanwhile, when the laser fluence of the LS1 increased to 51 mJ/cm^2 , the nanopillars or LIPSSs could be obtained. On the other hand, Fig. 11 illustrates that the nanostructures induced with different LS2 fluences on the LIPSS generated by the LS1 with the laser fluence of 95–528 mJ/cm^2 . The

leftmost column of Fig. 11 illustrates that the laser fluence of the LS2, $F_2 = 28 \text{ mJ/cm}^2$, was not high enough to induce the nanopillars on the created LIPSS. The LS2 with $F_2 = 37 \text{ mJ/cm}^2$ generated the clear nanopillars as shown in the middle column of Fig. 11, while the LS2 with $F_2 = 95 \text{ mJ/cm}^2$ destroyed the first LIPSS and generated a new one, as shown in the rightmost column of Fig. 11.

Based on Section 3.1, the laser fluence of the LS1 should be around 0.1 J/cm^2 or more to induce the LIPSS structure. Then, the created LIPSS irradiated by the LS2 with the laser fluence should be within a suitable range, i.e., a too-low laser fluence of the LS2 cannot induce the nanopillars or LIPSS and a too-high laser fluence destroys the existed LIPSS and generates a new one. Thus, it concludes that the laser fluences with $F_1 = 95\text{--}528 \text{ mJ/cm}^2$ and $F_2 = 37\text{--}70 \text{ mJ/cm}^2$ are suitable to form the nanopillars when both scanning speeds are fixed at 300 $\mu\text{m/s}$.

Fig. 12 shows that the relationship between the maximum (S_z) or

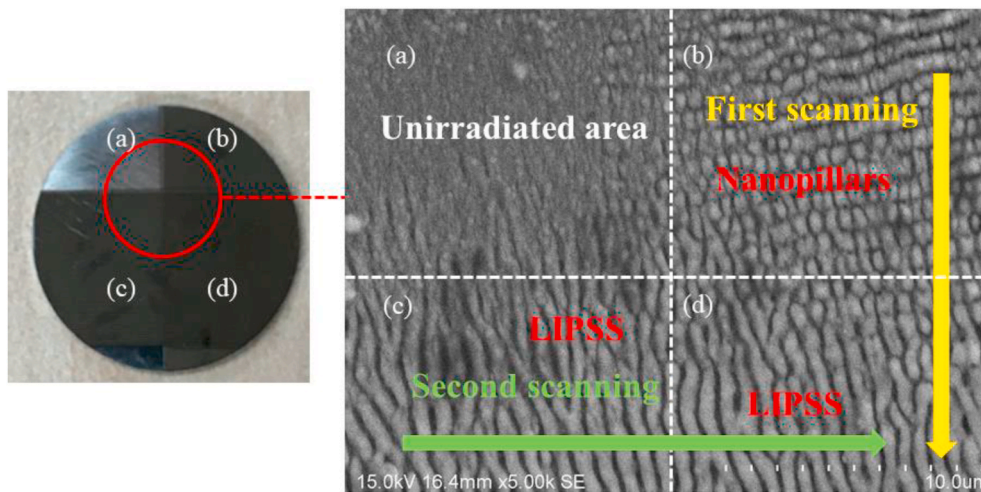


Fig. 14. SEM micrographs of the polished sample modified by the VCS method. (a) Polished surface not irradiated, (b) irradiated once by the first scanning, (c) the second scanning, and (d) irradiated twice.

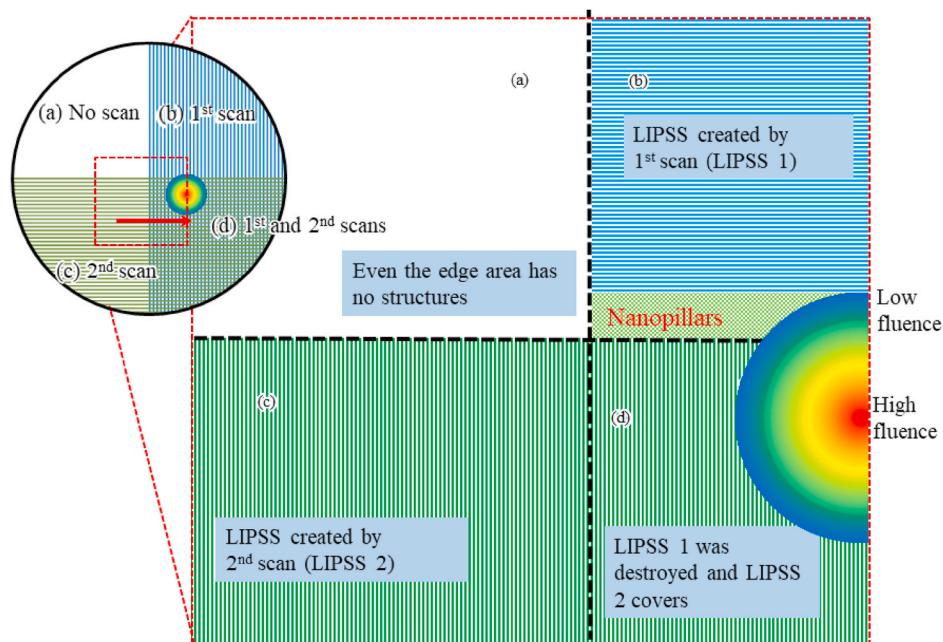


Fig. 15. Schematic of the polished sample irradiated by VSC. Polished surface (a) not irradiated by laser, (b, c) irradiated once by laser, (d) irradiated twice by laser.

arithmetic mean roughness (S_a) and the laser fluences of the LS1 and LS2. It concludes that S_z and S_a increase with the increasing of the laser fluences of laser scans. Meanwhile, S_a can express the average height of LIPSS; therefore, the mean height of LIPSS can be increased with the laser fluence increasing.

3.4. Distance between scan lines

Based on the results of Sections 3.2 and 3.3, the VCS strategy could be an advantageous method to create nanopillars on the mirror-polished surface via control of the laser fluence and scanning speed of the LS2. Besides, the hatch distance is also an essential factor to induce nanopillars to cover the whole material surface because it is also a factor of the effective accumulated fluence per unit area, as shown in Eq. (5). Fig. 13 shows the SEM micrographs of the nanostructures induced by the LS2 with different hatch distances on the LIPSS created by the LS1 with the scanning speed of $300 \mu\text{m/s}$ and the laser fluence of 417 mJ/cm^2 .

When the hatch distance of the LS2 was over narrow ($h = 100 \mu\text{m}$),

new nanostructures were induced on the nanopillars in the rescanned area, as shown in Fig. 13a. While the LS2 induced the nanopillars when the hatch distance was overbroad ($h = 160 \mu\text{m}$), but some LS1-induced LIPSS far from the scanning path remained, as shown in Fig. 13d. Meanwhile, the generated nanostructures were only nanopillars without LIPSS when the hatch distance a specific range ($120\text{--}140 \mu\text{m}$), as shown in Fig. 13b and c, where the effective accumulated fluence per unit area was ranged from 8.34 to 9.73 J/cm^2 . Therefore, it concluded that to induce the nanopillars covered on the entire mirror-polished surface, not only the laser fluence and scanning speed but also the hatch distance of the LS2 is a non-negligible factor.

4. Discussion

4.1. Mechanism of nanopillar fabrication by VCS method

The right half of the workpiece was irradiated by the LS1, and the LS2 irradiated the bottom half, i.e., only the right-bottom area was

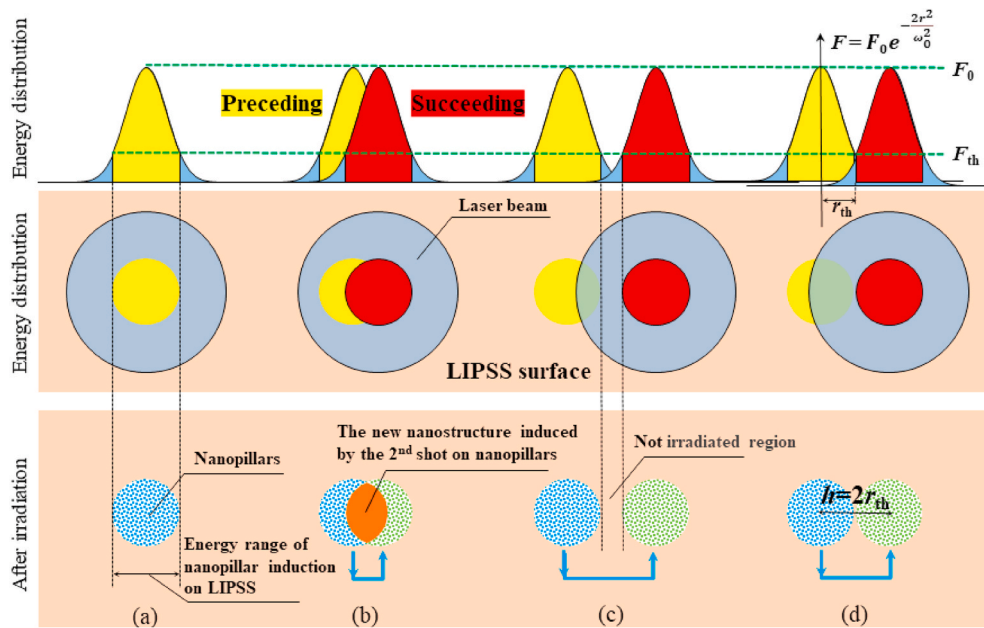


Fig. 16. Schematic of the nanostructures induced on the LIPSS by the second scanning laser with the (a) one-shot, (b) two shots with a short hatch distance, (c) two shots with a long hatch distance, and (d) two shots with a suitable hatch distance.

Laser parameter ($f, 2\omega_0, v$)

Overlap factor $OF \approx 1 - v/f\omega_0$

Accumulated fluence $\varphi = P/vh$

Suitable hatch distance

$$h_{th} = \omega_0 \sqrt{2 \ln \frac{F_2}{F_{th}}}$$

F_2 mJ/cm ²	F_1 mJ/cm ²				
	37	95	282	528	≥ 528
28	\emptyset	LIPSS1			Δ
33		✓			
69					
≥ 95	LIPSS2				

Fig. 17. The generated nanostructures generated by different combinations of F_1 and F_2 , unclear nanostructures or nothing can be observed due to the low laser fluence (\emptyset); expected nanopillars (\checkmark); unclear nanostructures due to the over laser fluence (Δ); LIPSS generated by LS1 combined the low fluence of LS2 (LIPSS1); LIPSS generated high fluence of LS2 destroyed LIPSS1 (LIPSS2). The scanning speed set as fast as possible to improve efficiency, overlap factor can be simplified as $1 - v/f\omega_0$ when $v/f \ll \omega_0$.

irradiated twice, as shown in Fig. 14. The fluences, scanning speeds, and hatch distances of the LS1 and LS2 were the same as 0.1 J/cm^2 , $300 \mu\text{m/s}$, and $120 \mu\text{m}$, respectively. No difference was observed in the nanostructures between Areas (c) and (d) of Fig. 14 though they received different laser irradiations. On the other hand, nanopillars were generated in Area (b), where the LIPSS was supposed to be induced by the LS1 rather than LS2. Fig. 15 schematically explains this situation: the laser beam is considered as a moving Gaussian light source, and the fluence at the center of the laser beam was high enough to destroy the existing LIPSS and recreate a new one in Area (d). While, the peripheral region of the laser beam with a lower fluence, which was not high enough to induce LIPSS or nanopillars on the mirror-polished surface newly, but sufficient to modify the existing LIPSS to nanopillars. It demonstrates that compare with the LS1, a relatively lower laser fluence of the LS2 might irradiate the nanopillars on the LIPSS. Therefore, the experiment results in Fig. 14 depict the workpiece surface that explains the mechanism of the nanopillars' generation in the VCS method within one figure.

To summarize how to obtain nanopillars with the VCS method: when the scanning speed of the LS1 and LS2 are both $300 \mu\text{m/s}$, the laser fluence of the LS1 must exceed the LIPSS generation criterion, which should be around 0.1 J/cm^2 because otherwise, it does not induce the LIPSS during the LS1 as shown in Fig. 5. The laser fluence of the LS2 then must exceed the nanopillar induction criterion, which should be around 37 mJ/cm^2 , and not higher than the LIPSS destruction criterion around

70 mJ/cm^2 .

4.2. Hatch distance of the second laser scan

The distance between scan lines, hatch distance, is also an essential factor in fabricating the nanopillars on the entire surface. Section 3.3 shows that when the laser fluence of the LS2 is within limits, the nanopillars could be created on the crossed area of the LS1 and LS2; when the hatch distance of the LS2 is narrow, as shown in Fig. 16b, the following irradiation deforms the nanopillars fabricated by the previous irradiation to new nanostructures; besides, when the hatch distance is broad as shown in Fig. 16c, nanopillars are not created on the space between two scanning lasers, and the new induced nanostructures combined with nanopillars and LIPSS. In those two situations, nanopillars could not cover the entire mirror-polished surface. Therefore, setting a suitable hatch distance of the LS2 is a vital process in inducing nanopillars to cover the whole surface.

The LS2 with an appropriate hatch distance generates nanopillars on LIPSS to cover the entire surface, as shown in Fig. 16d. The laser fluence distribution F is supposed to be a Gaussian distribution that can be expressed as:

$$F(r) = F_0 e^{-\frac{2r^2}{\omega_0^2}} \quad (7)$$

where ω_0 is the laser beam radius, F_0 is the peak laser fluence of the

Gaussian beam, and r represents the distance to the laser beam center.

The fluence of the LS2 ranged from 37 to 70 mJ/cm² could induce nanopillars on the LIPSS as shown in Section 3.3; therefore, the threshold fluence for the nanopillars generation, F_{th} , can be assumed as 37 mJ/cm². Reversely, when the fluence of the LS2 is fixed to 51 mJ/cm² as in Section 3.4, the threshold hatch distance, h_{th} , can be expected with F_{th} , as shown in Fig. 16d. Considering that $h_{th} = 2r_{th}$, h_{th} can be obtained by modifying Eq. (7) as:

$$h_{th} = \omega_0 \sqrt{2 \ln \frac{F_2}{F_{th}}} \quad (8)$$

Substituting the experimental conditions and results, $F_{th} = 37$ mJ/cm², $F_0 = 51$ mJ/cm², and $\omega_0 = 150$ μm, $h_{th} = 120.17$ μm. It agrees with the results in Section 3.4, which is that the hatch distance ranged from 120 μm to 140 μm could induce the nanopillars on the entire mirror-polished surface.

To sum up, there are two conditions on the fluence of LS2 to induce the nanopillars: (1) F_2 has to exceed the minimum fluence to induce nanopillars but be lower than the fluence destroying the existing LIPSS as concluded in Section 4.1, and (2) h has to set the distance to avoid destroying the nanopillars generated by the preceding scan path. The suitable value can be calculated by Eq. (8). Fig. 17 shows the laser conditions (v , F_1 , F_2 , h) combination to generate the expected nanopillars.

5. Conclusions

This work shows that the micro/nanostructure generated on the Ti6Al4V alloy surface is closely related to the laser conditions and scanning strategy. The generated nanostructures were fabricated via two laser scans, and the effective accumulated fluence per unit area (ϕ) of LS1 and LS2 is the critical factor for LIPSS or nanopillars generation. ϕ is decided by the laser scanning speed (v), laser fluence (F), hatch distance (h), and the desired nanostructures can only be obtained when all of these factors are controlled together and to be in the appropriate range. When the scanning speed is fixed or within a particular range, the combination of laser fluence of LS1 and LS2 is the most critical factor to irradiate expected nanopillars. When the scanning speeds of both LS1 and LS2 were 300 μm/s, and the laser fluence of the LS1 was ranged from 0.1 to 0.5 J/cm², that of the LS2 should be higher than 37 mJ/cm² and should not exceed 70 mJ/cm² to obtain nanopillars. Meanwhile, the mean height (h_0) of LIPSS or nanopillars, which can be expressed by S_a , is also influenced by laser fluence; it increases with the increasing laser fluence. However, the periodic length (λ) of LIPSS is not changed by the laser fluence; therefore, the aspect ratio (h_0/λ) of LIPSS could be increased by the laser fluence increasing. To fabricate the nanopillar on the entire surface, the hatch distance of the LS2 should set in a specific range. It is set according to the diameter of the laser beam and the ratio of F_2 and the threshold fluence to induce the nanopillar.

Declaration of competing interest

The authors declare that they have no known competing financial interests or personal relationships that could have appeared to influence the work reported in this paper.

Acknowledgments

The authors gratefully acknowledge the financial support of the National Key Research and China Scholarship Council (Grant Numbers 201906270253 and 201906060188). This study was supported in part by JSPS KAKENHI (Grant Numbers JP17K06074 and JP17KK0126) and by Machine Tool Engineering Foundation.

References

- [1] Tavangar A, Tan B, Venkatakrishnan K. Sustainable approach toward synthesis of green functional carbonaceous 3-D micro/nanostructures from biomass. *Nano-scale Res Lett* 2013;8:1–6. <https://doi.org/10.1186/1556-276X-8-348>.
- [2] Liu Z, Zhou X, Qian Y. Synthetic methodologies for carbon nanomaterials. *Adv Mater* 2010;22:1963–6. <https://doi.org/10.1002/adma.200903813>.
- [3] Hoheisel TN, Schretil S, Szilluweit R, Frauenrath H. Nanostructured carbonaceous materials from molecular precursors. *Angew Chem Int Ed* 2010;49:6496–515. <https://doi.org/10.1002/anie.200907180>.
- [4] Hu YZ, Ma TB. Tribology of nanostructured surfaces. *Elsevier Compr. Nanosci. Nanotechnol.* 2019;1–5:309–42. <https://doi.org/10.1016/B978-0-12-803581-8.00614-7>.
- [5] Jaggessar A, Shahali H, Mathew A, Yarlagadda PKDV. Bio-mimicking nano and micro-structured surface fabrication for antibacterial properties in medical implants. *J Nanobiotechnol* 2017;15. <https://doi.org/10.1186/s12951-017-0306-1>.
- [6] Cunha A, Elie AM, Plawinski L, Serro AP, Botelho Do Rego AM, Almeida A, et al. Femtosecond laser surface texturing of titanium as a method to reduce the adhesion of *Staphylococcus aureus* and biofilm formation. *Appl Surf Sci* 2016;360:485–93. <https://doi.org/10.1016/j.apsusc.2015.10.102>.
- [7] Ivanova EP, Hasan J, Webb HK, Truong VK, Watson GS, Watson JA, et al. Natural bactericidal surfaces: mechanical rupture of *Pseudomonas aeruginosa* cells by cicada wings. *Small* 2012;8:2489–94. <https://doi.org/10.1002/smll.201200528>.
- [8] Gudur A, Ji H-F. Bio-applications of nanopillars. *Front Nanosci Nanotechnol* 2016;2. <https://doi.org/10.15761/fnn.1000140>.
- [9] Cunha A, Oliveira V, Vilar R. Ultrafast laser surface texturing of titanium alloys. *Elsevier Inc. Laser Surf. Modif. Biomater. Tech. Appl.* 2016:301–22. <https://doi.org/10.1016/B978-0-08-100883-6.00011-3>.
- [10] Chen N, Li HN, Wu J, Li Z, Li L, Liu G, et al. Advances in micro milling: from tool fabrication to process outcomes. *Int J Mach Tool Manufact* 2020;160:103670. <https://doi.org/10.1016/j.ijmactools.2020.103670>.
- [11] Xu S, Kuriyagawa T, Shimada K, Mizutani M. Recent advances in ultrasonic-assisted machining for the fabrication of micro/nano-textured surfaces. *Front Mech Eng* 2017;12:33–45. <https://doi.org/10.1007/s11465-017-0422-5>.
- [12] Kodama S, Suzuki S, Shibata A, Shimada K, Mizutani M, Kuriyagawa T. Effect of crystal structure on fabrication of fine periodic surface structures with short pulsed laser. *Int J Autom Technol* 2018;12:868–75. <https://doi.org/10.20965/ijat.2018.p0868>.
- [13] Gao S, Huang H. Recent advances in micro- and nano-machining technologies. *Front Mech Eng* 2017;12:18–32. <https://doi.org/10.1007/s11465-017-0410-9>.
- [14] Yang HZ, Wang WJ, Jiang GD, Mei XS, Pan AF, Chen T. Nanostructures with good photoelectric properties fabricated by femtosecond laser and secondary sputtering on ITO films. *Opt Mater* 2020;109:110302. <https://doi.org/10.1016/j.optmat.2020.110302>.
- [15] Chen T, Wang W, Tao T, Mei X, Pan A. Deposition and melting behaviors for formation of micro/nano structures from nanostructures with femtosecond pulses. *Opt Mater* 2018;78:380–7. <https://doi.org/10.1016/j.optmat.2018.02.051>.
- [16] Nielsen CS, Balling P. Deep drilling of metals with ultrashort laser pulses: a two-stage process. *J Appl Phys* 2006;99. <https://doi.org/10.1063/1.2193648>.
- [17] Chung CK, Lin SL. CO₂ laser micromachined crackless through holes of Pyrex 7740 glass. *Int J Mach Tool Manufact* 2010;50:961–8. <https://doi.org/10.1016/j.ijmactools.2010.08.002>.
- [18] Cheng J, Perrie W, Sharp M, Edwardson SP, Semaltianos NG, Dearden G, et al. Single-pulse drilling study on Au, Al and Ti alloy by using a picosecond laser. *Appl Phys Mater Sci Process* 2009;95:739–46. <https://doi.org/10.1007/s00339-008-5037-6>.
- [19] Weck A, Crawford THR, Wilkinson DS, Haugen HK, Preston JS. Laser drilling of high aspect ratio holes in copper with femtosecond, picosecond and nanosecond pulses. *Appl Phys Mater Sci Process* 2008;90:537–43. <https://doi.org/10.1007/s00339-007-4300-6>.
- [20] Tan B, Panchatsharam S, Venkatakrishnan K. High repetition rate femtosecond laser forming sub-10 μm diameter interconnection vias. *J Phys D Appl Phys* 2009;42. <https://doi.org/10.1088/0022-3727/42/6/065102>.
- [21] Tan B, Venkatakrishnan K. Nd-YAG laser microvia drilling for interconnection application. *J Micromech Microeng* 2007;17:1511–7. <https://doi.org/10.1088/0960-1317/17/8/013>.
- [22] Venkatakrishnan K, Sudani N, Tan B. A high-repetition-rate femtosecond laser for thin silicon wafer dicing. *J Micromech Microeng* 2008;18. <https://doi.org/10.1088/0960-1317/18/7/075032>.
- [23] Chen JK, Tzou DY, Beraun JE. Numerical investigation of ultrashort laser damage in semiconductors. *Int J Heat Mass Tran* 2005;48:501–9. <https://doi.org/10.1016/j.ijheatmasstransfer.2004.09.015>.
- [24] Heise G, Domke M, Konrad J, Pavic F, Schmidt M, Vogt H, et al. Monolithic serial interconnects of large cis solar cells with picosecond laser pulses. *Phys Procedia* 2011;12:149–55. <https://doi.org/10.1016/j.phpro.2011.03.117>.
- [25] Račiukaitis G, Gečys P. Picosecond-laser structuring of thin films for CIGS solar cells. *J Laser Micro Nanoeng* 2010;5:10–5. <https://doi.org/10.2961/jlmm.2010.01.0003>.
- [26] Gečys P, Račiukaitis G, Miltenisa E, Braun A, Ragnow S. Scribing of thin-film solar cells with picosecond laser pulses. *Phys Procedia* 2011;12:141–8. <https://doi.org/10.1016/j.phpro.2011.03.116>.
- [27] Moorhouse C. Advantages of picosecond laser machining for cutting-edge technologies. *Phys Procedia* 2013;41:381–8. <https://doi.org/10.1016/j.phpro.2013.03.091>.

- [28] Tanvir Ahmmed KM, Grambow C, Kietzig AM. Fabrication of micro/nano structures on metals by femtosecond laser micromachining. *Micromachines* 2014; 5:1219–53. <https://doi.org/10.3390/mi5041219>.
- [29] Yan J, Noguchi J, Terashi Y. Fabrication of single-crystal silicon micro pillars on copper foils by nanosecond pulsed laser irradiation. *CIRP Ann - Manuf Technol* 2017;66:253–6. <https://doi.org/10.1016/j.cirp.2017.04.134>.
- [30] Oliveira V, Cunha A, Vilar R. Multi-scaled femtosecond laser structuring of stationary titanium surfaces. *J Optoelectron Adv Mater* 2010;12:654–8.
- [31] Mustafa H, Mezera M, Matthews DTA, Römer GRBE. Effect of surface roughness on the ultrashort pulsed laser ablation fluence threshold of zinc and steel. *Appl Surf Sci* 2019;488:10–21. <https://doi.org/10.1016/j.apsusc.2019.05.066>.
- [32] Albu C, Dinescu A, Filipescu M, Ulmeanu M, Zamfirescu M. Periodical structures induced by femtosecond laser on metals in air and liquid environments. *Appl Surf Sci* 2013;278:347–51. <https://doi.org/10.1016/j.apsusc.2012.11.075>.
- [33] Fraggelakis F, Mincuzzi G, Lopez J, Manek-Hönninger I, Kling R. Controlling 2D laser nano structuring over large area with double femtosecond pulses. *Appl Surf Sci* 2019;470:677–86. <https://doi.org/10.1016/j.apsusc.2018.11.106>.
- [34] Kodama S, Suzuki S, Hayashibe K, Shimada K, Mizutani M, Kuriyagawa T. Control of short-pulsed laser induced periodic surface structures with machining - picosecond laser micro/nanotexturing with ultraprecision cutting. *Precis Eng* 2019;55:433–8. <https://doi.org/10.1016/j.precisioneng.2018.10.013>.
- [35] Gregorčić P, Sedlaček M, Podgornik B, Reif J. Formation of laser-induced periodic surface structures (LIPSS) on tool steel by multiple picosecond laser pulses of different polarizations. *Appl Surf Sci* 2016;387:698–706. <https://doi.org/10.1016/j.apsusc.2016.06.174>.
- [36] Li Y, Yang C, Zhao H, Qu S, Li X, Li Y. New developments of ti-based alloys for biomedical applications. *Materials* 2014;7:1709–800. <https://doi.org/10.3390/ma7031709>.
- [37] Feng Q, Zhang L, Pang H, Zhang P, Tong X, Wang D, et al. Microstructure and properties of low cost TC4 titanium alloy plate. *MATEC Web Conf* 2016;67. <https://doi.org/10.1051/mateconf/20166705025>.
- [38] Liu S, Shin YC. Additive manufacturing of Ti6Al4V alloy: a review. *Mater Des* 2019;164:107552. <https://doi.org/10.1016/j.matdes.2018.107552>.
- [39] Gnilitzky I, Pogorielov M, Viter R, Ferraria AM, Carapeto AP, Oleshko O, et al. Cell and tissue response to nanotextured Ti6Al4V and Zr implants using high-speed femtosecond laser-induced periodic surface structures. *Nanomed Nanotechnol Biol Med* 2019;21:102036. <https://doi.org/10.1016/j.nano.2019.102036>.
- [40] Rotella G, Orazi L, Alfano M, Candamano S, Gnilitzky I. Innovative high-speed femtosecond laser nano-patterning for improved adhesive bonding of Ti6Al4V titanium alloy. *CIRP J Manuf Sci Technol* 2017;18:101–6. <https://doi.org/10.1016/j.cirpj.2016.10.003>.
- [41] Rodriguez GM, Bowen J, Zelzer M, Stamboulis A. Selective modification of Ti6Al4V surfaces for biomedical applications. *RSC Adv* 2020;10:17642–52. <https://doi.org/10.1039/c9ra11000c>.
- [42] Florian C, Wonneberger R, Undisz A, Kirner SV, Wasmuth K, Spaltmann D, et al. Chemical effects during the formation of various types of femtosecond laser-generated surface structures on titanium alloy. *Appl Phys Mater Sci Process* 2020; 126:1–11. <https://doi.org/10.1007/s00339-020-3434-7>.
- [43] Kodama S, Shimada K, Mizutani M, Kuriyagawa T. Effects of pulse duration and heat on laser-induced periodic surface structures. *Int J Autom Technol* 2020;14: 552–9. <https://doi.org/10.20965/ijat.2020.p0552>.
- [44] Romano JM, Garcia-Giron A, Penchev P, Dimov S. Triangular laser-induced submicron textures for functionalising stainless steel surfaces. *Appl Surf Sci* 2018; 440:162–9. <https://doi.org/10.1016/j.apsusc.2018.01.086>.
- [45] Cardoso JT, Garcia-Girón A, Romano JM, Huerta-Murillo D, Jagdheesh R, Walker M, et al. Influence of ambient conditions on the evolution of wettability properties of an IR-, ns-laser textured aluminium alloy. *RSC Adv* 2017;7:39617–27. <https://doi.org/10.1039/c7ra07421b>.
- [46] Alamri S, Fraggelakis F, Kunze T, Krupop B, Mincuzzi G, Kling R, et al. On the interplay of DLIP and LIPSS upon ultra-short laser pulse irradiation. *Materials* 2019;12:1–9. <https://doi.org/10.3390/ma12071018>.
- [47] Martínez-Calderon M, Rodríguez A, Dias-Ponte A, Morant-Miñana MC, Gómez-Aranzadi M, Olaizola SM. Femtosecond laser fabrication of highly hydrophobic stainless steel surface with hierarchical structures fabricated by combining ordered microstructures and LIPSS. *Appl Surf Sci* 2016;374:81–9. <https://doi.org/10.1016/j.apsusc.2015.09.261>.
- [48] San-Blas A, Casquero N, Pérez N, Martínez-Calderon M, Sanchez-Brea LM, Buencuerpo J, et al. Polarization conversion on nanostructured metallic surfaces fabricated by LIPSS, vol. 53; 2019. <https://doi.org/10.1117/12.2506982>.

軸対称非球面研削における研削条件の最適化*

吉原信人** 嶋田慶太*** 水野雅裕** 厨川常元†

Optimization of Grinding Conditions of Axisymmetric Aspherical Grinding

Nobuhito YOSHIHARA, Keita SHIMADA, Masahiro MIZUNO and Tsunemoto KURIYAGAWA

With the recent increase in the size and image quality of optical equipment, there is a strong demand for higher precision aspherical lenses. Generally, an aspherical glass lens or its mold is formed by grinding and then finished by polishing. Since the shape accuracy deteriorates in this polishing process, it is necessary to keep the polishing amount small. Therefore, it is desirable to optimize the grinding conditions and reduce the grinding surface roughness. In this paper, to optimize the grinding conditions of axisymmetric aspherical surface, maximum height roughness of axisymmetric aspherical ground surface is analyzed theoretically utilizing the statistical grinding theory. From the view point of relationship between the grain cutting direction and workpiece feed direction, grinding can be classified into parallel grinding and cross grinding. And it is found that the parallel grinding is suited to axisymmetric aspherical grinding.

Key words: parallel grinding, cross grinding, grain cutting direction, statistical grinding theory, ground surface roughness

1. 緒言

近年の光学機器の小型・高画質化に伴い非球面レンズの高精度化が強く求められている。一般的に非球面ガラスレンズあるいはその金型は研削により成形された後、研磨により仕上げ加工がなされる。この研磨加工の工程において形状精度が劣化するため、研磨量を小さく抑える必要がある。そのため研削条件を最適化し、研削面粗さを小さくすることが望ましい。

筆者らはこれまで軸対称非球面研削の方法としてパラレル研削法を考案し、従来法であるクロス研削法と比較して研削面粗さが小さくなることを実験により明らかにしてきた¹⁾。しかし、パラレル研削法により研削面粗さが小さくなる理由は十分な検討がなされていない。一方、筆者らは統計的研削理論に基づいた手法による研削面粗さの解析法を提案している。これまで、同理論により研削面粗さの定量的な評価が可能であることを示し、非軸対称非球面研削における研削条件と研削面粗さの関係を明らかにした²⁾。

本報では、工作物送り方向と砥粒切削方向の関係を含めて、最適な研削条件を理論的に求めることを目的として、統計的研削理論を用いた軸対称非球面研削面の粗さ解析を可能にする。

2. 統計的研削理論

統計的研削理論は1960年代に松井・庄司により提案された、研削条件と研削面粗さの関係を示すことが可能な研削理論である³⁾⁴⁾。統計的研削理論における研削モデルを図1に示す。ここでOは砥石の回転軸、Dは砥石直径、Vは砥石周速、vは工作物送り速度、 α は砥粒半頂角、AXは工作物の理想的な仕上がり面である。断面OAを高さHで切削する砥粒が砥石円周方向に角度 θ 、砥石最外周からの距離 δ の位置にあるとき、 (θ, δ) が描く曲線を等高切削曲線と呼ぶ。この高さHが最大高さ粗さ H_m であるときの、等高切削曲線と砥石外周面に囲まれる立体Wの体積

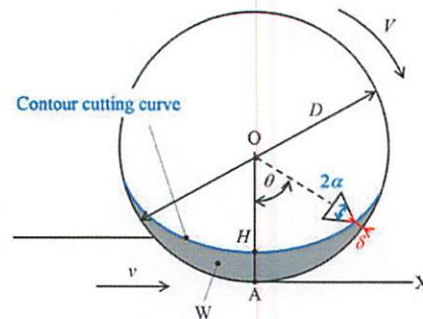


Fig. 1 Grinding model in statistical grinding theory

を W_m とする。この体積 W_m は内部に砥粒が存在しように取り得る最大の体積であり、ランダム係数 n と砥粒1個が占める体積 W_0 の積で表される⁵⁾。また立体の体積 W_m は研削条件と最大高さ粗さ H_m および D, α, V, v から幾何学的に求められるため⁶⁾、次式が成り立つ。

$$W_m(D, H_m, \alpha, V, v) = nW_0 \quad (1)$$

ここでランダム係数 n は砥石の種類によらず、平均3.3であることがわかっている⁶⁾。また、他の研削条件に関するパラメータは既知の値であるため、立体の体積を求め、同式を解くことにより最大高さ粗さ H_m を算出することが可能である。

3. 軸対称非球面研削面粗さの解析

本報で検討する軸対称非球面研削モデルを図2に示す。一定の回転数で回転する工作物上を、一定の回転数で回転する平底砥石が一定速度で工作物中心部から外周部に向けて送られる。このとき工作物円周方向に対して、砥粒切削方向が垂直な場合(図2(a)参照)をクロス研削、平行な場合(図2(b)参照)をパラレル研削と呼ぶ。統計的研削理論では砥粒切削方向に対して垂直方向の研削面粗さが算出される。そのためクロス研削の解析を行った場合、工作物円周方向の研削面粗さが算出される。またパラレル研削の解析を行った場合、工作物半径方向の研削面粗さが算出される。一般的に砥粒切削方向に対して平行方向の粗さよりも、垂直方向の粗さの方が大きい。すなわちクロス研削、

* 原稿受付 令和3年6月14日

掲載決定 令和3年10月18日

** 正会員 岩手大学(岩手県盛岡市上田4-3-5)

*** 正会員 高エネルギー加速器研究機構(茨城県つくば大穂1-1)

† 正会員 東北大学(宮城県仙台市青葉区荒巻字青葉6-6-01)

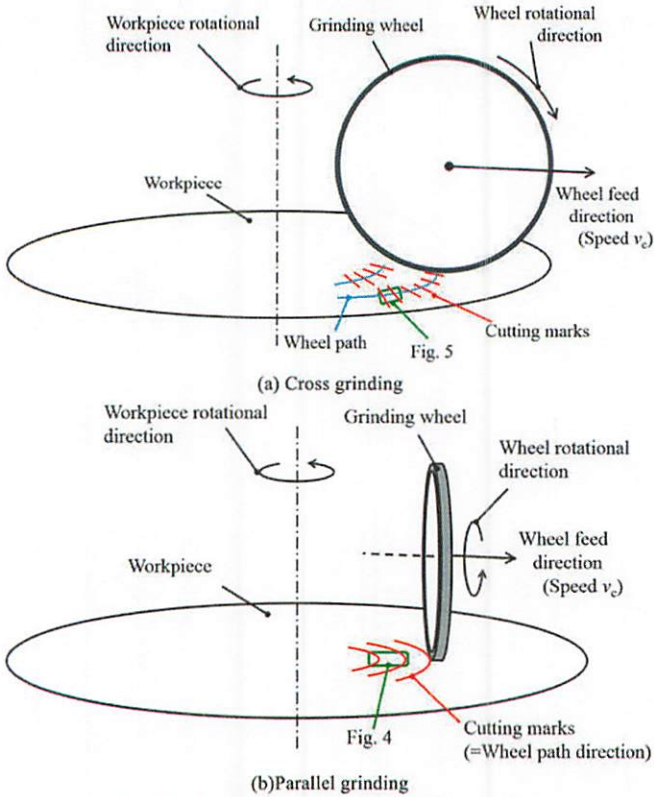


Fig. 2 Models of axisymmetric aspherical grinding

パラレル研削ともに研削面粗さの大きい方向の粗さが算出されることになる。

3.1 パラレル研削面の解析

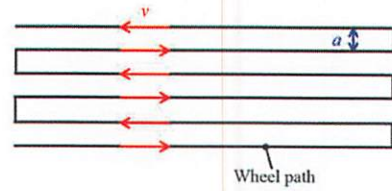
非軸対称非球面研削における研削面粗さの解析に用いた砥石送りの軌跡を図3(a)に示す²⁾。一方、今回解析を行う軸対称非球面研削における砥石送りの軌跡を図3(b)に示す。工作物送り速度は、その研削点における工作物の周速に等しいため、次式から求めることが可能である。

$$v = r\omega \tag{2}$$

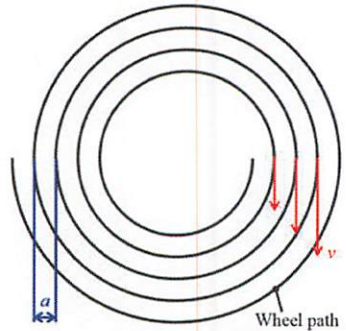
ここで r は工作物中心から研削点までの距離、 ω は工作物回転の角速度である。また軸対称非球面研削におけるピックフィード a は、工作物が1回転する間に砥石が送られる距離であり、砥石送り速度を v_c とすると次式で求められる。

$$a = \frac{2\pi}{\omega} v_c \tag{3}$$

砥石周速 V 、砥粒1個が占める体積 W_0 、砥石幅 b 、砥石径 D 、砥粒切れ刃の半頂角 α 、ランダム係数 n に関しては軸対称非球面研削と非軸対称非球面研削の間に違いは無い。そこで非軸対称非球面研削面の最大高さ粗さ解析時に導出した式における工作物送り速度 v として式(2)、ピックフィード a として式(3)を代入して、軸対称非球面研削面の最大高さ粗さを求める式を導出した。パラレル研削における研削の状態は、立体 W の幅とピックフィードの関係、立体 W の θ の範囲と 2π の関係から5つのケースに分類される。図2(b)中に示した隣り合う2つの軌跡を抽出し、それぞれに存在する立体 W の関係を分類ごとに表したものを図4に示す。ここで $\theta=0$ における立体 W の幅を $2k_{max}$ 、 $\theta=\pi$ における立体 W の幅を $2k_0$ 、立体 W の θ の最大値 θ_{max} はそれぞれ次

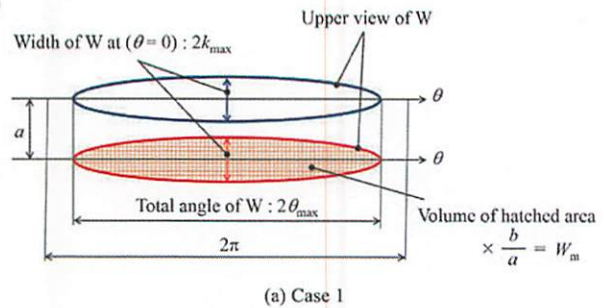


(a) non-axisymmetric aspherical grinding

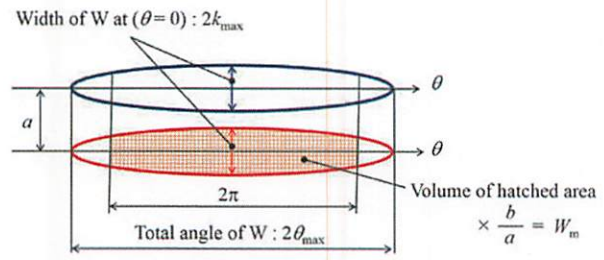


(b) Axisymmetric aspherical grinding

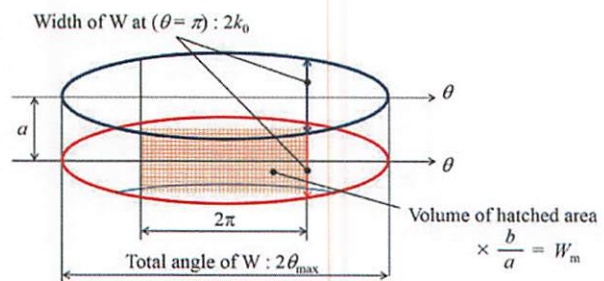
Fig. 3 Wheel paths of non-axisymmetric aspherical grinding and axisymmetric aspherical grinding



(a) Case 1



(b) Case 2



(c) Case 3

Fig. 4 Cases of parallel grinding conditions according to the size of W (continue to next page)

式で表される。

$$k_{\max} = H_m \tan \alpha \quad (4)$$

$$k_0 = \left\{ H_m - \frac{\pi^2}{4} D \left(\frac{v}{V} \right)^2 \right\} \tan \alpha \quad (5)$$

$$\theta_{\max} = \frac{2V}{v} \sqrt{\frac{H_m}{D}} \quad (6)$$

軸対称非球面研削において、工作物中心から研削点までの距離 r によって工作物送り速度 v が変化するため、隣り合う立体 W の体積は異なる。しかしピックフィード a が十分小さいため、工作物送り速度 v の変化も小さく、無視できるものとした。

図4に示した分類に基づき、それぞれの立体 W_m の体積を計算した結果を以下に記す。

ケース1：立体 W が占める θ の範囲が 2π を超えず、隣り合う立体 W が互いに干渉しない場合、すなわち $k_{\max} < a/2$ かつ $\theta_{\max} < \pi$ のとき(図4(a))

$$\begin{aligned} W_m &= nW_0 \\ &= \frac{8}{15\pi} \frac{Vb}{rv_c} D^{0.5} H_m^{2.5} \tan \alpha - \frac{32}{105\pi} \frac{Vb}{rv_c} D^{-0.5} H_m^{3.5} \tan \alpha \end{aligned} \quad (7)$$

ケース2：立体 W が占める θ の範囲が 2π を超え、隣り合う立体 W が互いに干渉しない場合、すなわち $k_{\max} < a/2$ かつ $\theta_{\max} > \pi$ のとき(図4(b))

$$\begin{aligned} W_m &= nW_0 \\ &= \frac{\omega b}{2\pi v_c} \left[\left\{ -\frac{\pi^3}{6} \left(\frac{r\omega}{V} \right)^2 - \frac{\pi^5}{40} \left(\frac{r\omega}{V} \right)^4 \right\} H_m D^2 \tan \alpha \right. \\ &\quad + \left\{ \pi + \frac{\pi^3}{6} \left(\frac{r\omega}{V} \right)^2 \right\} H_m^2 D \tan \alpha - \frac{2}{3} \pi H_m^3 \tan \alpha \\ &\quad \left. + \frac{\pi^5}{80} \left(\frac{r\omega}{V} \right)^4 D^3 \tan \alpha + \frac{\pi^7}{672} \left(\frac{r\omega}{V} \right)^6 D^3 \tan \alpha \right] \end{aligned} \quad (8)$$

ケース3：隣り合う立体 W が互いに干渉し、干渉している部分が占める θ の範囲が 2π を超える場合、すなわち $k_0 > a/2$ かつ $\theta_{\max} > \pi$ のとき(図4(c))

$$\begin{aligned} W_m &= nW_0 \\ &= \frac{\omega b}{2\pi v_c} \left[\left\{ -\frac{\pi^4}{6} \left(\frac{r\omega}{V} \right)^2 D^2 - \frac{\pi^4}{40} \left(\frac{r\omega}{V} \right)^4 D^2 + 2\pi^2 D H_m \right. \right. \\ &\quad + \frac{\pi^4}{3} \left(\frac{r\omega}{V} \right)^2 H_m D - \frac{\pi^2}{4} \left(\frac{r\omega}{V} \right)^2 H_m \left. \right\} \frac{v_c}{\omega} + \left\{ -\frac{\pi^3 D}{\tan \alpha} \right. \\ &\quad - \frac{\pi^5}{6} \frac{D}{\tan \alpha} \left(\frac{r\omega}{V} \right)^2 + \frac{\pi^3}{4} \left(\frac{r\omega}{V} \right)^2 \frac{H_m}{\tan \alpha} \left. \right\} \left(\frac{v_c}{\omega} \right)^2 \\ &\quad \left. - \frac{\pi^4}{12\omega} \left(\frac{r}{V} \right)^2 \frac{v_c^3}{\tan^2 \alpha} \right] \end{aligned} \quad (9)$$

ケース4：隣り合う立体 W が互いに干渉し、干渉している部分が占める θ の範囲が 2π を超えない場合、すなわち $k_0 < a/2$ かつ $\theta_{\max} > \pi$ のとき(図4(d))

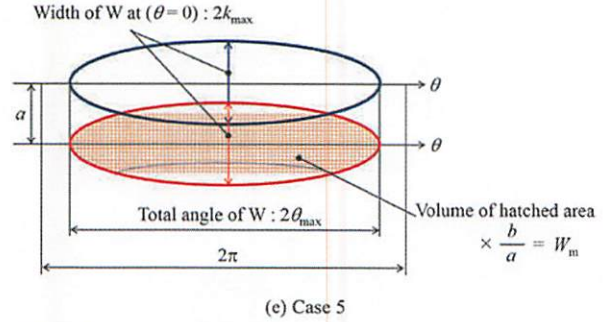
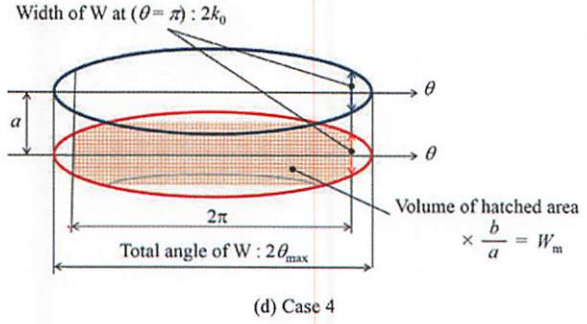


Fig. 4 Cases of parallel grinding conditions according to the size of W

$$\begin{aligned} W_m &= nW_0 \\ &= \frac{\omega b}{2\pi v_c} D^3 \left[\left\{ -\frac{\pi^3}{6} \left(\frac{r\omega}{V} \right)^2 - \frac{\pi^5}{40} \left(\frac{r\omega}{V} \right)^4 \right\} \frac{H_m}{D} \right. \\ &\quad + \left\{ \pi + \frac{\pi^3}{6} \left(\frac{r\omega}{V} \right)^2 \right\} \frac{H_m^2}{D^2} - \frac{2\pi}{3} \frac{H_m^3}{D^3} \\ &\quad + \frac{\pi^5}{80} \left(\frac{r\omega}{V} \right)^4 + \frac{\pi^7}{672} \left(\frac{r\omega}{V} \right)^6 \left. \right] \tan \alpha \\ &\quad - \frac{8}{15\pi} \frac{Vb}{rv_c} D^{0.5} \left(H_m - \frac{\pi v_c}{\omega \tan \alpha} \right)^{2.5} \tan \alpha \\ &\quad + \frac{32}{105\pi} \frac{Vb}{rv_c} D^{-0.5} \left(H_m - \frac{\pi v_c}{\omega \tan \alpha} \right)^{3.5} \tan \alpha \end{aligned} \quad (10)$$

ケース5：立体 W が占める θ の範囲が 2π を超えず、隣り合う立体 W が互いに干渉しない場合、すなわち $k_{\max} > a/2$ かつ $\theta_{\max} < \pi$ のとき(図4(e))

$$\begin{aligned} W_m &= nW_0 \\ &= \frac{8}{15\pi} \frac{Vb}{rv_c} \tan \alpha \left\{ D^{0.5} H_m^{2.5} - \frac{4}{7} D^{-0.5} H_m^{3.5} \right. \\ &\quad - D^{-0.5} \left(H_m - \frac{\pi v_c}{\omega \tan \alpha} \right)^{2.5} \\ &\quad \left. + \frac{4}{7} D^{-0.5} \left(H_m - \frac{\pi v_c}{\omega \tan \alpha} \right)^{3.5} \right\} \end{aligned} \quad (11)$$

式(7)~(11)に研削条件の数値を代入することにより、最大高さ粗さ H_m を算出することが可能である。

3.2 クロス研削面の解析

クロス研削面についてもパラレル研削と同様に、砥石送り速度を式(2)に基づいて変換することにより得られる。クロス研削における研削の状態は立体 W の幅と砥石が1回転する間に送ら

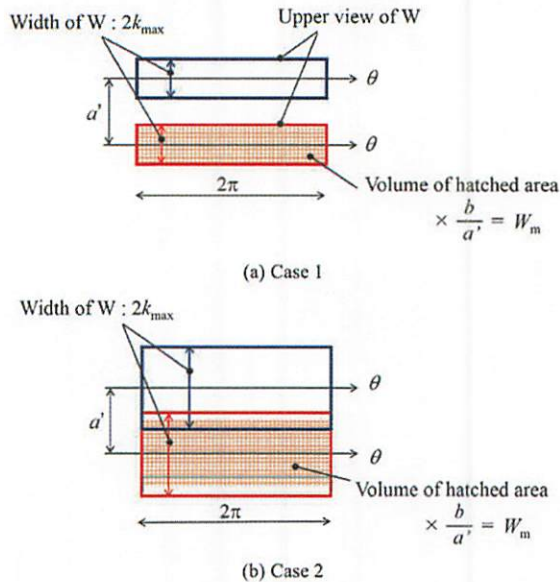


Fig. 5 Cases of cross grinding conditions according to the size of W

Table 1 Calculation conditions

W_0 mm ³	0.00001
Random coefficient n	3.3
Wheel revolution speed min ⁻¹	100 ~ 30000
Wheel feed rate v_c mm/min	0.1 ~ 30
Width of wheel b mm	1
Wheel diameter D mm	10
Workpiece revolution speed $\omega 2\pi$ mm ⁻¹	0.1 ~ 1000
Distance from center of workpiece to grinding point r mm	0.5 ~ 5
Half-top angle of abrasive grain α °	80

れる距離との関係から、2つのケース²⁾に分類される。図2(a)中に示した隣り合う2つの軌跡を抽出し、それぞれに存在する立体Wの関係进行分类ごとに表したものを図5に示す。ここで立体間の距離は砥石が1回転する間に送られる距離 a' となり、次式で求められる。

$$a' = \pi D v / V \quad (12)$$

図5に基づき、立体Wの体積をそれぞれ計算した。結果を次式に示す。

ケース1：隣り合う立体Wが互いに干渉しない場合、すなわち $2k_{max} < a'$ のとき(図5(a))

$$W_m = n W_0 = b \frac{V}{r \omega} H_m^2 \left(1 - \frac{2}{3} \frac{H_m}{D} \right) \tan \alpha \quad (13)$$

ケース2：隣り合う立体Wが互いに干渉しない場合、すなわち $2k_{max} > a'$ のとき(図5(b))

$$W_m = n W_0 = \pi b H_m (D - H_m) - \frac{\pi^2 b D r \omega}{4 V \tan \alpha} (D - 2 H_m) - \frac{\pi^3 b D^2 r^2 \omega^2}{12 V^2 \tan^2 \alpha} \quad (14)$$

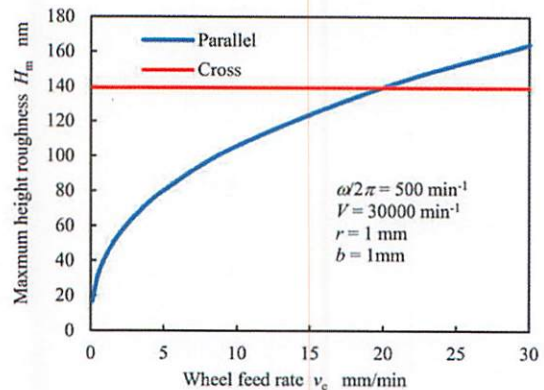


Fig. 6 Effect of wheel feed rate

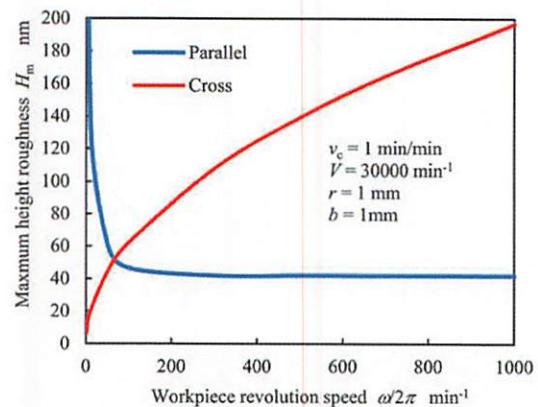


Fig. 7 Effect of workpiece revolution speed

式(13)、(14)に研削条件の数値を代入することにより、クロス研削による研削面粗さ H_m を算出することが可能である。

4. 研削条件と研削面粗さの関係

前章で得られた理論式を用いて、パラレル研削による研削面の粗さとクロス研削による研削面の粗さの解析を行う。研削条件として代入した値を表1に示す。砥石送り速度 v_c と最大高さ粗さ H_m の関係について解析した結果を図6に示す。式(13)、式(14)に砥石送り速度 v_c が含まれていないことからわかるように、クロス研削による研削面粗さは砥石送り速度の影響を受けない。一方、パラレル研削では砥石送り速度が速くなるほど研削面粗さが大きくなる結果となった。そのため、低い砥石送り速度においてはパラレル研削面の方が平滑になり、ある砥石送り速度を越えるとクロス研削の方が平滑な研削面が得られる。しかし、研削面粗さを比較したとき、パラレル研削法を用いて低い砥石送り速度に設定することが望ましいことがわかる。

次に工作物回転数と最大高さ粗さの関係について解析を行った。結果を図7に示す。パラレル研削面は工作物回転数が高いほど平滑になり、クロス研削面は工作物回転数が低いほど平滑になる結果となった。したがって工作物回転数を低く設定すると、クロス研削の方が平滑な研削面が得られる場合があることがわかる。しかし工作物回転数を低く設定した場合、削り残しによる形状精度の悪化が生じる。この形状精度の悪化を抑えるためには、砥石送り速度も低くする必要がある。そこで砥石送り速度 v_c を変化させて最大高さ粗さの変化を比較した。結果を図8に示す。同図より、砥石送り速度を低く設定した場合、パラレル

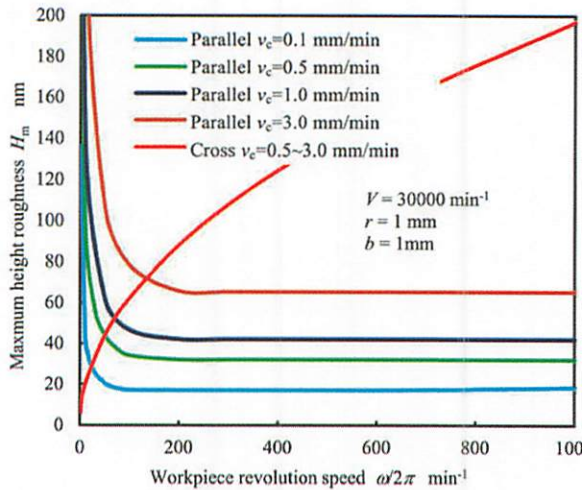


Fig. 8 Effect of workpiece revolution speed and wheel feed rate

研削面粗さも小さくなることがわかる。また、パラレル研削面の粗さは工作物送り速度に対して安定しており、均一な研削面が得られると考えられる。したがって、工作物回転数の観点からも、一般的な研削条件の範囲内においてパラレル研削の方がクロス研削よりも優位であると考えられる。ただし、工作物回転数を数 min^{-1} オーダまで低く設定できる環境に限り、クロス研削の方が優位となる。

工作物中心からの距離 r と最大高さ粗さの関係を図 9 に示す。クロス研削、パラレル研削共に工作物中心から遠くなるほど、研削面粗さが大きくなる結果となった。また、全面にわたってパラレル研削の方がクロス研削よりも平滑な研削面が得られることがわかる。また、砥石周速 V と最大高さ粗さの関係を図 10 に示す。この結果からも、パラレル研削の方が平滑な研削面が得られることがわかる。

5. 結 言

本研究では、軸対称非球面研削における研削条件の最適化を目的として、砥粒切削方向と最大高さ粗さの関係を統計的研削理論により検討した。本研究で得られた結論を以下に示す。

- (1) 砥石送り速度、工作物回転数を変化させた場合、パラレル研削面粗さとクロス研削面粗さが交差する点が現れる。一方、工作物中心からの距離あるいは砥石周速が変化しても交差する点は現れない。

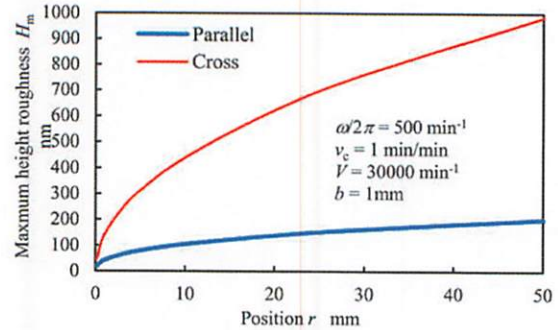


Fig. 9 Effect of position

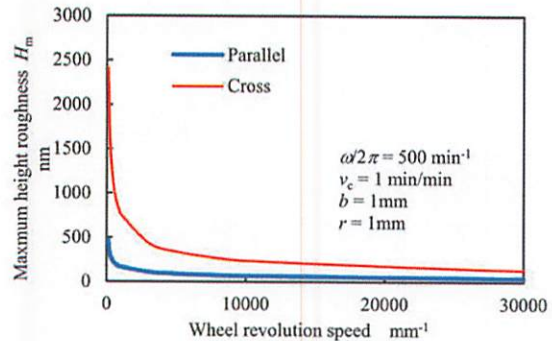


Fig. 10 Effect of wheel revolution speed

- (2) 通常の軸対称非球面研削に用いられる研削条件の範囲においてはパラレル研削の方が平滑な研削面が得られる。ただし、工作物回転数が低い条件においてはクロス研削の方が平滑な研削面が得られる。

参 考 文 献

- 1) 佐伯優, 厨川常元, 庄司克雄: パラレル研削法による非球面金型加工に関する研究, 精密工学会誌, **68**, 8(2002)1067.
- 2) 吉原信人, 関紀旺, 厨川常元: 砥粒切削方向が研削面粗さに及ぼす影響について—非軸対称非球面研削に関する研究—, 精密工学会誌, **76**, 7(2010)781.
- 3) 松井正己, 庄司克雄: 研削仕上げ面粗さに関する一考察, 機械の研究, **19**, 10(1967)1341.
- 4) 松井正己, 庄司克雄: 統計的手法による研削機構の考察(第1報)—砥粒切削長さについて—, 精密機械, **36**, 2(1970)115.
- 5) 松井正己, 庄司克雄: 研削砥石の有効切れ刃に関する研究, 精密機械, **34**, 11(1968)743.
- 6) S. Matsui and K. Syoji: On the Maximum Height Roughness of Ground Surface, Technology Reports, Tohoku Univ., **38**, 2(1973)615.

Plenary Talk 2

Pico-Precision & Hybrid Machining for High Value Manufacturing

Dr. Tsunemoto Kuriyagawa
Professor, Tohoku University, Japan

Professor Tsunemoto Kuriyagawa is the professor of Nano-Precision Mechanical Fabrication Laboratory in Graduate School of Engineering, and the Professor of Bio-Medical Interface Fabrication Laboratory in Graduate School of Biomedical Engineering at Tohoku University.

Professor Kuriyagawa received his Bachelor of Engineering in 1979, Master of Engineering in 1981, and Ph.D. 1987, all from Tohoku University, Japan. He then served as a lecturer (assistant professor) from 1990 to 1992, an associate professor since 1992 and a full professor since 2003. He was the Dean of Graduate School of Biomedical Engineering of Tohoku University (2017.4-2020.3).



From 1991 to 1992, he carried out research on “Creep feed grinding of turbine blade of jet engine” at the Center for Grinding Research and Development, University of Connecticut, USA, as a visiting professor. At 2003, stayed at Center for Precision Metrology of University of North Carolina at Charlotte, USA, for a sabbatical leave.

He is a member of Science Council of Japan, and was a council member of Science Council of Japan (2014.10-2020.9). And he was the Chairman of the International Committee for Abrasive Technology (ICAT) (2007-2008), and the President of the Japan Society of Abrasive Technology (JSAT)(2017-2019).

Prof. Kuriyagawa’s research interest includes Pico & Nano-Precision Mechanical Manufacturing, Functional Generation Machining, and Particle Jet Processing. He has published over 400 refereed journal papers, 10 book chapters, over 50 patents. He has been granted 56 awards and prizes.

Control of the Porosity and Its Orientation of Bio-implants adopting Metal Additive Manufacturing

Masayoshi Mizutani^{1, a*}, Shinji Ishibashi¹, Masaki Tsukuda¹, Takumi Mizoi¹,
Masataka Chuzenji¹, Keita Shimada¹ and Tsunemoto Kuriyagawa¹

¹Graduate school of engineering, Tohoku university, 6-6-01 Aoba, Aramaki, Aoba-ku, Sendai
980-8579, Japan

^amasayoshi.mizutani.b6@tohoku.ac.jp

Keywords: Additive manufacturing, Selective laser melting, Biomaterials, Bio-implants, Porous metal

Abstract. Porous metals are attracting considerable attention for solving problems and improving functions of the metal implants. This study proposes a “rhizoid porous structure (RPS)” utilizing vacancy defects present in an object produced via selective laser melting (SLM). Herein, we attempted to control the formation of the RPS pores by manipulating the building conditions. The results demonstrate that pores are oriented along the direction when the laser scanning is limited to a uniaxial direction. Furthermore, the specimens with oriented pores have mechanical anisotropy. Moreover, these results indicate that the proposed method can realize highly functional implants with mechanical functions equivalent to that of living bones.

Introduction

As people in societies across several countries continue to age, the development of sophisticated implants that can increase the healthy life expectancy and quality of life of elderly patients has become an urgent task. Porous metal materials have attracted considerable attention to achieve this goal. The benefits of porous implants include their ability to reduce the stress-shielding effect [1] and achieve a strong bony union due to the bone growth inside the pores [2]. Owing to the development of Metal Additive Manufacturing (MAM) techniques such as Selective Laser Melting (SLM), manufacturing porous structures with a high degree of freedom is currently possible in terms of shape design. However, the geometric design of porous structures requires complex work using dedicated software; additionally, it is constrained by the limits in the dimensions that can be used to allow the reproducibility of the shapes. Therefore, techniques for manufacturing porous metal materials that are simple and unaffected by the size of the design domain are desired.

Thus, this paper proposes a “Rhizoid Porous Structure (RPS),” which utilizes the vacancy defects formed within an object created using SLM. This structure has pores that are several tens to hundreds of μm in size, and is named after the characteristic shape of its connected pores. Previously, we have succeeded in controlling the porosity of these structures by manipulating the laser scanning speed, together with achieving higher mechanical strengths than those of conventional porous materials [3]. By deriving appropriate fabrication conditions from preliminary mechanical or functional designs, we ultimately aim to produce sophisticated implants that combine multiple functionalities using near net shape manufacturing.

This study focuses on the orientation of the pores to control the pore shapes in RPS materials with a much higher degree of freedom. First, we investigate the effect of the properties of the top surface of a specimen on the formation of the pores. Herein, the “top surface” of a specimen refers to the newest surface on which melting using a laser and solidification has been completed. Based on the results, we propose a technique for controlling the orientation of the pores and evaluate the orientation angle of the pores in the specimens using image processing. Furthermore, we evaluate the mechanical characteristics of the specimens using tensile testing based on the prediction that oriented pores create mechanical anisotropy.

Relation between Roughness of Top Surface and Porosity

Experimental Method. The specimens were fabricated using the ProX100 metal additive manufacturing device from 3D Systems. Gas atomized powder of the Ti-6Al-4V alloy (64Ti) from Osaka Titanium Technologies was used as the starting material. The specimens were fabricated under the conditions listed in Table 1 as 7-mm square cubes. To vary the surface properties of the top surface of the specimens, two types of laser scan strategies (i.e., X^1Y^1 and X^2Y^2 strategies) were employed in this experiment. In the X^1Y^1 strategy, the direction of the laser scan was rotated by 90° for each layer and six different speeds were used for the laser scan speed, s , as shown in the Table 1. In the X^2Y^2 strategy, two laser scans were made along the same path for each layer, where the scan speed for the first scan, s_1 , was varied across the same six speeds as in the X^1Y^1 strategy and that for the second scan, s_2 , was 100 mm/s. In summary, specimens were obtained under 12 different conditions comprising six different conditions for each strategy. The top surface of the fabricated specimens was observed using a shape analysis laser microscope VK-X1000 from KEYENCE, and the three-dimensional shape data obtained from it were used to obtain the surface roughness, S_a . The porosity of the specimens was obtained using X-ray computed tomography (CT) scans.

Table 1. Building conditions

Spot diameter of laser	80 μm
Wave length	1070 nm
Transmission method	Continuous wave laser
Laser power	50 W
Layer thickness	45 μm
Laser scanning distance	70 μm
Atmosphere	Argon
Laser scan strategy and laser scan speed	
X^1Y^1 Strategy	
s [mm/s]	100, 150, 240, 300, 400, 430
X^2Y^2 Strategy	
s_1 [mm/s]	100, 150, 240, 300, 400, 430
s_2 [mm/s]	100

Results and Discussions. Figure 1(a) shows the relation between the laser scan speed and surface roughness for each specimen. Herein, surface roughness exhibited a decreasing tendency with decreasing scan speed and double scanning, whereas it is assumed that the top surface formed a rugged shape because of cohesion of molten metal in the melt pool due to surface tension [4]. Additionally, the decrease in roughness was presumably caused by a decrease in the surface tension of the molten 64Ti, following an increase in the temperature of the melt pool, as well as by re-melting of the rugged shape by the laser.

Figure 1(b) shows the presence of a clear, positive correlation between the top surface roughness of the specimens and their porosity. Furthermore, from the cross-section profiles of the top surface shown in Figure 2, the development of a remarkably rugged shape could be observed for the sample with the higher roughness. At areas corresponding to the troughs of the rugged surface, the thickness of the next powder layer that was supplied became large, which could possibly result in insufficient melting of the metal along the depth direction and eventually causes the formation of unmelted areas

and easily traps the metal vapor. Thus, the trough areas were conceived to be a starting point of pore formation. In contrast, there were no deep troughs observed in the specimen at lower scan speed, which is conceived to have resulted in the reduction of areas where pore formation occurred preferentially, i.e., where the specimen displayed lower porosity.

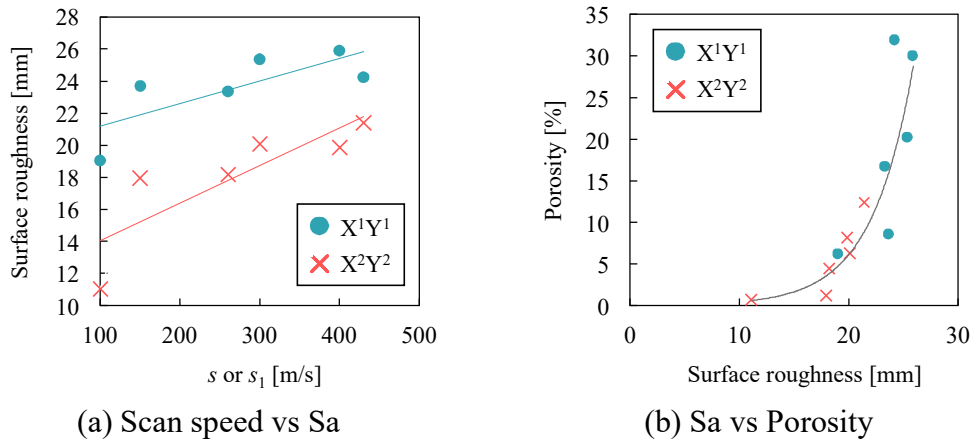
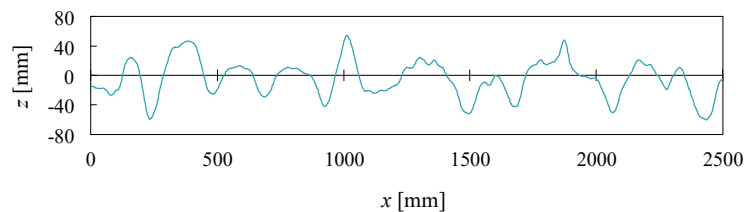
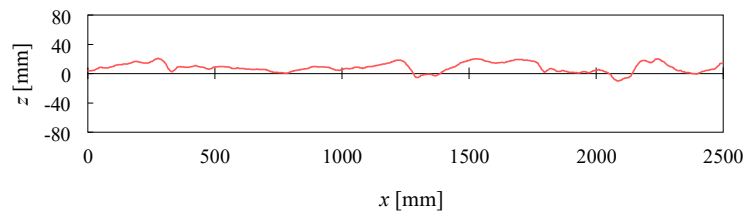


Figure 1. Evaluation of manufactured structure



(a) $s = 430$ (X^1Y^1 Strategy)



(b) $s_1 = 100, s_2 = 100$ (X^2Y^2 Strategy)

Figure 2. Section profile of top surface

Orientation of Pores and Mechanical Anisotropy

From the previous section, it was implied that the geometric shape of a specimen's top surface formed by the laser scan affects the shape of pores in the specimen. We performed an experiment in an attempt to control the orientation of the pores, based on this assumption.

Experimental Method. Figure 3 shows the laser scan strategy employed in this experiment. It was assumed that limiting the laser scan direction to a uniaxial direction would orient the rugged peaks and troughs of the top surface, as well as the pores formed along with them. We used a scan speed of 240 mm/s and retained all other fabrication conditions as in the previous section.

We evaluated the orientation of the pores via image processing. First, we used the image processing program ImageJ to binarize computed tomography (CT) images of the X–Y sections obtained using X-ray CT scans, and extracted all pores subject to evaluation. Next, we approximated each pore by a 1-pixel wide line using a thinning process and defined the angle between the line segment that was formed by connecting the two ends of each line. The positive x direction was defined

as the pore orientation angle θ ($-90^\circ < \theta < 90^\circ$). We obtained the orientation angles for all pores existing in a CT images, and ultimately accumulated all values obtained from 880 images for each specimen to create a histogram of the orientation angles.

Additionally, we performed tensile tests to evaluate the mechanical characteristics of the specimens. Two types of specimens were used: one was “vertical specimen,” whose tensile direction was made to be perpendicular to the laser scan direction; another was “horizontal specimen,” whose tensile direction was made to be parallel to the laser scan direction.

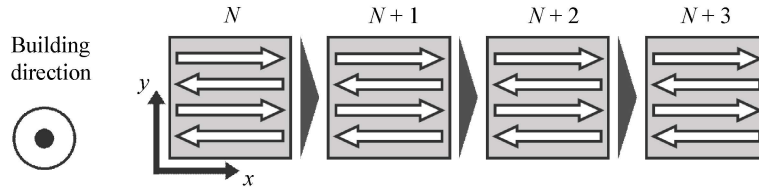


Figure 3. Schematic of X[∞] strategy

Results and Discussions. Figure 4 shows part of the X-ray CT image (after binarization) of two specimens for this experiment, created using an identical scan speed and the X¹Y¹ strategy, for comparison. The specimen fabricated with the X[∞] strategy displayed pores that were elongated in the direction of the laser scan. A remarkable orientation of the pores in the direction coincident with that of the laser scan direction could also be observed from the orientation angle histogram in Figure 5. In contrast, for the specimen fabricated using the X¹Y¹ strategy, pore orientation was not observed in either the CT image or the histogram.

Accordingly, the tensile strengths of the “vertical” and “horizontal” specimens were 278 [MPa] and 368 [MPa], respectively, with a significant difference observed between them ($p < 0.05$). More particularly, the “vertical” specimen was conceived to exhibit lower strength than the “horizontal” specimen because it had a higher ratio of pores that were elongated perpendicularly to the tensile direction, whereas crack growth in mode I (opening mode) initiated by stress concentration at the ends of the pores was likely to have induced fracture.

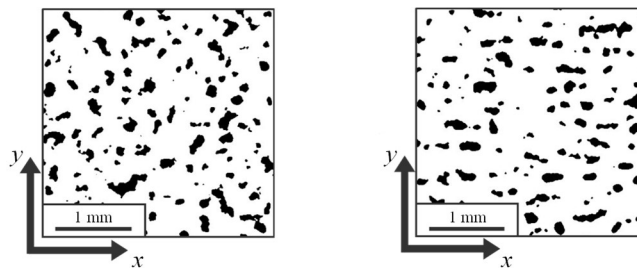


Figure 4. XY section of CT images

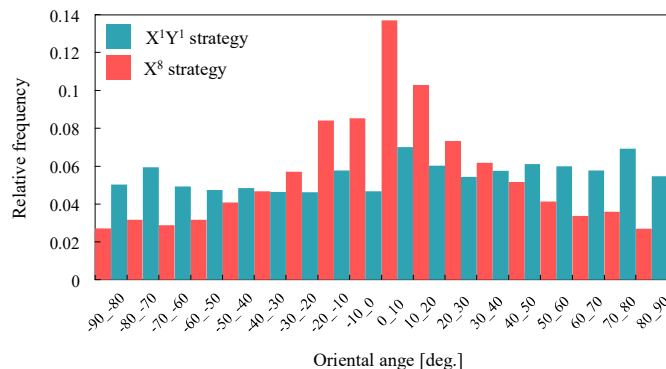


Figure 5. Histogram of orientation angle

Conclusions

The conclusions of this study are as follows:

- 1) A clear, positive correlation exists between the surface roughness of the top surface of a specimen being fabricated and its porosity. The geometric shape of the top surface was implied to induce a dominant effect on pore formation in RPS materials.
- 2) Limiting the laser scan direction toward uniaxial direction during specimen fabrication leads to pore orientation in the specimen toward the same direction. Furthermore, the tensile strength of specimens with oriented pores changes depending on the tensile direction.

Accordingly, these findings demonstrate that we can control the orientation of pores in a specimen by manipulating the laser scan strategy. Moreover, we can possibly develop bone replacement materials for implants that exhibit mechanical anisotropy equivalent to that of bone.

Acknowledgements

This study was supported in part by JSPS KAKENHI Grant Numbers JP17K06074 and JP17KK0126, and by the 2014 Grant for Strengthening Innovation Platforms at National Universities. The authors would like to express their gratitude to the Technical Division of the School of Engineering at Tohoku University and to the staff of the Innovation Plaza, for their valuable support in conducting the experiments.

References

- [1] Sajad, A., Burnett, J., Michel, T., Damiano, P. (2017) Fully Porous 3D Printed Titanium Femoral Stem to Reduce Stress-Shielding Following Total Hip Arthroplasty. *J. Orthop. Res.*, 35, 8 (2017) 1774-1783.
- [2] Ken, N., Jun T., Ryo, U., Hirotada K., Toshio M. (2015) Bone Ingrowth into Ti-Zr Porous Implant and Bone Bonding Strength. *J. Japanese Society of Oral Implantology*. 19, 4, 29-35.
- [3] Masaki, T., Shinji, I. Takumi, M., Hidekazu, M., Hiroyasu, K., Osamu, S., Keita, S., Masayoshi, M., Tsunemoto, K. (2018) Development of high performance porous implants by metal additive manufacturing. *Proceedings of 2018 JPSE Spring Conference*.
- [4] Takayuki, N., Selective laser sintering of high carbon steel powder studied as a function of carbon content. *Journal of Materials Processing Technology*, 209, 5653-5660.



Keynote Speaker: Prof. Tsunemoto Kuriyagawa
Presentation Title: The exploration of the frontiers of high value manufacturing based on nanotechnology

Biography:

Professor Tsunemoto Kuriyagawa is the professor of Nano-Precision Mechanical Fabrication Laboratory in Graduate School of Engineering, and the Professor of Bio-Medical Interface Fabrication Laboratory in Graduate School of Biomedical Engineering at Tohoku University.

Professor Kuriyagawa received his Bachelor of Engineering in 1979, Master of Engineering in 1981, and Ph.D. 1987, all from Tohoku University, Japan. He then served as a lecturer (assistant professor) from 1990 to 1992, an associate professor since 1992 and a full professor since 2003. He was the Dean of Graduate School of Biomedical Engineering of Tohoku University (2017.4-2020.3).

From 1991 to 1992, he carried out research on “Creep feed grinding of turbine blade of jet engine” at the Center for Grinding Research and Development, University of Connecticut, USA, as a visiting professor. At 2003, stayed at Center for Precision Metrology of University of North Carolina at Charlotte, USA, for a sabbatical leave. He is a member of Science Council of Japan, and was a council member of Science Council of Japan (2014.10-2020.9). And he was the Chairman of the International Committee for Abrasive Technology (ICAT) (2007-2008), and the President of the Japan Society of Abrasive Technology (JSAT)(2017-2019).

Prof. Kuriyagawa’s research interest includes Pico & Nano-Precision Mechanical Manufacturing, Functional Generation Machining, and Particle Jet Processing. He has published over 400 refereed journal papers, 10 book chapters, over 50 patents. He has been granted 56 awards and prizes.

Abstract:

We aim to promote innovations of pico- & nano-precision Micro/Meso Mechanical Manufacturing (M4 process) at the frontier of manufacturing technology, including ultra-precision mechanical manufacturing technologies for various shapes, nano-precision fabrication for 3D microstructures, atom/molecule manipulation for nanostructures and so on. Our goal is not only to create high-precision shapes, but also to generate functional structures on the shape by controlling the micro textures. Today, I will introduce pico-precision advanced processes (PPAP) and hybrid machining processes for function generation machining, which aim for high value manufacturing. In the hybrid process, Hybrid vibration machining, Ultrasonic vibration assisted electrolytic grinding, Ultrasonic vibration assisted plasma discharge grinding, and Laser assisted micro-cutting will be introduced.

Effect of heat treatment on blanking of Fe-Si-B-Cr amorphous alloys

Chieko Kuji*, Masayoshi Mizutani*, Keita Shimada, Toyohiko J Konno, Momoji Kubo, and Tsunemoto Kuriyagawa

¹ *Iwate Industrial Promotion Center, Morioka, Iwate 020-0857, Japan*

² *Graduate School of Engineering, Tohoku University, Sendai, Miyagi 980-8579, Japan*

³ *Currently, Applied Research Laboratory, High Energy Accelerator Research Organization, Tsukuba, Ibaraki 305-0801, Japan*

⁴ *Institute for Materials Research, Tohoku University, Sendai, Miyagi 980-8577, Japan*

E-mail:chieko.kuji.t5@dc.tohoku.ac.jp, masayoshi.mizutani.b6@tohoku.ac.jp

We discovered that optimal blanking characteristics could be obtained by adjusting the microstructure of amorphous alloys by heat treatment. To investigate the extending behavior of shear bands, which play a key role in the deformation of amorphous alloys, a blanking model of the amorphous alloy composed of metal and semimetallic was built using molecular dynamics. The simulation results indicate that micro shear bands generated at the tool contact point were connected and propagated in the depth direction generating a network of multiple shear zones. The blank test of the as-received amorphous alloy showed high blanking resistance and left significant shear marks drooping on the blanked surface. Whereas the heat-treated specimens showed much lower blanking resistance, and the lowest blanking resistance was achieved with the one whose crystal nuclei started to sparsely precipitate and its blanked surface was composed of microscopic multiple shear bands. Furthermore, excessive heat treatment caused an increase in the number of crystals, which caused chip fractures and burrs due to the crystalline deformation mechanism. The thickness of the fracture surface became non-uniform as the grain size increased.

高付加価値ものづくりを目指す機能創成加工

To the New Frontier of Function Creation Processing for High Value Manufacturing



厨川常元*
Prof. Tsunemoto
KURIYAGAWA

We have shown that the future of manufacturing will not be limited to “the creation of form”, but will also include “the creation of function” by creating structures that express functions on or inside the machined surface. This kind of “functional creation processing” is exactly what we are aiming for in “high value manufacturing”, and we believe that it will become increasingly important. In this report, we introduce the UV-assisted tape grinding technology for gallium nitride substrates, plasma shot technology for creating low-friction and low-wear surfaces, and new surface function creation technology (ex. lattice coating) and functional material creation technology based on 3D modeling technology.

Key Words: high value manufacturing, function creation processing, UV-assisted tape grinding, gallium nitride, plasma shot

1. はじめに

“ものづくり”は我が国の基盤であり、その将来ビジョンを明確にすることは重要である。そのために大学をはじめ、公設試や企業、行政も含めたオールジャパンでの取り組みが活性化している。例えば、近年ではカーボンニュートラル社会や超高齢社会対応といった大きな目標を設定し、その実現を宣言したのはその一例である。それでは、ものづくりの分野での対応はどうしたらよいのだろうか？前報¹⁾では、これからの“ものづくり”を考える上で重要であると思われるキーワードについて紹介した。すなわち、これまでの単なる“形状創成”だけにとどまらず、その表面あるいは内部に機能を発現する構造を作り込む“機能創成”が重要な役割を担うようになるであろうことを説明した。このような“機能創成加工”の提案は、まさに“高付加価値ものづくり”を目指すもので、ますますその重要度が増していくものと考ええる。これ以降、筆者の研究室では、ポストナノ精度加工としてのピコ精度加工や、表面機能創成技術、さらには噴射加工の歯科治療への応用と臨床試験に取り組んできた。本報ではこれらの中から、窒化ガリウム基板の紫外線援用テープ研削技術、低摩擦・低摩耗表面創成のた

めのプラズマショット技術、3D造形技術を応用した新しい表面機能創成技術や機能性材料創成技術について紹介する。

2. 窒化ガリウム基板の紫外線援用テープ研削技術

シリコン (Si) の限界を超えるパワーエレクトロニクスデバイス用新材料として炭化珪素 (SiC) や窒化ガリウム (GaN) 等の半導体材料が注目されている。特に GaN デバイスは、白色 LED での実用化が始まり、一般照明用やヘッドライトなどの車載用光源として普及が進んでいる。さらには今後ますます需要が伸びると予想される電気自動車やエアコンなどで使用されるパワーデバイスへの適用も検討が始まっている。しかしながら GaN デバイスの普及を加速させるためには、高品質かつ大口径の GaN 基板を低価格で製造する技術の確立が必須である。しかし GaN 材料は Si 材料と比較して高硬度で化学的に安定であるため、加工時間が 100 ~ 150 時間と Si 材料と比較し一桁近く長くなっている。

従来から Si 基板の研磨工程には化学機械研磨法 (Chemical Mechanical Polishing, 以下 CMP) が用いられてきた。これは化学的な除去作用で大きな加工量を確保し、機械的作用で平坦性を担保する複合加工法である。例えば、Si 基板では強アルカリ環境下でコロイダ

*東北大学 大学院工学研究科 教授

ルシリカ粒子を用いて研磨が行われている。しかし GaN 単結晶は化学的に安定であるため、Si と比較して極端に加工能率が低下する。そこで久保ら²⁾とともに、GaN 基板に作用させる砥粒の種類により、どのような反応が生じ、GaN 基板表面からどのように Ga 原子が分離していくのかを、Tight-binding 量子分子動力学シミュレーションを用いて解明した。その結果、中性環境下でナノダイヤモンド (ND) 砥粒を用いた場合、OH ラジカルを援用することにより砥粒・基板間結合が起点となって表面 Ga 原子が脱離することが分かった。さらに塩基性環境下では、OH⁻ の作用によって砥粒・基板間結合が形成されやすくなり、研磨が促進されることが示唆された。この知見に基づき、過酸化水素水 (HP) に紫外線 (UV) を照射して OH ラジカルを発生させながら ND 砥粒で加工する手法を考案した。

通常の研磨方法では工作物 (基板) と研磨定盤とが面接触となるため、研磨中に紫外線を効率的に照射できない。一般的に OH ラジカルの寿命は非常に短いため、加工領域近傍で紫外線照射が可能、さらに効果的に ND 砥粒を連続的に加工領域に供給する方法として図 1 に示すような紫外線援用テープ研削装置を試作した³⁻⁵⁾。この装置では、ウレタン製のコンタクトホールを介して研磨テープを GaN 基板に押しつける構造とした。この場合、接触状態 (コンタクトホールの直径、弾性率、加圧力、加工速度等) を変えることにより GaN 基板との接触面積を精密に制御でき、有効切れ刃数を制御することが可能となる。基板は油静圧の超精密高速反転テーブル (最大 1 000 ストローク/分) に固定されて往復運動する。さらに研磨テープであるため固定砥粒方式となり、テープをフィードすれば、加工領域には次々と新しい砥粒が供給されるという利点も生じる。最終的には、これまで一般的であった遊離砥粒方式の基板加工プロセスをすべて固定砥粒方式にすることも可能であり、大幅な工程の簡略化が期待される。

研磨実験の結果、UV + HP の援用効果とテープ研削機構を複合することにより、初期表面の 5.3nmRa が 10 分加工後に表面粗さが 1nm 以下になった。UV と HP を用いない場合では表面粗さが 1nm 以下になるまで平均 60 分の時間を要したことから、UV + HP 援用により、援用効果を使用しない場合と比較して 6 倍以上の加工速度向上の効果があることが分かった (図 2)。

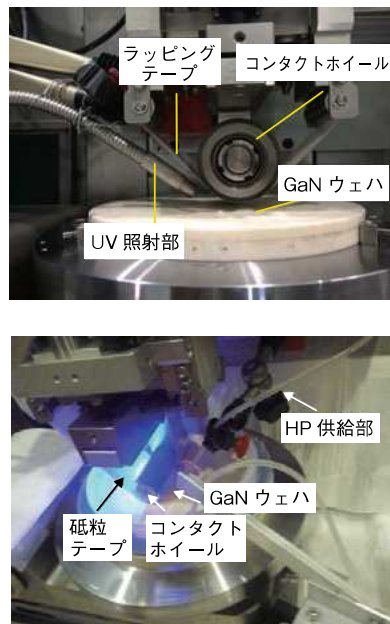


図 1 紫外線援用テープ研削装置
UV-assisted tape grinding equipment

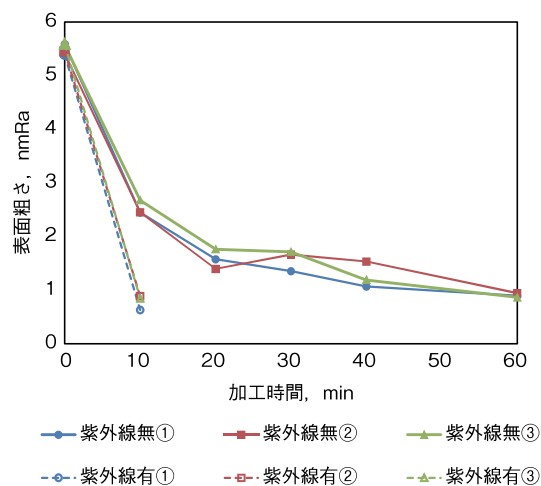


図 2 紫外線援用の効果 (UV 照射強度: 1.0W, UV 波長: 365nm, HP 濃度: 98%)
(加工条件: ダイヤモンド砥粒 #10000, 揺動幅 ±1.5mm, 揺動回数 500 回/min)
UV-assisted effects (UV irradiation intensity: 1.0W, UV wavelength: 365nm, HP concentration: 98%)
(Processing conditions: diamond abrasive #10000, oscillation width ±1.5mm, oscillation frequency 500 times/min)

3. プラズマショット法による低摩擦・低摩耗表面創成

プラズマショット (PS) 法は放電加工を応用した表面処理手法である⁶⁻⁹⁾。図 3 に示すように、PS 法は、電極・工作物間に連続的なパルス放電を発生させることにより電極を溶融させ、工作物上に移行させることで改

質層を形成する。本手法では、微細なパルス状の放電が局所的に繰り返されるため、被処理材表面には微細な凹凸（マイクロディンプル：油潤滑下では油だまりとして作用）が形成される。またそれと同時に、電極材料が溶融した状態で工作物側に移行し、一部基材と混合溶融することで密着性の高い改質層が形成される。これらの特徴を活かすことで、低摩擦かつ低摩耗を有する魅力的な表面の創成が期待できる。

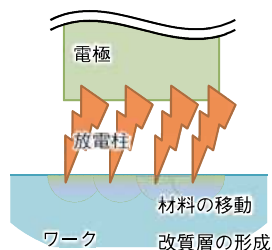


図3 プラズマショット法の概略図

Schematic diagram of the plasma shot method

図4は電極として TiC や Si を用いてステンレス基板上にプラズマショット処理をしたときの、改質面のビッカース硬度を測定したものである。プラズマショット処理を行うことにより、硬度は約5倍以上になることが分かった。なお本手法は、鋳鉄やアルミニウム等の鋳造製品のように、硬化処理が困難なものにも対応可能で、かつ表面にはマイクロディンプルが生成されるので、潤滑性能も向上することが期待される。さらにプラズマショット面のマイクロディンプルの凹凸を研削加工等により除去加工すれば、硬化処理した部分の境界が分からなくなるため、工程のブラックボックス化が図れる。

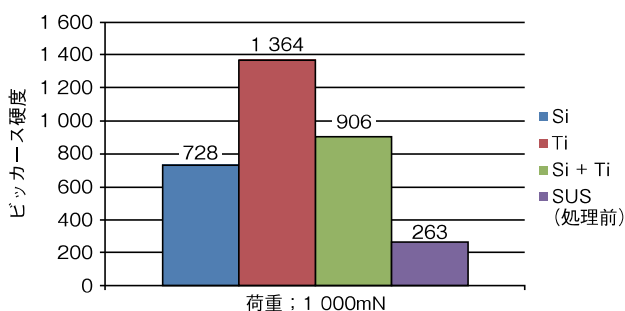


図4 プラズマショット法による表面硬度の増加
Increase of hardness by plasma shot treated surface

4. 3D 積層造形技術による機能性 インターフェース創成

3D 積層造形は、目的とする構造物の3次元形状情報があれば複雑形状の造形も可能になる基盤技術として普及してきた。特に近年では、金属やセラミックスの3D 積層造形技術は、医療分野ではテーラーメイドのインプラント（人工骨、骨固定材など）作製技術として期待されている。しかし造形条件によって造形物の表面性状や結晶構造、あるいは組織が変化し、その変化に伴って製品自体の機械的な性質も変化することが知られている。本報では特にレーザービーム 3D 金属積層造形技術を応用し、単なる形状創成だけではなく、機能創成、特に表面機能創成法として開発した技術について紹介する。

4.1 微細ラティスコーティング技術

製品の表面に周期的なテクスチャを形成することで、例えば濡れ性、潤滑性、生体親和性、アンカー効果などの機能を発現させることが可能になれば、製品自体の付加価値が向上する。そこで、切削や研削といった通常の機械加工で製品の寸法形状の大枠を作り上げた後に、その表面に3D 金属積層造形技術でテクスチャを創成する方法を提案する。

著者らは、任意の自由曲面上に微細なラティス構造をプリンティングするという新手法“微細ラティスコーティング法”を開発した。金属積層造形では「粉末床溶融結合法 (Powder Bed Fusion, 以下 PBF 法)」と「指向エネルギー堆積法 (Direct Energy Deposition, 以下 DED 法)」という二つのプロセスが主流である。通常、複雑な構造体を造形する場合には PBF 法が用いられるが、平坦なベースプレート上に構造を造形することになる。一方、自由曲面に対して造形をする場合には DED 法を用いることになるが、この場合には複雑形状の造形は困難となる。これらに対し微細ラティスコーティング法は自由曲面上に複雑な構造体を造形することが可能で、得られる構造の最小造形幅はおおよそ粒子一つ分という点で、類をみない革新的なプロセスである¹⁰⁻¹²⁾。

図5に微細ラティスコーティング法により金属円筒表面にテクスチャリングした例を示す。

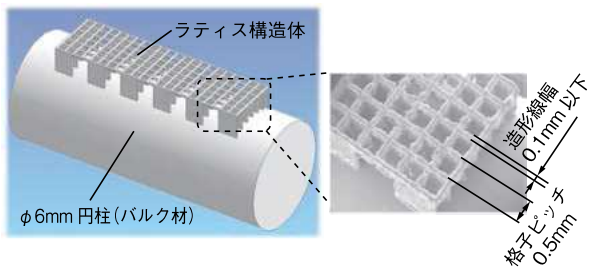


図5 微細ラティスコーティング法による造形例
Sample of micro-lattice coating

4.2 機能性材料創成技術

金属積層造形において最小単位の基礎的現象をとらえるべく、粉末粒子単体の微視的な熔融挙動を明らかにし、造形プロセスで生じるミクロな現象を解明することで、造形プロセスの原理を明らかにした。その結果、レーザービームの走査速度やエネルギー密度を制御することにより造形物内部の結晶構造や組織を任意に制御可能であることを示した。図6はレーザー条件を変えて造形した構造体の結晶構造の違いを示した電子線後方散乱回折 (EBSD) により結晶方位を色別表示した IPF (Inverse pole figure) Map である。その結果、レーザー条件を制御することにより、結晶構造を微細化させたり、逆に任意の方向に粗大化させることも可能で、造形物の機械的特性やその異方性にも影響を与える可能性が期待できる。

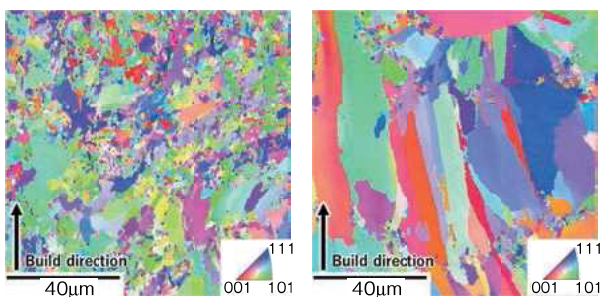


図6 レーザー条件による結晶構造の相違
Difference of crystal structure by laser condition

さて 3D 金属積層創成においては、その造形物内に空孔が残留することはその機械的強度を低下させる一因となるため、極力避けるべきとされている。しかし造形過程で偶発的に生じるこれらの空孔を積極的に利用することで、造形物内部に多孔質構造を付与することを考えた。もしそれが可能となれば、新たな機能性構造体の創成法として有効である。我々は、さらに無作為に発生するこれらの空孔を、造形条件の制御により、その分布や形態

も含めて計画的に造形物内部に配置することを可能とする方法を開発した^{13, 14)}。

この方法で作成した連結空孔を有する機能性構造体 (根状多孔質構造 Rhizoid Porous Structure, 以下 RPS と略記) の断面画像と CT 画像を図7に示す。図に示すように、連結空孔はその形状や方向、分布状態を制御できることが明らかになった。また図8は、その空孔分布状態を半径方向に傾斜させて造形した一例である。この技術は歯科治療の分野にも応用可能である。図9は我々が目指す高機能性インプラントの内部構造コンセプトである。このような RPS を利用したインプラントは、顎骨との接着性の向上や、自然歯に近い弾性体を実現できるなど、多くの利点をもたらすものと期待されている。

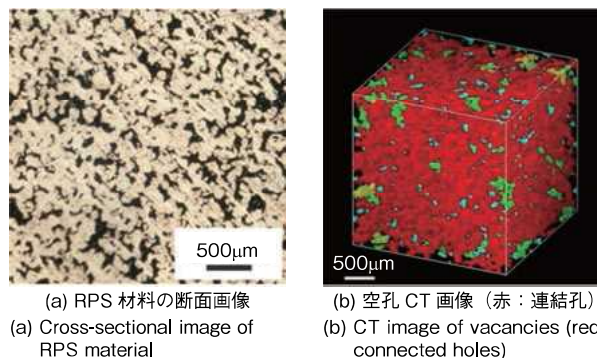


図7 作成した RPS
Sample of Rhizoid Porous Structure (RPS)

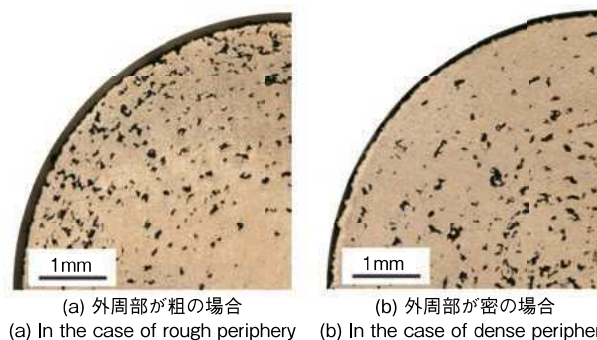


図8 RPS の空孔傾斜分布
Porosity gradient distribution of RPS

5. まとめ

本報では、今後の“ものづくり”を考える上で重要となる“高付加価値ものづくり”を目指す加工方法として、窒化ガリウム基板の紫外線援用テープ研削技術、低摩擦・低摩耗表面創成のためのプラズマショット技術、3D 造形技術を応用した新しい表面機能創成技術 (微細

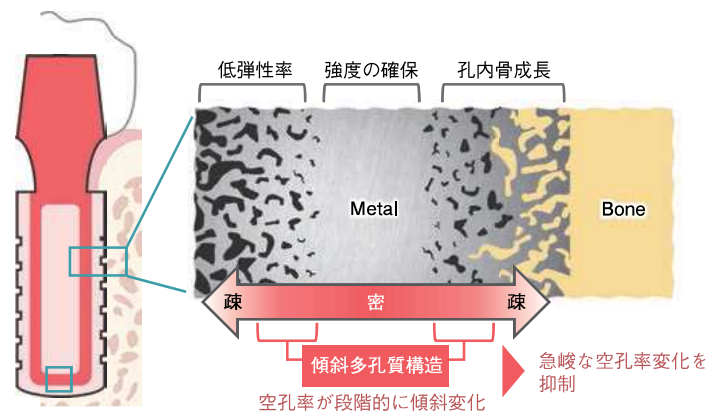


図9 歯科用高性能インプラントの内部構造コンセプト
Proposed new internal structure of high performance dental implant

ラティスコーティング法) や機能性材料創成技術について紹介した。

これからの“ものづくり”のための加工技術基盤実現のためには、「ナノの世界の現象の本質を把握した科学的な合理性を持ったものづくり」を実現することが必要不可欠である。また革新技术の創出、すなわちハードウェアの高度化のみに偏重してはならない。ハードウェアの開発はもちろん重要であるが、それらを如何に組み合わせ、使いこなしていくのかといったソフトウェアの開発も必要不可欠である。

最後に、ものづくりの根幹は、生産から廃棄、さらにはリサイクル（リユースも含む）までを考慮した“循環型ものづくり”でなくてはならない。このような“もの”の一生の流れの中で発生するCO₂など温室効果ガスをゼロにする、ライフサイクルアセスメントを設計、満足することが最も重要であることは言うまでも無い。

参考文献

- 1) 厨川常元：これからの“ものづくり”とは（形状創成から機能創成へ），JTEKT ENGINEERING JOURNAL, No. 1010(2012)2-8.
- 2) 五十嵐拓也，河口健太郎，大谷優介，樋口祐次，尾澤伸樹，久保百司：計算科学手法を用いた GaN CMP における砥粒－基板間の化学反応機構の検討，2017 年精密工学会秋季大会学術講演論文集，(2017)F20.
- 3) Keita Shimada, Ayaka Watanabe, Yoshifumi Takasu, Masayoshi Mizutani, Tsunemoto Kuriyagawa : Stochastic simulation of tape grinding for wafer-like workpiece, Materials Science Forum, 874, (2016)91-96.
- 4) 鷹巢良史，嶋田慶太，水谷正義，厨川常元：GaN のスクラッチ加工におけるクラック発生機構の研究，砥粒加工学会誌，61(7)，(2017)，392－397.
- 5) 鷹巢良史，嶋田慶太，水谷正義，厨川常元：単結晶窒化ガリウム (GaN) 基板の高速高精度加工法の開発－紫外線援用テープ研削法の提案，砥粒加工学会誌，63(11)，(2019)，569－574.
- 6) Nobuyuki Sumi, Chihiro Kato, Keita Shimada, Masayoshi Mizutani, Tsunemoto Kuriyagawa : Influence of workpiece materials on the characteristics of the layers by electrical discharge coating, International Journal of Automation Technology, 10(5)，(2016)，773－779.
- 7) Nobuyuki Sumi, Chihiro Kato, Keita Shimada, Takashi Yuzawa, Hiroyuki Teramoto : Masayoshi Mizutani, Tsunemoto Kuriyagawa, Mechanism of defect generation in the TiC layer and Si layer by electrical discharge coating, 18TH CIRP CONFERENCE ON ELECTRO PHYSICAL AND CHEMICAL MACHINING (ISEM XVIII), 42, (2016), 221－225.
- 8) 鷺見信行，一宮正和，京泉朋希，江川諒仁，嶋田慶太，水谷正義，厨川常元，山縣延樹：SPH 粒子法によるプラズマショット現象の解明，日本計算工学会論文集，20180006，(2018)。
- 9) 京泉朋希，江川諒仁，柴田頼人，加藤千拓，鷺見信行，嶋田慶太，水谷正義，厨川常元：プラズマショット法と研削加工による低摩擦・低摩耗の創成，砥粒加工学会誌，62(7)，(2018)，371－376.
- 10) 前花英一，石橋信治，嶋田慶太，水谷正義，厨川常元：パルスレーザーによる純チタン粒子の熔融接合プロセス，砥粒加工学会誌，61(1)，(2017)，40－46.
- 11) 前花英一，長森亜弓，石橋信治，溝井琢巳，嶋田慶太，水谷正義，厨川常元：レーザー金属積層造形法による微細

構造の創成—純 Ti 単粒子層に対する狭小ビード造形,
砥粒加工学会誌, 62(10), (2018), 527 – 534.

- 12) 前花英一, 臼沢太一, 石橋信治, 嶋田慶太, 水谷正義,
厨川常元: 微細ラティスコーティング技術の開発—重力
落下式粉末供給手法による壁構造の評価, 砥粒加工学会
誌, 64(1), (2020), 39 – 46.
- 13) Shinji Ishibashi, Masataka Chuzenji, Takumi Mizoi,
Masaki Tsukuda, Hidekazu Maehana, Keita
Shimada, Masayoshi Mizutani, Tsunemoto
Kuriyagawa: Design of pore morphology in porous
metal manufactured via selective laser melting, The
Proceedings of the 8th Conference of Asian Society
for Precision Engineering and Nanotechnology,
(2019) A29.
- 14) Shinji Ishibashi, Keita Shimada, Hiroyasu Kanetaka,
Masaki Tsukuda, Takumi Mizoi, Masataka Chuzenji,
Shoichi Kikuchi, Masayoshi Mizutani, Tsunemoto
Kuriyagawa: Porosity and Tensile Properties of
Rhizoid Porous Structure Fabricated Using
Selective Laser Melting, International Journal of
Automation Technology, 14 (4), (2020), 582-591.

ウルトラファインバブルを含有した研削クーラントの濡れ性評価

畑山陽介^{*1*2}, 大越広夢^{*1}, 水谷正義^{*1}, 厨川常元^{*1}

Effect of Ultrafine Bubbles on Wettability of Grinding Fluid

Yousuke HATAYAMA, Hiromu OKOSHI, Masayoshi MIZUTANI, Tsunemoto KURIYAGAWA

Key words : ultrafine bubbles, grinding fluid, wettability, contact angle, surface tension, sliding angle

1. 緒言

ウルトラファインバブル(以下, UFB)は, 直径 1 μm 以下の気泡であり, 名称は ISO で定義されている。UFB は洗浄, 殺菌, 水質浄化などの機能を必要とする分野で使用が進められている。また近年では, 研削加工に UFB を含むクーラント(以下, UFB クーラント)を用いることで, 研削性能や加工精度が向上することが報告されている^{2)~7)}。しかしその一方で, UFB クーラントの基礎特性に関する評価は十分に行われていないのが現状であり, UFB が研削性能や加工精度向上に寄与する機序の解明には至っていない。

そこで本研究ではまず, UFB クーラントの基礎特性について明らかにし, それを踏まえて UFB が研削特性に及ぼす影響について明らかにすることとした。その中で本報ではとくに UFB クーラントの接触角や表面張力, 滑落角を測定することで, 濡れ性の観点から UFB クーラントの基礎特性に関して検討・考察を行った。

2. ウルトラファインバブル(UFB)生成装置

図1に使用したUFB生成装置の模式図を示す。図中の矢印は, 水道水またはクーラント, および空気の流れを示している。本装置では, 気液混合部, ポンプ, せん断部が一体となっている。せん断部を構成する内筒および外筒の壁面には凹凸が多数設けられている。気液混合部で空気と混合された液体は, 内筒と外筒の隙間を内筒部の回転により螺旋を描きながら下流側へと流れていく。このとき凹部での大小の渦の発生と消滅の繰り返しにより, 気泡が微細化されてUFBが生成される。なお, 0.5 minで液体が1回循環するように液体容量やUFB生成装置の液体流量を設定した。

本報では, UFBクーラントの基礎特性評価のため, 表1に示す5種類の評価液を比較した。なお, 評価液2は, 水道水をベースにUFBを生成した。表2に本報で使用するクーラントの仕様を示す。

3. UFBクーラントの特性評価

本報では, 表1に示した各種UFBクーラントの接触角, 表面張力および滑落角を測定し, UFBクーラントの基礎特性について検討を行う。

まず, 表3に接触角の測定条件を, 図2に測定結果を示す。なお, 評価液2のUFB密度は13.1 億個/mLで, このUFB水を用いて評価液4を作製した。評価液3は, 所定の希釈倍率となるようにUFB生成装置のタンクに水道水とクーラントの原液を入れ, 空気送入なしで5分間循環させて作製した。評価液5は, 評価液3を空気送入しながらUFB生成装置を120分運転し作製した。

図2より, 水のグループ(評価液1・2)に対しクーラントのグループ(評価液3~5)は接触角が小さくなり, 親水化している

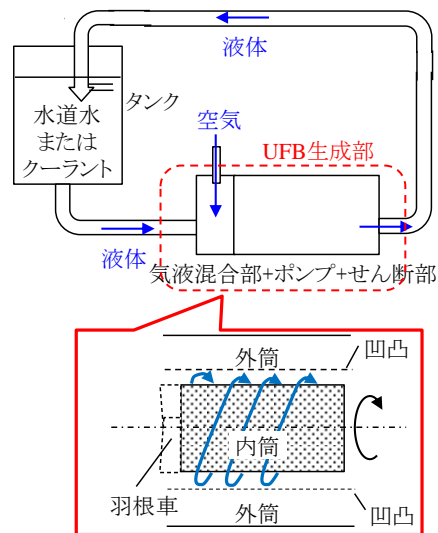


図1 UFB生成装置の模式図

表1 評価液一覧

評価液	内容
1	水道水
2	UFB水
3	水道水で希釈したクーラント
4	UFB水で希釈したクーラント
5	UFBクーラント

*1 東北大学大学院工学研究科: 〒980-8579 宮城県仙台市青葉区荒巻字青葉6-6-01

Graduate School of Engineering, Tohoku University

*2 KYB株式会社: 〒509-0206 岐阜県可児市土田60
KYB Corporation

表2 クーラント仕様

項目	内容
メーカー	ユシロ化学工業
銘柄	ユシローケン FGC822J
希釈倍率	40倍
タイプ	水溶性ソリューション

表3 測定条件

接触角 滑落角	測定機	協和界面科学(株) DM-501Hi
	算出法	接線法
	相手材	BK7 ガラス
表面張力	測定機	協和界面科学(株) DMo-501
	算出法	懸滴 ヤング・ラプラス法
	滴下量 μL	2

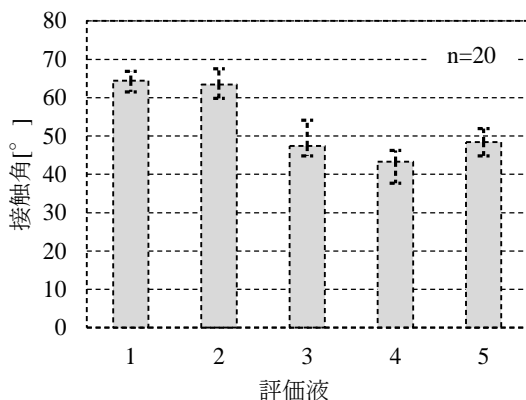


図2 接触角測定結果

ことがわかる。また、各グループ内でUFBの有無による接触角の差はほとんど認められなかった。

次に、図3に表面張力の測定結果を示す。なお、表面張力測定には接触角と同一バッチで作製したサンプルを使用した。同図より、表面張力は接触角と比較的類似した傾向となった。具体的には水のグループ(評価液1・2)に対し、クーラントのグループ(評価液3~5)は約46%表面張力が小さくなるが、グループ内でのUFBの有無による差はほとんど確認されなかった。

以上の結果から、UFBの存在が接触角を小さくし、濡れ性を改善させているというわけではなく、クーラントの存在による親水化によりUFBが加工点に効率的に運搬され、加工点でUFBが何らかの作用を及ぼすことで研削性能が変化するものと考えられる。なお、別途行った実験により、UFBクーラントの使用により研削性能が改善することを確認しているが、加工点に運搬されたUFBが加工点でどのような作用をもたらしているかについては今後詳細に検討する予定である。

図4に滑落角の測定結果を示す。滑落角は、接触角と同じ実験系で測定した。液滴を着滴させたガラス板を徐々に傾けていき、液滴が0.15 mm動いた時の傾斜角を滑落角とした。同図より、接触角や表面張力とは異なり、滑落角は、クーラントやUFBの有無による差はほとんど認められなかった。このことから、UFBクーラントによる研削性能に対して、滑落角は影響を及ぼさないと考えられる。

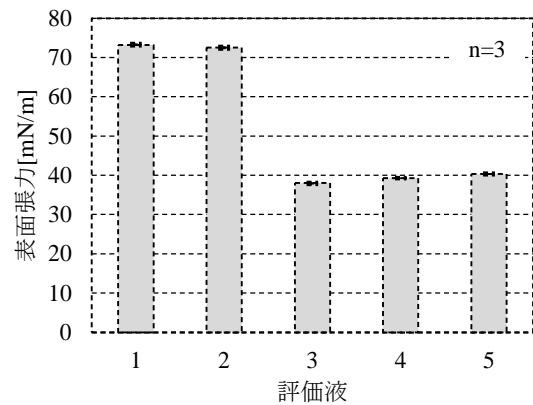


図3 表面張力の測定結果

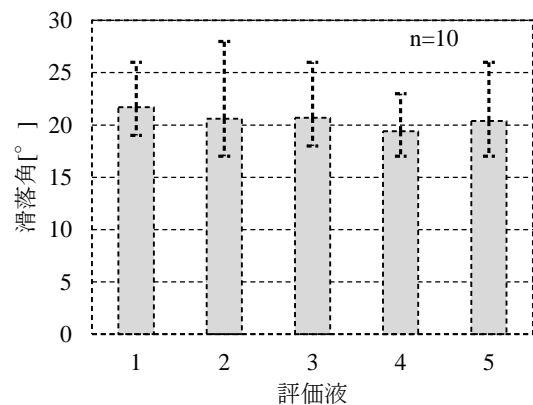


図4 滑落角の測定結果

4. 結論

- (1) 接触角や表面張力には、UFB有無の影響はほとんどないが、クーラント自体の影響が作用し、加工点にUFBを運搬している可能性があることが示唆された。
- (2) 滑落角には、クーラントやUFBの有無による影響はほとんどないことがわかった。

5. 参考文献

- 1) ISO 20480-1:2017. Fine bubble technology – General principles for usage and measurement of fine bubbles – Part 1: Terminology.
- 2) 岩井学, 神谷和秀, 細江拳, 牧野公博, 二ノ宮進一, 鈴木清: マイクロ・ナノバブルクーラントによる除去加工の研究, 2017年度精密工学会春季大会学術講演会講演論文集, (2017), 111-112.
- 3) 岩井学, 神谷和秀, 石坂達也, 二ノ宮進一, 古賀文雄, 野田大輔, 鈴木清: マイクロ・ナノバブルクーラントによる除去加工の研究 第2報: 高機能マイクロ・ナノバブルクーラントによる除去加工性能, 2018年度精密工学会春季大会学術講演会講演論文集, (2018), 281-282.
- 4) 稲澤勝史, 江面篤志, 篠原尚也, 加藤克紀, 大森整, 伊藤伸英: ファインバブルクーラントのバブル条件が研削加工に及ぼす影響, 2018年度精密工学会秋季大会学術講演会講演論文集, (2018), 262-263.
- 5) 稲澤勝史, 江面篤志, 篠原尚也, 加藤克紀, 大森整, 伊藤伸英: 各種気体を用いたファインバブルクーラントが研削加工に及ぼす影響, 2019年度精密工学会秋季大会学術講演会講演論文集, (2019), 33-34.
- 6) 小林秀彰, 上條雄樹, 平野正浩, 荒木和成: ウルトラファインバブル生成技術のクーラントへの適用と研削加工の高効率化, 2020年度精密工学会春季大会学術講演会講演論文集, (2020), 717-718.
- 7) 渡辺剛, 鈴木浩文, 高田亮, 深見信吾, 毛利茂樹, 竹下朋春: ウルトラファインバブルクーラントを用いた高精度・高効率研削技術の開発 第1報: 気泡が超硬合金の研削特性に及ぼす影響, 砥粒加工学会誌, 65巻5号, (2021), 248-253.

歯科用着色ジルコニアクラウンの 3D 造形技術の開発

第 1 報: 着色ジルコニア粉末を用いたセラミックス 3D 造形への適応

近藤直樹*¹, 水谷正義*², 佐々木啓一*³, 厨川常元*²

Development of 3D printing technology for dentistry crown by colored zirconia

1st report : Adaptation to ceramics 3D printing by colored zirconia powder

Naoki KONDO, Masayoshi MIZUTANI, Keichi SASAKI, Tunemoto KURIYAGAWA

歯科治療における歯冠の作製は、鋳造法から CAD/CAM システムによる切削法に変わりつつあり、近年ではセラミックス 3D 造形技術の適用が注目されている。本研究ではこのセラミックス 3D 造形技術に注目し、造形体の機械的特性や生体適合性、さらには審美性などの複数の機能を同時に付与するための革新的な造形プロセスの構築を目的としている。本稿ではとくに審美性に着目し、自然歯に近いカラーグラデーションを達成するための造形条件について詳細な検討を行った。その結果、色調の異なる粉末と樹脂の配合率を変えることにより造形体の色調を制御可能であるということが明らかとなった。また、それらを多層化することで明確な境界のない色調のグラデーションを実現できた。

Key words : zirconia, 3D printing, stereolithography, dentistry crown, aesthetics

1. 緒言

近年、3D 造形に関する技術は日々発展しており、樹脂や金属の造形による実用品が作製されている¹⁾。最近ではセラミックスの 3D 造形にも注目が集まっており、それを実現する装置の開発も進められている²⁾。

セラミックス 3D 造形は様々な分野での応用が期待されており³⁾、そのアプリケーションの1つとして人工歯冠が挙げられる⁴⁾。歯科治療における人工歯冠の多くは精密鋳造法により作製されているが、近年では金属単価の高騰や金属アレルギーの観点から脱金属化として硬質レジンやセラミックス材料にシフトし始めている。また最近では CAD/CAM システムによる削り出しの手法にも変わりつつあり、さらに保険適用により広く普及しつつある。

人工歯冠に求められる機能の一つとして、とくに国内では周囲の歯との色調を合わせる審美性が挙げられる。これに関して現状では材料の配合や盛り付け方等、歯科技工士の技量に頼る部分が多く再現が難しい。一方で、CAD/CAM システムではあらかじめカラーグラデーションが施された削り出しディスク/ブロック材料を使用することで対応しているが、あくまで数種類のバリエーションによるレディメイドでの対応となるため、患者一人一人に合わせたオーダーメイドとは言えない。さらに、除去加工により加工後の色調までを制御することは極

めて困難であり、この点についても課題が残されている。

以上の課題を解決する方策として、本研究ではセラミックス 3D 造形技術による人工歯冠の作製に着目した。すなわち所望の審美性を満たす手法として、積層造形の特徴を活かし層ごとに材料の色調を自由に選択することでカラーグラデーションをオーダーメイドで作製可能ではないかと考えた。具体的には人工歯冠材料として最も広く使用されているジルコニアを素材とし、カラーグラデーション実現を目指した。その第一段階として、本法では白色のジルコニア粉末と黄色に着色されたジルコニア粉末を用いてセラミックス 3D 造形を行い、その際の色調の変化および造形挙動について検討を行った。

2. セラミックス 3D 積層造形技術

セラミックスの 3D 造形技術は大きく分類して①材料押出方式、②バインダージェット方式、③粉末焼結積層、④光造形法がある⁵⁾。その中でも高精度、高密度の複雑形状を造形するのに適しているのが光造形法であり、本研究ではその方式を採用した。

図 1 に光造形法による造形機構を示す。材料にはセラミックス粉末と光硬化性樹脂とを混合し、ペースト状にしたもの(以下、ペースト材料)を用いる。本手法ではまず、ペースト材料をタンクから定量切り出し、それをドクターブレード方式によって 1 層分の膜に成膜する。膜厚は材料によっても異なるが、およそ数十 μm である。得られた成膜面に対して UV レーザを照射することで造形個所を選択的に硬化させる。その後造形

* 1 新東工業株式会社 : 〒442-8505 愛知県豊川市穂ノ原 3-1 SINTOKOGIO, LTD.

* 2 東北大学 大学院工学研究科: 〒980-8579 仙台市青葉区荒巻字青葉 6-6 School of Engineering, Tohoku University

* 3 東北大学 大学院歯学研究科: 〒980-8575 仙台市青葉区星陵町 4-1 School of Dentistry, Tohoku University

テーブルが1層分降下し、再び材料の成膜、UV照射を繰り返すことで成形体を作製する。セラミックスの3D造形ではあくまでもセラミックス粉末を樹脂で固めた成形体の作製であり、その後、加熱炉にて脱脂(脱バインダー)及び焼成を行う必要がある。

従来のセラミックス光造形法では、主に炭化ケイ素やアルミナといった粉末が用いられており、それらを用いて3D造形用ペースト材料⁶⁾、3D成形体⁷⁾およびその焼成体⁸⁾⁹⁾の作製という観点で研究が進められている。また材料の複合化という観点では、複数のセラミックス粉末を混ぜ合わせた混合材料による造形が試みられている¹⁰⁾。その一方で、層ごとに異なる材料を積層し、造形体を作製するという事例はこれまでにない。本研究ではこの点に着眼し、歯科的に高い審美性を有するカラーグラデーション造形体の作製を目的として、層ごとに色調の異なる材料を用いた造形を試みた。

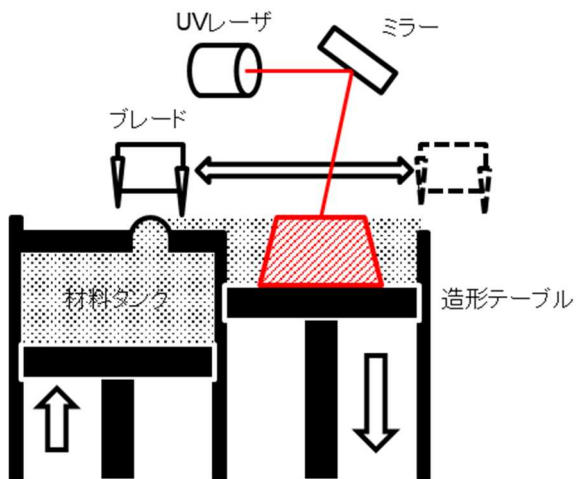


図1 セラミックス 3D プリンター (光造形法) の造形機構

3. 実験方法

3. 1. 供試材料

粉末には白色、黄色の2種類のジルコニアを用いた。白色粉末にはTZ-PX-245(東ソー製)を用い、黄色粉末にはTZ-PX-364(東ソー製)を用いた。各粉末に分散剤、光硬化性樹脂、光重合開始剤を適量配合し、自動乳鉢 AMN-1000 型(日陶科学株式会社製)にて混ぜ合わせ、3D造形用のペースト材料を作製した。本研究では表1に示すように2種類の粉末を用いて3種類の配合のものを作製した。なお、これら粉末と樹脂の配合比は①粉末:樹脂=30vol%:70vol%、②粉末:樹脂=50vol%:50vol%の2種類とした。

3. 2. 粘度測定

セラミックス粉末と樹脂の配合によって見掛けの粘度が変化する。そこで、配合したペースト材料の物性の一つとして粘度を測定した。粘度の測定はTVE-25形粘度計(東機産業製)

を用いた。ペースト材料は非ニュートン流体であり、チクソトロピー性を示すため見掛け粘度として測定を行った。見掛け粘度の測定はJIS R1665¹¹⁾セラミックススラリーの回転粘度計によるチクソトロピー性測定方法を参考とした。測定温度は23度に設定し、せん断速度は0.2, 2.0, 20.0, 200.0 s^{-1} とした。また、高せん断速度で10分間十分な速度を与え、その3分後に各せん断速度にて見掛け粘度を測定した。

3. 3. 成形方法

3D成形装置にはCeramaker100(3D CERAM-SINTO製)を用いた。レーザーの出力は300mWとし、積層厚さは25 μm とした。各色のTP(テストピース)は $\square 10mm \times$ 厚さ2mmの板状とした。また本研究では3種類の材料を用いた3層構造のTPも準備した。このTPは $\square 20mm \times$ 厚さ3mmの板状であり、1mm毎に材料の種類を変えて成形を行った。なお、全ての成形体は成形後に未硬化のペースト材料に覆われている。そのため、有機系溶剤等を用いて洗浄し硬化した成形体のみを取り出した。

3. 4. 脱脂・焼成

脱脂炉には熱風循環式常圧脱脂炉 DC-6060-SP(モトヤマ製)を使用した。温度500 $^{\circ}C$ 、保持時間3hの条件で脱脂を行った。炉内雰囲気は①大気、②窒素雰囲気の2条件とした。焼成炉には高速昇温電気炉 NE-3035F-SP(モトヤマ製)を使用し、温度1435 $^{\circ}C$ 、保持時間2h、の条件で焼成を行った。

3. 5. 熱分析

脱脂工程の分析には熱分析(TG-DTA)を行った。分析装置はTherm Plus2(リガク製)を用いた。昇温速度は20 $^{\circ}C/min$ とした。各TP作製時に $\square 2mm \times$ 厚さ1mmのサイズのサンプルを一緒に成形し熱分析用試料として用いた。

3. 6. 単層膜厚測定

各ペースト材料の3D造形時の硬化度合いを比較するため、単層膜を作製し、その膜厚の計測を行った。単層膜は造形テーブルに十分な高さ(約1mm)のペースト層を準備し、 $\square 10mm$ のサイズにUV光を1層分照射させることで作製した。作製した単層膜を膜厚計にて3か所測定しその平均値を膜厚とした。

配合	ジルコニア粉末	
	TZ-PX-245 (白色) wt%	TZ-PX-364 (黄色) wt%
白色 TP	100	0
中間色 TP	50	50
黄色 TP	0	100

表1 供試粉末の配合比

4. 実験結果および考察

4.1. ジルコニア TP 作製における粉末配合率の影響

前述の通り、セラミックス粉末と樹脂の配合によって見掛けの粘度が変化するが、光造形法ではこのときの粘度が造形条件として重要な要素となる。とくに同手法ではドクターブレード方式により数十 μm の膜厚を成膜するため、可能な限り低粘性であることが好ましい。そこで本研究ではまず、粉末と樹脂の配合率と見掛け粘度の関係について評価を行った。その結果を図2に示す。同図より、粉末濃度が高くなるほど見掛け粘度も高くなる傾向が確認された。また、各配合比の材料を用いて3D造形を行った。その結果、粉末濃度が50vol%を超えると、ペーストの状態を保てなくなり、造形が不可となった。

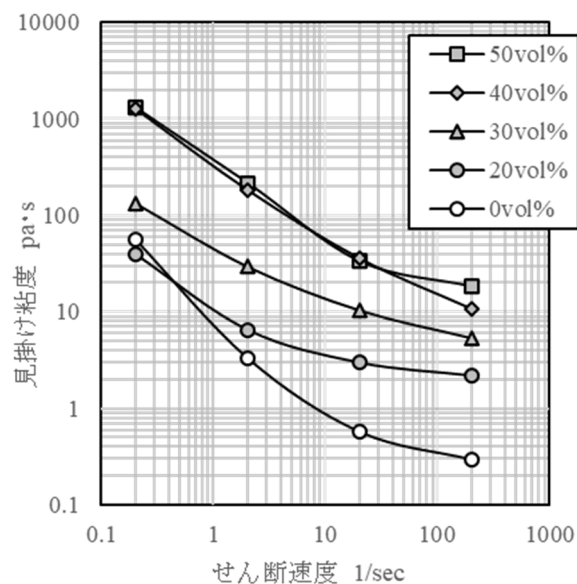


図2 粉末濃度と見掛け粘度の関係

次に、粉末濃度 30vol%と 50vol%で配合したペースト材料を使用して3D造形を行った。図3にその成形体、脱脂体および焼成体を示す。粉末濃度 50vol%で作製したTPは脱脂後に一部の変形が確認されたが破損までには至らず、焼成まで行うことができた。それに対して粉末濃度 30vol%で作製したTPは、脱脂時に著しい変形が生じ、破損にまで至ったため焼成が行えなかった。これは、脱脂工程で材料に含まれる樹脂分が加熱され、多量のガスが発生したためであると考えられる。つまり脱脂時に内部で発生したガスが外部へ放出される際に成形体の変形を引き起こしていると考えられる。そのため、粉末濃度が低く樹脂分が多い、粉末濃度 30vol%のTPにおいて、変形、破損が生じたものと考えられる。そのため次節以降は粉末濃度 50vol%を材料配合の基準として採用し、実験を行った。

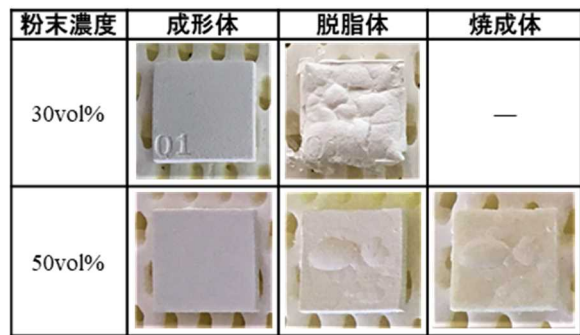


図3 白色粉末を用いた成形体および脱脂体、焼成体

4.2. 造形体のカラーグラデーション化

着色されたジルコニアTPを作製するにあたり、本研究ではまず、白色粉末のみを使用して造形したTP(白色TP)、黄色粉末のみを使用して造形したTP(黄色TP)およびそれらを50wt%ずつ配合した粉末を使用して造形したTP(中間色TP)を造形した。3種類の成形体、脱脂体および焼成体を図4に示す。同図に示した通り、どのTPも脱脂時に変形が生じた。また、黄色粉末が含まれる黄色TPおよび中間色TPでは、脱脂によって赤く変色することが確認された。この赤い変色はTPの表面だけに現れており、内部では変色が認められなかった。このことから、黄色粉末が含まれるTPの変色は、黄色粉末に含まれる微量の酸化鉄成分による影響であると考えられる。ただし、これらの変色は焼成後には確認されないため、上述の脱脂時における変色は焼成体の色調には影響を及ぼさないと考える。以上のことから、粉末の配合率を変化させ、色調を変えたペースト材料を用いることによって、その色調に応じた色味を有する造形体を作製可能になることが明らかとなった。

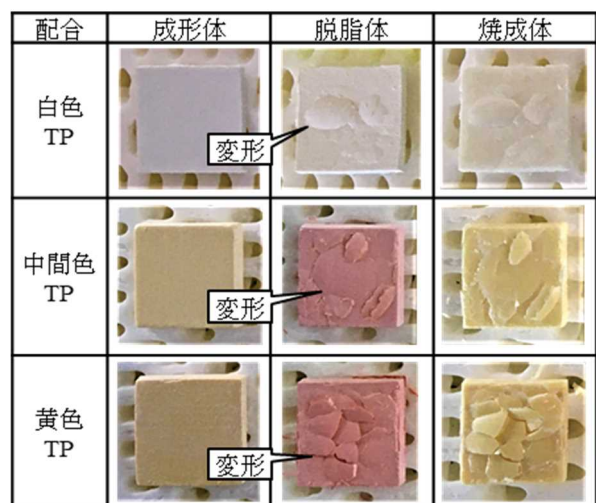


図4 各配合で作製した成形体、脱脂体および焼成体

次に作製した3種類の材料を用いて3層構造のカラーグラデーションを有する造形体の作製を試みた。なお、最下層から黄色、中間色、白色の順で3層構造とした。図5にそれらの成形体、脱脂体および焼成体を示す。同図より、図4と同様、脱脂時に変形が生じ、焼成体にその変形が残留しているものの破損までには至らなかった。また、焼成体の最上面は白色、最下面は黄色を示しているが、側面から見ると下方から上方に黄色味が減少している様子が確認できた。このことは、色調の異なる粉末の配合比を変化させた材料を適切に供給することにより、造形体のカラーグラデーション化が図れることを示すものである。

ただし、焼成体の側面では黄色層と中間色層の層間に割れが生じていた。この層間の割れは完全な剥離には至っていないが、目視できるほどの大きさであった。その一方で、中間色層と白色層の層間には上記のような割れは確認されず、色調の境界線も認められなかった。この点については4.4節で検討、考察を行う。

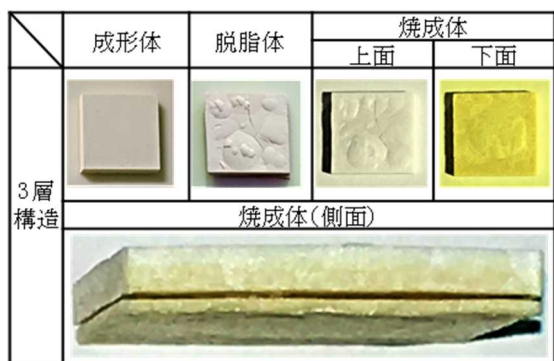


図5 3層構造 TP の成形体、脱脂体および焼成体

4. 3. 成形体の変形に及ぼす脱脂雰囲気の影響

前節までの TP の造形において、脱脂工程での変形が課題となった。これは脱脂時に生じる樹脂の燃焼反応および発生するガスに起因するものであると考えた。そこで、これまでの大気雰囲気での脱脂から、窒素雰囲気に変えることで酸素の供給を抑え燃焼反応を抑制することで脱脂時の変形を抑制することを試みた。

まず、4.2節で使用した3層構造を有するTPに対して窒素雰囲気での脱脂および焼成を行った。図6に窒素雰囲気での脱脂したTPの成形体、脱脂体および焼成体を示す。なお、窒素雰囲気での脱脂後には樹脂由来の炭素が表面に残存しており、焼成前に脱炭処理を行った。同図より、焼成体の上面および下面には目立った変形は確認されなかった。

次に、大気雰囲気と窒素雰囲気における脱脂時の燃焼反応について調べるため、各雰囲気での発熱量を測定した。その結果を図7に示す。同図より、大気雰囲気では400℃付近

に大きな発熱量のピークがあり、燃焼反応が起きていることが確認された。また図8に熱分析時の雰囲気温度の変化を測定した結果を示す。昇温速度 20℃/min で制御されているにもかかわらず、大気雰囲気では400℃付近に昇温速度の上昇が確認された。これらの結果から、大気雰囲気では燃焼反応により大きな発熱反応が生じていることが明らかとなった。

以上の結果から、脱脂時における成形体の変形は樹脂の燃焼反応に伴うガスの発生によるものであるといえ、窒素雰囲気での脱脂を行うことで上記の反応を抑制でき、変形の問題を解決可能であることが明らかとなった。

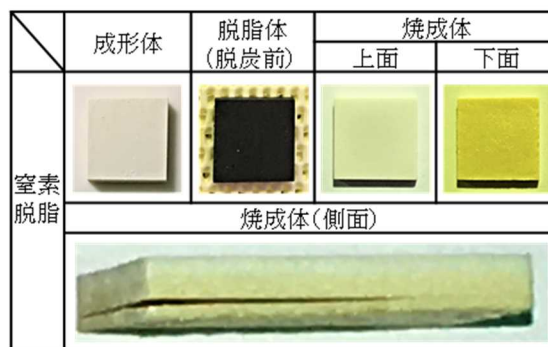


図6 窒素雰囲気での脱脂した3層構造 TP

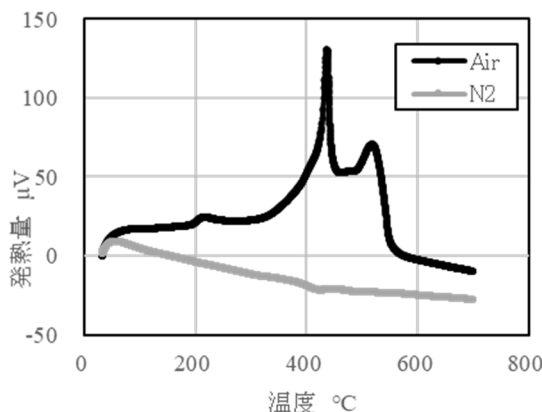


図7 各雰囲気での熱分析結果(発熱量)

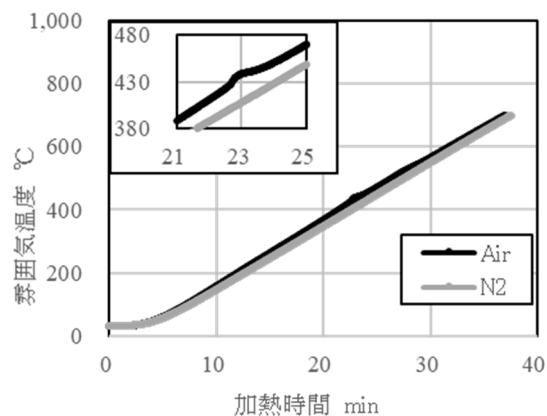


図8 各雰囲気での熱分析結果(雰囲気温度)

4. 4. 造形体の層間割れに及ぼす粉末配合率の影響

前節において、脱脂時の雰囲気を変更することにより成形体の変形抑制が可能となった。ただしその一方で、焼成体には大気雰囲気中での脱脂時と同様、1層目(黄色層)と2層目(中間色層)の層間に割れが生じた。これは脱脂条件だけでなく成形時点で何らかのひずみが発生したためであると考えられる。とくに、3層構造TPの層間の割れは黄色TPと中間色TPの層間にのみ生じていたことから、色調(粉末配合率)の違いが何らかの影響を及ぼしていると考えた。

そこでまず、各ペースト材料に対してUV光を照射した際の硬化の度合いを比較した。具体的にはUV硬化させた単層膜を作製し、その膜厚の比較を行った。その結果を図9に示す。同図より、膜厚は白色60.0 μm 、中間色54.3 μm 、黄色48.0 μm であり、配合する粉末の色調によってUV硬化の度合いが変化した。これは、各ペースト材料に含まれる樹脂配合率に違いがないことを踏まえると、各粉末の持つ色調によってUV光に対する光学特性(吸光率)が異なることに起因するものであると考えられる。すなわち、色調の異なるペースト材料では硬化に寄与する樹脂量の割合が異なり、その結果として成形体1層当たりの膜厚が変化したと考えられる。

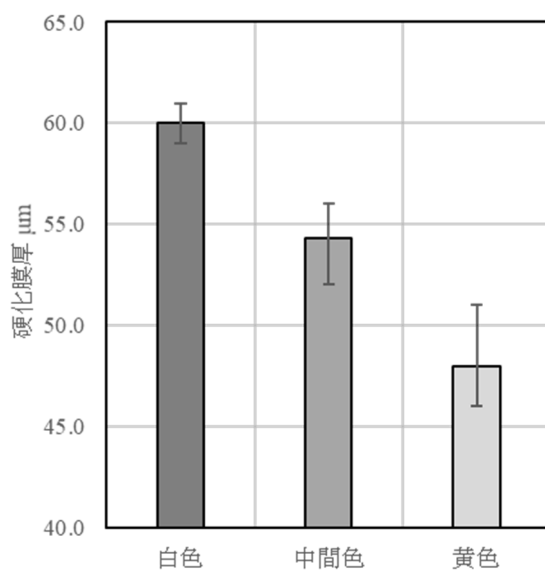


図9 各材料の単層膜厚測定の結果

次に各成形体の熱分析を行った。その結果を図10に示す。同図より、各成形体はいずれも前節で発熱が生じた400 $^{\circ}\text{C}$ 付近で重量が減量し、600 $^{\circ}\text{C}$ 付近で一定の値に収束するという挙動を示した。ただし各成形体で収束する値が異なり、白色、中間色、黄色の順に減量割合は大きく、それぞれ20.5wt%、18.9wt%、16.2wt%であった。この重量減量は造形体の収縮をもたらすものと考えられる。

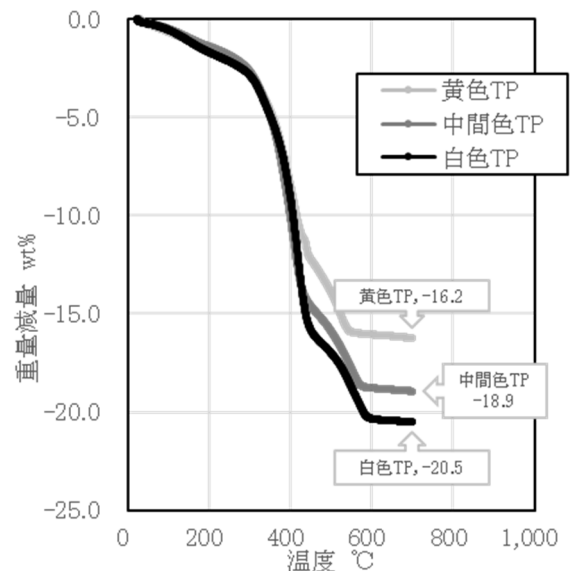


図10 各成形体の熱分析結果(重量減量)

図9, 10で得られた結果から3層構造造形体の層間で生じた割れの原因について考察する。まず図9より、色調の異なるペースト材料では硬化に寄与する樹脂の割合が変化することが明らかとなった。このことは色調の違いにより硬化後に残留する樹脂量に違いが生じることを示している。

次に図10から各TPの重量減量が変わることが明らかとなった。この重量減量割合は白色TPの重量減量を1.0とすると中間色TPは0.9, 黄色TPは0.8に相当し、この割合は図9の膜厚の割合とも一致している。粉末のみの熱分析では重量減量が生じないこと、また焼成後には樹脂はほとんど残留していないことを考えると、図10で得られた重量減量分は、硬化後に成形体に残留している樹脂量に対応していると考えられる。

以上のことから、まず造形時の硬化に寄与する樹脂量が色調(粉末配合率)によって変化し、1層当たりの膜厚が変化すると言える。また、それによって成形後に残留する樹脂量も変化し、それに伴って脱脂時、焼成時のTPの収縮率が変化するということが言える。すなわち、色調の違いによる成形体1層当たりの膜厚と、脱脂時、焼成体の収縮の関係により造形体に発生するひずみ量が変わり、そのバランスによって割れが発生したものと考えられる。ただしこのひずみの発生機構については今後詳細に分析し改めて報告する予定である。

5. 結論

本研究では白色および黄色のジルコニア粉末およびその混合粉末を用いてセラミックス3D造形体を作製し、その際の色調の変化および造形挙動について検討、考察を行った。その結果、以下の知見が得られた。

1. 各色の粉末と樹脂の配合率を変えることで、造形体の色

調を制御可能であることを示した。またそれらを層状に重ねた造形体では層間での色調の境界は確認されなかった。このことから色調を更に多段階にわけることで自然なグラデーションを有する造形体を作製できる可能性が示唆された。

2. 大気雰囲気中で脱脂を行った場合、樹脂の燃焼反応に伴うガスの発生により、色調に関わらず成形体に変形することが明らかとなった。この点に対して、雰囲気を窒素雰囲気に変えることで発熱反応が抑制され、成形体の変形を制御可能であることを示した。

3. 色調(粉末配合率)の異なる造形体を層状に重ねた場合、その重ね方によっては層間で割れが生じることが明らかとなった。この割れは各造形体層における成形、脱脂、焼成時に生じる変形に起因することを示し、そのバランスを考慮することで割れのない多層造形体を作製できる可能性を示した。

6. 参考文献

- 1) 萩原 恒夫, 3D プリント材料の最新動向と今後の展望, 日本画像学会誌, 54, 4(2015)293.
- 2) 萩原 恒夫, 光造形によるセラミックスの高精細三次元積層造形の最新動向, OPTRONICS, 5(2016)1.
- 3) 桐原 聡秀, 光造形 3D プリントを用いた機能性構造体のスマート創製, スマートプロセス学会誌, 3, 3(2014)182.
- 4) 桐原 聡秀, 光造形アディティブ・マニュファクチャリングによるバイオセラミックス製インプラントの作製, まてりあ, 57, 4(2018)155.
- 5) セラミックス 3D 積層造形技術の現状と今後の市場性の検討(2020年版), 株式会社素材産業研究所.
- 6) 尾畑 成造, 紫外線硬化樹脂を用いた濃厚炭化ケイ素スラリーの作製, 粉体工学会誌, 54(2017)576.
- 7) 清水 那弥, スマートプロセス学会誌, 9, 4(2020)185.
- 8) 立石賢司, 紫外線硬化樹脂を用いたセラミックス固化技術の開発(第4報), 岐阜県セラミックス研究所研究報告(2019)7.
- 9) 横田 耕三, DLP式光造形法によるアルミナ三次元積層造形緻密体の作製, 粉体工学会誌, 53(2016)492.
- 10) 横田 耕三, DLP式光造形法による三次元積層造形 Al_2O_3 - ZrO_2 - TiO_2 セラミックスの作製, 粉体工学会誌, 56(2019)261.
- 11) JIS R1665 セラミックススラリーの回転粘度計によるチクソトロピー性測定方法

アモルファス金属の加工技術開発

^a公益財団法人いわて産業振興センター

久慈 千栄子^a

目的

アモルファス金属は、結晶構造を有する金属とは異なり、ガラスのような非晶質構造を保って固化した金属である。その特殊な構造に起因して、高強度、高軟磁性、高耐食性等の優れた特性を発現し、特に軟磁性材料としての応用が期待されている。一方で、機械的強度の高さから加工抵抗が非常に高く、工具摩耗が激しい等といった難加工性を示す材料である。申請者は、アモルファス金属の諸特性がその構造に起因することに着目し、熱処理を援用した新たな加工手法の開発を試みている。加熱によりアモルファス金属は核生成・成長機構により結晶を析出することが知られているが、その析出形態は組成比に依存して異なる挙動を示す。そこで本課題では、最適熱処理条件の選定に向け、Fe系アモルファス金属に対して一様な熱処理を行い、その結晶化挙動を明らかにすることを目的とした。

成果

試料には、日立金属製のFe基アモルファス薄帯Metglas 2605S-3A ($\text{Fe}_{77}\text{B}_{16}\text{Cr}_2\text{Si}_5$) を用いた。還元雰囲気下 ($0.998\%\text{H}_2\text{-Ar}$) において、昇温速度 $20^\circ\text{C}/\text{min}$ で室温からそれぞれ任意の温度まで昇温した。熱処理した試料は、集束イオンビーム加工観察装置 (FIB) を用いて薄膜化し、透過型電子顕微鏡 (TEM) を用いて内部構造の観察を行った (図1)。

TEM観察結果を図2に示す。非加熱の試料からは、アモルファス構造特有のグレーの観察像が得られた (図2(a))。最高加熱温度 753K の試料では (図2(b))、試料内部は非加熱試料と同様のグレーパターンが得られたのに対し、試料表層には約数十ナノメートル厚の結晶相が析出した。回折像から、この表層に析出した結晶相は $\alpha\text{-Fe}$ であることが判明した。最高加熱温度 773K の試料では (図2(c))、表層の結晶相に加え、試料内部ではアモルファス相に約 100nm 程度の結晶粒が分散して析出した。さらに加熱温度を上昇させ、最高加熱温度 873K の場合では (図2(d))、試料内部に分散した結晶が結晶粒同士が隣接するほどに成長することが分かった。

本課題では、熱処理温度に対応した結晶の析出形態を調査した。今後は、様々な構造に対する加工性の評価を行う事により、加工性能を向上させる最適な熱処理条件を導くことが出来るものと期待される。



図1 透過型電子顕微鏡 (TEM/JEOL JEM-2000EXII)

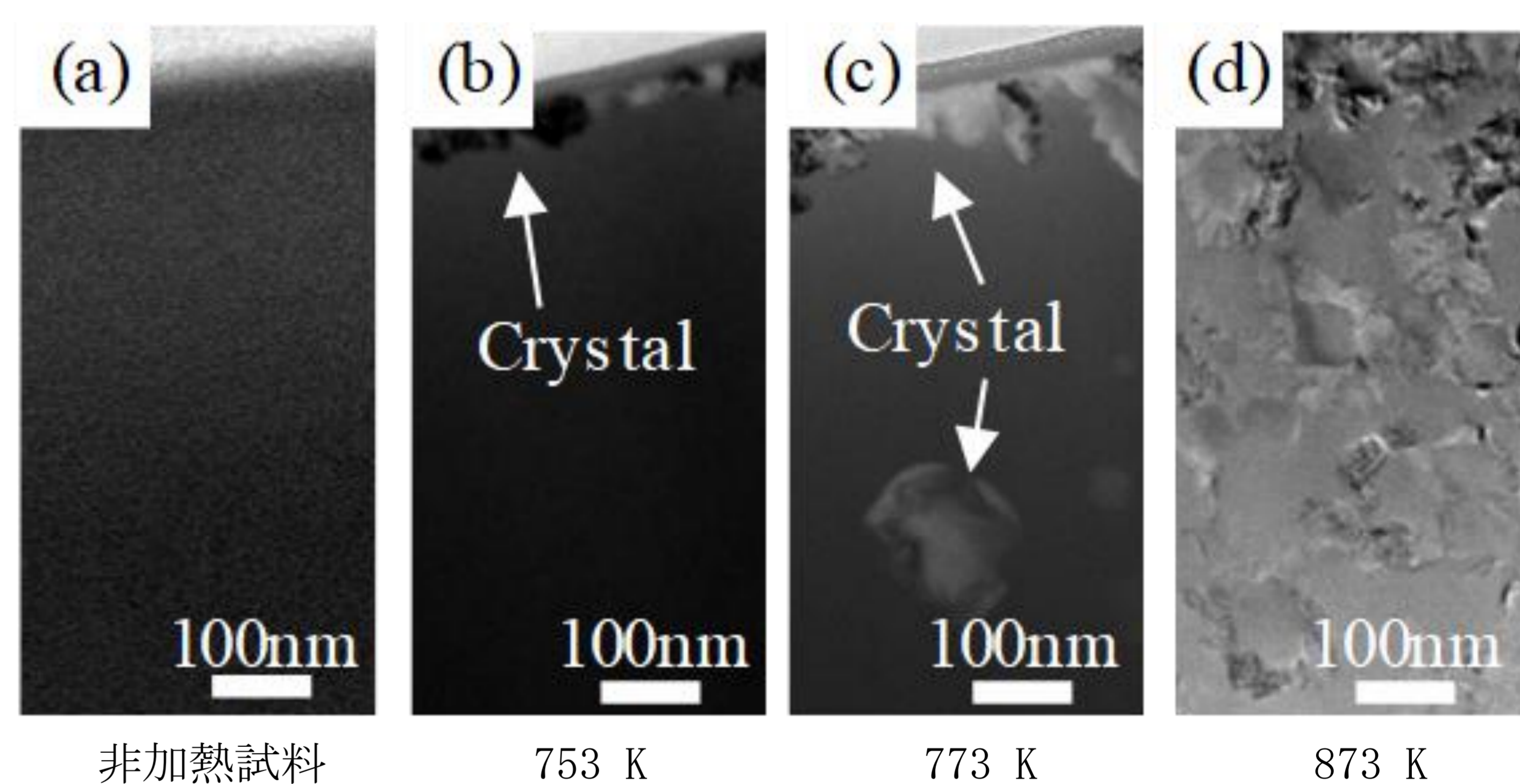


図2 TEM観察結果

実施機関からのコメント

本課題において利用者は工業的利用を念頭においたFe-Si-B系アモルファス金属の結晶化挙動の解明を必要としており、精密な熱処理と構造解析が必須であった。DSC, XRD, FIB/TEM/STEM を用いた支援に基づいた議論を進める中で、この材料が呈する機械的性質が微細構造の影響を強く受けていることが判明し、最適な加工法につながる熱処理条件を材料科学的な観点から導出することができた。応用上の重要性だけでなく、一連の結果は学術誌でも公表されることが決定し、「産業は学問の道場なり」を体現できた。(支援実施者：竹中佳生、今野豊彦)

放電加工時のデブリ発生とジャンプパラメータが加工効率に及ぼす影響

○湯田健太郎*1, 黒川聡昭*2, 齊藤大揮*2, 水谷正義*1, 厨川常元*1

Debris generation during electrical discharge machining and the Effect of Jump Parameters on Machining Efficiency

Kentaro YUDA, Toshiaki KUROKAWA, Daiki SAITO, Masayoshi MIZUTANI and Tsunemoto KURIYAGAWA

In die-sinking EDM, it is important to remove machining debris from the discharging gap for machining stability and efficiency. In the jump flushing method, which is the main method of removing debris, it is necessary to consider appropriate jump parameters in order to achieve both machining efficiency and flushing effect. However, it is still difficult to select the optimum jump parameters without some experiments because it is difficult to observe the gap space and the discharge phenomenon is not yet fully understood. Therefore, in this study, as a means of clarifying the discharge phenomenon, we analyzed the debris generated from multiple discharge conditions. In addition, the optimal jump parameters under specific conditions and the effect of each parameter on machining efficiency were investigated by conducting actual machining experiments.

1 緒言

形彫放電加工において、デブリの滞留は加工速度の低下や異常放電の原因となる。そのため、デブリの高効率な排出は放電の安定性維持、あるいは加工の高効率化にとって重要な役割を果たす¹⁾。ジャンプフラッシング (JF) 法は電極を周期的に上下に往復運動させるもので、ギャップ間のデブリを排出する手法であり¹⁾、放電加工におけるデブリの排出に最も一般的に用いられている。JF法はこれまでに様々な研究¹⁾²⁾がなされてきたが、デブリの挙動を解析的に解明し、加工条件に適したジャンプパラメータを導出する手法の確立には至っていない。本研究は、JF法におけるデブリ排出挙動をモデル化し、解析的に表現することを目的としている。本報はその第一段階であり、種々の条件下でジャンプフラッシングを行った際の加工効率の変化を実験的に評価し、その関係性について検討・考察を行った。

2 実験装置と実験条件

本実験では電極に 5×5×27 mm の銅電極、工作物に 10×10×30 mm の SUS420J2 系ステンレス合金を用いた。加工は形彫放電加工機を使用し、表 1 に示す条件 1 から 3 の放電条件で Z 軸単軸方向の止まり穴加工を行った。本研究では、ジャンプ速度 (JS)、ジャンプアップ量 (JU)、ジャンプダウン時間の (JD) の 3 つのジャンプパラメータを扱う。3 つのパラメータと加工の概要を図 1 に示す。異常放電発生による電極位置の制御はなく、ジャンプおよび放電は周期的に行う。また、デブリの分析では、乾燥させたデブリを粒度分布計、走査型電子顕微鏡 (SEM) を用いて分析を行った。

3 デブリの粒度分布測定

条件 1 から 3 のそれぞれのデブリについてその粒度分布を測定した結果を図 2 に示す。同図から、いずれの条件においても 30 ~ 50 μm 程度の粒子の存在割合が最も高く、条件 1 では 200 μm 程度の粒子群、条件 2 では 10 μm 程度の粒子群も存在していることが確認できる。また、放電エネルギーの大き

表 1 放電条件

条件	ピーク電流 [A]	サーボ電圧 [V]	パルス幅 [μs]	休止時間 [μs]
1	13	41	128	128
2	5	55	24	16.0
3	1.5	100	6.4	30.4

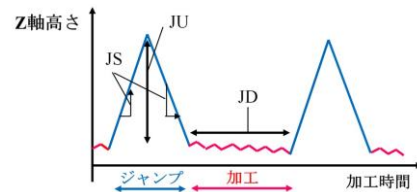


図 1 ジャンプパラメータと加工の概要

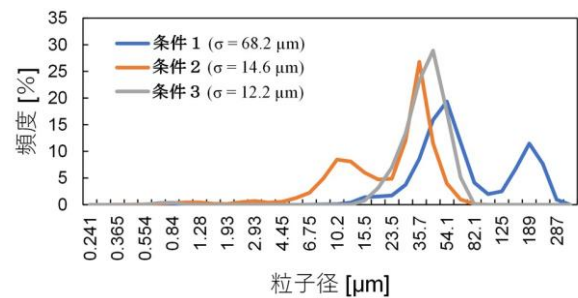


図 2 デブリの粒度分布

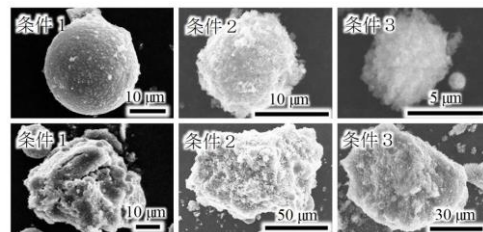


図 3 デブリの SEM 画像

い条件 1 では粒度が高く、ばらつきも大きいことがわかる。これは放電エネルギーが大きくなるほど、溶解部の体積が大き

*1 東北大学大学院工学研究科機械機能創成専攻

*2 三菱電機株式会社 先端技術総合研究所

くなり、飛散するデブリの粒径が大きくなるためであると考
えられる。図 3 は排出されたデブリを SEM により観察した
画像である。デブリには、同図上段のように粒径が数 μm ~ 30
 μm と比較的小さく円形度が高い粒子と、下段のように粒径
が比較的大きく複雑な形状の 2 種類が存在していることが確
認できた。

4 放電加工実験による最適ジャンプパラメータの選定

表 1 の条件 1 を用いて、加工深さを 5 mm と固定し、3 つ
のジャンプパラメータを変化させ、各パラメータが加工速度
に及ぼす影響を検討し、最適パラメータを実験的に求めた。

4.1 電極の消耗が加工時間に与える影響

図 4 は同一ジャンプパラメータ、同一電極で繰り返し加工し
たときの加工時間の変化を示したグラフである。4 回目まで
は加工を重ねるにつれ加工時間が減少するが、5 回目以降は
加工回数の影響を受けないことがわかる。図 5 は上記実験に
て、各回測定後の電極の様子をデジタルマイクロSCOPE で
観察したもので、図中右上のエッジ部分の消耗具合に注目
する。その結果、電極の消耗度は 3 回目の加工終了時まで
は徐々に大きくなっていくが、4 回目終了時以降はほとんど
変化がないことがわかる。図 4 と図 5 の結果より加工時間の減
少は電極の形状に起因しており、これは、電極角部が消耗す
ることで、加工穴の角部に溜まったデブリの存在による集中
放電が起きにくくなるからであると考えられる³⁾。本結果より、
以降の試験では 4 回以上加工を行った電極を使用する。

4.2 ジャンプパラメータが加工時間に与える影響

各ジャンプパラメータを変化させたときの加工時間の測定
結果を図 6 (a) ~ (c) に示す。また、このとき、形彫放電加工機
で測定した異常放電が発生したことを示す不良パルスの発
生率を図 7 (a) ~ (c) に示す。不良パルス率が高いほど、デブリ
による影響が大きいとされる。図 6 (a) の通り、JS が 5 m/min
の際に加工時間は最短となった。図 7 (a) より、この範囲でデ
ブリ排出効果に明確な優劣が存在しないため、JS が大きいも
のほど加工効率が良くなったと考えられる。また、図 6 (b)
より、JU が 0.6 mm の時に加工時間は最短となった。これは
図 7 (b) のように小さい JU ではデブリの影響を受けやすい一
方で、大きい JU では加工が進行しない時間（非加工時間）
が長くなり加工効率の低下を招くことが要因と考えられる。
また、図 5 (c) および図 6 (c) より、JD が 0.25 ms で加工時間
が最短となったが、これは JD が大きくなるほどデブリの影
響を受けやすくなり、逆に JD が小さすぎても非加工時間が長
くなってしまふからであると考えられる。

5 結 言

本研究では、初めにデブリの分析を行った。また、最適ジ
ャンプパラメータを実験的に求めるとともに、各パラメータ
が加工時間に与える影響について検討した。以下に得られた知
見をまとめる。

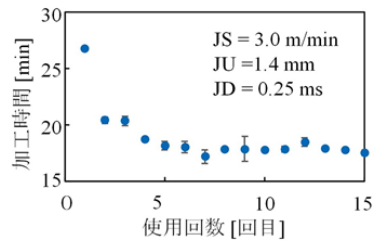


図 4 電極の使用回数と加工時間

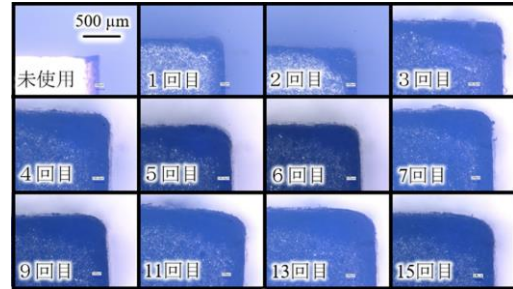


図 5 電極の使用回数と消耗度

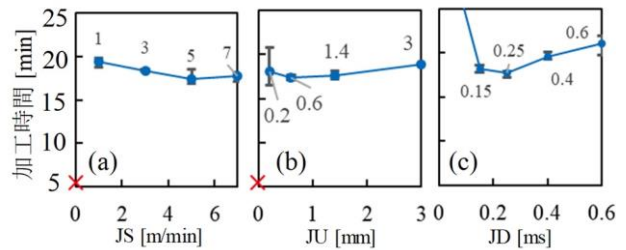


図 6 各ジャンプパラメータの加工時間

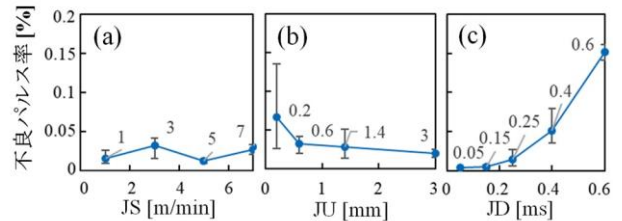


図 7 各ジャンプパラメータの不良パルス率

- (1) いずれの条件についても 30 ~ 50 μm 程度の粒子の存在割合が最も高く、放電エネルギーが大きい条件では粒度が高く、ばらつきも大きくなることが確認できた。
- (2) 条件 1, 加工深さ 5 mm の場合、各パラメータについてそれぞれ JS = 5 m/min, JU = 0.6 mm, JD = 0.25 ms のとき加工効率が最大となることがわかった。
- (3) JU が小さい場合、実際に加工が進行したことを示す有効加工時間が長くなるがデブリによる影響が大きくなる。一方、JU が大きい場合は、デブリ排出効果が大きくなるが非加工時間が長くなる。
- (4) JD が小さい場合、デブリによる影響が小さくなるが加工効率が低下する。一方、JD が大きい場合は、有効加工時間が長くなるが加工層による影響は大きくなる。

参考文献

- 1) 土屋 政光ほか: ジャンプフラッシング放電加工に関する研究 (第 1 報) -, 精密工学会誌, Vol. 56, No. 5, (1990)

- 2) 増沢 隆久ほか:放電加工におけるに加工屑処理の研究-, 精密工学会誌, Vol. 51, No. 7, (1985)
- 3) 中島 宣洋, わかる放電加工の実際, オーム社, (2019)

Creation of Functional Three-Dimensional Structure with Metal Additive Manufacturing Technology

Shinji Ishibashi

Abstract

While most industrial products made by humans are made of dense materials, most structures made by nature are porous materials. Porous structures have characteristics such as light weight, heat insulation, sound absorption, and energy absorption, and these effects vary depending on the shape and size of the pores. Metals with this porous structure are called porous metals, and are expected to be used in various industries, including the automotive industry for weight reduction, noise reduction, and safety; the electronics industry for cooling performance and miniaturization; and the medical industry for biocompatibility. One of the functionalities of porous materials is the graded function. Since interfaces between dissimilar materials whose composition and structure change continuously can alleviate the stress concentration that occurs at intermittent interfaces, gradient functional materials are being developed for aircraft, cutting tools, biomaterials, and other applications. This study focuses on the creation of gradient structures by porous materialization, because the realization of gradient functions in porous structures leads to the creation of materials that express both functionalities. An example of the application of the graded porous structure to an implant was shown. The method to realize the graded porous structure requires a wide range of porosity controllability, flexibility in forming complex shapes, and processing of difficult-to-process biometals. These conditions, which are difficult to realize in conventional porous metal fabrication methods, inspired this dissertation to develop a new method using selective laser melting (SLM). Rhizoid porous structure (RPS) refers to the porous structure accidentally formed inside the SLM objects, and the RPS appearing on the cross section of the SLM object suggested that the laser conditions were able to control the pore properties of RPS. Therefore, the purpose of this dissertation is to control the pore properties of RPS using SLM for the realization of the functional graded structure. The material is Ti-6Al-4V powder and X-ray CT was used to evaluate the pore properties. Additionally, tensile and fatigue tests were conducted to investigate the mechanical functionality of the SLM objects with RPS. This dissertation is consisted of the following six chapters.

Chapter 1 describes the flow from porous structure to the requirement of RPS control and clarifies the purpose of this dissertation.

Chapter 2 evaluates the effects of energy density, sintered area, and laser time interval on the porosity of 7^3 mm³-cubic SLM objects. Energy density refers to the laser energy input into the metal powder bed per unit volume, sintered area refers to the area sintered by the laser in a layer, and time interval refers to the time required for the laser to sinter from a point on one pass to a point on an adjacent pass. The decrease in energy density and increase in sintered area caused the increase in porosity, while the time interval had little effect on porosity. The three-dimensional (3D) visualization of the pores inside the SLM model showed that the decrease in energy density caused the cell structure to change from a closed cell structure to an open cell structure as the porosity increased. The scan speed and hatch spacing are elements of the energy density and the effect of scan speed on the porosity was larger than that of hatch spacing. The insufficient sintering due to the low energy density and the created pores

suggested that the shrinkage of the melt pool caused the porosity increase at high scan speed. The images of spatter scattering and adhesion during sintering suggested that the degradation of the properties of the powder bed and sintered surface led to the increase of porosity in the high sintered area. By using a laser scanning speed that linearly changes the porosity, graded porous structures were successfully created in SLM objects.

Chapter 3 evaluates the effects of scan speed, sintered area, and time interval on pore morphology (inclusion angle, flattening, formed distribution, and spatial frequency) to control the pore shape. The integrated results of the four pore morphologies analogize the 3D morphology of the porous structure produced by each shaping parameter. The scan speed and sintered area having a significant effect on the porosity also showed characteristic results for the pore morphology. While the porous structure created by high scan speed showed orientation and distribution perpendicular to the building direction and the periodicity related to layer thickness and hatch spacing, the porous structure created by the high sintered area showed an orientation and distribution parallel to the stacking direction and the periodicity related to hatch spacing. The difference of about 90° in the pore orientation between the high scan speed and high sintered area porous structures implied that the shape of the melt pool took the form of teardrops or keyholes, depending on the temperature state of the object during sintering. The pores of the high scan speed specimens were oriented perpendicular to the building direction because the pores formed preferentially around the teardrop-shaped melt pools that shrank with increasing scan speed. The increase in the sintered area would have increased the heat input to the object more than the heat escaping to the powder bed, thus increasing the temperature of the object. The increased temperature caused the melt pool to penetrate deeper into the object, and a pore was created at the tip of the keyhole-shaped melt pool. The increased object temperature caused the melt pool to penetrate deeper into the object and a pore was created at the tip of the keyhole-shaped melt pool. In other words, the pores of the porous structure are oriented perpendicular to the building direction when the melt pool is teardrop shaped, and those of the porous structure are oriented parallel to the building direction when the melt pool is keyhole shaped. The time interval did not affect the pore morphology as well as the porosity.

Chapter 4 prepares tensile test specimens with RPS and evaluates the tensile properties of RPS. The tensile strength decreased with increasing scanning speed, and the specimen with scanning speed of 150 mm/s showed tensile strength exceeding that of conventionally annealed material. The RPS tensile specimens fractured brittle in a zigzag pattern, but the fracture surface showed equiaxial dimples caused by ductile fracture with necking. The microstructure of the SLM objects did not change significantly over a wide range of energy densities and was dominated by acicular α -phase grains. The tensile strength of RPS tensile specimens with high porosity was lower than that of conventional heat-treated specimens, even when the effective cross-sectional area calculated from the porosity was considered. This suggests that the decrease in strength of the high porosity RPS tensile specimens is not only due to the decrease in effective cross-sectional area but also because of pore shape. The local area between the pores with stress concentration at the corners becomes similar to the fracture with necking and then the fracture progression should cause the connection of the pores and the formation of equiaxial dimples on the fracture surface.

Chapter 5 evaluates the effects of building direction, energy density, and laser path direction on fatigue life. The fatigue life of the rectangular SLM model was maximized by layering with high energy density in the height direction and the direction of the laser path was parallel to the short side. The fatigue life of the longitudinally layered fatigue specimens with the weakest orientation and distribution against bending stress was affected by their pore morphology more than by their porosity. The pores of the specimens layered in the height direction were

strong morphologies against bending stress. The fatigue life of the high energy density specimen did not reach the fatigue limit due to the lower limit of porosity. To break through the lower limit of the porosity, the laser path was fixed in the direction parallel to the short side. The fixed short laser path stabilizes the shape of melt pool, achieved a porosity of less than 1%, and reached the fatigue limit at a stress amplitude of 100 MPa.

Chapter 6 describes the conclusion of this dissertation and engineering and industrial significance.

Study of Processing Mechanism in Dental Powder Jet Deposition

Akihiko TOMIE

Abstract

In the current dental treatment, various dental materials are used for restorative treatment and prosthetic treatment. Dental materials must have sufficient mechanical strength to replace lost oral functions, while also being biocompatible to be functional in the body for a long time. In addition, aesthetic characteristics of the treated tooth are also required since it is an exposed tissue. However, no ideal dental material exists satisfying all those characteristics at the present time, and the conventional materials are applied to the treatments with the risk of secondary caries. Therefore, the author has proposed a new dental treatment method by utilizing hydroxyapatite (HA), which is the main element of the teeth enamel. By applying this material, a treatment could be realized with long-term stability and aesthetics in an oral cavity due to its high biocompatibility. In the proposed method, powder jet deposition (PJD) is utilized to form a HA film on a tooth surface. PJD is a process in which fine particle of several micrometers are injected onto a target object at high speed to adhere the particle material, and it can be applied in atmospheric pressure at room temperature. The objective of this study is to summarize the HA film formation technique for dental treatment. The first phase of the study was to clarify the stable deposition conditions under which HA films could be formed without removing the existing healthy teeth. This study applied a computational fluid dynamics (CFD) method to clarify the motion trajectory of HA particle. HA particle size appropriate for dental treatment was determined by comparing the analysis results with those of the processing experiments. In addition, the human teeth possess a curved surface, indicating that the particle may impact obliquely. In this case, a shear force acts on the impacted object, however, the processing phenomenon has not been investigated in previous studies. Therefore, this study adopted the particle impact angle as a parameter of processing conditions. The second step of this study was the investigation of thickening and multifunctionalization of HA films. Focusing on the crystal structure of HA particle surface, the particle structure enabling effective thick film formation was discussed. Furthermore, the method of creating functional film by combining HA particle with functional material was also developed, and the guideline of particle design for PJD was established. As the final phase, PJD handpiece was designed for use by dentists in treatment, and prototype evaluation was conducted.

In Chapter 2, the relationship between the impact velocity of HA particle and processing characteristics was investigated. First, a computational fluid dynamics model was developed to determine the impact velocity of HA particle. An analytical model for a compressible fluid was developed using the finite volume method and compared with the results of particle image velocimetry (PIV) measurements. The analytical results for the free jet were in accurate agreement with the PIV measurements. Next, the collisional jet was analyzed to obtain the collision velocity of the particle. At the same time, processing experiments were carried out on human tooth enamel using five different sizes of HA particles. From the results of the analysis and processing experiments, the following experimental equation was obtained for the calculated transition velocity v_t for each particle size.

$$v_t = 398d^{0.324} \quad (4.4 \leq d \leq 9.5)$$

The transition velocity for the particle sizes below 3.1 μm is expected to be close to or even greater than the speed of sound. Since the particle velocity achievable with the PJD nozzle used in this study is less than the speed of sound at most, particle with a diameter of 3.1 μm or less can be regarded as stable deposition conditions that do not cause removal processing. Therefore, HA particle with a diameter of 3.1 μm or less will be used in subsequent

investigations.

In Chapter 3, the relationship between the impact angle of the HA particle and the processing characteristics was investigated. HA particle with a diameter of 2.44 μm were injected into the HA substrate at four different nozzle angles: 30 deg., 45 deg., 60 deg., and 90 deg. When the nozzle angle was 90 deg., PJD condition was observed in which the film layer was formed on the entire surface. As the nozzle angle became sharper, a removal area was generated, and for a nozzle angle of 30 deg. a removal area was generated on 79.2 % of the processed surface. The cross-section of the machined surface was observed by transmission electron microscopy, and it was found that the substrate surface was amorphized in all specimens. In the case of oblique particle impact, the substrate surface was deformed in the shear direction, and the depth of the deformation increased as the impact angle became sharper. Following this, the Smoothed particle hydrodynamics (SPH method) was used to analyze the stress state at the collision interface. In the analysis, the speed of HA particle was fixed at 300 m/s and the impact angle was the same as in the experiment. The results showed that the strain and temperature of the impact surface increased significantly as the impact angle became sharper. In particular, the interface temperature reached 767 K at the sharpest angle of impact, 30 deg. From the results, it was clarified that in case of the oblique particle impact, the cutting action due to the shear force became dominant and the processing phenomenon was transitioned to the removal process.

In Chapter 4, the relationship between the crystal structure of HA particle and their processing properties was investigated. Typically, HA particle are synthesized by a wet process and then milled and classified to a predetermined particle size. During the milling process, the crystalline structure of the particle surface is often damaged and the surface becomes amorphous. Hence, the author investigated the relationship between the crystal structure of the HA particle surface and the processing characteristics. Two types of HA particles with different crystalline structures were produced as specimens: the first, type A particle, contained a few tens of nanometers of amorphous layer on the surface, and the second, type B particle, was produced by heating type A particle to 230 $^{\circ}\text{C}$ for 12 hours to grow the amorphous layer into a crystal. The processing experiment was carried out by injecting two types of particles onto HA substrate under the same conditions. As a result, the film removal occurred during the deposition process only for type A particle, indicating the difficulty of forming a thick film. The decrease of particle diameter caused by the impact was almost the same for both type A and B particles, suggesting that the heating did not significantly change the mechanical properties of the particle, but changed the adhesion force at the collision interface. The cross-sectional area near the boundary between the deposition layer and the HA substrate was observed by transmission electron microscopy. It was observed that the highly crystalline layer of type B particle did not damage the HA substrate, but rather formed a dense layer of HA particle pulverized to the order of several nanometers to tens of nanometers. On the other hand, the layer deposited by type A particle had a polycrystalline structure, as did the layer deposited by type B particle. However, cracks of about 300 nm were observed in the layer. This suggests that the adhesion strength of the film layer of type A particle is not strong enough to withstand the stresses from the impacting particles and jet stream. This result indicates that the HA particle suitable for film formation requires a heating process to grow the surface crystals.

In Chapter 5, composite film of HA and zirconia was designed to add new dental functionalities to PJD films. The composite film was designed by mechanically mixing HA and zirconia particles beforehand, which were then utilized as injection particle for PJD. Two types of HA/zirconia composite particles with different mechanical energies particles were produced using a dry particle-composite apparatus: one was an ordered-mixture composite

particle (OM-typed particle) that was mixed by applying lower mechanical energy to the particle during processing at a stirring blade speed of 400 rpm and a processed particle volume of 12.5 mL. The other was mixed with higher mechanical energy (3000 rpm and 50 mL, respectively) to promote mechanofusion particle (MF-typed particle). The manufactured particles were analyzed by using TEM and EDS. The results showed that the zirconia particle of the MF-typed particle was combined with the HA particle, while the particle of the OM-typed particle was easily separated from each other due to its lower bonding strength. At the same time, it was also clarified that the crystal structure of the MF-typed particle was transformed due to strain induced by applying higher mechanical energy. Processing experiments using both types of particles showed that the MF-typed particle formed 96 % lower amount of film compared to that of the OM-typed particle. As shown in Chapter 4, the decrease in crystallinity of the particle is considered to affect the deposition efficiency. From TEM and EDS analysis of the formed films using the same method as for the particle, the deposited layers were observed to be composed of crystal grains with a size of about 10 nm, and zirconia was confirmed to be solid solution in a flattened state that was crushed in the direction of particle impact, regardless of the composite conditions. Therefore, it is appropriate to utilize the composite particle of the ordered mixture, which have superior deposition efficiency as the PJD injection particle.

In Chapter 6, PJD handpiece was designed for use by dentists in treatment. the micron-order HA particle shows a high degree of cohesiveness, which results in residual particle on the pipe transporting the particle from the particle tank to the handpiece. Therefore, the author developed a dental PJD handpiece without a particle-transporting pipe, utilizing a particle feed mechanism of tablet cutting. The experiments were conducted to investigate the relationship between the nozzle shape and the dispersion of the generated particle as well as the processing characteristics by using the designed device. As a result, the residual particle in the pipe could be cleared and the HA film was formed. Moreover, it was clarified that the particle dispersion characteristics depended on the nozzle shapes and that the film removal appeared under the conditions of the aggregated particle remained. This result showed that the particle dispersive characteristics needs to be considered in the PJD system design. By applying the elemental technology established in this chapter to future designs, it will be possible to realize a handpiece with high deposition efficiency that is easy to set up and handle by dentists.

In Chapter 7, the general conclusions of this study were summarized.

Study on machinability of amorphous alloys

by localized microstructure control

Chieko Kuji

Abstract

Amorphous alloys have random atomic structures without the long-periodic regularity of crystalline metals. Owing to their characteristic structure, in particular, Fe-based amorphous alloys exhibit excellent material properties such as high strength and toughness, high corrosion resistance, and high soft magnetic properties. The development of motors that take advantage of their high soft magnetic properties is expected to provide a clue to solving energy conservation problems. Nevertheless, high strength and toughness cause many machining defects, such as cutting faults, burrs, and excessive shear droop. The machining resistance is also high, and which results in severe tool wear. Although the various difficulties in machining have been pointed out, the novel machining method to overcome these problems has not yet been developed. In this study, we focused on the various properties of amorphous alloys are attributed to their random atomic structure. Therefore, we propose the new machining method, blanking, in which we transform the structure only the machining area of several micrometers by local heat treatment with an ultrashort pulsed laser. We attempted to develop a new machining method to improve the machinability without degrading the product quality. In order to obtain the basic knowledge necessary for the development of a new machining method using local heating, we have systematically prepared diverse microstructure by heat treatment and comprehensively investigated the effects of the microstructure on the mechanical and soft magnetic properties, and thus on the machinability. Finally, the effect of localized heat treatment by ultrashort pulsed laser is demonstrated, and the influence of microstructural changes due to local thermal effects on machining resistance and machining quality is discussed based on the obtained basic knowledge.

Chapter 1 is an overview of this study. The energy problems of modern society and the trends in the development of soft magnetic materials are introduced. Among various magnetic materials, we reviewed the amorphous alloys with excellent soft magnetic properties that have been developed in recent years. In addition, we survey the research trend of machining on amorphous alloys and explained the difficulty of machining that has been pointed out in the past. Finally, we present a research guideline for the development of the heat-treatment assisted machining method in this study.

In Chapter 2, the Fe-based amorphous alloy, Metglas 2605S-3A ($\text{Fe}_{77}\text{B}_{16}\text{Cr}_2\text{Si}_5$), was selected for this study. The systematic heat treatment was performed on the research material to clarify its microstructural change behavior. Thermal phase transformation behavior is investigated by differential scanning calorimetry (DSC), structural analysis was performed by X-ray diffraction (XRD), and the structures were directly observed by transmission electron microscopy (TEM). At a heating rate of 20 K/min, the selected amorphous alloy undergoes structural relaxation followed by heterogeneous nucleation of α -Fe in the extreme surface layer of the material (753 K). Uniform nucleation and growth of Fe_3B to a size of 50 nm in the interior of the sample (763 K) and nucleation and growth of α -Fe on the core of Fe_3B (773 K) are progressed. At temperatures above 873 K, the grains precipitate so densely that they are close to each other, and at high temperatures, 1073 K, the metastable crystalline phase grows into a stable phase and the grains become coarse. In this chapter, amorphous alloys with different microstructures are fabricated by homogeneous heat treatment. These samples are used to investigate the physical properties and machinability as a basis for the blanking method with the aid of local heat treatment.

In Chapter 3, mechanical properties such as Vickers hardness and tensile properties were evaluated on different microstructures amorphous alloys which were fabricated in the previous chapter. The results show that the Vickers hardness increases with structural relaxation and increases in the amount of crystal precipitation, 873 K sample showed the maximum hardness, while the coarsening of crystal grains results in softening due to the Hall-Petch effect. Moreover, the strength and toughness of the amorphous alloy gradually decreased with structural relaxation and the sparse precipitation of crystals, and the lowest values were found in the 773 K sample. The soft magnetic properties are favorable up to 763 K, where the primary crystals begin to precipitate, but decrease significantly from 773 K, where the composite crystals begin to precipitate, due to the influence of α -Fe.

In Chapter 4, the effects of slight differences in energy states and structures, such as structural relaxation, on shear deformation are analyzed using molecular dynamics (MD). Structural relaxation is difficult to identify by direct observation, and shear deformation plays a major role in the deformation of amorphous alloys. From the MD analysis, we found that the medium-range ordered structure, which is formed from the icosahedral short-range ordered structure causes changes in mechanical properties such as Young's modulus. In the structurally relaxed state, the amount of icosahedral short-range ordered structures characteristic of amorphous alloys is small. In addition, the specific icosahedral short-range order structure is rapidly reduced by shear strain. Such a decrease in the specific icosahedral ordered structure is thought to contribute to the change in mechanical properties due to structural relaxation. We also investigated the extensional behavior of the shear band generated by the compressive force from the tool, which determines the quality of the blanking process. As a result, the shear band propagates toward the cutting direction due to structural relaxation, suggesting that a high-quality machined surface can be obtained. In particular, in the structural relaxation model with more than 15% half-metals, the short-range ordered structure inside the shear band changes to a structure similar to BCC crystal.

In Chapter 5, cutting and blanking tests were performed on the amorphous alloys with different microstructures fabricated in Chapter 2. The effect of the change in mechanical properties caused by the change in microstructure on the machinability is discussed based on the findings of Chapters 2, 3, and 4. In both machining tests, the as-received specimens with high strength and toughness showed high machining resistance and many machining defects such as burrs. On the other hand, from the 713 K specimen with structural relaxation to the 763 K specimen, where the primary crystal precipitates, the machining mode changes to crack propagation due to embrittlement, which improves the machining quality and reduces the machining resistance. Note that the lowest machining resistance values for both cutting and blanking were obtained for the 763 K sample, where crystal nuclei start to appear. In the 773 K sample, where core-shell crystals are precipitated, the plastic deformation ability recovers as the number of precipitated crystals increases, slightly increasing the machining resistance, while the best machining quality is obtained without burrs or extension. In contrast, excessive grain precipitation leads to an increase in machining resistance and a worsening of machining quality.

In Chapter 6, we proposed a new blanking method using local heating by an ultrashort pulsed laser. Even when an ultrashort pulsed laser is used, which has a small thermal effect on the material, it is possible to heat treat an amorphous alloy to the extent that it crystallizes. It was also shown that localized crystallization does not degrade the magnetic properties of the material. Crystallization by laser irradiation proceeds by increasing the heat accumulation effect after the ablation of the irradiated area is completed. The crystallization range can be controlled by adjusting the repetition rate, pulse width, and power of the laser. The blanking resistance was reduced by structural relaxation and crystallization and the machined cross-section showed a favorable machined surface without defects that have been reported in the past. In this way, the usefulness of the blanking method with the aid of local heating was demonstrated.

Chapter 7 is the conclusion and summarizes the results of this study.

Research on the creation of three-dimensional nitrogen-diffused titanium structures using metal additive manufacturing

Yuta Itou

Abstract

Metallic medical implants are rapidly spreading as effective countermeasures against motor disorders and oral disorders. Therefore, they play an important role in the elderly patient prolongation of healthy life expectancy and improvement in the quality of life. In developed countries with aging populations, the demand for these products is expected to grow, but there are several issues to overcome. Cobalt-chromium alloy, which has excellent frictional properties, is used for the sliding part of artificial hip joints. However, the Implant-to-implant contact, and wear particles of cobalt-chromium alloy are generated, which adversely affect the human body. Therefore, we wanted to use titanium material, which has excellent biocompatibility, for the sliding part.

The wear resistance of titanium material is inferior to that of other metals, and it is necessary to improve the wear resistance. Therefore, we proposed a "three-dimensional nitrogen-diffused titanium structure" in which a nitrogen diffusion layer is arranged three-dimensionally inside the titanium. We have already succeeded in improving the wear resistance by sintering nitrided powder (Ti-TiN) using the discharge plasma sintering (SPS) method. However, since the SPS method uses a mold, machining is required after sintering.

Therefore, the author adopted the metal additive manufacturing (MAM) method, a kind of additive manufacturing technology, because the MAM method has a very high degree of freedom in design, which enables not only optimization of implant shape but also reduction of the number of processes because it can directly fabricate the desired shape, which leads to lower cost of made-to-order implants.

In this study, microstructural analysis and mechanical tests were performed on pure titanium (CPTi) and Ti-TiN structures fabricated by MAM method to clarify whether it is possible to fabricate three-dimensional nitrogen-diffused titanium structures for sliding parts by AM technology, and to demonstrate the feasibility of multifunctional implants.

This thesis is composed of the following six chapters.

In Chapter 1, the background and purpose of this thesis are introduced.

In Chapter 2, X-ray diffraction measurements and mechanical tests (friction test, tensile test, and Vickers hardness test) were conducted on Ti-TiN (550°C) with nitriding temperature of 550°C and CPTi. The X-ray diffraction results of Ti-TiN (550°C) powder showed a TiN peak, indicating that the pure titanium powder was nitrided. In the friction test, Ti-TiN (550°C) with a laser scanning speed of 100 mm/s showed the lowest friction coefficient among the four conditions. In the tensile test, the obtained stress-strain diagrams showed that all the specimens behaved like ductile materials, and the gradient of the graph at the time of fracture was steeper for Ti-TiN (550°C), suggesting that Ti-TiN (550°C) was stronger from the relationship of $E = \sigma / \epsilon$. Finally, in the Vickers hardness test, Ti-TiN (550°C) showed slightly greater Vickers hardness than CPTi regardless of the scanning speed, but there was no significant difference between these values.

In Chapter 3, we introduced a new powder (Ti-TiN (600°C)) with a higher nitriding temperature and a larger

proportion of nitrogen diffusion layer, and performed modeling, but the plate of foundation and the modeling object detached in the process. In order to clarify the cause of this problem, we measured the particle size distribution of the powders and the surface roughness of the top surface. The median diameters of the powders were larger for CPTi, Ti-TiN (550°C), and Ti-TiN (600°C), in that order. Surface roughness measurements later revealed that the surface roughness of the top surface of the Ti-TiN (600°C) model was the greatest. Therefore, it was considered that the sintering of Ti-TiN (600°C), which contains a lot of enlarged powders, affected the surface roughness, and hindered the fabrication process.

In Chapter 4, we considered that the enlargement of Ti-TiN (600°C) powder was the cause of the inability to form, and first classified Ti-TiN (550°C) powder and Ti-TiN (600°C) powder so that they were less than 32 μm . The molding of the Ti-TiN (550°C) powder after classification was completed, but the molding of the Ti-TiN (600°C) powder after classification was not completed because the plate and delamination occurred during the molding process. From the molding results, XRD, and SEM images of the delaminated surface, it was concluded that the cause of the failure was not the enlargement of the particles, but the inability of the laser to melt the powder sufficiently because the nitride layer occupied most of the Ti-TiN (600°C) powder and the melting point was high. Friction and wear tests were then conducted on CPTi, Ti-TiN (550°C), and Ti-TiN (600°C) with the same porosity, and the average friction coefficient decreased in the order of CPTi, Ti-TiN (550°C), and Ti-TiN (600°C). The amount of wear was found to be the lowest for Ti-TiN (550°C). Finally, in the Vickers hardness test, the Vickers hardness of Ti-TiN (600°C) showed the maximum value.

In Chapter 5, we focused on the crystal structure peculiar to the MAM method and the crystal structure of Ti-TiN. First, EBSD measurements were performed on cast and MAM CPTi specimens. As a result, there was no significant difference in the crystal structure of both specimens. Next, we examined the change in crystal structure with and without nitriding and at different nitriding temperatures and confirmed that the crystal structure changed to a needle-like structure when the powder was nitrided and fabricated by the MAM method, and that the needle-like crystals became finer when the nitriding temperature was increased. Finally, we investigated the feasibility of controlling the crystal direction by using a unidirectional laser scan. As a result, it was confirmed that crystals facing the same direction were dominant, indicating that it is possible to control the crystal direction by controlling the laser scanning direction in one direction.

In Chapter 6, summarized the results and conclusions of this thesis. Additionally, engineering and industrial significations of this study were stated.

Development of uniform dispersion classification technology for nano-precision grinding wheels

Yuu Kijima

Abstract

In recent years, a variety of information devices have been developing and spreading at a dizzying pace. The evolution of semiconductor devices has become indispensable in the development of high performance and high functionality in a wide range of devices, from information devices such as smartphones, optical drives, and SD cards, to medical devices such as MRIs, and precision devices used in various parts of cars. Currently, silicon (Si) semiconductors are the main material used to form integrated circuits in information equipment. On the other hand, in recent years, the performance of elemental semiconductors using Si has reached its limit, and in view of the fact that the world's electricity consumption is increasing by about 3% per year, there is a growing need for next-generation semiconductor devices that can save energy. Among them, single-crystal gallium nitride (GaN) has a band gap of 3.4 eV, which is larger than that of Si (1.2 eV), the current material, and has such characteristics as the ability to operate at high temperatures, fast electron saturation, and high breakdown voltage. Therefore, it is expected to be a semiconductor device with low power loss. The hardness of GaN is 9 on the Mohs scale, which is the second hardest after diamond. The hardness of GaN is 9 on the Mohs scale, which is the second hardest after diamond, so it is necessary to use diamond abrasives for grinding. Grinding is a method of mechanical processing using a grinding wheel made up of small abrasive grains. In grinding, the uniformity of the grain size of these small abrasive grains has three major advantages. The first is the suppression of machining defects. Scratches can be cited as a cause of machining defects in the grinding process. This is caused by the inclusion of coarse grains and grain aggregates in the processing area, and can be suppressed by making the particle size uniform. The second is to improve the processing capacity of the grinding process. If a grinding wheel with a small variation in grain diameter is used, it is possible to reduce the surface roughness by up to a quarter under the same grinding conditions with the same grain ratio. Third is the reduction of processing time. By making the abrasive grain diameter uniform, it is possible to reduce the surface roughness in the pre-processing and middle processing, and as a result, it is possible to reduce the processing time in the finishing process.

On the other hand, diamond particles are expensive, so in this study, we developed a technique called classification to separate small amounts of abrasive grains according to their grain size.

This paper is composed of the following five chapters.

In Chapter 1, the background and purpose of this paper are introduced.

In Chapter 2, numerical fluid dynamics analysis is performed to observe the decrease inside the experimental apparatus and to find the optimum conditions for classification. As a result of the analysis, it was found that the flow rate at inlet 2 has a significant effect on the pass rate, and that the pass rate decreases as the particle size increases. When the classification experiment was conducted under the conditions where the classification effect was confirmed by this analysis, there was no significant change in the particle size distribution before and after the classification experiment. When the filter after the classification experiment was observed, the abrasive grains were laminated on the adhesive surface, and it is thought that due to this lamination, the particles with a large diameter that should have been supplemented due to the loss of the supplementing force were not supplemented, but were supplemented at the outlet by the airflow, and thus there was no significant change in the particle size distribution before and after the classification experiment.

In Chapter 3, since classification may not have been performed correctly due to the stacked abrasive grains, we attempted to solve the problem by increasing the number of holes in the filter and increasing the adhesive surface. However, as in Chapter 2, there was no significant change in the particle size distribution before and after the classification experiment. Therefore, when the analysis of the laminated abrasive grains was conducted, it was found that the grain size distribution of the laminated abrasive grains did not change significantly from the grain size distribution before the classification experiment.

In Chapter 4, since the diamond particles used until the previous chapter had a narrow particle size distribution of 1.5~3 μm , and it was difficult to confirm the classification effect, a classification experiment was conducted using alumina particles with a wide particle size distribution of 0.3~20 μm . When the classification experiment was conducted, it was confirmed that the particles were accurately classified, but when the numerical fluid dynamics analysis was conducted under the same conditions, the results were not as good as in the experiment, and it was thought that an error occurred because the abrasive grains formed coarse abrasive grains. In addition, when the classification experiment similar to that in Chapter 3 was conducted, the classification effect was confirmed even though laminated abrasive grains could be seen on the bonded surface, so it was found that laminated abrasive grains were not one of the causes of the failure to classify diamond particles, and it was found necessary to reconsider the simulation conditions.

In addition, since the filter in this study was formed using a 3D printer, we checked whether the classification effect was affected by making the hole a special shape such as a star shape, and we were able to confirm a change, albeit a slight one. However, due to the small number of samples, it was not possible to determine why this change occurred.

Chapter 5 summarizes the results and conclusions of this paper.

Study on the Effect of Tool Texturing on the Tool Performance in Cutting Ti alloy

Atsuki Minakawa

Abstract

Titanium alloys have excellent corrosion resistance and mechanical properties, and their demand has been increasing in recent years in the medical and aerospace fields. However, due to their low thermal conductivity and high chemical activity, titanium alloys have the disadvantage of rapid tool wear in cutting processes. Therefore, there is a need to develop a new surface treatment technology with higher performance than the conventional surface treatment technology. In this paper, we first clarify the relationship between the machining conditions and the quality of the machined surface during the cutting of alloys. Furthermore, we propose LIPSS (Laser-induced periodic surface structures) over the coating as a new surface treatment. The properties of this coating + LIPSS surface are evaluated by contact angle measurement and friction test. Finally, cutting experiments are conducted to evaluate the effectiveness of creating this structure on the rake surface of cutting tools. This paper is composed of five chapters.

Chapter 1 is the introduction of this study. With the increasing demand for titanium alloys in the medical and aerospace fields, tool wear due to the hardness and low thermal conductivity of titanium alloys is a problem. A new surface treatment combining coating and surface microstructure creation is proposed as a method to improve this problem, and the purpose and structure of this thesis are described.

In Chapter 2, the relationship between the machining conditions and the effect on the surface of the machined part and the effect on the inside of the machined surface was investigated when a commonly used titanium alloy, Ti-6Al-4V alloy, was cut with ordinary coated tools. First, samples were prepared by cutting at different depths of cut, cutting speeds, and tool nose radius. The arithmetic mean height, which is a typical parameter of the machined surface, and the residual stress, which is a typical parameter of the machined surface, were measured. In addition, cutting simulation was conducted to examine the effect of temperature during cutting. As a result, it was found that there was a strong negative correlation between the arithmetic mean height and the nose radius of the tool, while there was little correlation between the depth of cut and the cutting speed. The effect of tool nose R on residual stress was also significant, with a larger effect on residual stress perpendicular to the tool scanning direction when the cutting speed was large, and a larger effect on residual stress in the tool scanning direction when the cutting speed was small. In the cutting simulation, it was found that there was a positive correlation between the amount of heat generated by cutting, depth of cut and cutting speed. It was also found that the depth of cut and the maximum temperature had a logarithmic relationship. These results suggest that by controlling the nose radius of the tool tip, i.e., by suppressing tool wear, it is possible to reduce the surface roughness of the work material and control residual stress.

In Chapter 3, LIPSS is applied to TiN and TiCN, which are the most commonly used coatings for cutting Ti alloys, and the effect of LIPSS on the coated surface is discussed. First, samples with coated + LIPSS surfaces were fabricated using a picosecond pulsed laser. We also simulated the electric field intensity to examine the difference in the formation of LIPSS on the fabricated samples. In addition, contact angle measurement and friction test were conducted to investigate the effect of LIPSS formation on the coated surface. First, the simulation of electric field intensity showed that the surface shape and refraction angle of the processed material affected the

ease of LIPSS formation. The contact angle was significantly reduced by the creation of LIPSS, suggesting that LIPSS may increase the affinity with the work fluid and reduce the load on the tool during cutting when it is applied to tools. The friction coefficient increased with the development of the LIPSS, but it was suggested that the friction coefficient could be reduced by developing a more fragile LIPSS.

In Chapter 4, LIPSS was created on the rake face of a TiN-coated tool to investigate the effect of LIPSS on the quality of the machined surface of the tool and workpiece. First, the LIPSS was created on the rake surface of a tool with the cutting edge facing downward in the horizontal and vertical directions. Using this tool, cutting tests were conducted at different depths of cut and cutting speeds to produce samples. The cutting resistance was measured during the cutting tests, and the tool wear and adhesion were evaluated after machining. The arithmetic mean height and residual stress of the samples were also measured. First of all, the maximum value of cutting resistance was significantly reduced in the LIPSS-generated tool. In addition, the effect of cutting resistance in the z-direction was larger when the depth of cut was small (about 10 μm), and the effect of cutting resistance in the y-direction was larger when the depth of cut was large ($\geq 50 \mu\text{m}$). This is thought to be due to the decrease in the contact angle of the rake surface of the tool, which increases the affinity of the tool with the machining fluid, decreases the temperature of the cutting area, and facilitates the evacuation of chips. The direction of LIPSS had almost no correlation with cutting resistance. In addition, it was found that the adherends on the tool adhered gently and the height of the adherends decreased. This is considered to be one of the factors for the reduction of cutting resistance. It was also found that cutting with the LIPSS tool had little effect on the arithmetic mean height and residual stress of the work piece.

In Chapter 5, the general conclusions of this study are summarized.

Study on atmospheric-pressure plasma assisted Powder Jet Deposition

Ryuki MORITA

Abstract

The human teeth, which are hard tissues in the human oral cavity, are important structures related to mastication, pronunciation, respiration, and facial features. The occlusal abnormalities from cavities or periodontal diseases have been pointed out that they can have adverse effects on the body and mind, so maintaining healthy teeth is extremely important for improving quality of life. In the current caries treatment method, the prepared cavities where the decayed part is removed are filled by a dental restoration made of metal, resin, etc., using medical adhesive. However, these dental restorations have problems of mismatching in mechanical characteristics, biocompatibility, and aesthetics; consequently, the use of the original materials of the human teeth is ideal for restorative treatment. To realize the ideal, a new dental treatment method has been proposed by using powder jet deposition (PJD) technique to make coatings on human teeth. With this technology, a powerful coating can be formed by colliding particles at high speed under room temperature and atmospheric pressure. By using particles of hydroxyapatite (HA), a major component of human hard tissue, films with properties similar to human enamel can be formed directly on human teeth. The PJD has not been applied to aesthetic dental treatment because the HA film hardly conceals the base color due to its transparency. Therefore, HA particles covered with ZrO₂ small particles (HA/ZrO₂ particles) were employed in the PJD to create an aesthetic composite film on the tooth. However, the shape of the HA/ZrO₂ particles changed and the thickness of the deposited film became low. In this study, we proposed the atmospheric-pressure plasma assisted PJD method as basic study to solve this problem and investigated the change in the deposition thickness.

Chapter 1 is the introduction of this thesis. The background of the present research, the achievements and remaining problems of the previous study and the objectives of the present study are described.

In Chapter 2, the surface modification phenomenon by plasma treatment was analyzed in order to apply the plasma technology to the PJD method. A negative correlation was found between the contact angle and the plasma treatment time, and a positive correlation was found between the contact angle and the waiting time. These results demonstrate that plasma surface modification has an effect on the removal of organic matter and hydrophilization of HA substrate surfaces. A policy for plasma application to substrates and stacked surfaces was established.

In Chapter 3, the effect of the plasma treatment on the HA substrate on the film thickness was examined and the mechanism was clarified. From the experimental results, it was found that plasma application to the substrate

was effective in increasing the film thickness. A positive correlation was found between the thickness and the plasma treatment time, and a negative correlation was found between the waiting time and the thickness. This is due to the removal of organic matter from the bonded surface by the surface modification effect of plasma and the high adsorption of hyaluronan to hydroxyl groups. We also analyzed the deposition mechanism of the PJD method and found that the initial layer formation took place around 10 s of HA injection time, and that the organic contamination on the substrate surface inhibited the film formation. Based on these results, we compared the effect of plasma application near the initial layer formation, and found that the film thickness near the initial layer differed by a factor of about 4 depending on whether plasma treatment was applied or not. The thickness of the film near the initial layer differed by a factor of about four depending on whether plasma treatment was applied or not. These results demonstrate that plasma application to the substrate makes a significant contribution to the smooth formation of the initial layer.

In Chapter 4, the effects of plasma treatment on the HA stacked surface on the film thickness were examined. A system that simultaneously performs plasma treatment and PJD deposition was constructed, and simultaneous plasma injection experiments were conducted. By applying plasma to the deposition layer, an improvement of about 10 μm was confirmed. The removal of organic matter from the sprayed particles and the smooth formation of the initial layer are considered to be the reasons for the improvement in film thickness. As a conclusion of this study, plasma application to the substrate and stacked surface was determined to be the optimal plasma assisted PJD method.

In Chapter 5, the general conclusions of this research are summarized.

2003～2021 年度 厨川研究室博士論文一覧

【2003 年度】

佐伯 優 (社会人)

パラレル研削法による軸対称非球面の加工に関する研究

(Study of processing of axisymmetric aspheric by Parallel Grinding Method)

西原 和成

平面ホーニングに関する研究(Research on Surface Honing)

山崎 繁一

超高速研削切断用ブレードの開発に関する研究

吉原 信人

非球面研削における検索模様に関する研究

【2006 年度】

加来 剛

電気粘性流体援用マイクロ非球面研磨に関する研究

(Study of electrorheological fluid-assisted polishing of micro aspherical surfaces)

鈴木 眞哉

超精密平面ホーニングに関する研究

(Study on Ultra-Precision Plane Honing)

野村 光由 (社会人)

超音波援用小径内面研削に関する研究

(Investigation of Ultrasonically Assisted Internal Grinding of Small Bore)

松浦 寛 (社会人)

レーザーコンディショニングに関する研究

(Study on Laser-Conditioning Method for Ultra-Precision Grinding)

【2008 年度】

太田 努 (社会人)

半導体材料の高効率超精密切削加工に関する研究

(Study of high-efficiency ultra-precision machining of semiconductor materials)

長池 康成 (社会人)

非球面形状の高精度測定に関する研究

(High-precision Measurements of Aspherical Lenses)

正木 健 (社会人)

ナノメートル精度マイクロ放電加工に関する研究

(Study of the nanometer accuracy micro-EDM)

【2009 年度】

周 天豊

Research on High-Precision Glass Molding Press for Optical Elements

(ガラス光学素子の高精度成形に関する研究)

立石 匠

電気粘性流体援用マイクロ超音波加工に関する研究 (Study on electrorheological fluid-assisted micro ultrasonic machining)

【2010 年度】

張 志宇

Ultraprecision Cutting of Reaction-Bonded Silicon Carbide

(反応焼結 SiC の超精密切削)

姚 鵬

High Efficiency Ultra-Precision Grinding of Fused Silica

(石英ガラスの高能率超精密研削に関する研究)

【2011 年度】

嶋田 慶太

振動研削に関する研究

(Study on Vibration Grinding)

【2013 年度】

劉 佩盈

Micro Electrical Discharge Machining of Reaction-Bonded Silicon Carbide

(反応焼結炭化珪素のマイクロ放電加工に関する研究)

西川 智弘

パウダージェットデポジションに関する研究(Investigation on Powder Jet Deposition)

【2014 年度】

徐 少林

Study on Ultrasonic Assisted Micro/Nano Texturing

(超音波振動援用マイクロ・ナノテクスチャリング創成に関する研究)

【2015 年度】

柴田 章弘 (社会人)

超短パルスレーザーによるガラス表面への微細構造創成に関する研究

(Nanofabrication on Glass by Ultrashort Pulse Laser Irradiation)

【2016 年度】

王 静思

Study on Material Removal Mechanism in Micro Ultrasonic Machining

(マイクロ超音波加工における材料除去メカニズムに関する研究)

小林 龍一

Study of Ultra-Precision Cutting of Amorphous Alloy

(アモルファス金属のマイクロ切削加工に関する研究)

【2017 年度】

鷺見 信行 (社会人)

機能性表面創成のためのプラズマショット法に関する研究

(Plasma-Shot Treatment for Functional Interface Generation)

孫 岳

**Friction Behaviour of Micro-Textured Surface under Mixed and Hydrodynamic
Lubrication**

(マイクロテクスチャ創成による混合潤滑および流体潤滑環境下における流体摩擦低減に関する研究)

【2018 年度】

小玉 脩平

**Study on Short-Pulsed Laser-Induced Periodic Surface Structures Assisted by
Mechanical Processing**

(機械加工援用短パルスレーザによる微細構造創成に関する研究)

【2019 年度】

鷹巣 良史 (社会人)

窒化ガリウムウエハの紫外線援用高効率・低ダメージ加工に関する研究

(Ultraviolet assisted processing of gallium nitride wafer for high efficiency and low damage.)

前花 英一 (社会人)

微細ラティスコーティングに関する研究(Studies on the Fine Lattice Coating)

【2021 年度】

石橋 信治

**Creation of Functional Three-Dimensional Structure with Metal Additive
Manufacturing Technology**

(金属積層造形技術による機能性 3次元構造創成に関する研究)

富江 瑛彦 (社会人)

歯科用パウダージェットデポジションにおける加工メカニズムに関する研究

(Study of Processing Mechanism in Dental Powder Jet Deposition)

久慈 千栄子 (社会人)

局在微細組織制御を援用したアモルファス合金の加工性向上に関する研究

(Study on machinability of amorphous alloys by localized microstructure control)

2002～2021 年度 厨川研究室修士論文一覧

【2002 年度】

小林 謙介

マイクロ超音波砥粒加工に関する研究

高木 剛

電気粘性流体を援用したマイクロ非球面研磨に関する研究

成田 歩

アブレイシブジェット加工に関する研究

【2003 年度】

加来 剛

電気粘性流体援用マイクロ非球面研磨に関する研究

金子 卓也

マイクロ放電加工に関する研究

鈴木 眞哉

超精密平面ホーニングに関する研究

西村 健

マイクロアイスジェットに関する研究

原 伸夫

極微粒ダイヤモンド砥石の電解コンディショニングに関する研究

【2004 年度】

小野 裕道

超精密加工面のナノトポグラフィーに関する研究

末松 和宏

マイクロ超音波砥粒加工に関する研究

安富 裕也

パウダージェットデポジションに関する研究

【2005 年度】

天羽 優

アブレイシブジェット加工法に関する研究

内田 和義

マイクロ放電加工による微小工具の成形

【2006 年度】

朝見 徹

単結晶シリコンのナノ切削における相転移現象の研究

立石 匠

マイクロ超音波加工に関する研究

【2007 年度】

児玉 壮平

小径ダイヤモンド砥石のレーザコンディショニングに関する研究

中野 裕之

軸対称非球面加工におけるナノトポグラフィーに関する研究

水谷 公一

パウダージェットデポジションに関する研究

【2008 年度】

大和田 崇

超精密マイクロ切削に関する研究

馬場 弘泰

超精密ダイヤモンド工具のナノ精度計測に関する研究

武藤 聖也

レーザ照射による半導体ウエハの加工欠陥修復に関する研究

嶋田 慶太

マイクロ超音波研削加工に関する研究

廣松 諒子

レーザ援用パウダージェットデポジションに関する研究

【2009 年度】

高橋 昌泰

ナノ精度研削加工のためのダイヤモンド砥石の開発

中川 裕太郎

ナノ切削による超薄型フレネルレンズ製造に関する研究

堀越 章弘

インデンテーション法を用いた微細形状創成に関する研究

【2010 年度】

小林 隆明

レーザ照射による表面テクスチャリングに関する研究

田中 裕介

マイクロ超精密切削に関する研究

西川 智弘

高速粒子衝突による加工現象に関する研究

横澤 成憲

ダイヤモンド工具のナノ精度形状創成に関する研究

木原 勇輝

複合粒子によるパウダージェットデポジション

【2011 年度】

阿部 卓朗

硬脆材料の延性モード研削に関する研究

片平 智博

超音波加工における材料除去メカニズムに関する研究

小林 史典

単結晶シリコン加工変質層のレーザ修復に関する研究

松本 薫

ナノ精度研削加工のための均一分散分級ダイヤモンド砥石の開発

渡辺 智之

ガラスプレス用 NiP メッキ金型の開発に関する研究

【2012 年度】

佐藤 慧

高速粒子衝突による付着現象の歯科治療への適用

萩原 隆行

複合粒子によるパウダージェットデポジションに関する研究

福島 靖規

レーザマイクロ加工に関する研究

ボロトフ セルゲイ

ナノ・マイクロ複合構造体の超音波援用成形法に関する研究

渡辺 健太

超精密揺動切削に関する研究

【2013 年度】

王 静思

Material Removal Mechanisms in Ultrasonic Machining

(超音波加工における材料除去メカニズムに関する研究)

大澤 晋作

レーザ援用切削に関する研究

小栗 健

超短パルスレーザによる表面微細周期構造創成に関する研究

郭 崇逸

硬脆材料の超精密平面ホーニングに関する研究

小林 和矢

均一分散分級ダイヤモンド砥石の開発と超仕上加工への応用展開

小林 龍一

屈折・回折複合ガラスレンズの超音波援用プレス成形に関する研究

菅井 亨

超音波振動切削に関する研究

【2014 年度】

富江 瑛彦

パウダージェットデポジションによる歯科治療に関する研究

橋詰 正春

ガラス表面への大規模微細構造創成に関する研究

益子 直人

レーザー援用マイクロ切削に関する研究

【2015 年度】

久慈 千栄子

パウダージェットデポジションによる歯科治療に関する研究

小玉 脩平

短パルスレーザーによる機能性インターフェース創成に関する研究

寺岡 祥平

レーザー援用マイクロ切削に関する研究

長谷川 翔

複合構造体創成と機能性に関する研究

渡邊 彩香

高硬度ウェハのテープ研削法の開発

渡部 龍

3D 超音波振動援用ミーリングに関する研究

【2016 年度】

石橋 信治

3D 金属積層造形に関する基礎的研究

大久 洋幸

複合粒子によるパウダージェットデポジションに関する研究

梶原 功貴

短パルスレーザーを用いた機能性表面創成

加藤 千拓

プラズマ放電改質に関する研究(旧：プラズマ放電研削に関する研究)

高柳 俊

レーザデバリングに関する研究

田中 悠

切削工具における微細表面構造に関する研究

角田 譲

紫外線援用による半導体基板加工に関する研究

平井 拓弥

超音波テクスチャリングによる機能性表面創成に関する研究

【2017 年度】

伊藤 貴仁

レーザマイクロ加工に関する研究

江川 諒仁

プラズマショット法における改質層形成機構に関する研究

康 媛

CO₂ Laser Repair of Cracks Caused by Ultrasonic Machining

(CO₂ レーザによる加工欠陥修復に関する研究)

京泉 朋希

プラズマショット法と研削加工による低摩擦・低摩耗面の創成

田村 駿人

窒化ガリウムウエハのテープ研削法の開発

佃 将希

インプラントの金属積層造形法に関する研究

永松 諒一

機能性マイクロ切削工具創成に関する研究

西村 俊亮

歯科用パウダージェットデポジションハンドピースの開発

【2018 年度】

清水 康平

局所加熱によるナノ結晶金属改質に関する研究

鈴木 一起

ウルトラファインバブルによる表面活性効果に関する研究

簾内 崇彰

複合粒子によるパウダージェットデポジションに関する研究

陳 子奇

超音波マイクロ切削による微細構造の創成に関する研究

原井 智広

ナノ秒パルスレーザーによるジルコニアインプラントへの生体適合性付与に関する研究

福井 一裕

レーザー誘起微細周期構造の摩擦特性に関する研究

松田 創太郎

摩擦界面におけるウルトラファインバブルの影響に関する研究

溝井 琢巳

金属積層造形法による高機能性インプラントの開発

【2019 年度】

折野 光汰

窒化ガリウムウエハのテープ CMP 研磨法に関する研究

柴田 頼人

プラズマショット法による工具の高機能化に関する研究

高瀬 稜平

短パルスレーザー照射による V 溝への微細構造創成に関する研究

山本 浩己

歯科用パウダージェットデポジションハンドピースの開発

瀧田 千秋 (医工学)

レーザー照射による機能性バイオインターフェース創成に関する研究

【2020 年度】

小西 健介

ウルトラファインバブルに関する研究

坂入 勇輔

ハイブリッドテクスチャリングによる高機能切削工具の開発

中善寺 優昂

根状多孔質構造体を有する高機能インプラントの開発

付 体強

Study on Micro-Textured Surface Generated by Ultrasonic Vibration-Assisted Cutting

(超音波マイクロ切削による微細構造創成に関する研究)

本郷 那美

パウダージェットデポジションによる歯冠色修復に関する研究

兼子 周也 (社会人)

微細構造を有する金属と生体組織との界面で生じる挙動解析

【2021 年度】

伊藤 優汰

金属積層造形法を用いた 3 次元窒素拡散チタン構造体創成に関する研究

木島 悠

ナノ精度研削砥石のための均一分散分級技術の開発

皆川 敦暉

Ti 合金の切削加工における工具テクスチャリングの影響

森田 隆輝

プラズマ援用パウダージェットデポジションに関する研究

【令和3年度卒業生】

	氏名	研究テーマ	所属先・勤務先
学部生	高野直輝	Effect of Multiscale Surface Texture Modification on the Adhesive Strength of 3D Printed Ti-6Al-4V and CFRP Hybrid Joints	進学（工学研究科）
	金井玲於	表面微細構造の濡れ性に関する研究	進学（工学研究科）
	寺田悠一郎	UFB によるバイオフィルムの剥離に関する研究	進学（工学研究科）
	山崎竜之介	3次元窒素拡散チタン構造体創成における積層現象解明	進学（工学研究科）
	渡邊純名	パルスレーザによる人工皮膚材料のテクスチャリング	進学（医工学研究科）
大学院 博士課程前期	伊藤優汰	金属積層造形法を用いた 3次元窒素拡散チタン構造体創成に関する研究	ヤマハ株式会社
	木島 悠	ナノ精度研削砥石のための均一分散分級技術の開発	パナソニック株式会社
	皆川敦暉	Ti合金の切削加工における工具テクスチャリングの影響	アクセンチュア株式会社
	森田隆輝	プラズマ援用パウダージェットデポジションに関する研究	三菱商事株式会社
博士課程後期	石橋信治	Creation of Functional Three-Dimensional Structure with Metal Additive Manufacturing Technology（金属積層造形技術による機能性3次元構造創成に関する研究）	株式会社ニコン
	富江瑛彦	歯科用パウダージェットデポジションにおける加工メカニズムに関する研究	株式会社ニコン （社会人ドクターとして所属）
	久慈千栄子	局在微細組織制御を援用したアモルファス合金の加工性向上に関する研究	いわて産業振興センター （社会人ドクターとして所属）

【研究室だより】

昨年も寒さ身に染みる厳しい冬となりましたが、最近ではすっかり春らしく、穏やかな気候に心む季節となりました。一昨年、昨年と引き続き新型コロナウイルスの猛威は収まらず、新しい生活様式も気付けば何十年も続く日常のようにすら感じられます。

当研究室は、昨年度をもって厨川先生が退官され、水谷研究室として新たな一歩を踏み出しました。厨川先生の長年のご貢献に感謝するとともに、新天地でのご活躍とご健康をお祈り申し上げます。水谷先生は研究や学生に対する指導、鞭撻に加え、新体制への準備で忙しい日々を送っています。藤田秘書には事務手続きなど研究室の仕事をサポートしていただいております。

現在研究室では、博士課程（社会人）が7名、博士課程後期学生は4名、博士課程前期（修士）学生は2年生が2名、1年生に留学生2名が加わり、IMACの1名と合わせて7名、学部4年生が2名となっております。

今年度も私たち水谷研究室一同、一丸となって日々研究をはじめあらゆる活動に励み、有意義な1年を過ごしていきたいと考えております。

令和4年5月

博士課程前期1年 寺田 悠一郎